Kinetic equations and non-equilibrium dynamics of magnons and charge-density waves

Dissertation
zur Erlangung des Doktorgrades
der Naturwissenschaften

vorgelegt beim Fachbereich Physik
der Johann Wolfang Goethe-Universität
in Frankfurt am Main

von
Viktor Hahn
aus Alexejewka

Frankfurt 2023
(D 30)

Vom Fachbereich Physik der

Johann Wolfgang Goethe - Universität als Dissertation angenommen.

Dekan: Prof. Dr. Roger Erb

Gutachter: Prof. Dr. Peter Kopietz
Prof. Dr. Falko Pientka

Datum der Disputation: 26.01.2024

Contents

1 Introduction

In this work two different types of systems will be investigated. The first one is a thin stripe of a ferrimagnet consisting of the magnetic insulator yttrium iron garnet (YIG, $Y_3Fe_5O_{12}$). This is a particularly interesting material because it features the lowest known spin-wave damping [1]. Spin waves or their quanta, magnons, can for example be excited by microwave magnetic fields. During the interaction of the microwave field with the YIG film, a photon with very small momentum close to $\mathbf{0}$ is annihilated and two magnons with wave vectors $\pm\boldsymbol{k}$ are created. A theory of parametrically pumped magnon gases was developed in the 1970's by Zakharov, L'vov, and Starobinets [2] building on the early works of Suhl [3] and Schlömann et al. [4]. Within this theory, which is called 'S-theory' in this context, non-linear kinetic equations were derived within the time-dependent self-consistent Hartree-Fock approximation [2, 5]. Pumped magnon gases in magnetic insulators often have been investigated by various authors using this theory [1, 6, 7, 8, 9, 10, 11, 12, 13, 14]. However, rather than taking into account microscopic collision integrals, a relaxation rate was introduced by hand into the equations of motion of the magnon distribution functions. While in Ref. [8] the collision integrals have been derived within Born approximation, the collision integrals have been evaluated only for the thermal equilibrium state. To my knowledge the effect of the microscopic collision integrals on the non-equilibrium magnon dynamics has not been discussed in the literature of the 1970's. A possible explanation is the complicated structure of the collision integrals which makes numerical calculations necessary to evaluate the collision integrals outside of the thermal equilibrium state. The collision integrals involve energy and momentum conservation which makes the numerical calculations technically challenging.

A particularly interesting observation is the formation of a Bose-Einstein condensate of magnons in a pumped magnon gas [12, 15, 16, 17]. Bose-Einstein condensation (BEC) is a fundamental quantum effect where a certain bosonic state becomes macroscopically occupied. Often - but not always - this state is characterized by the lowest eigenenergy of the system. Usually, extremely small temperatures on the order of mK are required for quantum gases to condense. Systems of bosonic quasi-particles may allow for higher densities of bosons. Because the number of quasi-particles is not conserved they can be injected into the system. Therefore, condensation can be observed at much higher temperatures in quasi-particle systems. In the case of YIG, BEC of magnons is even possible at room temperature [15, 17]. The injection of magnons leads to an increase of the chemical potential of the system due to the increased magnon density. When the chemical potential reaches the magnon energy in the minimum of the magnon dispersion during the thermalization process, a magnon condensate with a wave vector larger than zero forms at the bottom of the magnon spectrum. Essential for BEC is a $U(1)$ symmetry (particle conservation). For YIG there is an approximate $U(1)$ symmetry for magnons

near the bottom of the magnon spectrum due to the fact that the dispersion is very flat in that region.

Magnons and magnon BECs have potential technical applications for information transport, processing, and storage within magnonic devices [18, 19]. The magnon dispersion is more complex than for example the phonon dispersion. It is anisotropic even for isotropic materials. Magnons are highly non-linear. The higher complexity of magnon systems allows more physical mechanisms that can possibly be exploited for technical applications but it also leads to technical difficulties which also explains the current lack of technical applications. Magnonic devices could possibly offer functionalities that are unavailable for electronic or phononic devices. For instance, the magnon condensate can be utilized to generate coherent microwave radiation from incoherent electromagnetic radiation. Furthermore, there is no Joule heating making magnonic devices significantly more energy efficient than electronic devices [18, 19].

Another interesting topic which is also relevant for possible technical applications is opened up by hybrid quasi particles, i.e. the hybridized quanta of a quasi particle and another particle or quasi particle. For example, magnons and phonons hybridize due to magnon-phonon interactions. While the theoretical investigation of magnon-phonon interactions has started 1952 [20] the interest has waned over the years. Often in the literature the effects of magnon-phonon interactions were not taken into account explicitly and phonons have merely been considered as a heat bath. Recently, the topic of magnon-phonon interactions has gained renewed interest because new methods to study phenomena that are dominated by magnon-phonon interactions and hybridization of magnons and phonons became available by now [21, 22, 23, 24, 25, 26, 27]. Magnetoelastic bosons, the hybrid quasi-particles of magnons of phonons, combine properties of both particles and thus offer some potential technical applications in magnon spintronic devices. For example, they can have group velocities close to the phonon velocity and they have an increased decay length compared to magnons [22, 23, 27, 28]. These properties make them interesting as information carriers.

The second type of system investigated in this work are quasi-one-dimensional conductors where charge-density waves (CDWs) can be observed. Charge-density waves are a collective phenomenon which is characterized by a spatial modulation of the charge density. They arise due to a Peierls distortion where phonons with momenta close to $2k_F$ condense [29]. This leads to an additional periodic potential for the electrons resulting in the spatial modulation of the charge density,

$$\rho(x) = \rho_0 + \Delta\rho \sin(qx + \varphi). \tag{1.1}$$

Due to the lower energy of the CDW ground state compared to the translationally invariant ground state a spontaneous phase transition occurs below a critical temperature T_c, breaking the translation symmetry. The CDW ground state is a semiconducting state with a gap Δ in the electronic dispersion close to the Fermi surface. The order parameter Δ is proportional to the vacuum expectation values of the condensed phonon field with momentum $2k_F$. The case where the charge-density waves are incommensurate with the

lattice is particularly interesting,

$$k_F \neq \frac{n}{m}\frac{\pi}{a}, \tag{1.2}$$

where $n, m \in \mathbb{N}$ and a is the lattice constant. In this case the order parameter Δ is complex and the collective modes can be classified with amplitude modes and phase modes, while the electronic degrees of freedom are usually described by fermionic quasiparticles [29, 30].

The theoretical investigation of charge-density waves has a long history starting with the work of Lee, Rice, and Anderson in the 1970's [30, 31, 32] where the Fröhlich Hamiltonian [33] has been used as starting point and the random-phase approximation has been employed. However, a full theoretical understanding is still missing. For instance, in most older publications only a single phonon mode has been considered even though in some early papers many-phonon coupling has been introduced [32]. Furthermore, there are some topics that are controversial from the theoretical side, e.g. the role of long-range Coulomb interactions [34, 35, 36, 37]. During the following decades interest in CDWs has waned until recently they were found to be competing or co-existing excitations in high-T_c superconductors [38, 39, 40] and topological insulators [41]. CDWs have also been observed in graphene- and carbon-nanotube-based materials [42, 43]. The relation between the CDW phase and the superconducting phase could possibly shed some light on the physical mechanism which is responsible for high-T_c superconductivity and still remains elusive up to now.

In this work I use kinetic equations to investigate the systems mentioned above. The method is briefly explained in chapter 2. Within this approach, a set of equations of motions for particle distribution functions is obtained. In principle, the kinetic equations can be derived from the Heisenberg equations of motion in terms of n-point functions. However, usually one ends up with an infinite hierarchy of equations of motion for n-point functions. For example, a two-body interaction produces terms that contain four-point functions in the equations of motion of two-point functions. Now, the equations of motion of the four-point functions need to be derived in turn. They contain six-point functions, however. This leads to an infinite hierarchy of equations of motion. This set of equations contains the same information as the full Heisenberg equations of motion. By writing down the infinite hierarchy of equations of motion one does not gain any benefit regarding the complexity of the problem. For interacting systems the infinite hierarchy of kinetic equations is impossible to solve. In order to solve the problem one needs to decouple the equations of motion in an approximate way and truncate the infinite hierarchy at finite order. This is the main difficulty when working with the method of kinetic equations. Here, I use connected correlation functions instead of n-point functions to carry out this truncation. It will be shown in chapter 2 that working with connected correlations allows for a perturbative expansion in orders of the interaction strength [44]. Furthermore, a diagrammatic method to derive kinetic equations for connected equal-time correlation functions is introduced [44]. The method is based on the generating functional of connected correlations and also allows the treatment of anomalous correlation functions [45]. Finally, I present a truncation scheme to decouple the infinite hierarchy of equations of motion within a perturbative expansion in the

interaction vertices. Carrying out the expansion in connected correlations is essential for this truncation scheme [44]. From the numerical solution of these kinetic equations the time evolution of the correlation functions can be obtained. One advantage of the method of kinetic equations is that it is also valid far away from equilibrium. It is furthermore possible to find non-equilibrium stationary states in driven systems. These advantages make the method suited to investigate the properties of the systems which are relevant in this work. Of course, kinetic equations also have limitations. For instance, kinetic equations are not suited to investigate phase transitions. This is due to the fact that the method relies on a perturbative expansion. Close to critical points terms of all orders in the interaction strength become relevant; correlation lengths and the susceptibility diverge. By applying a perturbative expansion quantum correlations will be dramatically underestimated in this case.

In chapter 3 the method of expansion in connected correlation functions is used firstly to investigate magnons in the ferrimagnetic insulator YIG subject to a microwave pumping field. My investigation is motivated by the experiment [46] where the total magnon density is measured for different strengths of the external magnetic field. While the magnon density is approximately linear to the external field strength in a large parameter regime, there appear peak structures near a certain external field strength in the experiment. Existing theories that consider the magnon damping only phenomenologically [2, 5, 9, 11, 12] suggest an approximately linear dependence of the magnon density on the external field strength. In chapter 3 I derive kinetic equations where the magnon damping due to three-magnon processes is explicitly considered by calculating the microscopic collision integrals using an effective magnon Hamiltonian. In the strong pumping regime a non-equilibrium stationary state can be found numerically which agrees with the experimental observations.

In chapter 4 the kinetic theory for magnons is extended by also including the effects of magnon-phonon hybridization. Again, the motivation for my investigations are experimental observations. In a recent series of experiments [28, 47] an accumulation of magnetoelastic bosons in a thin YIG film has been found. To explain the accumulation effect, magnon-phonon interactions have to be included in the Hamiltonian so that kinetic equations for the correlation functions of magnetoelastic bosons can be derived. The stationary non-equilibrium state for magnetoelastic bosons close to the magnon-phonon hybridization region is obtained numerically. The results agree well with the experiment. Furthermore, it can be seen that the accumulation is purely incoherent.

In chapter 5 I use my kinetic equation approach to investigate a different type of system, charge-density waves in quasi-one-dimensional systems. The starting point is the Fröhlich Hamiltonian from which kinetic equations for electron and phonon correlation functions and the order parameter are derived. Linearizing the kinetic equations allows to obtain the properties of the collective modes. The frequencies and damping rates of amplitude and phase phonon modes can be obtained and compared to experimental measurements [48, 49]. I also investigate the relation of my kinetic theory with two existing theories, namely the Gaussian approximation [37] (which is equivalent to the random-phase approximation) and the phenomenological time-dependent Ginzburg-Landau equation [50, 51]. It turns out that the linearized kinetic equations have the

same form as the Ginzburg-Landau equations. It is also possible to investigate the time evolution of the order parameter out of equilibrium and the influence of Coulomb interactions as well as screening.

Finally, a short summary is presented in chapter 6.

Note that I use units where $\hbar$ is set to 1 throughout this work. Therefore, energies and frequencies have the same units.

2 Kinetic equations

This chapter is motivated by the Refs. [44, 45, 52, 56]. A systematic method to derive kinetic equations has been introduced in Refs. [44, 56] by Fricke. In Ref. [45] Wetterich proposed to use generating functionals for the derivation of a systematic method and in Ref. [52] the derivation has been done for 1PI connected functions. Here, a derivation based on the proposal of Ref. [45] is presented in terms of connected correlation functions analogously to Ref. [52]. I obtain the same formalism as introduced earlier in Refs. [44].

2.1 Introduction

The standard method to derive non-equilibrium kinetic equations is the Keldysh formalism [57, 58, 59, 60, 61, 62]. It is a Green's-function technique and leads to a Dyson equation. Within this formalism an integration path in complex time, the Keldysh contour, is introduced which is necessary to handle two-time correlations. However, the Keldysh formalism is inconvenient for my purpose because it produces differential equations for two-time correlations. Equal-time correlations can be obtained via the generalized Kadanoff-Baym ansatz [63]. The problem of this procedure is that it is cumbersome. For this reason, a different method to derive kinetic equations that produces directly equations of motion for equal-time correlations is developed in this chapter.

In principle, kinetic equations can be derived from the Heisenberg equations of motion. When calculating the commutator, terms of order m in the Hamiltonian will produce distribution functions of order $m+n-2$ in the equation of motion of n-point functions. For example, two-body interactions will produce four-point functions in the equation of motion of two-point functions. Thus, the equations of motion of four-point functions need to be calculated as well. In turn, higher order n-point functions appear in the equation of motion of four-point functions. In general, one ends up with an infinite hierarchy of equations of motions for n-point functions. For practical calculations this infinite hierarchy of equations of motion needs to be decoupled. The difficulty is not to derive the hierarchy of equations of motion but to find a consistent decoupling scheme. As pointed out by Fricke in Refs. [56, 44] it is convenient to formulate the kinetic equations in terms of connected n-point correlation functions because it allows for a systematic decoupling at arbitrary order in the interaction vertices.

In Ref. [44] a method that allows for a perturbative expansion of connected equal-time correlations in powers of connected correlations was developed. The idea is to carry out the calculations in terms of connected correlation functions instead of n-point functions and to employ the cluster expansion. The method takes into account correlations as dynamical quantities and produces an infinite hierarchy of coupled differential equations for connected equal-time correlations. Furthermore, the method provides a systematic

scheme to decouple these equations at arbitrary order of interaction vertices [56]. When using the method of Green's functions, a perturbative expansion in terms of one-particle functions is done. This is the main difference when using the method of expansion in powers of connected correlations where the collision term is expanded in powers of connected correlations instead. In principle, the method can be applied to two-time correlations as well [44].

An alternative approach to obtain the equal-time dynamics using generating functionals has been developed in Refs. [45, 52]. An exact functional differential equation for the time evolution of the generating functional of 1PI irreducible correlations is presented in Ref. [45]. The time evolution of 1PI irreducible correlations can be obtained from the time evolution of the generating functional. In Ref. [52] a diagrammatic method has been developed. The biggest difference between this method and the aforementioned method of expansion in connected correlations is that the expansions is carried out in 1PI irreducible correlations instead of connected correlations. Connected correlations can then in turn be obtained from the explicit expressions of the 1PI irreducible correlations. While this additional step makes the method more complicated, the expansion in 1PI irreducible vertices also allows non-perturbative expansions, as for example the large-N expansion [52].

2.2 Generating functional for connected correlation functions

As I am mainly interested in perturbative expansions in orders of interaction vertices, I develop a method based on generating functionals using connected correlations. The generating functional approach has the advantage of being mathematically more transparent than the formulation used in Ref. [44].

Let us consider a general Hamiltonian of the form

$$\mathcal{H} = \sum_{r,s} \sum_{\substack{q'_1,\ldots,q'_r \\ q_1,\ldots,q_s}} \Gamma^{r,s}_{q'_1,\ldots,q'_r;q_1,\ldots,q_s} \psi^\dagger_{q'_1} \ldots \psi^\dagger_{q'_r} \psi_{q_1} \ldots \psi_{q_s}, \tag{2.1}$$

where $\psi^\dagger_k$ and ψ_k are bosonic or fermionic creation and annihilation operators in the Heisenberg picture. In the following I consider the case of a purely bosonic and purely fermionic Hamiltonian separately.

2.2.1 Bosons

The generating functional for equal-time n-point functions can be defined as

$$Z[j;t] = \mathrm{Tr}\left[: \hat{\rho}_0 e^{\sum_k \left(\psi^\dagger_k(t) j_k + j^*_k \psi_k(t) \right)} : \right], \tag{2.2}$$

where ρ_0 is a density operator at time t_0, j_k are the source fields and : ... : is the normal-ordering operator. I will refer to the generating functional $Z[j;t]$ as partition function. Note that the time-ordering operator corresponds to the normal-ordering operator because I only consider equal-time n-point functions and therefore all operators appearing

in the definition of the generating functional (2.2) must be evaluated at time t. The equal-time n-point functions can be obtained from the partition function $Z[j;t]$ by repeatedly differentiating with respect to the source fields and evaluating the resulting expression for vanishing source fields. I am, however, interested only in the connected equal-time correlations functions. Therefore, I introduce the Schwinger functional

$$W[j;t] = \ln Z[j;t], \tag{2.3}$$

which is the generating functional of equal-time connected correlations. They can then be evaluated as [52]

$$\langle \psi^\dagger_{q'_1} \dots \psi^\dagger_{q'_r} \psi_{q_1} \dots \psi_{q_s} \rangle^c_t = \left. \frac{\delta^n W[j;t]}{\delta j_{q'_1} \cdots \delta j_{q'_r} \delta j^*_{q_1} \cdots \delta j^*_{q_s}} \right|_{j_i = j_i^* = 0}, \tag{2.4}$$

where the superscript c denotes connected correlation functions.

In order to find the time evolution of the partition function $Z[j;t]$ I apply the time derivative on Eq. (2.2) leading to the equation

$$\partial_t Z[j;t] = \mathrm{Tr}\left[: \hat{\rho}_0 \sum_k \left(\partial_t \psi^\dagger_k j_k + \partial_t j^*_k \psi_k \right) e^{\sum_k \left(\psi^\dagger_k j_k + j^*_k \psi_k \right)} : \right]. \tag{2.5}$$

The time evolution of the creation and annihilation operators can be obtained from the Heisenberg equations of motion

$$i\partial_t \psi_k = \left[\psi_k, \mathcal{H} \right] = F_k\left(\psi, \psi^\dagger \right), \tag{2.6a}$$

$$i\partial_t \psi^\dagger_k = \left[\psi^\dagger_k, \mathcal{H} \right] = F^*_k\left(\psi, \psi^\dagger \right), \tag{2.6b}$$

where for a general Hamiltonian of the form (2.1) the function F is given by

$$F_k\left(\psi, \psi^\dagger \right) = -i \sum_{r,s} r \sum_{\substack{q'_1,\dots,q'_{r-1} \\ q_1,\dots,q_s}} \Gamma^{r,s}_{q'_1,\dots,q'_{r-1},k;q_1,\dots,q_s} \psi^\dagger_{q'_1} \dots \psi^\dagger_{q'_{r-1}} \psi_{q_1} \dots \psi_{q_s}, \tag{2.7a}$$

$$F^*_k\left(\psi, \psi^\dagger \right) = i \sum_{r,s} s \sum_{\substack{q'_1,\dots,q'_r \\ q_1,\dots,q_{s-1}}} \Gamma^{r,s}_{q'_1,\dots,q'_r;q_1,\dots,q_{s-1},k} \psi^\dagger_{q'_1} \dots \psi^\dagger_{q'_r} \psi_{q_1} \dots \psi_{q_{s-1}}. \tag{2.7b}$$

Note that the terms in the sums of the above equations need to be normal ordered. Using the Heisenberg equations of motion (2.6) I find [45]

$$\begin{aligned} \partial_t Z[j;t] &= \sum_k j^*_k F_k\left[\psi, \psi^\dagger \right] Z[j;t] + \sum_k j_k F^*_k\left[\psi, \psi^\dagger \right] Z[j;t] \\ &= \sum_k j^*_k F_k\left[\frac{\delta}{\delta j^*}, \frac{\delta}{\delta j} \right] Z[j;t] + \sum_k j_k F^*_k\left[\frac{\delta}{\delta j^*}, \frac{\delta}{\delta j} \right] Z[j;t], \end{aligned} \tag{2.8}$$

where in the second line I used the fact that creation and annihilation operators ψ and $\psi^\dagger$ can be generated by applying derivatives with respect to j and j^* respectively. Using the fact that

$$\partial_t W\left[j;t\right] = \partial_t \ln Z\left[j;t\right] = \frac{1}{Z\left[j;t\right]} \partial_t Z\left[j;t\right], \tag{2.9}$$

the time evolution of the Schwinger functional $W\left[j;t\right]$ can be obtained from the time evolution of the partition function $Z\left[j;t\right]$. For this purpose I insert Eq. (2.8) on the right-hand side of the above equation. Then, in order to restore the expression $W\left[j;t\right]$, $1/Z\left[j;t\right]$ has to be permuted with $r+s-1$ partial derivatives from the r and s sums of $F_k\left[\frac{\delta}{\delta j^*}, \frac{\delta}{\delta j}\right]$ and $F_k^*\left[\frac{\delta}{\delta j^*}, \frac{\delta}{\delta j}\right]$. This procedure produces extra terms as $1/Z\left[j;t\right]$ does not commute with the partial derivatives with respect to the source fields.

As example, let us consider the Hamiltonian

$$\mathcal{H} = \sum_k \epsilon_k \psi_k^\dagger \psi_k + \sum_1 \sum_2 \sum_3 \left[\frac{1}{2} \Gamma^{\bar{\psi}\psi\psi}_{1;2,3} \psi^\dagger_{-1} \psi_2 \psi_3 + \frac{1}{2} \Gamma^{\bar{\psi}\bar{\psi}\psi}_{1,2;3} \psi^\dagger_{-1} \psi^\dagger_{-2} \psi_3 \right], \tag{2.10}$$

where I abbreviate $k_1 \equiv 1$, etc.. For this Hamiltonian I find using the Heisenberg equations of motion (2.6)

$$F_k\left[\frac{\delta}{\delta j^*}, \frac{\delta}{\delta j}\right] = -i\epsilon_k \frac{\delta}{\delta j_k^*} - i \sum_q \sum_{q'} \left(\frac{1}{2} \Gamma^{\bar{\psi}\psi\psi}_{-k;q,q'} \frac{\delta}{\delta j_q^*} \frac{\delta}{\delta j_{q'}^*} + \Gamma^{\bar{\psi}\bar{\psi}\psi}_{-k,-q;q'} \frac{\delta}{\delta j_q} \frac{\delta}{\delta j_{q'}^*} \right). \tag{2.11}$$

The procedure described above yields the time evolution of the Schwinger functional,

$$\begin{aligned}
\partial_t W\left[j;t\right] = & -i \sum_k \epsilon_k j_k^* \frac{\delta W\left[j;t\right]}{\delta j_k^*} \\
& -\frac{1}{2} i \sum_{k,q,q'} \Gamma^{\bar{\psi}\psi\psi}_{-k;q,q'} j_k^* \left[\frac{\delta^2 W\left[j;t\right]}{\delta j_q^* \delta j_{q'}^*} + \left(\frac{\delta W\left[j;t\right]}{\delta j_q^*} \right) \left(\frac{\delta W\left[j;t\right]}{\delta j_{q'}^*} \right) \right] \\
& -i \sum_{k,q,q'} \Gamma^{\bar{\psi}\bar{\psi}\psi}_{-k,q;q'} j_k^* \left[\frac{\delta^2 W\left[j;t\right]}{\delta j_q^* \delta j_{q'}} + \left(\frac{\delta W\left[j;t\right]}{\delta j_q^*} \right) \left(\frac{\delta W\left[j;t\right]}{\delta j_{q'}} \right) \right] + \text{c.c.}.
\end{aligned} \tag{2.12}$$

The structure of this equation is analogous to FRG equations: for three-point vertices a second derivative and the product of two first derivatives with respect to the source fields appear. The only difference to the FRG equations is the source field that appears as a factor in the above equation.

In order to obtain the time evolution of correlation functions from the time evolution of the Schwinger functional (2.12) one has to apply partial derivatives with respect to the source fields j^* and j and take the limit $j^* = j = 0$ which can be easily seen from Eq. (2.4). For example, the time evolution of the two-point correlation $\langle \psi_k^\dagger \psi_k \rangle_t^c$ can be obtained from

$$\partial_t \langle \psi_k^\dagger \psi_k \rangle_t^c = \left. \frac{\delta^2}{\delta j_k^* \delta j_k} \partial_t W\left[j;t\right] \right|_{j^*=j=0}. \tag{2.13}$$

Using Eq. (2.12) I get

$$\begin{aligned}
\partial_t \langle \psi_k^\dagger \psi_k \rangle_t^c &= -i\epsilon_k \left. \frac{\delta^2 W\left[j;t\right]}{\delta j_k \delta j_k^*} \right|_{j^*=j=0} + i\,\epsilon_k \left. \frac{\delta^2 W\left[j;t\right]}{\delta j_k^* \delta j_k} \right|_{j^*=j=0} \\
&+ \sum_{q,q'} \mathrm{Im} \Bigg[\Gamma^{\bar{\psi}\psi\psi}_{-k;q,q'} \left(\frac{\delta^3 W\left[j;t\right]}{\delta j_k \delta j_q^* \delta j_{q'}^*} + \frac{\delta^2 W\left[j;t\right]}{\delta j_k \delta j_q^*} \frac{\delta W\left[j;t\right]}{\delta j_{q'}^*} + \frac{\delta W\left[j;t\right]}{\delta j_q^*} \frac{\delta^2 W\left[j;t\right]}{\delta j_k \delta j_{q'}^*} \right) \\
&+ 2\Gamma^{\bar{\psi}\bar{\psi}\psi}_{-k,q;q'} \left(\frac{\delta^3 W\left[j;t\right]}{\delta j_k \delta j_q^* \delta j_{q'}} + \frac{\delta^2 W\left[j;t\right]}{\delta j_k \delta j_q^*} \frac{\delta W\left[j;t\right]}{\delta j_{q'}} + \frac{\delta W\left[j;t\right]}{\delta j_q^*} \frac{\delta^2 W\left[j;t\right]}{\delta j_k \delta j_{q'}} \right) \Bigg] \Bigg|_{j^*=j=0} \\
&= \sum_{q,q'} \mathrm{Im} \Bigg[\Gamma^{\bar{\psi}\psi\psi}_{-k;q,q'} \left(\langle \psi_k^\dagger \psi_q \psi_{q'} \rangle_t^c + \langle \psi_{q'} \rangle_t^c \langle \psi_k^\dagger \psi_q \rangle_t^c + \langle \psi_q \rangle_t^c \langle \psi_k^\dagger \psi_{q'} \rangle_t^c \right) \\
&+ 2\Gamma^{\bar{\psi}\bar{\psi}\psi}_{-k,q;q'} \left(\langle \psi_k^\dagger \psi_q \psi_{q'}^\dagger \rangle_t^c + \langle \psi_{q'}^\dagger \rangle_t^c \langle \psi_k^\dagger \psi_q \rangle_t^c + \langle \psi_q \rangle_t^c \langle \psi_k^\dagger \psi_{q'}^\dagger \rangle_t^c \right) \Bigg]. \qquad (2.14)
\end{aligned}$$

Returning to the general Hamiltonian (2.1), the time evolution of the Schwinger functional $W\left[j;t\right]$ can be derived by using the definition (2.3). Expressions of the form

$$e^{-W[j;t]} F_k \left[\frac{\delta}{\delta j^*}, \frac{\delta}{\delta j} \right] e^{W[j;t]} \qquad (2.15)$$

appear during the calculation. In total $r+s-1$ derivatives with respect to the source field from the expression $F_k \left[\frac{\delta}{\delta j^*}, \frac{\delta}{\delta j} \right]$ need to be applied to $e^{W[j;t]}$:

$$\begin{aligned}
& e^{-W[j;t]} \sum_{r,s} r \sum_{\substack{q'_1,\ldots,q'_{r-1} \\ q_1,\ldots,q_s}} \Gamma^{r,s}_{q'_1,\ldots,q'_{r-1},k;q_1,\ldots,q_s} \frac{\delta}{\delta j^*_{q_s}} \cdots \frac{\delta}{\delta j^*_{q_1}} \frac{\delta}{\delta j_{q'_{r-1}}} \cdots \frac{\delta}{\delta j_{q'_1}} e^{W[j;t]} \\
&= e^{-W[j;t]} \sum_{r,s} r \sum_{\substack{q'_1,\ldots,q'_{r-1} \\ q_1,\ldots,q_s}} \Gamma^{r,s}_{q'_1,\ldots,q'_{r-1},k;q_1,\ldots,q_s} \frac{\delta}{\delta j^*_{q_s}} \cdots \frac{\delta}{\delta j^*_{q_1}} \frac{\delta}{\delta j_{q'_{r-1}}} \cdots \frac{\delta}{\delta j_{q'_2}} \frac{\delta W\left[j;t\right]}{\delta j_{q'_1}} e^{W[j;t]} \\
&= e^{-W[j;t]} \sum_{r,s} r \sum_{\substack{q'_1,\ldots,q'_{r-1} \\ q_1,\ldots,q_s}} \Gamma^{r,s}_{q'_1,\ldots,q'_{r-1},k;q_1,\ldots,q_s} \frac{\delta}{\delta j^*_{q_s}} \cdots \frac{\delta}{\delta j^*_{q_1}} \frac{\delta}{\delta j_{q'_{r-1}}} \cdots \frac{\delta}{\delta j_{q'_3}} \\
&\qquad \times \left[\frac{\delta^2 W\left[j;t\right]}{\delta j_{q'_2} \delta j_{q'_1}} + \frac{\delta W\left[j;t\right]}{\delta j_{q'_1}} \frac{\delta W\left[j;t\right]}{\delta j_{q'_2}} \right] e^{W[j;t]} \\
&= \ldots
\end{aligned} \qquad (2.16)$$

Apparently, all possibilities to distribute $r+s-1$ derivatives with respect to the source field to the terms of the expression $F_k \left[\frac{\delta}{\delta j^*}, \frac{\delta}{\delta j} \right]$ need to be taken into account while keeping track of the ordering of the derivatives. In order to give an explicit expression I first define the partition P of a set I. It is defined as the set of all non-empty subsets J

of I so that all elements of I appear once. Therefore the subsets J need to be disjoint and fulfill the relation $\bigcup_{J\in P} J = I$. P_I refers to the set of all partitions of I. With this definition and

$$I_{r,s} \equiv \left\{q'_1, \ldots, q'_{r-1}, q_1, \ldots, q_s\right\} \tag{2.17}$$

I can write the above expression (2.16) as

$$\sum_{r,s} \sum_{P\in P_{I_{r,s}}} \sum_{\substack{q'_1,\ldots,q'_{r-1}\\ q_1,\ldots,q_s}} \Gamma^{r,s}_{q'_1,\ldots,q'_{r-1},k;q_1,\ldots,q_s} \prod_{J\in P} \frac{\delta^{\#J} W\left[j;t\right]}{\delta j^{(*)}_{j_1} \ldots \delta j^{(*)}_{j_{\#J}}}, \tag{2.18}$$

where $\#J$ is the cardinality of J. It will be shown below that for bosons the operators of correlation functions of order larger than two commute. For fermions the sign changes under a permutation of two operators. For two-point correlation functions the commutator relations are non-trivial. Therefore, in general it is necessary to keep track of the ordering of the derivatives. The above equation can be shown via induction. $j^{(*)}_{j_i}$ denotes either $j^*_{j_i}$ if the momentum j_i corresponds to one of the momenta $q'_1, \ldots, q'_r$ or j_{j_i} if j_i corresponds to one of the momenta $q_1, \ldots, q_s$. The time evolution of the Schwinger functional can now be written as

$$\begin{aligned}\partial_t W\left[j;t\right] = &-i \sum_k j^*_k \sum_{r,s} \sum_{P\in P_{I_{r,s}}} \sum_{\substack{q'_1,\ldots,q'_{r-1}\\ q_1,\ldots,q_s}} \Gamma^{r,s}_{q'_1,\ldots,q'_{r-1},k;q_1,\ldots,q_s} \prod_{J\in P} \frac{\delta^{\#J} W\left[j;t\right]}{\delta j^{(*)}_{j_1} \ldots \delta j^{(*)}_{j_{\#J}}} \\ &+i \sum_k j_k \sum_{r,s} \sum_{P\in P_{I'_{r,s}}} \sum_{\substack{q'_1,\ldots,q'_r\\ q_1,\ldots,q_{s-1}}} \Gamma^{r,s}_{q'_1,\ldots,q'_r;q_1,\ldots,q_{s-1},k} \prod_{J\in P} \frac{\delta^{\#J} W\left[j;t\right]}{\delta j^{(*)}_{j_1} \ldots \delta j^{(*)}_{j_{\#J}}},\end{aligned} \tag{2.19}$$

where

$$I'_{r,s} \equiv \left\{q'_1, \ldots, q'_r, q_1, \ldots, q_{s-1}\right\}. \tag{2.20}$$

The time evolution of correlation functions can be obtained from the time evolu-

tion (2.19) of the Schwinger functional using the relation (2.4),

$$\begin{aligned}
\partial_t \langle \psi^\dagger_{k'_1} \dots \psi^\dagger_{k'_r} \psi_{k_1} \dots \psi_{k_s} \rangle^c_t &= \left. \frac{\delta^n \partial_t W[j;t]}{\delta j_{k'_1} \cdots \delta j_{k'_r} \delta j^*_{k_1} \cdots \delta j^*_{k_s}} \right|_{j_i = j_i^* = 0} \\
&= -i \frac{\delta^n}{\delta j_{k'_1} \cdots \delta j_{k'_r} \delta j^*_{k_1} \cdots \delta j^*_{k_s}} \sum_k j^*_k \sum_{r,s} \sum_{P \in P_{I_{r,s}}} \\
&\quad \sum_{\substack{q'_1,\dots,q'_{r-1} \\ q_1,\dots,q_s}} \Gamma^{r,s}_{q'_1,\dots,q'_{r-1},k;q_1,\dots,q_s} \prod_{J \in P} \left. \frac{\delta^{\#J} W[j;t]}{\delta j^{(*)}_{j_1} \dots \delta j^{(*)}_{j_{\#J}}} \right|_{j_i = j_i^* = 0} \\
&\quad + i \frac{\delta^n}{\delta j_{k'_1} \cdots \delta j_{k'_r} \delta j^*_{k_1} \cdots \delta j^*_{k_s}} \sum_k j_k \sum_{r,s} \sum_{P \in P_{I'_{r,s}}} \\
&\quad \sum_{\substack{q'_1,\dots,q'_r \\ q_1,\dots,q_{s-1}}} \Gamma^{r,s}_{q'_1,\dots,q'_r;q_1,\dots,q_{s-1},k} \prod_{J \in P} \left. \frac{\delta^{\#J} W[j;t]}{\delta j^{(*)}_{j_1} \dots \delta j^{(*)}_{j_{\#J}}} \right|_{j_i = j_i^* = 0} .
\end{aligned} \tag{2.21}$$

It can be seen directly from this equation that only connected diagrams contribute to the equations of motion of connected correlation functions. As derivatives with respect to the source fields with labels k'_i or k_i are applied to the products over all partitions it is guaranteed that there is at least one correlation function within the product that contains at least one of the external labels k'_i or k_i and within each of the terms of the product there is at least one label of the interaction vertex. The above equation can also be written as

$$\begin{aligned}
&\partial_t \langle \psi^\dagger_{k'_1} \dots \psi^\dagger_{k'_r} \psi_{k_1} \dots \psi_{k_s} \rangle^c_t = \\
&\quad -i \sum_{r,s,l} \sum_{P \in P^c_{K_l + I_{r,s}}} \sum_{\substack{q'_1,\dots,q'_r \\ q_1,\dots,q_s}} \Gamma^{r,s}_{q'_1,\dots,q'_r;q_1,\dots,q_s} \prod_{J \in P} \left. \frac{\delta^{\#J} W[j;t]}{\delta j^{(*)}_{j_1} \dots \delta j^{(*)}_{j_{\#J}}} \right|_{j_i = j_i^* = 0} \\
&\quad +i \sum_{r,s,l} \sum_{P \in P^c_{K'_l + I'_{r,s}}} \sum_{\substack{q'_1,\dots,q'_r \\ q_1,\dots,q_s}} \Gamma^{r,s}_{q'_1,\dots,q'_r;q_1,\dots,q_s} \prod_{J \in P} \left. \frac{\delta^{\#J} W[j;t]}{\delta j^{(*)}_{j_1} \dots \delta j^{(*)}_{j_{\#J}}} \right|_{j_i = j_i^* = 0} ,
\end{aligned} \tag{2.22}$$

where

$$K_l \equiv \left\{ k'_1, \dots, k'_r, k_1, \dots, k_{l-1}, k_{l+1}, \dots, k_s \right\}, \tag{2.23a}$$

$$K'_l \equiv \left\{ k'_1, \dots, k'_{l-1}, k'_{l+1}, \dots, k'_r, k_1, \dots, k_s \right\}, \tag{2.23b}$$

and $P^c_{K_l + I_{r,s}}$ refers to the set of connected diagrams and is defined by

$$P^c_{K_l + I_{r,s}} = \left\{ P \in P_{K_l + I_{r,s}} | \forall J \in P : J \cap I_{r,s} \neq 0 \right\}. \tag{2.24}$$

The additional condition appears here, because in Eq. (2.21) terms that contain only derivations with respect to source fields from the set K_l or K_l' do not appear.

In section 2.3 it will be explained how the equations of motion of correlations can be obtained from the above equation (2.21). First, I want to consider the fermionic case and show that the Schwinger functional for fermions obeys an analogous time evolution equation.

2.2.2 Fermions

In order to describe Fermions I introduce the set $\{\Theta_{k_1}, \ldots, \Theta_{k_N}\}$ of N Grassmann variables. They obey the relation

$$\Theta_{k_i}\Theta_{k_j} + \Theta_{k_j}\Theta_{k_i} = 0, \tag{2.25}$$

for $i \neq j$. An arbitrary element g of the Grassmann algebra can be expressed by a series in Θ_k,

$$g = g^{(0)} + \sum_{k_1} g^{(1)}_{k_1}\Theta_{k_1} + \sum_{k_1<k_2} g^{(2)}_{k_1,k_2}\Theta_{k_1}\Theta_{k_2} + \ldots. \tag{2.26}$$

Furthermore, by using the above representation an average value of g can be defined as

$$\langle g\rangle \equiv \langle g^{(0)}\rangle + \sum_{k_1}\langle g^{(1)}_{k_1}\rangle\Theta_{k_1} + \sum_{k_1<k_2}\langle g^{(2)}_{k_1,k_2}\rangle\Theta_{k_1}\Theta_{k_2} + \ldots. \tag{2.27}$$

The exponential function and the logarithm of a Grassmann variable can both be defined via a series,

$$\exp(g) \equiv 1 + \sum_{n=1}^{\infty}\frac{1}{n!}g^n, \tag{2.28}$$

$$\ln(1+g) \equiv \sum_{n=1}^{\infty}\frac{(-1)^{n-1}}{n}g^n, \tag{2.29}$$

so that the generating functional can be defined analogously to the bosonic case as

$$Z[\Theta;t] = \mathrm{Tr}\left[:\hat{\rho}_0 e^{\sum_k\left(\Psi_k^\dagger\Theta_k + \Theta_k^*\Psi_k\right)}:\right]. \tag{2.30}$$

Note that due to the definition of the average value (2.27) $Z[\Theta;t]$ is a complicated functional of the Grassmann variables. Thus there is no reasonable physical interpretation of $Z[\Theta;t]$. It can be considered as a formal definition of a generating functional.

By defining

$$\begin{aligned}\partial_q\Theta_{k_1}\ldots\Theta_{k_N} \equiv{}& \delta_{q,k_1}\Theta_{k_2}\ldots\Theta_{k_N} - \delta_{q,k_2}\Theta_{k_1}\Theta_{k_3}\ldots\Theta_{k_N}\\ &+ (-1)^{N-1}\delta_{q,k_N}\Theta_{k_1}\ldots\Theta_{k_{N-1}},\end{aligned} \tag{2.31}$$

it is easy to see that the generating functional $Z[\Theta;t]$ can be used to produce fermionic n-point functions by applying partial derivatives, i.e.

$$\langle\Psi_{k_1}\ldots\Psi_{k_n}\rangle = \partial_{k_1}\ldots\partial_{k_n}\, Z[\Theta;t]|_{\Theta=\Theta^*=0}. \tag{2.32}$$

I conclude that with the definitions in this section fermions can be treated analogously to bosons with the need of an additional sign rule in the equations (2.19) and (2.21) which originates from the fact that two Grassmann variables do not commute (see Eq. (2.25)). Note that the above treatment does not forbid correlations that contain an odd number of fermionic operators. While correlations with even numbers of fermionic operators are in general complex valued, correlations with odd numbers of fermionic operators are Grassmann variables according to the above definitions. Because Grassmann valued correlations do not have a reasonable physical interpretation it may be forbidden for correlations to have an odd number of fermionic operators, i.e. I demand

$$\langle \Psi^\dagger_{k'_1} \dots \Psi^\dagger_{k'_r} \Psi_{k_1} \dots \Psi_{k_s} \rangle^c \equiv 0 \quad \forall r, s, n \in \mathbb{N} : r + s = 2n - 1, \tag{2.33}$$

for fermionic operators.

2.3 Diagrammatic method

In principle, equations of motion for connected correlations can be derived from the time evolution of $W[j;t]$ by applying derivatives with respect to the source fields to Eq. (2.19) and taking the limit where the source fields vanish. The resulting equation of motion is given by Eq. (2.21) and may be evaluated directly by hand. It is, however, more convenient to develop a diagrammatic method for this purpose because it reduces the amount of work and the chance of making mistakes. Note that the diagrams introduced in this chapter differ from Feynman diagrams because they represent contributions to the differential equations for connected equal-time correlations at time t. Therefore, they do not involve time or energy integration [44].

First of all, let us introduce external vertices as shown in Fig. 2.1. They represent a single creation or annihilation operator. The diagrammatic symbol for the interaction vertex is shown in Fig. 2.2 where incoming lines represent annihilation operators and outgoing lines represent creation operators. From the structure of the time evolution of $W[j;t]$ (2.12) it is obvious that only one interaction vertex appears in the time evolution of correlations contrary to Feynman diagrams. Furthermore, one of the derivations with respect to the source field must apply to the factor of $j^*_{\boldsymbol{k}}$ or $j_{\boldsymbol{k}}$ appearing in Eq. (2.21) as otherwise the terms drop out in the limit $j^* = j = 0$. Thus, at least one external vertex must be connected to the interaction vertex.

Figure 2.1: External vertices representing the creation operator $\psi^\dagger_{\boldsymbol{k}'_r}$ (left) or the annihilation operator $\psi_{\boldsymbol{k}_s}$ (right).

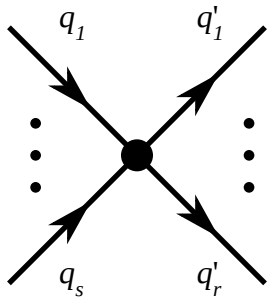

Figure 2.2: Interaction vertex with matrix element $\Gamma^{r,s}_{q'_1,\ldots,q'_r,q_1,\ldots,q_s}$.

Correlation bubbles representing connected correlations are denoted by the graphical symbol shown in Fig. 2.3. At this point, the behavior of connected correlations under permutation of the order of operators becomes relevant. The creation and annihilation operators obey the commutation relations

$$\{\psi_i, \psi_j\}_\pm = 0, \tag{2.34a}$$
$$\{\psi_i, \psi_j^\dagger\}_\pm = \delta_{i,j}, \tag{2.34b}$$

where $\{\ldots\}_\pm$ is the commutator if the operators are bosonic and the anti-commutator if the operators are fermionic. The commutation relation implies

$$\langle\psi_i\psi_j\rangle^c = \pm\langle\psi_j\psi_i\rangle^c, \tag{2.35a}$$
$$\langle\psi_i\psi_j^\dagger\rangle^c = \delta_{ij} \pm \langle\psi_j^\dagger\psi_i\rangle^c, \tag{2.35b}$$

where the upper sign is for bosons and the lower sign is for fermions. Correlations of order greater than two obey the trivial commutation relation [56, 44]

$$\langle\cdots\psi_i\psi_j\cdots\rangle^c = \pm\langle\cdots\psi_j\psi_i\cdots\rangle^c, \tag{2.36a}$$
$$\langle\cdots\psi_i\psi_j^\dagger\cdots\rangle^c = \pm\langle\cdots\psi_j^\dagger\psi_i\cdots\rangle^c, \tag{2.36b}$$

where, again, the upper sign is for bosons and the lower sign is for fermions. In order to show these equations I use the Baker-Campbell-Hausdorff formula,

$$e^{j_1\psi_1}e^{j_2\psi_2} = e^{j_2\psi_2}e^{j_1\psi_1}e^{j_1j_2\langle[\psi_1,\psi_2]\rangle}. \tag{2.37}$$

Note that the above relation is only valid if the commutator $[\psi_1, \psi_2]$ is complex valued. This is the case for bosons as well as fermions. From the definition of the generating functional (2.3) it follows for bosons it that

$$\ln\left(\mathrm{Tr}\left[:\hat\rho_0\left(\cdots e^{\psi_{q_i}j^*_{q_i}}e^{\psi_{q_j}j^*_{q_j}}\cdots\right):\right]\right) = \ln\left(\mathrm{Tr}\left[:\hat\rho_0\left(\cdots e^{\psi_{q_j}j^*_{q_j}}e^{\psi_{q_i}j^*_{q_i}}\cdots\right):\right]\right) + j^*_{q_i}j^*_{q_j}\,\mathrm{Tr}\left[\hat\rho_0\big[\psi_{q_i},\psi_{q_j}\big]\right], \tag{2.38a}$$

$$\ln\left(\mathrm{Tr}\left[:\hat\rho_0\left(\cdots e^{\psi_{q_i}j^*_{q_i}}e^{\psi^\dagger_{q_j}j_{q_j}}\cdots\right):\right]\right) = \ln\left(\mathrm{Tr}\left[:\hat\rho_0\left(\cdots e^{\psi^\dagger_{q_j}j_{q_j}}e^{\psi_{q_i}j^*_{q_i}}\cdots\right):\right]\right) + j^*_{q_i}j_{q_j}\,\mathrm{Tr}\left[\hat\rho_0\big[\psi_{q_i},\psi^\dagger_{q_j}\big]\right]. \tag{2.38b}$$

For fermions analogous expressions can be obtained but with the source fields being Grassman variables. As a result, a minus sign appears on the right-hand side of the equations,

$$\ln\left(\mathrm{Tr}\left[:\hat{\rho}_0\left(\cdots e^{\Psi_{q_i}\Theta^*_{q_i}}e^{\Psi_{q_j}\Theta^*_{q_j}}\cdots\right):\right]\right) = -\ln\left(\mathrm{Tr}\left[:\hat{\rho}_0\left(\cdots e^{\Psi_{q_j}\Theta^*_{q_j}}e^{\Psi_{q_i}\Theta^*_{q_i}}\cdots\right):\right]\right) + \Theta^*_{q_i}\Theta^*_{q_j}\,\mathrm{Tr}\left[\hat{\rho}_0\{\Psi_{q_i},\Psi_{q_j}\}\right], \quad (2.39a)$$

$$\ln\left(\mathrm{Tr}\left[:\hat{\rho}_0\left(\cdots e^{\Psi_{q_i}\Theta^*_{q_i}}e^{\Psi^\dagger_{q_j}\Theta_{q_j}}\cdots\right):\right]\right) = -\ln\left(\mathrm{Tr}\left[:\hat{\rho}_0\left(\cdots e^{\Psi^\dagger_{q_j}\Theta_{q_j}}e^{\Psi_{q_i}\Theta^*_{q_i}}\cdots\right):\right]\right) + \Theta^*_{q_i}\Theta_{q_j}\,\mathrm{Tr}\left[\hat{\rho}_0\{\Psi_{q_i},\Psi^\dagger_{q_j}\}\right]. \quad (2.39b)$$

It is now obvious how from the above Eqs. (2.38) and (2.39) the relations (2.35) and (2.36) follow: in order to obtain two-point correlations, two derivatives with respect to the source fields need to be applied. Thus, both of the prefactors of the second term on the right-hand side of Eqs. (2.38) or (2.39) cancel out to one and Eq. (2.35) is reproduced. For higher order correlations this term drops out and Eq. (2.36) is reproduced.

As we can see, permuting a creation and an annihilation operator in a two-point correlation results in an additional term while higher order correlations obey trivial commutation relations. Therefore, I denote only correlations of order greater than two with the correlation bubble 2.3. Following Ref. [44], I call correlations of order two 'contractions' and denote them with a different diagrammatic element shown in Fig. 2.4.

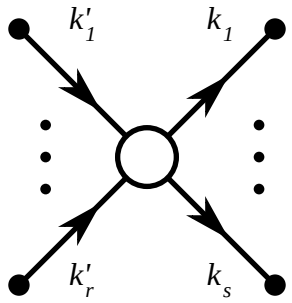

Figure 2.3: The correlation bubble representing the correlation $\langle\psi_{k_1}\ldots\psi_{k_s}\psi^\dagger_{k'_1}\ldots\psi^\dagger_{k'_r}\rangle^c$.

Figure 2.4: The contraction representing the two-point correlation $\langle\psi_{k_s}\psi^\dagger_{k'_r}\rangle^c$.

Let us assume that the interaction Hamiltonian has the form

$$\mathcal{V} = \frac{1}{r!s!} \sum \Gamma^{r,s}_{\boldsymbol{q}'_1,\ldots,\boldsymbol{q}'_r,\boldsymbol{q}_1,\ldots,\boldsymbol{q}_s} \psi^\dagger_{\boldsymbol{k}'_1} \ldots \psi^\dagger_{\boldsymbol{k}'_r} \psi_{\boldsymbol{k}_1} \ldots \psi_{\boldsymbol{k}_s}. \tag{2.40}$$

Usually, the interaction matrix $\Gamma^{r,s}_{\boldsymbol{q}'_1,\ldots,\boldsymbol{q}'_r,\boldsymbol{q}_1,\ldots,\boldsymbol{q}_s}$ fulfills certain symmetry properties so that permuting two creation or two annihilation operators of the interaction term gives the same contribution. Assuming this symmetry property, the prefactor $1/(r!s!)$ drops out. The reason is that by swapping and renaming the labels the diagram produces the same contribution. In this case it is sufficient to write down one unlabeled graph. The situation where two lines connected to a correlation bubble show into the same direction is an exception, however. In this case a prefactor of $1/2!$ remains [44], because swapping the labels does not produce the same contribution. I call these two lines a pair of equivalent lines.

Furthermore, if the Hamiltonian contains fermionic operators an additional sign rule is necessary due to the minus sign appearing in commutation relation (2.36) for fermionic correlations. The sign rule can be proven the same way as for usual Green's function methods. In order to read out the sign from the diagrams introduced in this work one needs to regroup the fermionic external vertices in pairs of creation and annihilation operators so that ψ_{q_1} and $\psi^\dagger_{q'_1}$ form the first pair, ψ_{q_2} and $\psi^\dagger_{q'_2}$ form the second pair, and so on. This procedure deforms the diagrams. The sign is then given by [44]

$$(-1)^n \, (-1)^L \,, \tag{2.41}$$

where n is the number of permutations that are necessary to normal order the external vertices and L is the number of fermionic loops in the deformed graphs.

Let us consider again Eq. (2.21) which shows how the equation of motion of connected correlations can be obtained from the time evolution of the Schwinger functional. A prefactor of i appears originating from the equation of motion (2.21). The equation of motion for correlations has the form

$$\begin{aligned} \left[\frac{\mathrm{d}}{\mathrm{d}t} + i\left(\epsilon_{\boldsymbol{k}_1} + \cdots + \epsilon_{\boldsymbol{k}_s} - \epsilon_{\boldsymbol{k}'_1} - \cdots - \epsilon_{\boldsymbol{k}'_r}\right)\right] \langle \psi_{\boldsymbol{k}_1} \cdots \psi_{\boldsymbol{k}_s} \psi^\dagger_{\boldsymbol{k}'_1} \cdots \psi^\dagger_{\boldsymbol{k}'_r} \rangle^c_t \\ = i \sum_{\text{diagrams}} \frac{1}{2^{n_e}} \sum_{\substack{\boldsymbol{q}'_1,\ldots,\boldsymbol{q}'_r \\ \boldsymbol{q}_1,\ldots,\boldsymbol{q}_s}} \Gamma^{r,s}_{\boldsymbol{q}'_1,\ldots,\boldsymbol{q}'_r,\boldsymbol{q}_1,\ldots,\boldsymbol{q}_s} X_{\text{diagram}}, \end{aligned} \tag{2.42}$$

where X_{diagram} is the collision term and n_e is the number of equivalent pairs of lines. The second term on the left-hand side of the above equation originates from the Heisenberg equations of motion for the quadratic part of the Hamiltonian. The collision term X_{diagram} contains the correlations that are produced by applying the derivatives with respect to the source fields to the generating functional $W[j;t]$ in Eq. (2.21). The diagrammatic rules need to take into account all possibilities to apply the partial derivatives with respect to the external source fields to the partitions over the source fields of the interaction vertex. Furthermore, it is important to keep track of the ordering of partial derivatives as they do not commute in general. X_{diagram} contains the product of all

correlations denoted by correlation bubbles and the contributions of the contractions. Furthermore, if fermionic operators appear in the correlations the sign (2.41) has to be taken into account as well. For fermionic operators the sign of the correlations depend on the ordering of the fermionic creations and annihilation operators. For this reason it is convenient to regroup the fermionic operators as pairs of creation and annihilation operators similar to the above described procedure to obtain the sign (2.41). At least one derivative needs to act on the source field $j^*_{\boldsymbol{k}}$ or $j_{\boldsymbol{k}}$ from Eq. (2.21) so that this factor drops out to 1 as otherwise the term vanishes in the limit $j^*_{\boldsymbol{k}} = j_{\boldsymbol{k}} = 0$. This derivative is diagrammatically represented by one contraction connected to the interaction vertex. Contractions that start and end at the interaction vertex give a normal-ordered contribution of the form $\langle \psi^\dagger_{\boldsymbol{q}_i} \psi_{\boldsymbol{q}_j} \rangle^c$ while contraction that start and end at external vertices give an anti-normal-ordered contribution of the form $\langle \psi_{\boldsymbol{k}'_i} \psi^\dagger_{\boldsymbol{k}'_j} \rangle^c$. Furthermore, if off-diagonal correlation functions do not vanish there are also contributions that contain $\langle \psi_{\boldsymbol{q}_i} \psi_{\boldsymbol{q}_j} \rangle^c$ and $\langle \psi^\dagger_{\boldsymbol{q}_i} \psi^\dagger_{\boldsymbol{q}_j} \rangle^c$ which counts as a pair of equivalent lines regarding the rule for the combinatorial prefactor.

Let us now consider the remaining contributions $\tilde{X}_{\text{diagram}}$ from contractions which can be diagrammatically written as Fig. 2.5. A total number of $r + s$ external vertices is connected to the interaction vertex via contractions. The first contraction needs to cancel out the prefactor of $j^*_{\boldsymbol{k}}$ or $j_{\boldsymbol{k}}$. Otherwise the term vanishes in the limit $j^*_{\boldsymbol{k}} = j_{\boldsymbol{k}} = 0$. Therefore, up to $r + s - 1$ contractions appear in those contributions. Contractions with the creation operators are normal ordered and contractions with annihilation operators are anti-normal ordered. All possibilities of assigning the derivatives with respect to the source fields to the factors of the form $\frac{\delta W}{\delta j_{\boldsymbol{q}'_i}}$ or $\frac{\delta W}{\delta j^*_{\boldsymbol{q}_j}}$ appearing in the time evolution of the generating functional (2.19) need to be taken into account. Without the presence of anomalous terms $\tilde{X}_{\text{diagram}}$ consists of all terms that are the product of up to $r + s - 1$ terms of the form $\left(-\langle \psi^\dagger_{\boldsymbol{q}_1} \psi_{\boldsymbol{k}_1} \rangle^c_t\right)$, …, $\left(-\langle \psi^\dagger_{\boldsymbol{q}_s} \psi_{\boldsymbol{k}_s} \rangle^c_t\right)$, $\langle \psi_{\boldsymbol{q}'_1} \psi^\dagger_{\boldsymbol{k}'_1} \rangle^c_t$, …, $\langle \psi_{\boldsymbol{q}'_r} \psi^\dagger_{\boldsymbol{k}'_r} \rangle^c_t$. The minus signs appear here because terms with an even number of normal ordered correlations originate from the first term in Eq. (2.21) and terms with an odd number of normal ordered correlations originate from the second term. Furthermore, if anomalous two-point correlations exist, i.e. correlations of the form $\langle \psi_{-\boldsymbol{q}_i} \psi_{\boldsymbol{k}_i} \rangle^c$ or $\langle \psi^\dagger_{\boldsymbol{k}_i} \psi^\dagger_{-\boldsymbol{q}_i} \rangle^c$, contractions can be replaced by the anomalous two-point correlations. All possibilities of replacing contractions with anomalous two-point correlations need to be taken into account as well. Note that at least one contraction needs to connect the interaction vertex with an external vertex as explained above. In the absence of anomalous two-point correlations $\tilde{X}_{\text{diagram}}$ consists of the sum over all products of up to $r + s - 1$ contractions. It is easy to see that the product

$$\begin{aligned} &\left(-\langle \psi_{\boldsymbol{k}_1} \psi^\dagger_{\boldsymbol{q}_1} \rangle^c_t + \delta_{\boldsymbol{k}_1, \boldsymbol{q}_1}\right) \cdots \left(-\langle \psi_{\boldsymbol{k}_s} \psi^\dagger_{\boldsymbol{q}_s} \rangle^c_t + \delta_{\boldsymbol{k}_s, \boldsymbol{q}_s}\right) \\ &\quad \times \left(\langle \psi^\dagger_{\boldsymbol{k}'_1} \psi_{\boldsymbol{q}'_1} \rangle^c_t + \delta_{\boldsymbol{k}'_1, \boldsymbol{q}'_1}\right) \cdots \left(\langle \psi^\dagger_{\boldsymbol{k}'_r} \psi_{\boldsymbol{q}'_r} \rangle^c_t + \delta_{\boldsymbol{k}'_r, \boldsymbol{q}'_r}\right) \end{aligned} \tag{2.43}$$

contains all these terms but in addition there is a term which is the product of all contractions, $\langle \psi_{\boldsymbol{k}_1} \psi^\dagger_{\boldsymbol{q}_1} \rangle^c_t \cdots \langle \psi_{\boldsymbol{k}_s} \psi^\dagger_{\boldsymbol{q}_s} \rangle^c_t \left(-\langle \psi^\dagger_{\boldsymbol{k}'_1} \psi_{\boldsymbol{q}'_1} \rangle^c_t\right) \cdots \left(-\langle \psi^\dagger_{\boldsymbol{k}'_r} \psi_{\boldsymbol{q}'_r} \rangle^c_t\right)$. Therefore, by adding

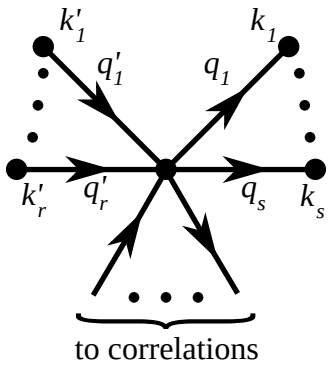

Figure 2.5: Schematic diagram showing the interaction part of diagrams. There are r incoming and s outgoing lines connecting the interaction vertex with external vertices. The other lines go to correlation bubbles which can also be connected to further external vertices.

and subtracting this term the contributions that do not involve anomalous correlations can be written in the compact form

$$\begin{aligned}
\tilde{X}_{\text{diagram}} &= \left(-\langle\psi_{\boldsymbol{k}_1}\psi^\dagger_{\boldsymbol{q}_1}\rangle^c_t + \delta_{\boldsymbol{k}_1,\boldsymbol{q}_1}\right)\cdots\left(-\langle\psi_{\boldsymbol{k}_s}\psi^\dagger_{\boldsymbol{q}_s}\rangle^c_t + \delta_{\boldsymbol{k}_s,\boldsymbol{q}_s}\right) \\
&\quad\times\left(\langle\psi^\dagger_{\boldsymbol{k}'_1}\psi_{\boldsymbol{q}'_1}\rangle^c_t + \delta_{\boldsymbol{k}'_1,\boldsymbol{q}'_1}\right)\cdots\left(\langle\psi^\dagger_{\boldsymbol{k}'_r}\psi_{\boldsymbol{q}'_r}\rangle^c_t + \delta_{\boldsymbol{k}'_r,\boldsymbol{q}'_r}\right) \\
&\quad-\langle\psi_{\boldsymbol{k}_1}\psi^\dagger_{\boldsymbol{q}_1}\rangle^c_t\cdots\langle\psi_{\boldsymbol{k}_s}\psi^\dagger_{\boldsymbol{q}_s}\rangle^c_t\left(-\langle\psi^\dagger_{\boldsymbol{k}'_1}\psi_{\boldsymbol{q}'_1}\rangle^c_t\right)\cdots\left(-\langle\psi^\dagger_{\boldsymbol{k}'_r}\psi_{\boldsymbol{q}'_r}\rangle^c_t\right) \\
&= \left(-\langle\psi^\dagger_{\boldsymbol{q}_1}\psi_{\boldsymbol{k}_1}\rangle^c_t\right)\cdots\left(-\langle\psi^\dagger_{\boldsymbol{q}_s}\psi_{\boldsymbol{k}_s}\rangle^c_t\right)\langle\psi_{\boldsymbol{q}'_1}\psi^\dagger_{\boldsymbol{k}'_1}\rangle^c_t\cdots\langle\psi_{\boldsymbol{q}'_r}\psi^\dagger_{\boldsymbol{k}'_r}\rangle^c_t \\
&\quad-\langle\psi_{\boldsymbol{k}_1}\psi^\dagger_{\boldsymbol{q}_1}\rangle^c_t\cdots\langle\psi_{\boldsymbol{k}_s}\psi^\dagger_{\boldsymbol{q}_s}\rangle^c_t\left(-\langle\psi^\dagger_{\boldsymbol{k}'_1}\psi_{\boldsymbol{q}'_1}\rangle^c_t\right)\cdots\left(-\langle\psi^\dagger_{\boldsymbol{k}'_r}\psi_{\boldsymbol{q}'_r}\rangle^c_t\right). \quad (2.44)
\end{aligned}$$

Lastly, only connected diagrams need to be considered as unconnected diagrams do not contribute to the time evolution of connected correlations. This is related to the structure of the time evolution of the Schwinger functional (2.19) and has already been explained in the end of section 2.2.1. The diagrammatic rules introduces here via Eq. (2.21) coincide with the rules obtained in Ref. [44] with the use of the cluster expansion instead of generating functionals.

In summary, the contributions to the collision term X_{diagram} are

1. the product of all correlation bubbles,
2. contractions that start and end at the interaction vertex in the normal ordered form $\langle\psi^\dagger_{\boldsymbol{q}_i}\psi_{\boldsymbol{q}_j}\rangle^c$,
3. contraction that start and end at external vertices in the anti-normal ordered form $\langle\psi_{\boldsymbol{k}'_i}\psi^\dagger_{\boldsymbol{k}'_j}\rangle^c$,

4. the contribution of the remaining contractions between the interaction vertex and the external vertices $\tilde{X}_{\text{diagram}}$ given by Eq. (2.44). If anomalous two-point correlations do not vanish all possibilities to replace contractions with anomalous two-point correlations in Eq. (2.44) have to be taken into account as well.

As we have seen, the diagrams introduced in this chapter do not involve energy integration contrary to Feynman diagrams. Furthermore, lines that begin or end at the interaction vertex involve a momentum integration. The diagrams have a different meaning than Feynman diagrams: they represent contributions to the equation of motion of correlation functions.

3 Damping of magnons in YIG

The material presented in this chapter is based on Refs. [53, 54].

3.1 Introduction

In this chapter the method of expansion in connected correlations developed in the previous chapter 2 is applied to the magnetic insulator yttrium iron garnet (YIG) in order to develop a microscopic kinetic theory that describes a gas of parametrically excited magnons. My investigation is motivated by the experiment [46] where magnons are excited with an oscillating external magnetic field $H_1(t)$. For a certain strength of the static magnetic field H_0 the spin-pumping effect is enhanced which can be observed by the increased magnon density in the stationary non-equilibrium state. This external field strength lies very close to the confluence magnetic field strength where confluence processes of two parametrically pumped magnons with the same momenta become kinematically possible. It is therefore expected that this type of magnon-magnon interaction is relevant for the explanation of the experimental observations.

A common method to observe the magnon density in YIG films which is also employed in the experiment [46] utilizes the inverse spin-Hall effect (ISHE) [64]. For this purpose a platinum layer is added on top of the YIG film. Due to the ISHE a spin current within the YIG film is converted to an electric current perpendicular to the external magnetic field and the direction of the spin current. The electric current induced in the platinum layer can be directly measured and is proportional to the total magnon density. The sensitivity for all magnons independent of the magnon energies or wave vectors is considered as an advantage of this method [65]. The ISHE can be explained analogously to the direct spin-Hall effect because both effects are caused by relativistic spin-orbit interactions [64]. The strong potential of atomic nuclei in solids further enhances this effect [66].

The system I investigate in this chapter is a spin system. The method developed in the previous chapter can only be applied to operators satisfying canonical commutator relations, though. Therefore, the method cannot be applied directly to a spin Hamiltonian. The solution for this problem is to expand the spin operators in terms of bosonic operators as it can be done with the Holstein-Primakoff transformation [67]. In the next section an effective bosonic Hamiltonian is derived that is capable of describing the relevant physics of the pumped magnon gas.

3.2 Effective Hamiltonian

I describe the pumped magnon gas in YIG by an effective spin Hamiltonian which is capable of describing the relevant physics [1, 11, 12, 13, 21, 68, 69, 70]

$$\mathcal{H}_m = -\frac{1}{2}\sum_{ij}\sum_{\alpha\beta}\left(J_{ij}\delta_{\alpha\beta} + D_{ij}^{\alpha\beta}\right) S_i^\alpha S_j^\beta - \left[h_0 + h_1\cos\left(\omega_0 t\right)\right]\sum_i S_i^z. \tag{3.1}$$

The spins are localized on a cubic lattice with lattice spacing $a \approx 12.376$ Å. The indices $i, j = 1, \ldots, N$ label the lattice sites $\boldsymbol{r}_i$ and $\boldsymbol{r}_j$ and $\alpha, \beta = x, y, z$ label the three components of the spin operators S_i^α. $J_{ij} = J\left(\boldsymbol{r}_i - \boldsymbol{r}_j\right)$ is the exchange coupling described within the nearest neighbor approximation where it has the value $J \approx 3.19$ K if i and j are nearest neighbors and vanishes otherwise. Furthermore, the dipolar tensor $D_{ij}^{\alpha\beta} = D^{\alpha\beta}\left(\boldsymbol{r}_i - \boldsymbol{r}_j\right)$ is given by [69, 71]

$$D_{ij}^{\alpha\beta} = \left(1 - \delta_{ij}\right)\frac{\mu^2}{\left|\boldsymbol{r}_{ij}\right|^3}\left[3\hat{r}_{ij}^\alpha \hat{r}_{ij}^\beta - \delta^{\alpha\beta}\right], \tag{3.2}$$

where $\boldsymbol{r}_{ij} = \boldsymbol{r}_i - \boldsymbol{r}_j$ and $\hat{\boldsymbol{r}}_{ij} = \boldsymbol{r}_{ij}/\left|\boldsymbol{r}_{ij}\right|$. h_0 denotes the Zeeman energy associated with the static external magnetic field $\mathbf{H}_0$ which is applied in z direction. Thus, the classical ground state is a saturated ferromagnet and the direction of the macroscopic magnetization is the z direction. In the setup of the so called parallel pumping geometry an oscillating microwave field H_1 is applied parallel to the static magnetic field H_0. The oscillating field H_1 is assumed to be small compared to the static field H_0 so that both fields point in the z direction. I consider an infinitely long stripe of YIG with thickness d and width $w \gg d$. The geometry is shown in Fig. 3.1. At $T = 0$ only the bulk mode may be considered so that the complex structure of the unit cell does not have to be taken into account explicitly. Instead, an effective cubic Hamiltonian can be used with the total spin of one unit cell being $S_t = 16$. However, the experiment has been performed at room temperature. Following Refs. [69, 72] I use the saturation magnetization $4\pi M_s = 175$ mT of YIG at room temperature ($T = 290$ K) to determine the effective spin as $S = \frac{M_s a^3}{\mu} \approx 14.2$ assuming that the g-factor is equal to two.

In order to apply the method developed in the previous chapter 2 an effective bosonic Hamiltonian is required. Therefore, the spin Hamiltonian (3.1) is bosonized via the Holstein-Primakoff transformation [67]

$$S_i^+ = \sqrt{2S}\sqrt{1 - \frac{b_i^\dagger b_i}{2S}}\, b_i = \sqrt{2S}\left[b_i - \frac{b_i^\dagger b_i b_i}{4S} + \ldots\right], \tag{3.3a}$$

$$S_i^- = \sqrt{2S}\, b_i^\dagger\sqrt{1 - \frac{b_i^\dagger b_i}{2S}} = \sqrt{2S}\left[b_i^\dagger - \frac{b_i^\dagger b_i^\dagger b_i}{4S} + \ldots\right], \tag{3.3b}$$

$$S_i^z = S - b_i^\dagger b_i. \tag{3.3c}$$

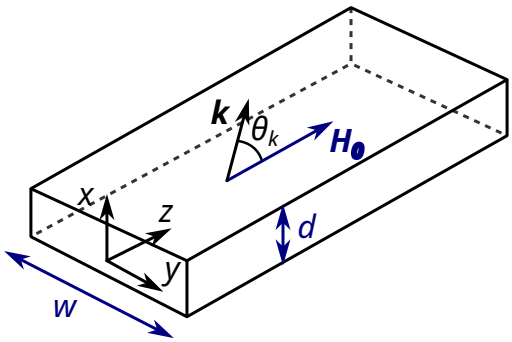

Figure 3.1: Sketch of the geometry I consider in this and the following chapter. The YIG stripe is infinitely long and has the thickness d and width $w \gg d$. The static magnetic field $\mathbf{H}_0$ is oriented along the z-direction. Wave vectors $\boldsymbol{k}$ are considered within the y-z-plane and the angle $\Theta_{\boldsymbol{k}}$ of the wave vector is measured towards the z-axis.

The resulting effective boson Hamiltonian can be expanded with respect to the small parameter $1/S$,

$$\mathcal{H}_m(t) = \mathcal{H}_m^{(0)}(t) + \mathcal{H}_m^{(2)}(t) + \mathcal{H}_m^{(3)} + \mathcal{H}_m^{(4)} + \mathcal{O}(S^{-1/2}). \tag{3.4}$$

The nth order Hamiltonian $\mathcal{H}_m^{(n)}$ contains the terms of order n in the boson operators b_i and $b_i^\dagger$, where b_i denotes the annihilation and $b_i^\dagger$ denotes the creation operator for magnons introduced by the Holstein-Primakoff transformation (3.3). Terms of order larger than four can be neglected because they scale with the small parameter $S^{-1/2}$. The quadratic terms scale with the factor S so that the fifth order terms are smaller by a factor of $S^{3/2} \approx 54$ compared to the quadratic terms. The approximated Hamiltonian is capable of describing small fluctuations around the classical ground state [73, 74]. Note that there are also other bosonization schemes available that can be used to obtain an effective boson Hamiltonian, such as the Dyson-Maleev transformation [75, 76]. The latter transformation gives the same result for $\mathcal{H}_m^{(2)}$ and $\mathcal{H}_m^{(3)}$ but different results for $\mathcal{H}_m^{(4)}$ and higher order terms [69]. Because the expansion is carried out in the small parameter $1/S$ it is expected that the deviation of the quartic Hamiltonian $\mathcal{H}_m^{(4)}$ between the two transformations does not change the results qualitatively.

For practical calculations it is convenient to use a momentum space representation instead of directly working with the Hamiltonian in real space. The bosonic operators can be transformed to momentum space via a partial Fourier transformation in the yz-plane. The zero order Hamiltonian $\mathcal{H}_m^{(0)}(t)$ may be dropped as it does not contain any operators and thus does not contribute to the Heisenberg equations of motion. The

remaining parts of the Hamiltonian up to fourth order are [70]

$$\mathcal{H}_m^{(2)}(t) = \sum_{\boldsymbol{k}}\left[A_{\boldsymbol{k}} b_{\boldsymbol{k}}^\dagger b_{\boldsymbol{k}} + \frac{B_{\boldsymbol{k}}}{2}\left(b_{\boldsymbol{k}}^\dagger b_{-\boldsymbol{k}}^\dagger + b_{-\boldsymbol{k}} b_{\boldsymbol{k}}\right)\right] + h_1 \cos(\omega_0 t)\sum_{\boldsymbol{k}} b_{\boldsymbol{k}}^\dagger b_{\boldsymbol{k}}, \quad (3.5a)$$

$$\mathcal{H}_m^{(3)} = \frac{1}{\sqrt{N}}\sum_{\boldsymbol{k}_1,\boldsymbol{k}_2,\boldsymbol{k}_3}\delta_{\boldsymbol{k}_1+\boldsymbol{k}_2+\boldsymbol{k}_3,0}\frac{1}{2!}\left[\Gamma^{\bar{b}bb}_{1;2,3} b_{-1}^\dagger b_2 b_3 + \Gamma^{\bar{b}\bar{b}b}_{1,2;3} b_{-1}^\dagger b_{-2}^\dagger b_3\right], \quad (3.5b)$$

$$\mathcal{H}_m^{(4)} = \frac{1}{N}\sum_{\boldsymbol{k}_1,\ldots,\boldsymbol{k}_4}\delta_{\boldsymbol{k}_1+\cdots+\boldsymbol{k}_4,0}\left[\frac{1}{(2!)^2}\Gamma^{\bar{b}\bar{b}bb}_{1,2;3,4} b_{-1}^\dagger b_{-2}^\dagger b_3 b_4 + \frac{1}{3!}\Gamma^{\bar{b}bbb}_{1;2,3,4} b_{-1}^\dagger b_2 b_3 b_4 + \frac{1}{3!}\Gamma^{\bar{b}\bar{b}\bar{b}b}_{1,2,3;4} b_{-1}^\dagger b_{-2}^\dagger b_{-3}^\dagger b_4\right], \quad (3.5c)$$

where I abbreviate $k_1 \equiv 1$, etc.. I define the Fourier transform of the exchange coupling and the dipolar matrix as

$$J_{\boldsymbol{k}} = \sum_{ij} \mathrm{e}^{-i\boldsymbol{k}\cdot\boldsymbol{r}_{ij}} J_{ij}, \quad (3.6a)$$

$$D_{\boldsymbol{k}}^{\alpha\beta} = \sum_{ij} \mathrm{e}^{-i\boldsymbol{k}\cdot\boldsymbol{r}_{ij}} D_{ij}^{\alpha\beta}. \quad (3.6b)$$

The coefficients $A_{\boldsymbol{k}}$ and $B_{\boldsymbol{k}}$ can be computed as

$$A_{\boldsymbol{k}} = h_0 + S\left(J_{\boldsymbol{0}} - J_{\boldsymbol{k}}\right) + S\left[D_{\boldsymbol{0}}^{zz} - \frac{1}{2}\left(D_{\boldsymbol{k}}^{xx} + D_{\boldsymbol{k}}^{yy}\right)\right], \quad (3.7a)$$

$$B_{\boldsymbol{k}} = -\frac{S}{2}\left[D_{\boldsymbol{k}}^{xx} - 2iD_{\boldsymbol{k}}^{xy} - D_{\boldsymbol{k}}^{yy}\right], \quad (3.7b)$$

while the three-point and four-point vertices in momentum space are [70]

$$\Gamma^{\bar{b}bb}_{1;2,3} = \sqrt{\frac{S}{2}}\left[D_{\boldsymbol{k}_2}^{zy} - iD_{\boldsymbol{k}_2}^{zx} + D_{\boldsymbol{k}_3}^{zy} - iD_{\boldsymbol{k}_3}^{zx} + \frac{1}{2}\left(D_{\boldsymbol{0}}^{zy} - iD_{\boldsymbol{0}}^{zx}\right)\right], \quad (3.8a)$$

$$\Gamma^{\bar{b}\bar{b}b}_{1,2;3} = \left(\Gamma^{\bar{b}bb}_{3;2,1}\right)^*, \quad (3.8b)$$

$$\Gamma^{\bar{b}\bar{b}bb}_{1,2;3,4} = -\frac{1}{2}\Big[J_{\boldsymbol{k}_1+\boldsymbol{k}_3} + J_{\boldsymbol{k}_2+\boldsymbol{k}_3} + J_{\boldsymbol{k}_1+\boldsymbol{k}_4} + J_{\boldsymbol{k}_2+\boldsymbol{k}_4} + D_{\boldsymbol{k}_1+\boldsymbol{k}_3}^{zz} + D_{\boldsymbol{k}_2+\boldsymbol{k}_3}^{zz} + D_{\boldsymbol{k}_1+\boldsymbol{k}_4}^{zz} + D_{\boldsymbol{k}_2+\boldsymbol{k}_4}^{zz} - \sum_{i=1}^{4}\left(J_{\boldsymbol{k}_i} - 2D_{\boldsymbol{k}_i}^{zz}\right)\Big], \quad (3.8c)$$

$$\Gamma^{\bar{b}bbb}_{1;2,3,4} = \frac{1}{4}\Big[D_{\boldsymbol{k}_2}^{xx} - 2iD_{\boldsymbol{k}_2}^{xy} - D_{\boldsymbol{k}_2}^{yy} + D_{\boldsymbol{k}_3}^{xx} - 2iD_{\boldsymbol{k}_3}^{xy} - D_{\boldsymbol{k}_3}^{yy} + D_{\boldsymbol{k}_4}^{xx} - 2iD_{\boldsymbol{k}_4}^{xy} - D_{\boldsymbol{k}_4}^{yy}\Big], \quad (3.8d)$$

$$\Gamma^{\bar{b}\bar{b}\bar{b}b}_{1,2,3;4} = \left(\Gamma^{\bar{b}bbb}_{4;1,2,3}\right)^*. \quad (3.8e)$$

The time-independent part of the above quadratic Hamiltonian (3.5a) can be diagonalized by a Bogoliubov transformation, introducing new bosonic creation and annihilation

operators $a^\dagger_{\boldsymbol{k}}$ and $a_{\boldsymbol{k}}$,

$$\begin{pmatrix} b_{\boldsymbol{k}} \\ b^\dagger_{-\boldsymbol{k}} \end{pmatrix} = \begin{pmatrix} u_{\boldsymbol{k}} & -v_{\boldsymbol{k}} \\ -v^*_{\boldsymbol{k}} & u_{\boldsymbol{k}} \end{pmatrix} \begin{pmatrix} a_{\boldsymbol{k}} \\ a^\dagger_{-\boldsymbol{k}} \end{pmatrix}, \tag{3.9}$$

where

$$u_{\boldsymbol{k}} = \sqrt{\frac{A_{\boldsymbol{k}} + \varepsilon_{\boldsymbol{k}}}{2\varepsilon_{\boldsymbol{k}}}}, \tag{3.10a}$$

$$v_{\boldsymbol{k}} = \frac{B_{\boldsymbol{k}}}{|B_{\boldsymbol{k}}|}\sqrt{\frac{A_{\boldsymbol{k}} - \varepsilon_{\boldsymbol{k}}}{2\varepsilon_{\boldsymbol{k}}}}, \tag{3.10b}$$

$$\varepsilon_{\boldsymbol{k}} = \sqrt{A^2_{\boldsymbol{k}} - |B_{\boldsymbol{k}}|^2}. \tag{3.10c}$$

Applying this transformation to Eq. (3.5a) produces non-diagonal time-dependent terms [70],

$$\begin{aligned} \mathcal{H}^{(2)}_m(t) &= \sum_{\boldsymbol{k}} \left[\varepsilon_{\boldsymbol{k}} a^\dagger_{\boldsymbol{k}} a_{\boldsymbol{k}} + \frac{\varepsilon_{\boldsymbol{k}} - A_{\boldsymbol{k}}}{2} + h_1 \cos(\omega_0 t) \left(\frac{A_{\boldsymbol{k}}}{\varepsilon_{\boldsymbol{k}}} a^\dagger_{\boldsymbol{k}} a_{\boldsymbol{k}} - \frac{\varepsilon_{\boldsymbol{k}} - A_{\boldsymbol{k}}}{2\varepsilon_{\boldsymbol{k}}} \right) \right] \\ &\quad + \sum_{\boldsymbol{k}} \left[V_{\boldsymbol{k}} \cos(\omega_0 t)\, a^\dagger_{\boldsymbol{k}} a^\dagger_{-\boldsymbol{k}} + V^*_{\boldsymbol{k}} \cos(\omega_0 t)\, a_{-\boldsymbol{k}} a_{\boldsymbol{k}} \right], \end{aligned} \tag{3.11}$$

where $\epsilon_{\boldsymbol{k}}$ is the magnon dispersion given by Eq. (3.10c) and $V_{\boldsymbol{k}}$ is the pumping energy given by

$$V_{\boldsymbol{k}} = -\frac{h_1 B_{\boldsymbol{k}}}{2\varepsilon_{\boldsymbol{k}}}. \tag{3.12}$$

Furthermore, applying the Bogoliubov transformation to the other parts of the Hamiltonian (3.5b) and (3.5c) gives [70]

$$\begin{aligned} \mathcal{H}^{(3)}_m(t) &= \frac{1}{\sqrt{N}} \sum_{\boldsymbol{k}_1,\boldsymbol{k}_2,\boldsymbol{k}_3} \delta_{\boldsymbol{k}_1+\boldsymbol{k}_2+\boldsymbol{k}_3,0} \Bigg[\frac{1}{2}\Gamma^{\bar{a}aa}_{1;2,3} a^\dagger_{-1} a_2 a_3 + \frac{1}{2}\Gamma^{\bar{a}\bar{a}a}_{1,2;3} a^\dagger_{-1} a^\dagger_{-2} a_3 \\ &\qquad + \frac{1}{3!}\Gamma^{aaa}_{1,2,3} a_1 a_2 a_3 + \frac{1}{3!}\Gamma^{\bar{a}\bar{a}\bar{a}}_{1,2,3} a^\dagger_{-1} a^\dagger_{-2} a^\dagger_{-3} \Bigg], \end{aligned} \tag{3.13}$$

$$\begin{aligned} \mathcal{H}^{(4)}_m(t) &= \frac{1}{N} \sum_{\boldsymbol{k}_1,\ldots,\boldsymbol{k}_4} \delta_{\boldsymbol{k}_1+\cdots+\boldsymbol{k}_4,0} \Bigg[\frac{1}{(2!)^2}\Gamma^{\bar{a}\bar{a}aa}_{1,2;3,4} a^\dagger_{-1} a^\dagger_{-2} a_3 a_4 + \frac{1}{3!}\Gamma^{\bar{a}aaa}_{1;2,3,4} a^\dagger_{-1} a_2 a_3 a_4 \\ &\quad + \frac{1}{3!}\Gamma^{\bar{a}\bar{a}\bar{a}a}_{1,2,3;4} a^\dagger_{-1} a^\dagger_{-2} a^\dagger_{-3} a_4 + \frac{1}{4!}\Gamma^{aaaa}_{1,2,3,4} a_1 a_2 a_3 a_4 + \frac{1}{4!}\Gamma^{\bar{a}\bar{a}\bar{a}\bar{a}}_{1,2,3,4} a^\dagger_{-1} a^\dagger_{-2} a^\dagger_{-3} a^\dagger_{-4} \Bigg], \end{aligned} \tag{3.14}$$

with cubic vertices given by

$$\begin{aligned}
\Gamma^{aaa}_{1,2,3} &= -\Gamma^{\bar{b}bb}_{1;2,3} v_1 u_2 u_3 - \Gamma^{\bar{b}bb}_{2;1,3} v_2 u_1 u_3 - \Gamma^{\bar{b}bb}_{3;1,2} v_3 u_1 u_3 + \Gamma^{\bar{b}\bar{b}b}_{1,2;3} v_1 v_2 u_3 \\
&\quad + \Gamma^{\bar{b}\bar{b}b}_{2,3;1} v_2 v_3 u_1 + \Gamma^{\bar{b}\bar{b}b}_{1,3;2} v_1 v_3 u_2, && \text{(3.15a)} \\
\Gamma^{\bar{a}aa}_{1;2,3} &= \Gamma^{\bar{b}bb}_{1;2,3} u_1 u_2 u_3 + \Gamma^{\bar{b}bb}_{2;1,3} v_1 v_2 u_3 + \Gamma^{\bar{b}bb}_{3;1,2} v_1 v_3 u_2 - \Gamma^{\bar{b}\bar{b}b}_{3,2;1} v_3 v_2 v_1 \\
&\quad - \Gamma^{\bar{b}\bar{b}b}_{1,2;3} v_2 u_1 u_3 - \Gamma^{\bar{b}\bar{b}b}_{1,3;2} v_3 u_1 u_2, && \text{(3.15b)} \\
\Gamma^{\bar{a}\bar{a}a}_{1,2;3} &= \left(\Gamma^{\bar{a}aa}_{3;2,1}\right)^*, && \text{(3.15c)} \\
\Gamma^{\bar{a}\bar{a}\bar{a}}_{1,2,3} &= \left(\Gamma^{aaa}_{1,2,3}\right)^*, && \text{(3.15d)}
\end{aligned}$$

and quartic vertices given by

$$\begin{aligned}
\Gamma^{aaaa}_{1,2,3,4} &= \Gamma^{\bar{b}\bar{b}bb}_{1,2;3,4} u_1 u_2 v_3 v_4 + \Gamma^{\bar{b}\bar{b}bb}_{1,3;2,4} u_1 u_3 v_2 v_4 + \Gamma^{\bar{b}\bar{b}bb}_{1,4;2,3} u_1 u_4 v_2 v_3 \\
&\quad + \Gamma^{\bar{b}\bar{b}bb}_{2,3;1,4} u_2 u_3 v_1 v_4 + \Gamma^{\bar{b}\bar{b}bb}_{2,4;1,3} u_2 u_4 v_1 v_3 + \Gamma^{\bar{b}\bar{b}bb}_{3,4;1,2} u_3 u_4 v_1 v_2 \\
&\quad - \Gamma^{\bar{b}bbb}_{4;1,2,3} u_1 u_2 u_3 v_4 - \Gamma^{\bar{b}bbb}_{3;1,2,4} u_1 u_2 u_4 v_3 - \Gamma^{\bar{b}bbb}_{2;1,3,4} u_1 u_3 u_4 v_2 \\
&\quad - \Gamma^{\bar{b}bbb}_{1;2,3,4} u_2 u_3 u_4 v_1 - \Gamma^{\bar{b}\bar{b}\bar{b}b}_{2,3,4;1} u_1 v_2 v_3 v_4 - \Gamma^{\bar{b}\bar{b}\bar{b}b}_{1,3,4;2} u_2 v_1 v_3 v_4 \\
&\quad - \Gamma^{\bar{b}\bar{b}\bar{b}b}_{1,2,4;3} u_3 v_1 v_2 v_4 - \Gamma^{\bar{b}\bar{b}\bar{b}b}_{1,2,3;4} u_4 v_1 v_2 v_3, && \text{(3.16a)}
\end{aligned}$$

$$\begin{aligned}
\Gamma^{\bar{a}aaa}_{1;2,3,4} &= -\Gamma^{\bar{b}\bar{b}bb}_{2,1;3,4} u_2 v_1 v_3 v_4 - \Gamma^{\bar{b}\bar{b}bb}_{3,1;2,4} u_3 v_1 v_2 v_4 - \Gamma^{\bar{b}\bar{b}bb}_{4,1;2,3} u_4 v_1 v_2 v_3 \\
&\quad - \Gamma^{\bar{b}\bar{b}bb}_{2,3;1,4} u_2 u_3 u_1 v_4 - \Gamma^{\bar{b}\bar{b}bb}_{2,4;1,3} u_2 u_4 u_1 v_3 - \Gamma^{\bar{b}\bar{b}bb}_{3,4;1,2} u_3 u_4 u_1 v_2 \\
&\quad + \Gamma^{\bar{b}bbb}_{1;2,3,4} u_1 u_2 u_3 u_4 + \Gamma^{\bar{b}bbb}_{4;3,2,1} u_3 u_2 v_1 v_4 + \Gamma^{\bar{b}bbb}_{3;4,2,1} u_4 u_2 v_1 v_3 \\
&\quad + \Gamma^{\bar{b}bbb}_{2;4,3,1} u_4 u_3 v_1 v_2 + \Gamma^{\bar{b}\bar{b}\bar{b}b}_{1,2,3;4} u_4 u_1 v_2 v_3 + \Gamma^{\bar{b}\bar{b}\bar{b}b}_{1,2,4;3} u_3 u_1 v_2 v_4 \\
&\quad + \Gamma^{\bar{b}\bar{b}\bar{b}b}_{1,3,4;2} u_2 u_1 v_3 v_4 + \Gamma^{\bar{b}\bar{b}\bar{b}b}_{4,3,2;1} v_4 v_2 v_3 v_1, && \text{(3.16b)}
\end{aligned}$$

$$\begin{aligned}
\Gamma^{\bar{a}\bar{a}aa}_{1,2;3,4} &= \Gamma^{\bar{b}\bar{b}bb}_{1,2;3,4} u_1 u_2 u_3 u_4 + \Gamma^{\bar{b}\bar{b}bb}_{1,3;4,2} u_1 u_4 v_3 v_2 + \Gamma^{\bar{b}\bar{b}bb}_{1,4;3,2} u_1 u_3 v_4 v_2 \\
&\quad + \Gamma^{\bar{b}\bar{b}bb}_{2,3;4,1} u_2 u_4 v_3 v_1 + \Gamma^{\bar{b}\bar{b}bb}_{2,4;3,1} u_2 u_3 v_4 v_1 + \Gamma^{\bar{b}\bar{b}bb}_{3,4;2,1} v_1 v_2 v_3 v_4 \\
&\quad - \Gamma^{\bar{b}bbb}_{4;3,2,1} u_3 v_2 v_1 v_4 - \Gamma^{\bar{b}bbb}_{3;4,2,1} u_4 v_2 v_1 v_3 - \Gamma^{\bar{b}bbb}_{2;3,4,1} u_2 u_3 u_4 v_1 \\
&\quad - \Gamma^{\bar{b}bbb}_{1;3,4,2} u_1 u_3 u_4 v_2 - \Gamma^{\bar{b}\bar{b}\bar{b}b}_{2,3,4;1} u_2 v_3 v_4 v_1 - \Gamma^{\bar{b}\bar{b}\bar{b}b}_{1,3,4;2} u_1 v_3 v_4 v_2 \\
&\quad - \Gamma^{\bar{b}\bar{b}\bar{b}b}_{1,2,4;3} u_1 u_2 u_3 v_4 - \Gamma^{\bar{b}\bar{b}\bar{b}b}_{1,2,3;4} u_1 u_2 u_4 v_3, && \text{(3.16c)} \\
\Gamma^{\bar{a}\bar{a}\bar{a}\bar{a}}_{1,2,3,4} &= \Gamma^{aaaa}_{1,2,3,4}, && \text{(3.16d)} \\
\Gamma^{\bar{a}\bar{a}\bar{a}a}_{1,2,3;4} &= \left(\Gamma^{\bar{a}aaa}_{4;3,2,1}\right)^*. && \text{(3.16e)}
\end{aligned}$$

Lastly, explicit expressions for the Fourier transforms of the exchange coupling $J_{\boldsymbol{k}}$ and the dipolar matrix $D^{\alpha\beta}_{\boldsymbol{k}}$ are necessary. In order to explain the relevant experimental observations it is sufficient to only retain the lowest magnon band. There are various approximations available to obtain an effective in-plane Hamiltonian that is capable of reproducing the dispersion of the lowest magnon band. Here, I use the uniform

mode approximation developed in Ref. [69]. I assume that the system is translationally invariant in the x-direction and approximate the lowest transverse mode by plane waves which is a reasonable approximation if we assume that the thickness d of the YIG film is small compared to its dimensions in the other directions and periodic boundary conditions can be applied. Parameterizing the in-plane wave vector as

$$\boldsymbol{k} = k_z \mathrm{e}_z + k_y \mathrm{e}_y = k \left[\cos\left(\theta_{\boldsymbol{k}}\right) \mathrm{e}_z + \sin\left(\theta_{\boldsymbol{k}}\right) \mathrm{e}_y\right], \tag{3.17}$$

the coefficients $A_{\boldsymbol{k}}$ and $B_{\boldsymbol{k}}$ can be written as [69]

$$A_{\boldsymbol{k}} = h_0 + JS\left[4 - 2\cos\left(k_y a\right) - 2\cos\left(k_z a\right)\right] - \frac{S}{2}\left(D_{\boldsymbol{k}}^{xx} + D_{\boldsymbol{k}}^{yy}\right) + \frac{\Delta}{3}, \tag{3.18a}$$

$$B_{\boldsymbol{k}} = -\frac{S}{2}\left(D_{\boldsymbol{k}}^{xx} - D_{\boldsymbol{k}}^{yy}\right), \tag{3.18b}$$

with the dipolar energy scale

$$\Delta = 4\pi\mu^2 S/a^3. \tag{3.19}$$

The dipolar sums (3.6) are difficult to compute due to their slow convergence. In Ref. [69] the Ewald summation technique [77] is used to analytically calculate the dipolar sums. The resulting expressions within the uniform mode approximation are

$$D_{\boldsymbol{k}}^{xx} = \frac{4\pi\mu^2}{a^3}\left[\frac{1}{3} - f_{\boldsymbol{k}}\right], \tag{3.20a}$$

$$D_{\boldsymbol{k}}^{yy} = \frac{4\pi\mu^2}{a^3}\left[\frac{1}{3} - \left(1 - f_{\boldsymbol{k}}\right)\sin^2\theta_{\boldsymbol{k}}\right], \tag{3.20b}$$

$$D_{\boldsymbol{k}}^{zz} = \frac{4\pi\mu^2}{a^3}\left[\frac{1}{3} - \left(1 - f_{\boldsymbol{k}}\right)\cos^2\theta_{\boldsymbol{k}}\right], \tag{3.20c}$$

$$D_{\boldsymbol{k}}^{yz} = D_{\boldsymbol{k}}^{zy} = -\frac{2\pi\mu^2}{a^3}\sin\left(2\theta_{\boldsymbol{k}}\right), \tag{3.20d}$$

$$D_{\boldsymbol{k}}^{xy} = D_{\boldsymbol{k}}^{yx} = 0, \tag{3.20e}$$

with the form factor

$$f_{\boldsymbol{k}} = \frac{1 - \mathrm{e}^{-|\boldsymbol{k}|d}}{|\boldsymbol{k}|\, d}. \tag{3.21}$$

Note that for $k_x = 0$, $k_z = k\cos\theta_{\boldsymbol{k}}$, and $k_y = k\sin\theta_{\boldsymbol{k}}$ there is $D_{\boldsymbol{k}}^{xz} = D_{\boldsymbol{k}}^{zx} = 0$ so that the only non-zero off-diagonal element of the dipolar matrix is $D_{\boldsymbol{k}}^{yz} = D_{\boldsymbol{k}}^{zy}$. It is easy to see that the dipolar matrix in real space (3.2) satisfies the relation $D_{ij}^{xx} + D_{ij}^{yy} + D_{ij}^{zz} = 0$. The above approximated dipolar matrix in momentum space satisfies the analog relation

$$D_{\boldsymbol{k}}^{xx} + D_{\boldsymbol{k}}^{yy} + D_{\boldsymbol{k}}^{zz} = 0. \tag{3.22}$$

The energy scale relevant for the experiments is relatively small so that it is sufficient to consider small wave vectors $|\boldsymbol{k}| \ll a$. The terms in $A_{\boldsymbol{k}}$ that involve the exchange interaction may be expanded for small $|\boldsymbol{k}|$,

$$S\left(J_0 - J_{\boldsymbol{k}}\right) = JS\left[4 - 2\cos\left(k_y a\right) - 2\cos\left(k_z a\right)\right] \approx JSa^2\boldsymbol{k}^2 = \rho\boldsymbol{k}^2, \tag{3.23}$$

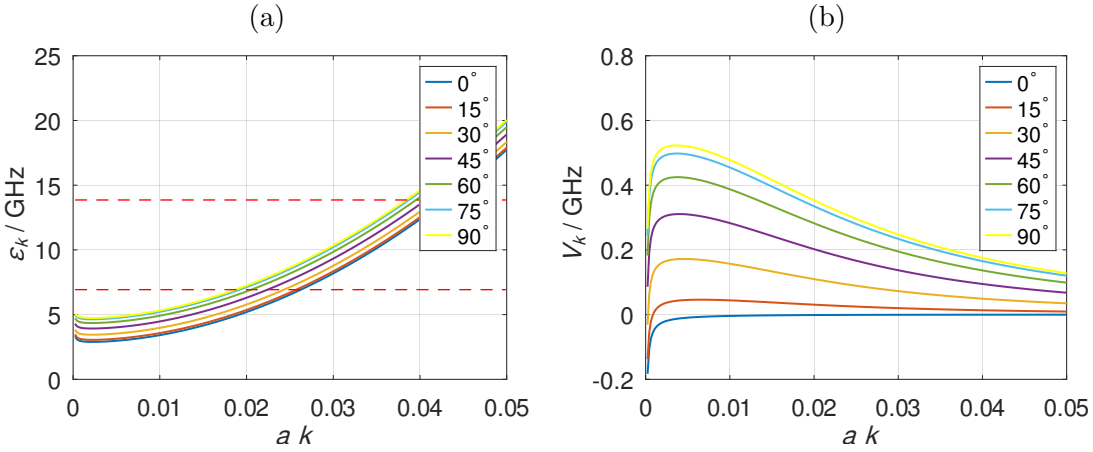

Figure 3.2: (a) The wave vector dependence of the dispersion relation (3.24) is shown for different angles $\theta_{\boldsymbol{k}}$ of the wave vector $\boldsymbol{k}$. There is a minimum at small wave vectors. The dashed red lines show the pumping frequency $\omega_0 = 13.857$GHz and $\omega_0/2$ which corresponds to the energy of parametric magnons generated by the pumping field. (b) The pumping energy given by equation (3.12) is plotted for different angles $\theta_{\boldsymbol{k}}$ of the $\boldsymbol{k}$ vector.

with $\rho = JSa^2$. Then, the long wavelength limit of the magnon dispersion is [69]

$$\begin{aligned} \epsilon_{\boldsymbol{k}} &= \sqrt{A_{\boldsymbol{k}}^2 - |B_{\boldsymbol{k}}|^2} = \sqrt{(A_{\boldsymbol{k}} - |B_{\boldsymbol{k}}|)\,(A_{\boldsymbol{k}} + |B_{\boldsymbol{k}}|)} \\ &\approx \sqrt{\left[h_0 + \rho \boldsymbol{k}^2 + \Delta\,(1 - f_{\boldsymbol{k}})\sin^2\theta_{\boldsymbol{k}}\right]\left[h_0 + \rho \boldsymbol{k}^2 + \Delta f_{\boldsymbol{k}}\right]}. \end{aligned} \tag{3.24}$$

This dispersion relation and the momentum dependence of the pumping energy (3.12) are shown in Fig. 3.2.

In order to study parametric resonance of magnons [8, 10, 11, 12] the Hamiltonian (3.11) is usually simplified by dropping the terms that do not contain a creation or annihilation operator as well as the term involving the combination $\cos(\omega_0 t)\, A_{\boldsymbol{k}} a_{\boldsymbol{k}}^\dagger a_{\boldsymbol{k}}$. Furthermore, using the Euler equation the factors appearing in the pumping terms can be written as

$$V_{\boldsymbol{k}} \cos(\omega_0 t) = \frac{V_{\boldsymbol{k}}}{2}\left(e^{-i\omega_0 t} + e^{i\omega_0 t}\right), \tag{3.25a}$$

$$V_{\boldsymbol{k}}^* \cos(\omega_0 t) = \frac{V_{\boldsymbol{k}}^*}{2}\left(e^{i\omega_0 t} + e^{-i\omega_0 t}\right). \tag{3.25b}$$

In the case of a single harmonic drive only the first term in the equations (3.25) is present. While this situation can be reproduced by applying the substitution

$$V_{\boldsymbol{k}} \cos(\omega_0 t) \rightarrow \frac{V_{\boldsymbol{k}}}{2} \mathrm{e}^{-i\omega_0 t}, \tag{3.26}$$

$$V_{\boldsymbol{k}}^* \cos(\omega_0 t) \rightarrow \frac{V_{\boldsymbol{k}}^*}{2} \mathrm{e}^{i\omega_0 t}, \tag{3.27}$$

the validity of this approximation in the context of YIG is not obvious. Apparently, the approximation has been accepted for many decades in the literature [13]. Let us assume here that the approximation of a single harmonic drive is sufficient to study at least some aspects of the experiments [15, 16, 78, 79, 80]. The quadratic boson Hamiltonian $\mathcal{H}^{(2)}$ is then approximated by

$$\mathcal{H}_m^{(2)}(t) \approx \sum_{\boldsymbol{k}} \left[\epsilon_{\boldsymbol{k}} a_{\boldsymbol{k}}^\dagger a_{\boldsymbol{k}} + \frac{1}{2} V_{\boldsymbol{k}} \mathrm{e}^{-i\omega_0 t} a_{\boldsymbol{k}}^\dagger a_{-\boldsymbol{k}}^\dagger + \frac{1}{2} V_{\boldsymbol{k}}^* \mathrm{e}^{i\omega_0 t} a_{-\boldsymbol{k}} a_{\boldsymbol{k}} \right]. \tag{3.28}$$

The explicit time dependence may be removed by a canonical transformation to the rotating reference frame,

$$\begin{aligned} \tilde{a}_{\boldsymbol{k}} &= \mathrm{e}^{\frac{i\omega_0 t}{2}} a_{\boldsymbol{k}}, \\ \tilde{a}_{\boldsymbol{k}}^\dagger &= \mathrm{e}^{-\frac{i\omega_0 t}{2}} a_{\boldsymbol{k}}^\dagger. \end{aligned} \tag{3.29}$$

The new creation and annihilation operators $\tilde{a}_{\boldsymbol{k}}^\dagger$ and $\tilde{a}_{\boldsymbol{k}}$ satisfy the Heisenberg equations of motion

$$\begin{aligned} i\partial_t \tilde{a}_{\boldsymbol{k}} &= \left[\tilde{a}_{\boldsymbol{k}}, \tilde{\mathcal{H}}_m(t) \right], \\ i\partial_t \tilde{a}_{\boldsymbol{k}}^\dagger &= \left[\tilde{a}_{\boldsymbol{k}}^\dagger, \tilde{\mathcal{H}}_m(t) \right], \end{aligned} \tag{3.30}$$

where $\tilde{\mathcal{H}}_m(t)$ is the new Hamiltonian in the rotating reference frame. The transformed quadratic Hamiltonian $\tilde{\mathcal{H}}_m^{(2)}$ does not explicitly dependent on the time and is given by [70]

$$\tilde{\mathcal{H}}_m^{(2)} = \sum_{\boldsymbol{k}} \left[E_{\boldsymbol{k}} \tilde{a}_{\boldsymbol{k}}^\dagger \tilde{a}_{\boldsymbol{k}} + \frac{V_{\boldsymbol{k}}}{2} \tilde{a}_{\boldsymbol{k}}^\dagger \tilde{a}_{-\boldsymbol{k}}^\dagger + \frac{V_{\boldsymbol{k}}^*}{2} \tilde{a}_{-\boldsymbol{k}} \tilde{a}_{\boldsymbol{k}} \right], \tag{3.31}$$

where

$$E_{\boldsymbol{k}} = \epsilon_{\boldsymbol{k}} - \omega_0/2 \tag{3.32}$$

is the shifted magnon energy. The transformed cubic and quartic Hamiltonians $\mathcal{H}_m^{(3)}$ and $\mathcal{H}_m^{(4)}$ are given by

$$\begin{aligned} \tilde{\mathcal{H}}_m^{(3)}(t) &= \frac{1}{\sqrt{N}} \sum_{\boldsymbol{k}_1,\boldsymbol{k}_2,\boldsymbol{k}_3} \delta_{\boldsymbol{k}_1+\boldsymbol{k}_2+\boldsymbol{k}_3,0} \Big[\frac{1}{2} \Gamma_{1;2,3}^{\bar{a}aa} e^{-i\omega_0 t/2} \tilde{a}_{-1}^\dagger \tilde{a}_2 \tilde{a}_3 + \frac{1}{2} \Gamma_{1,2;3}^{\bar{a}\bar{a}a} e^{i\omega_0 t/2} \tilde{a}_{-1}^\dagger \tilde{a}_{-2}^\dagger \tilde{a}_3 \\ &\quad + \frac{1}{3!} \Gamma_{1,2,3}^{aaa} e^{-3i\omega_0 t/2} \tilde{a}_1 \tilde{a}_2 \tilde{a}_3 + \frac{1}{3!} \Gamma_{1,2,3}^{\bar{a}\bar{a}\bar{a}} e^{3i\omega_0 t/2} \tilde{a}_{-1}^\dagger \tilde{a}_{-2}^\dagger \tilde{a}_{-3}^\dagger \Big], \end{aligned} \tag{3.33}$$

$$\begin{aligned} \tilde{\mathcal{H}}_m^{(4)}(t) &= \frac{1}{N} \sum_{\boldsymbol{k}_1,\boldsymbol{k}_2,\boldsymbol{k}_3,\boldsymbol{k}_4} \delta_{\boldsymbol{k}_1+\boldsymbol{k}_2+\boldsymbol{k}_3+\boldsymbol{k}_4,0} \Big[\frac{1}{(2!)^2} \Gamma_{1,2;3,4}^{\bar{a}\bar{a}aa} \tilde{a}_{-1}^\dagger \tilde{a}_{-2}^\dagger \tilde{a}_3 \tilde{a}_4 \\ &\quad + \frac{1}{3!} e^{-i\omega_0 t} \Gamma_{1;2,3,4}^{\bar{a}aaa} \tilde{a}_{-1}^\dagger \tilde{a}_2 \tilde{a}_3 \tilde{a}_4 + \frac{1}{3!} e^{i\omega_0 t} \Gamma_{1,2,3;4}^{\bar{a}\bar{a}\bar{a}a} \tilde{a}_{-1}^\dagger \tilde{a}_{-2}^\dagger \tilde{a}_{-3}^\dagger \tilde{a}_4 \\ &\quad + \frac{1}{4!} e^{-2i\omega_0 t} \Gamma_{1,2,3,4}^{aaaa} \tilde{a}_1 \tilde{a}_2 \tilde{a}_3 \tilde{a}_4 + \frac{1}{4!} e^{2i\omega_0 t} \Gamma_{1,2,3,4}^{\bar{a}\bar{a}\bar{a}\bar{a}} \tilde{a}_{-1}^\dagger \tilde{a}_{-2}^\dagger \tilde{a}_{-3}^\dagger \tilde{a}_{-4}^\dagger \Big]. \end{aligned} \tag{3.34}$$

3.3 Kinetic equations

3.3.1 Non-interacting system

To proceed, I introduce the diagonal and off-diagonal magnon distribution functions as

$$\tilde{n}_{\boldsymbol{k}}(t) \equiv \langle \tilde{a}^\dagger_{\boldsymbol{k}}(t)\tilde{a}_{\boldsymbol{k}}(t)\rangle = \langle a^\dagger_{\boldsymbol{k}}(t)a_{\boldsymbol{k}}(t)\rangle = n_{\boldsymbol{k}}(t), \tag{3.35a}$$

$$\tilde{p}_{\boldsymbol{k}}(t) \equiv \langle \tilde{a}_{-\boldsymbol{k}}(t)\tilde{a}_{\boldsymbol{k}}(t)\rangle = e^{i\omega_0 t}\langle a_{-\boldsymbol{k}}(t)a_{\boldsymbol{k}}(t)\rangle = e^{i\omega_0 t}p_{\boldsymbol{k}}(t), \tag{3.35b}$$

where the average $\langle \dots \rangle$ is defined via the trace over some initial density operator ρ_0 at time t_0. Note that for the diagonal distribution function the phase factors $e^{\pm i\omega_0 t/2}$ cancels out.

For now, I neglect all magnon-magnon interactions and consider only the quadratic Hamiltonian $\tilde{\mathcal{H}}^{(2)}_m$ to approximately describe the pumped magnon gas. Using the Heisenberg equations of motion (3.30) it is easy to show that

$$\partial_t n_{\boldsymbol{k}}(t) + i\left[V_{\boldsymbol{k}}\tilde{p}^*_{\boldsymbol{k}}(t) - V^*_{\boldsymbol{k}}\tilde{p}_{\boldsymbol{k}}(t)\right] = 0, \tag{3.36a}$$

$$\partial_t \tilde{p}_{\boldsymbol{k}}(t) + 2iE_{\boldsymbol{k}}\tilde{p}_{\boldsymbol{k}}(t) + iV_{\boldsymbol{k}}\left[2n_{\boldsymbol{k}}(t)+1\right] = 0, \tag{3.36b}$$

where $E_{\boldsymbol{k}} = E_{-\boldsymbol{k}}$ and $n_{\boldsymbol{k}} = n_{-\boldsymbol{k}}$ has been assumed in the second equation. These equation have an exact solution [13]. For $|E_{\boldsymbol{k}}| < |V_{\boldsymbol{k}}|$ the solutions show an oscillatory behavior and are given by [13]

$$\frac{n_{\boldsymbol{k}}(t)+\frac{1}{2}}{n^{(0)}_{\boldsymbol{k}}+\frac{1}{2}} = 1 + \gamma^2_{\boldsymbol{k}}\frac{1-\cos(2\alpha_{\boldsymbol{k}}t)}{\alpha^2_{\boldsymbol{k}}}, \tag{3.37a}$$

$$\frac{\tilde{p}_{\boldsymbol{k}}(t)}{n^{(0)}_{\boldsymbol{k}}+\frac{1}{2}} = -\gamma_{\boldsymbol{k}}\frac{E_{\boldsymbol{k}}\left[1-\cos(2\alpha_{\boldsymbol{k}}t)\right] + i\alpha_{\boldsymbol{k}}\sin(2\alpha_{\boldsymbol{k}}t)}{\alpha^2_{\boldsymbol{k}}}, \tag{3.37b}$$

with $\alpha_{\boldsymbol{k}} = \sqrt{E^2_{\boldsymbol{k}} - \gamma^2_{\boldsymbol{k}}}$. In the strong pumping regime where $|V_{\boldsymbol{k}}| > |E_{\boldsymbol{k}}|$ the solutions have an exponential behavior and diverge for $t \to \infty$ [3, 4, 13],

$$\frac{n_{\boldsymbol{k}}(t)+\frac{1}{2}}{n^{(0)}_{\boldsymbol{k}}+\frac{1}{2}} = 1 + \gamma^2_{\boldsymbol{k}}\frac{\cosh(2\beta_{\boldsymbol{k}}t)-1}{\beta^2_{\boldsymbol{k}}}, \tag{3.38a}$$

$$\frac{\tilde{p}_{\boldsymbol{k}}(t)}{n^{(0)}_{\boldsymbol{k}}+\frac{1}{2}} = -\gamma_{\boldsymbol{k}}\frac{E_{\boldsymbol{k}}\left[\cosh(2\beta_{\boldsymbol{k}}t)-1\right] + i\beta_{\boldsymbol{k}}\sinh(2\beta_{\boldsymbol{k}}t)}{\beta^2_{\boldsymbol{k}}}, \tag{3.38b}$$

with $\beta_{\boldsymbol{k}} = \sqrt{\gamma^2_{\boldsymbol{k}} - E^2_{\boldsymbol{k}}}$. Apparently, the non-interacting system has unphysical solutions in the strong pumping regime.

3.3.2 Time-dependent self-consistent Hartree-Fock approximation

It is necessary to take magnon-magnon interactions into account in order to obtain a reasonable behavior in the strong pumping regime. Doing so leads eventually to a saturation of the exponential growth. Taking two-body interactions into account is sufficient

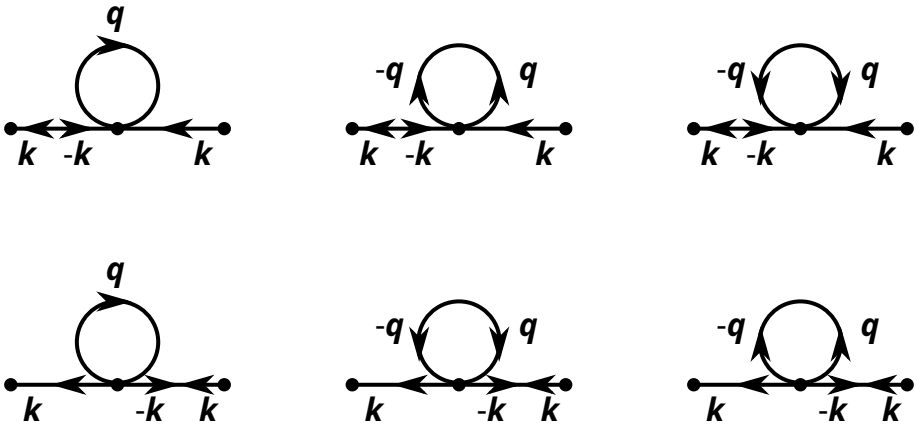

Figure 3.3: Diagrammatic representation of the contributions to the equation of motion of the diagonal connected magnon distribution function $n^c_{\boldsymbol{k}}(t)$ that originate from the quartic interactions. The diagrams contain the diagonal and off-diagonal distribution functions and one four-point interaction vertex. The middle and right diagrams have a pair of equivalent lines and thus an additional combinatorial prefactor of $1/2$ appears.

for this purpose. In the simplest case a time-dependent mean-field approximation, the so called time-dependent self-consistent Hartree-Fock approximation, is employed. In the literature this approximation is also known as "S-theory" in this context [2, 5, 9, 11, 12]. The above equations of motion (3.36) are replaced by

$$\partial_t n_{\boldsymbol{k}}(t) + i\left[\tilde{V}_{\boldsymbol{k}}(t)\tilde{p}^*_{\boldsymbol{k}}(t) - \tilde{V}^*_{\boldsymbol{k}}(t)\tilde{p}_{\boldsymbol{k}}(t)\right] = 0, \tag{3.39a}$$

$$\partial_t \tilde{p}_{\boldsymbol{k}}(t) + 2i\tilde{E}_{\boldsymbol{k}}(t)\tilde{p}_{\boldsymbol{k}}(t) + i\tilde{V}_{\boldsymbol{k}}(t)\left[2n_{\boldsymbol{k}}(t)+1\right] = 0, \tag{3.39b}$$

where $\tilde{E}_{\boldsymbol{k}}(t)$ and $\tilde{V}_{\boldsymbol{k}}(t)$ are the renormalized magnon dispersion and pumping energy respectively. They explicitly depend on the magnon distribution functions and are given by

$$\tilde{E}_{\boldsymbol{k}}(t) = E_{\boldsymbol{k}} + \frac{1}{N}\sum_{\boldsymbol{q}}\Big[\Gamma^{\bar{a}\bar{a}aa}_{-\boldsymbol{k},-\boldsymbol{q};\boldsymbol{q},\boldsymbol{k}} n_{\boldsymbol{q}}(t) + \frac{1}{2}\mathrm{e}^{-i\omega_0 t}\Gamma^{\bar{a}aaa}_{-\boldsymbol{k};-\boldsymbol{q},\boldsymbol{q},\boldsymbol{k}}\tilde{p}_{\boldsymbol{q}}(t) + \frac{1}{2}\mathrm{e}^{i\omega_0 t}\Gamma^{\bar{a}\bar{a}\bar{a}a}_{-\boldsymbol{k},-\boldsymbol{q},\boldsymbol{q};\boldsymbol{k}}\tilde{p}^*_{\boldsymbol{q}}(t)\Big], \tag{3.40a}$$

$$\tilde{V}_{\boldsymbol{k}}(t) = V_{\boldsymbol{k}} + \frac{1}{2N}\sum_{\boldsymbol{q}}\Big[\mathrm{e}^{i\omega_0 t}\Gamma^{\bar{a}\bar{a}\bar{a}a}_{-\boldsymbol{k},\boldsymbol{k},-\boldsymbol{q};\boldsymbol{q}} n_{\boldsymbol{q}}(t) + \frac{1}{2}\Gamma^{\bar{a}\bar{a}aa}_{-\boldsymbol{k},\boldsymbol{k};-\boldsymbol{q},\boldsymbol{q}}\tilde{p}_{\boldsymbol{q}}(t) + \frac{1}{2}\mathrm{e}^{2i\omega_0 t}\Gamma^{\bar{a}\bar{a}\bar{a}\bar{a}}_{-\boldsymbol{k},\boldsymbol{k},-\boldsymbol{q},\boldsymbol{q}}\tilde{p}^*_{\boldsymbol{q}}(t)\Big]. \tag{3.40b}$$

In order to derive the above equations of motion (3.39) it is possible to apply the diagrammatic method that I have developed in chapter 2 by only taking into account

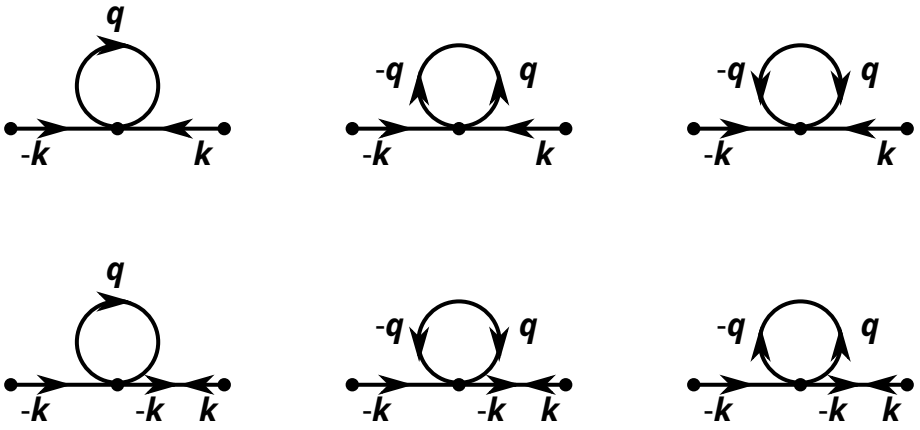

Figure 3.4: Diagrammatic representation of the contributions to the equation of motion of the off-diagonal connected magnon distribution function $\tilde{p}^c_{\boldsymbol{k}}(t)$ that originate from the quartic interactions. The diagrams contain the diagonal (lines with one arrow) and off-diagonal (lines with two arrows) distribution functions and one four-point interaction vertex. The middle and right diagrams have a pair of equivalent lines and thus an additional combinatorial prefactor of 1/2 appears.

the lowest order diagrams. They contain no correlations of order larger than two so that no correlation bubbles appear in the diagrams. The diagrams contributing to the time evolution of the diagonal magnon distribution function $n_{\boldsymbol{k}}$ are shown in Fig. 3.3 while the diagrams contributing to the time evolution of the off-diagonal magnon distribution function $\tilde{p}_{\boldsymbol{k}}$ are shown in Fig. 3.4. They lead to the contributions appearing in Eqs. (3.40). Note that the formulation in chapter 2 is only valid for the connected parts of the distribution functions. However, it is easy to see that for the diagrams shown here the n-point functions have no contributions from unconnected diagrams. Therefore, the equations of motion (3.39) have the same form for the connected and unconnected parts of the distribution functions. Alternatively, connected distribution functions can be defined as

$$\tilde{n}^c_{\boldsymbol{k}}(t) \equiv \langle \tilde{a}^\dagger_{\boldsymbol{k}}(t)\tilde{a}_{\boldsymbol{k}}(t)\rangle - |\langle \tilde{a}_{\boldsymbol{k}}(t)\rangle|^2 = n_{\boldsymbol{k}}(t) - |\tilde{\psi}_{\boldsymbol{k}}(t)|^2, \tag{3.41a}$$

$$\tilde{p}^c_{\boldsymbol{k}}(t) \equiv \langle \tilde{a}_{-\boldsymbol{k}}(t)\tilde{a}_{\boldsymbol{k}}(t)\rangle - \langle \tilde{a}_{-\boldsymbol{k}}(t)\rangle\langle \tilde{a}_{\boldsymbol{k}}(t)\rangle = \tilde{p}_{\boldsymbol{k}}(t) - \tilde{\psi}_{-\boldsymbol{k}}\tilde{\psi}_{\boldsymbol{k}}, \tag{3.41b}$$

where

$$\tilde{\psi}_{\boldsymbol{k}}(t) \equiv \langle \tilde{a}_{\boldsymbol{k}}(t)\rangle \tag{3.42}$$

is the condensate amplitude defined as the vacuum expectation value of the magnon annihilation operators. The diagrammatic method from chapter 2 can be directly applied to the correlation functions $n^c_{\boldsymbol{k}}$, $\tilde{p}^c_{\boldsymbol{k}}$, and $\tilde{\psi}_{\boldsymbol{k}}$ and it can be noted that the unconnected parts of the distribution functions $|\psi_{\boldsymbol{k}}|^2$ and $\psi_{-\boldsymbol{k}}\psi_{\boldsymbol{k}}$ obey equations of motion of the same form as Eq. (3.39) so that the connected and unconnected parts of the distribution functions can be combined into Eq. (3.39).

The rapidly oscillating terms proportional to $\mathrm{e}^{\pm i\omega_0 t}$ and $\mathrm{e}^{\pm 2i\omega_0 t}$ appearing in the renormalized self-energies (3.40) can be dropped within the rotating-wave approximation. They reduce to [53]

$$\tilde{E}_{\boldsymbol{k}}(t) = E_{\boldsymbol{k}} + \frac{1}{N}\sum_{\boldsymbol{q}} T_{\boldsymbol{k},\boldsymbol{q}} n_{\boldsymbol{q}}(t), \tag{3.43a}$$

$$\tilde{V}_{\boldsymbol{k}}(t) = V_{\boldsymbol{k}} + \frac{1}{2N}\sum_{\boldsymbol{q}} S_{\boldsymbol{k},\boldsymbol{q}} \tilde{p}_{\boldsymbol{q}}(t), \tag{3.43b}$$

with

$$T_{\boldsymbol{k},\boldsymbol{q}} = \Gamma^{\bar{a}\bar{a}aa}_{-\boldsymbol{k},-\boldsymbol{q};\boldsymbol{q},\boldsymbol{k}}, \tag{3.44a}$$

$$S_{\boldsymbol{k},\boldsymbol{q}} = \Gamma^{\bar{a}\bar{a}aa}_{-\boldsymbol{k},\boldsymbol{k};-\boldsymbol{q},\boldsymbol{q}}. \tag{3.44b}$$

In summary, within S-theory, the collision integrals containing three-point vertices in the kinetic equations are neglected and magnon-magnon interactions are described only by the time-dependent magnon self-energy [53]

$$\Sigma_{\boldsymbol{k}}(t) = \frac{1}{N}\sum_{\boldsymbol{q}} T_{\boldsymbol{k},\boldsymbol{q}} n_{\boldsymbol{q}}(t). \tag{3.45}$$

The kinetic equations (3.39) become integral differential equations. They are non-trivial because all modes are coupled via the magnon self-energy $\Sigma_{\boldsymbol{k}}(t)$. In Refs. [2, 5, 6] it was proposed to decouple the modes with different wave vectors $\boldsymbol{k}$. This is done by only taking into account the terms in the equations (3.43a) and (3.43b) where the loop momentum $\boldsymbol{q}$ inside the sums is equal to the external momentum $\boldsymbol{k}$,

$$\tilde{E}_{\boldsymbol{k}}(t) \approx E_{\boldsymbol{k}} + \frac{1}{N} T_{\boldsymbol{k},\boldsymbol{k}} n_{\boldsymbol{k}}(t), \tag{3.46a}$$

$$\tilde{V}_{\boldsymbol{k}}(t) \approx V_{\boldsymbol{k}} + \frac{1}{2N} S_{\boldsymbol{k},\boldsymbol{k}} \tilde{p}_{\boldsymbol{k}}(t). \tag{3.46b}$$

To justify this approximation, the authors of Ref. [2, 5, 6] first introduced (by hand) a phenomenological damping term. Secondly, they argued that in the stationary state only a pair of magnon modes with wave vector $\pm\boldsymbol{k}$ characterized by the smallest damping survives. As long as the damping is strong enough, the other modes are not significantly populated and thus their contributions to the equations (3.43a) and (3.43b) can be neglected for long times. Under this condition, the above approximation is sufficient to properly describe the asymptotic long-time dynamics of the magnon distribution functions while greatly reducing the mathematical complexity of the problem. In fact, in the strong pumping regime where

$$|V_{\boldsymbol{k}}| > |E_{\boldsymbol{k}}|\,, \tag{3.47}$$

an analytic solution can be found for the non-equilibrium stationary state. In order for this approximation to yield reasonable results it is, however, necessary to include damping. A simple way to achieve this is to insert (by hand) a phenomenological damping

rate $\gamma_{\boldsymbol{k}}$ into the Heisenberg equations of motions of magnon annihilation and creation operators,

$$\partial_t \tilde{a}_{\boldsymbol{k}}(t) = \left(-iE_{\boldsymbol{k}} - \gamma_{\boldsymbol{k}}\right) \tilde{a}_{\boldsymbol{k}} - iV_{\boldsymbol{k}} \tilde{a}^\dagger_{-\boldsymbol{k}}, \tag{3.48a}$$

$$\partial_t \tilde{a}^\dagger_{\boldsymbol{k}}(t) = \left(iE_{\boldsymbol{k}} - \gamma_{\boldsymbol{k}}\right) \tilde{a}^\dagger_{\boldsymbol{k}} + iV^*_{\boldsymbol{k}} \tilde{a}_{-\boldsymbol{k}}. \tag{3.48b}$$

The equations of motion (3.39) are modified to

$$\partial_t n_{\boldsymbol{k}}(t) + i\left[\tilde{V}_{\boldsymbol{k}}(t)\tilde{p}^*_{\boldsymbol{k}}(t) - \tilde{V}^*_{\boldsymbol{k}}(t)\tilde{p}_{\boldsymbol{k}}(t)\right] + 2\gamma_{\boldsymbol{k}} n_{\boldsymbol{k}}(t) = 0, \tag{3.49a}$$

$$\partial_t \tilde{p}_{\boldsymbol{k}}(t) + 2\left(i\tilde{E}_{\boldsymbol{k}}(t) + \gamma_{\boldsymbol{k}}\right)\tilde{p}_{\boldsymbol{k}}(t) + i\tilde{V}_{\boldsymbol{k}}(t)\left[2n_{\boldsymbol{k}}(t) + 1\right] = 0. \tag{3.49b}$$

In this case the stationary state is given by [2, 5, 6]

$$n_{\boldsymbol{k}} = N\frac{\sqrt{|V_{\boldsymbol{k}}|^2 - \gamma^2_{\boldsymbol{k}}} - |E_{\boldsymbol{k}}|}{T_{\boldsymbol{k},\boldsymbol{k}} + \frac{1}{2}S_{\boldsymbol{k},\boldsymbol{k}}}, \tag{3.50a}$$

$$\tilde{p}_{\boldsymbol{k}} = -\left(\sqrt{1 - \frac{\gamma^2_{\boldsymbol{k}}}{|V_{\boldsymbol{k}}|^2}} + i\frac{\gamma_{\boldsymbol{k}}}{|V_{\boldsymbol{k}}|}\right) n_{\boldsymbol{k}}, \tag{3.50b}$$

The magnons satisfying the resonance condition

$$\epsilon_{\boldsymbol{k}} = \omega_0/2 \tag{3.51}$$

are of particular interest. In the resonant case the stationary solution within S-theory simplifies to

$$n_{\boldsymbol{k}} = N\frac{\sqrt{|V_{\boldsymbol{k}}|^2 - \gamma^2_{\boldsymbol{k}}}}{T_{\boldsymbol{k},\boldsymbol{k}} + \frac{1}{2}S_{\boldsymbol{k},\boldsymbol{k}}}, \tag{3.52}$$

if the pumping energy is large enough to compensate the losses due to damping,

$$|V_{\boldsymbol{k}}| > |\gamma_{\boldsymbol{k}}|\,. \tag{3.53}$$

Note that this approximation is only valid if the damping rate $\gamma_{\boldsymbol{k}}$ is sufficiently large. The above condition (3.53) implies that there is a non-zero minimum pumping field strength $h_{1,\min}$ that is necessary for a non-vanishing stationary state [53].

Fig. 3.5 shows the stationary magnon density obtained from Eq. (3.52) in momentum space. I have chosen the parameters as $\omega_0 = 13.857$ GHz, $H_0 = 100$ mT, $H_1 = 1$ mT, $d = 22.8$ µm, $N = 6.529 \times 10^9$ corresponding to an area of 0.1 mm^2, and $\gamma = 0.95V_0$ where V_0 is the pumping energy for parametric magnons at the angle $\alpha = \pi/2$ of the wave vector in momentum space. Apparently, the magnon density is only non-vanishing near a small region around the resonance surface shell where the resonance condition (3.51) is fulfilled. The width of the distribution for $\alpha = \pi/2$ can be estimated by neglecting the anisotropy in the magnon dispersion so that

$$\rho\Delta k^2 \approx \sqrt{|V_0|^2 - \gamma^2}. \tag{3.54}$$

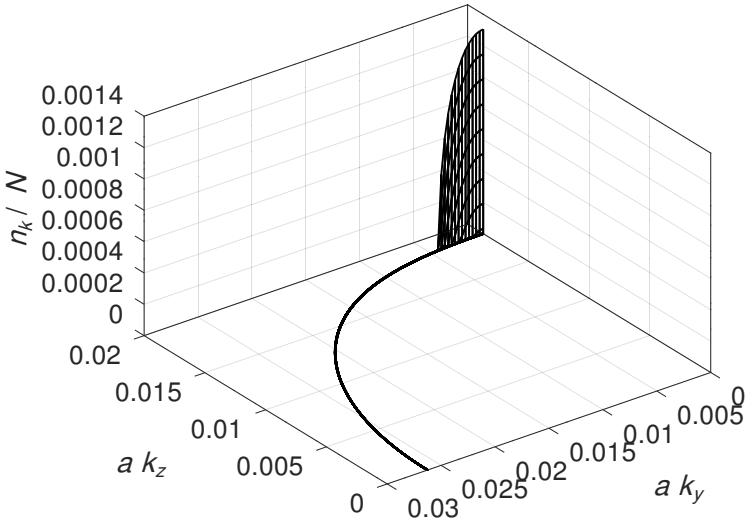

Figure 3.5: The stationary magnon density (3.52) is shown in momentum space for the parameters $\omega_0 = 13.857$ GHz, $H_0 = 100$ mT, $H_1 = 1$ mT, $d = 22.8$ µm, $N = 6.529 \times 10^9$, and for the largest damping rate of Fig. 3.6. The magnon density is only non-vanishing near a small region around the resonance surface shell where the resonance condition (3.51) is fulfilled.

For my set of parameters I find $a\Delta k \approx 5.0 \times 10^{-4}$ with the wave vector being $a\,|\boldsymbol{k}| \approx 1.8 \times 10^{-2}$ for the direction perpendicular to the external magnetic field. Therefore, the approximation of only taking into account the magnon distribution functions on the resonance surface is justified within S-theory. Fig. 3.6 shows the stationary magnon density for different damping rates plotted over the angle α of the wave vector $\boldsymbol{k}$ fulfilling the resonance condition (3.51). When the damping rate γ increases the magnon density drops to zero at larger angles α. As the area where the magnon density is non-vanishing decreases, the approximation of neglecting coupling of different magnon modes becomes more accurate. Lastly, Fig. 3.7 shows the magnon density in the stationary state (3.52) averaged over the wave vector $\boldsymbol{k}$ in dependence of the external magnetic field strength H_0 for different pumping strengths and fixed damping rate γ. In the relevant region the magnon density depends linearly on the magnetic field strength contrary to the experimental results of Ref. [46] where peaks or dips were observed in this parameter regime near the magnetic field strength where confluence processes of parametrically excited magnons with identical energy and momentum become kinematically possible.

Fig. 3.8 shows the time evolution of the diagonal and off-diagonal distribution functions in presence of a phenomenologically introduced damping constant $\gamma = 0.6V_0$. The initial values for the distribution functions were chosen as the thermal equilibrium distribution

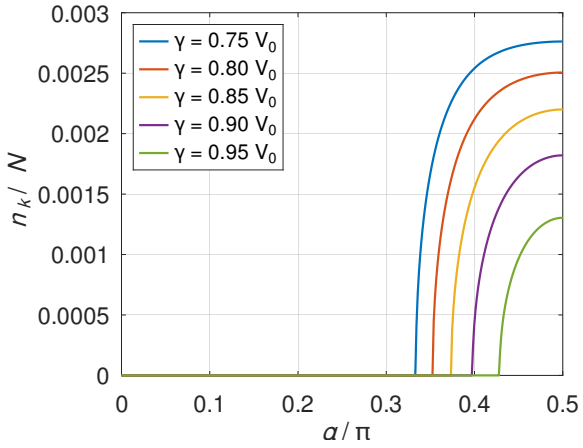

Figure 3.6: Stationary magnon density (3.52) plotted over the angle α of the wave vector $\boldsymbol{k}$ where $\boldsymbol{k}$ fulfills the resonance condition (3.51) and I chose the damping rate between $\gamma = 0.75V_0$ and $\gamma = 0.95V_0$ where V_0 is the pumping energy for parametric magnons at $\alpha = \pi/2$. The parameters chosen here are $\omega_0 = 13.857$ GHz, $H_0 = 100$ mT, $H_1 = 1$ mT, $d = 22.8$ µm, and $N = 6.529 \times 10^9$ corresponding to an area of 0.1 mm^2.

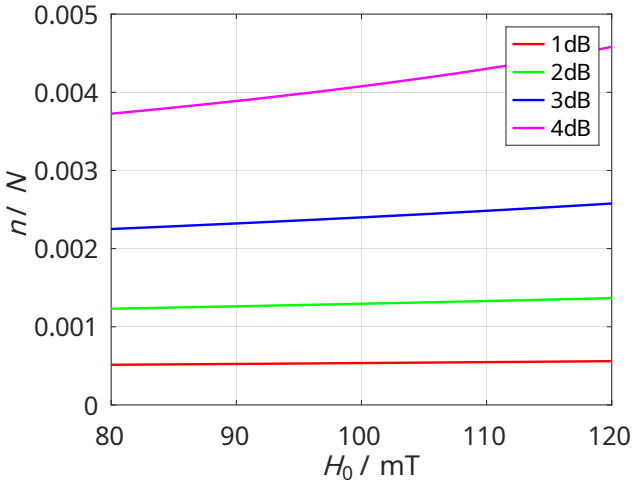

Figure 3.7: The magnon density in the stationary state (3.52) averaged over the resonance surface in momentum space is plotted over the external magnetic field strength H_0 for different pumping strengths and $\omega_0 = 13.857$ GHz and $d = 22.8$ µm. The damping rate γ was chosen to have the same value as the largest damping rate of Fig. 3.6 and N was chosen the same way as in Fig. 3.6. In the relevant region the magnon density depends linearly on the magnetic field strength contrary to the experimental result of Ref. [46].

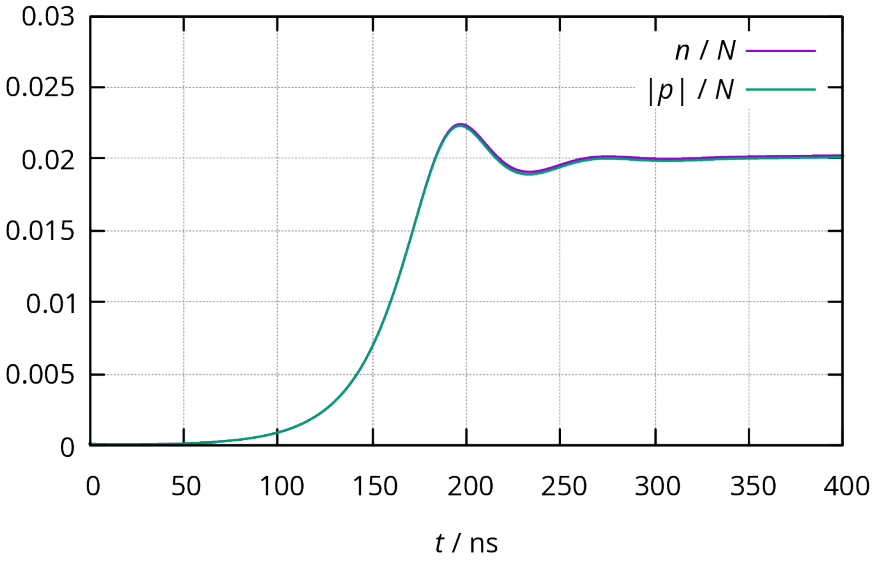

Figure 3.8: The time evolution of the diagonal and off-diagonal magnon densities $n(t)/N$ and $|\tilde{p}(t)|/N$ averaged over all momenta on a grid with $N_\theta = 80$ lattice points. Starting from the thermal distribution the distribution functions increase exponentially for small times and later saturate at a certain level depending on the pumping strength. The parameters chosen here are $\omega_0 = 13.857$ GHz, $H_0 = 100$ mT, $H_1 = 0.5$ mT, $d = 22.8$ µm, and $N = 8.08 \times 10^6$. A constant damping strength $\gamma = 0.6V_0$ has been included.

functions,

$$n_{\boldsymbol{k}}(t_0) = \frac{1}{e^{\beta\epsilon_{\boldsymbol{k}}} - 1}, \tag{3.55a}$$

$$\tilde{p}_{\boldsymbol{k}}(t_0) = 0. \tag{3.55b}$$

The numerical calculations are carried out for $N_\theta = 80$ different angles of the wave vector $\boldsymbol{k}$ chosen uniformly from the interval $[0, \pi/2]$. Only resonant magnons with $\epsilon_{\boldsymbol{k}} = \omega_0/2$ are considered. The connected distribution functions $n(t)$ and $|\tilde{p}(t)|$ are defined as the average over all wave vectors,

$$n(t) = \frac{1}{N_\theta} \sum_\theta n_{\boldsymbol{k}_\theta}(t), \tag{3.56a}$$

$$\tilde{p}(t) = \frac{1}{N_\theta} \sum_\theta \tilde{p}_{\boldsymbol{k}_\theta}(t). \tag{3.56b}$$

For small times the distribution functions grow exponentially while at larger times they saturate at a certain level that depends on the pumping strength. When the distribution functions reach the saturation level they exhibit an oscillatory behavior which is strongly

damped due to the large damping constant. Also, I find that the two curves in Fig. 3.8 lie very close to each others. For large times it is expected that the solution converges to the stationary solution given by Eq. (3.50b) so that I expect $n(t) = |p(t)|$ for large times. The convergence is rather slow, though. For large times the argument of the off-diagonal distribution function is $\arg(\tilde{p}_{\boldsymbol{k}}) \approx 0.64$ which agrees with the value $\arctan(3/4)$ expected from Eq. (3.50b) for the stationary state.

Another issue of the above approximation is that it is only valid if the damping rate $\gamma_{\boldsymbol{k}}$ is sufficiently large. However, this damping rate was added by hand and in the literature it is usually set to a constant value [2, 5, 6]. As we have seen in the above numerical treatment, the damping has a mode selecting effect that justifies the approximations of S-theory. A strong momentum dependence of the damping rate could possibly invalidate the argumentation, though. Furthermore, the experimental observations of Ref. [46] cannot be explained within these approximations. Because the damping plays such an important role on the stationary non-equilibrium state it should be explicitly taken into account in the microscopic calculations by deriving the collision integrals containing three-point vertices.

3.4 Collision integrals

For the purpose of deriving the kinetic equations it is more convenient to use connected correlations instead of n-point distribution functions. Here, the relevant connected correlations are given by the equations (3.41). For the spin-pumping enhancement effect observed in the experiment [46] the condensate amplitude is not relevant and may be neglected in this section. In that case the connected parts of the distribution functions $n^c_{\boldsymbol{k}}$ and $\tilde{p}^c_{\boldsymbol{k}}$ coincide with the total distribution functions $n_{\boldsymbol{k}}$ and $\tilde{p}_{\boldsymbol{k}}$.

The kinetic equations for the diagonal and off-diagonal connected distribution functions can be written in the form (see Eq. (3.39))

$$\partial_t n^c_{\boldsymbol{k}}(t) + i\left[\tilde{V}_{\boldsymbol{k}}(t)\,(\tilde{p}^c_{\boldsymbol{k}})^*(t) - \tilde{V}^*_{\boldsymbol{k}}(t)\tilde{p}^c_{\boldsymbol{k}}(t)\right] = I^n_{\boldsymbol{k}}(t), \tag{3.57a}$$

$$\partial_t \tilde{p}^c_{\boldsymbol{k}}(t) + 2i\tilde{E}_{\boldsymbol{k}}(t)\tilde{p}_{\boldsymbol{k}}(t) + i\tilde{V}_{\boldsymbol{k}}(t)\,[2n^c_{\boldsymbol{k}}(t)+1] = I^p_{\boldsymbol{k}}(t), \tag{3.57b}$$

where the collision integrals $I^n_{\boldsymbol{k}}(t)$ and $I^p_{\boldsymbol{k}}(t)$ on the right-hand side contain all interactions beyond S-theory, in particular the three-magnon processes originating from the cubic Hamiltonian $\mathcal{H}^{(3)}_m$ given by Eq. (3.33). I use the method developed in the previous chapter 2 to derive the contribution to the collision integrals containing three-point vertices. The corresponding diagrams are shown in Fig. 3.9 and 3.10 respectively. Note that, as explained in chapter 2, these diagrams differ from Feynman diagrams. They represent contributions to the time evolution of the equal-time correlation functions $n^c_{\boldsymbol{k}}(t)$ and $\tilde{p}^c_{\boldsymbol{k}}(t)$ at time t. As such they do not involve energy integration but momentum integration appears in loops. The contributions to the collision integrals containing

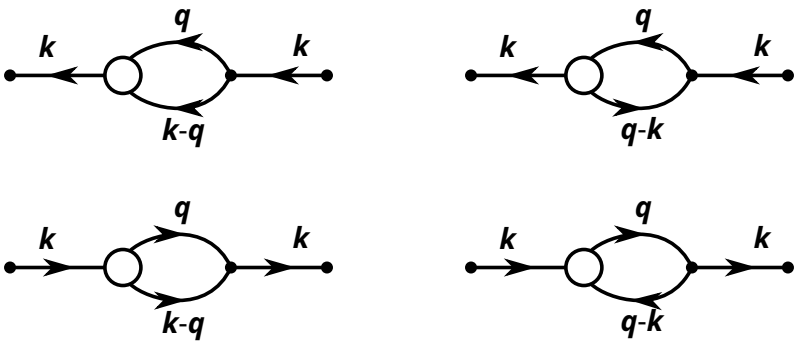

Figure 3.9: Diagrammatic representation of the contributions to the equations of motion of the connected two-point correlation $n^c_{\boldsymbol{k}}(t)$ that originate from the cubic interactions. The diagrams contain one three-point interaction vertex and one correlation bubble representing a three-point correlation. The two left diagrams have a pair of equivalent lines and thus an additional combinatorial prefactor of 1/2 appears. The two lower diagrams correspond to the complex conjugated contributions of the two upper diagrams.

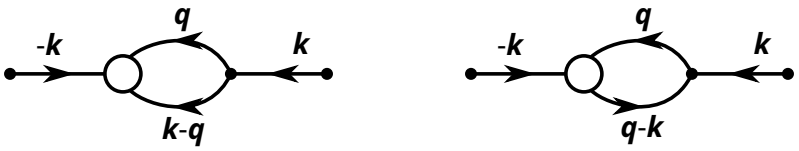

Figure 3.10: Diagrammatic representation of the contributions to the equations of motion of the off-diagonal two-point correlation $\tilde{p}^c_{\boldsymbol{k}}(t)$ that originate from the cubic interactions. The diagrams contain one three-point interaction vertex and one correlation bubble representing a three-point correlation. The left diagrams has a pair of equivalent lines and thus an additional combinatorial prefactor of 1/2 appears.

three-point vertices read [54]

$$I^n_{\boldsymbol{k}} = i\frac{1}{\sqrt{N}}\sum_{\boldsymbol{q}}\left[\frac{1}{2}\Gamma^{\bar{a}aa}_{\boldsymbol{k};\boldsymbol{q},\boldsymbol{k}-\boldsymbol{q}}e^{-i\omega_0 t/2}\langle\tilde{a}^\dagger_{\boldsymbol{q}}\tilde{a}^\dagger_{\boldsymbol{k}-\boldsymbol{q}}\tilde{a}_{\boldsymbol{k}}\rangle^c + \left(\Gamma^{\bar{a}aa}_{\boldsymbol{q};\boldsymbol{q}-\boldsymbol{k},\boldsymbol{k}}\right)^* e^{i\omega_0 t/2}\langle\tilde{a}^\dagger_{\boldsymbol{q}}\tilde{a}_{\boldsymbol{q}-\boldsymbol{k}}\tilde{a}_{\boldsymbol{k}}\rangle^c - \text{c.c.}\right], \tag{3.58a}$$

$$I^p_{\boldsymbol{k}} = -i\frac{1}{\sqrt{N}}\sum_{\boldsymbol{q}}\left[\frac{1}{2}\left(\Gamma^{\bar{a}aa}_{\boldsymbol{k};\boldsymbol{q},\boldsymbol{k}-\boldsymbol{q}}\right)^* e^{i\omega_0 t/2}\langle\tilde{a}_{-\boldsymbol{q}}\tilde{a}_{\boldsymbol{q}-\boldsymbol{k}}\tilde{a}_{-\boldsymbol{k}}\rangle^c + \Gamma^{\bar{a}aa}_{\boldsymbol{q}-\boldsymbol{k};\boldsymbol{q},\boldsymbol{k}}e^{-i\omega_0 t/2}\langle\tilde{a}^\dagger_{\boldsymbol{q}}\tilde{a}_{\boldsymbol{q}-\boldsymbol{k}}\tilde{a}_{-\boldsymbol{k}}\rangle^c\right]. \tag{3.58b}$$

At this point, the above expressions are still exact. They contain, however, three-point correlations so that the set of kinetic equations (3.57) is not closed. It is also necessary to derive the equation of motion of the three-point correlations that appear in the above equation. The lowest order diagrams for the three-point correlation $\langle\tilde{a}^\dagger_{\boldsymbol{q}}\tilde{a}^\dagger_{\boldsymbol{k}-\boldsymbol{q}}\tilde{a}_{\boldsymbol{k}}\rangle^c$ are

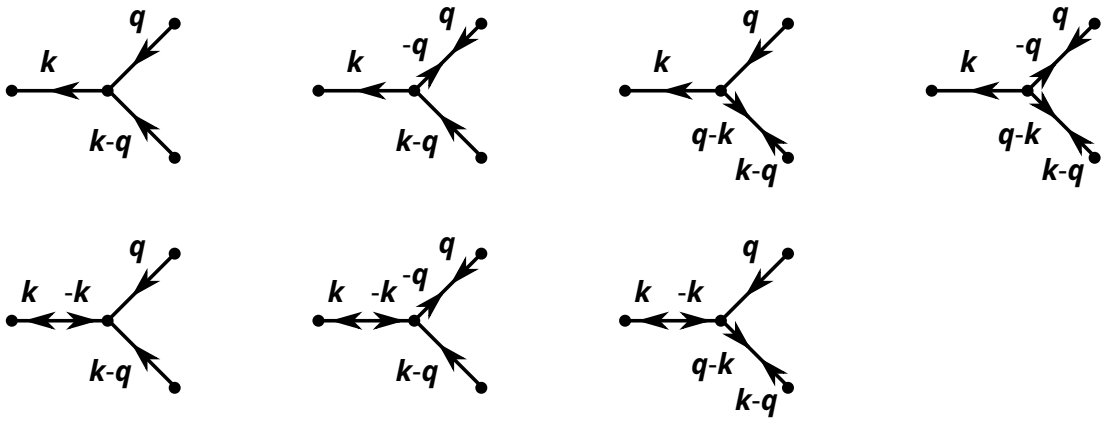

Figure 3.11: The lowest order diagrams contributing to the connected three-point correlation $\langle \tilde{a}^\dagger_{\boldsymbol{q}} \tilde{a}^\dagger_{\boldsymbol{k}-\boldsymbol{q}} \tilde{a}_{\boldsymbol{k}} \rangle^c$. The lines containing two arrows represent the off-diagonal correlation functions $\tilde{p}_{\boldsymbol{q}}$ while the other lines represent contractions. The diagrams for the other three-point correlation functions appearing in the collision integrals $I^n_{\boldsymbol{k}}$ and $I^p_{\boldsymbol{k}}$ have an analogous form.

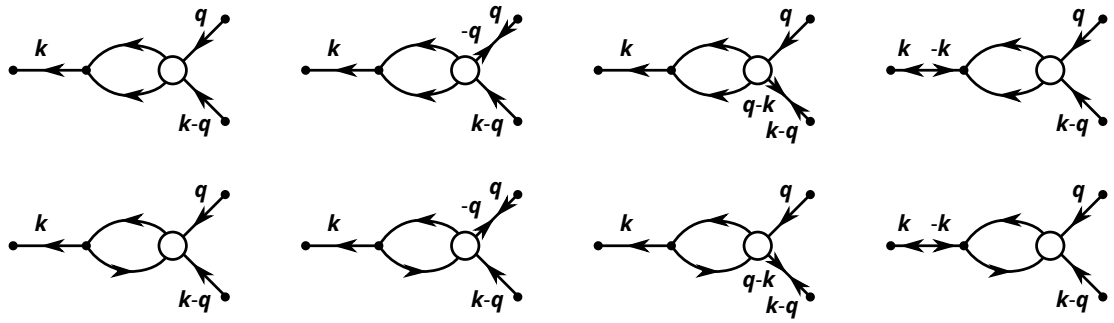

Figure 3.12: Higher order diagrams contributing to the connected three-point correlation $\langle \tilde{a}^\dagger_{\boldsymbol{q}} \tilde{a}^\dagger_{\boldsymbol{k}-\boldsymbol{q}} \tilde{a}_{\boldsymbol{k}} \rangle^c$ which are neglected here. The lines containing two arrows represent the off-diagonal correlation functions $\tilde{p}_{\boldsymbol{q}}$. The diagrams contain one interaction vertex and a four-point correlation.

shown in Fig. 3.11. The diagrams for the other three-point correlation functions appearing in the collision integrals (3.58) have the same form. For example, the resulting equation of motion for the first three-point correlation appearing in Eq. (3.58a) reads

$$\begin{aligned}\left[\frac{d}{dt}+i\left(\epsilon_{\boldsymbol{k}}-\epsilon_{\boldsymbol{q}}-\epsilon_{\boldsymbol{k}-\boldsymbol{q}}\right)\right]\langle\tilde{a}^\dagger_{\boldsymbol{q}}\tilde{a}^\dagger_{\boldsymbol{k}-\boldsymbol{q}}\tilde{a}_{\boldsymbol{k}}\rangle^c = \quad & i\frac{1}{\sqrt{N}}\sum_{\boldsymbol{q}}\Bigg[\frac{1}{2}\left(\Gamma^{\bar{a}aa}_{\boldsymbol{k};\boldsymbol{q},\boldsymbol{k}-\boldsymbol{q}}\right)^* e^{i\omega_0 t/2}\\ \times\left(n^c_{\boldsymbol{k}-\boldsymbol{q}}n^c_{\boldsymbol{q}}-n^c_{\boldsymbol{k}}\left[1+n^c_{\boldsymbol{k}-\boldsymbol{q}}+n^c_{\boldsymbol{q}}\right]\right)&-\frac{1}{2}\left(\Gamma^{\bar{a}aa}_{-\boldsymbol{q};\boldsymbol{k}-\boldsymbol{q},-\boldsymbol{k}}\right)^* e^{i\omega_0 t/2}\left(\tilde{p}^c_{\boldsymbol{k}}\left(\tilde{p}^c_{\boldsymbol{q}}\right)^*\right)\\ &-\frac{1}{2}\left(\Gamma^{\bar{a}aa}_{\boldsymbol{q}-\boldsymbol{k};-\boldsymbol{k},\boldsymbol{q}}\right)^* e^{i\omega_0 t/2}\left(\tilde{p}^c_{\boldsymbol{k}}\left(\tilde{p}^c_{\boldsymbol{k}-\boldsymbol{q}}\right)^*\right)\\ &-\frac{1}{2}\Gamma^{\bar{a}aa}_{\boldsymbol{k}-\boldsymbol{q};\boldsymbol{k},-\boldsymbol{q}}e^{-i\omega_0 t/2}\left(n^c_{\boldsymbol{k}-\boldsymbol{q}}\left(\tilde{p}^c_{\boldsymbol{q}}\right)^*-n^c_{\boldsymbol{k}}\left(\tilde{p}^c_{\boldsymbol{q}}\right)^*\right)\\ &-\frac{1}{2}\Gamma^{\bar{a}aa}_{\boldsymbol{q};\boldsymbol{k},\boldsymbol{q}-\boldsymbol{k}}e^{-i\omega_0 t/2}\left(n^c_{\boldsymbol{q}}\left(\tilde{p}^c_{\boldsymbol{k}-\boldsymbol{q}}\right)^*-n^c_{\boldsymbol{k}}\left(\tilde{p}^c_{\boldsymbol{k}-\boldsymbol{q}}\right)^*\right)\\ &+\frac{1}{3!}\Gamma^{aaa}_{-\boldsymbol{k},\boldsymbol{q}-\boldsymbol{k},\boldsymbol{q}}e^{-i\frac{3}{2}\omega_0 t}\left(\left(\tilde{p}^c_{\boldsymbol{k}-\boldsymbol{q}}\right)^*\left(\tilde{p}^c_{\boldsymbol{q}}\right)^*\right)\\ &-\frac{1}{3!}\Gamma^{\bar{a}\bar{a}\bar{a}}_{-\boldsymbol{k},\boldsymbol{k}-\boldsymbol{q},\boldsymbol{q}}e^{i\frac{3}{2}\omega_0 t}\left(\tilde{p}^c_{\boldsymbol{k}}\left(1+n^c_{\boldsymbol{k}-\boldsymbol{q}}+n^c_{\boldsymbol{q}}\right)\right)\Bigg].\end{aligned}\tag{3.59}$$

At this point I have neglected diagrams that contain higher order correlations. For example, Fig. 3.12 shows the diagrams that I have neglected in the above equation of motion. These contributions contain four-point correlations. It will be argued below that it is consistent to neglect these contributions. Furthermore, terms that lead to oscillating contributions in the collision integrals should be neglected. Therefore, I only take into account the terms in the above Eq. (3.59) that contain a factor of $e^{i\omega_0 t/2}$, i.e. I drop the last four lines. The following calculations are analogous for all three-point correlations, so let us consider the connected three-point correlation $\langle\tilde{a}^\dagger_{\boldsymbol{q}}\tilde{a}^\dagger_{\boldsymbol{k}-\boldsymbol{q}}\tilde{a}_{\boldsymbol{k}}\rangle^c$ as an example. The equation of motion (3.59) can be integrated to get the formal result

$$\begin{aligned}\langle\tilde{a}^\dagger_{\boldsymbol{q}}\tilde{a}^\dagger_{\boldsymbol{k}-\boldsymbol{q}}\tilde{a}_{\boldsymbol{k}}\rangle^c = i\frac{1}{2\sqrt{N}}\sum_{\boldsymbol{q}}\int_{t_0}^{t}dt' e^{-i\left(\epsilon_{\boldsymbol{k}}-\epsilon_{\boldsymbol{q}}-\epsilon_{\boldsymbol{k}-\boldsymbol{q}}\right)(t-t')}e^{i\omega_0 t'/2}\Bigg[\left(\Gamma^{\bar{a}aa}_{\boldsymbol{k};\boldsymbol{q},\boldsymbol{k}-\boldsymbol{q}}\right)^*\Bigg(n^c_{\boldsymbol{k}-\boldsymbol{q}}n^c_{\boldsymbol{q}}\\ -n^c_{\boldsymbol{k}}\left[1+n^c_{\boldsymbol{k}-\boldsymbol{q}}+n^c_{\boldsymbol{q}}\right]\Bigg)-\left(\Gamma^{\bar{a}aa}_{-\boldsymbol{q};\boldsymbol{k}-\boldsymbol{q},-\boldsymbol{k}}\right)^*\tilde{p}^c_{\boldsymbol{k}}\left(\tilde{p}^c_{\boldsymbol{q}}\right)^*-\left(\Gamma^{\bar{a}aa}_{\boldsymbol{q}-\boldsymbol{k};-\boldsymbol{k},\boldsymbol{q}}\right)^*\tilde{p}^c_{\boldsymbol{k}}\left(\tilde{p}^c_{\boldsymbol{k}-\boldsymbol{q}}\right)^*\Bigg].\end{aligned}\tag{3.60}$$

Inserting this equation into Eq. (3.58a) yields [54]

$$\begin{aligned}I^n_{\boldsymbol{k}}=\frac{1}{N}\sum_{\boldsymbol{q}}\Bigg[\frac{1}{2}\int_{t_0}^{t}dt'\cos\left(\left[\epsilon_{\boldsymbol{k}}-\epsilon_{\boldsymbol{q}}-\epsilon_{\boldsymbol{k}-\boldsymbol{q}}\right]\left[t-t'\right]\right)\mathrm{Re}\Bigg(\left|\Gamma^{\bar{a}aa}_{\boldsymbol{k};\boldsymbol{q},\boldsymbol{k}-\boldsymbol{q}}\right|^2\left[n^c_{\boldsymbol{k}-\boldsymbol{q}}n^c_{\boldsymbol{q}}\right.\\ \left.-n^c_{\boldsymbol{k}}\left(1+n^c_{\boldsymbol{k}-\boldsymbol{q}}+n^c_{\boldsymbol{q}}\right)\right]-\Gamma^{\bar{a}aa}_{\boldsymbol{k};\boldsymbol{q},\boldsymbol{k}-\boldsymbol{q}}\left(\Gamma^{\bar{a}aa}_{-\boldsymbol{q};\boldsymbol{k}-\boldsymbol{q},-\boldsymbol{k}}\right)^*\tilde{p}^c_{\boldsymbol{k}}\left(\tilde{p}^c_{\boldsymbol{q}}\right)^*\\ -\Gamma^{\bar{a}aa}_{\boldsymbol{k};\boldsymbol{q},\boldsymbol{k}-\boldsymbol{q}}\left(\Gamma^{\bar{a}aa}_{\boldsymbol{q}-\boldsymbol{k};-\boldsymbol{k},\boldsymbol{q}}\right)^*\tilde{p}^c_{\boldsymbol{k}}\left(\tilde{p}^c_{\boldsymbol{k}-\boldsymbol{q}}\right)^*\Bigg)+\ldots\Bigg],\end{aligned}\tag{3.61}$$

where the dots denote the other term of Eq. (3.58a) involving the correlation $\langle \tilde{a}^\dagger_{\boldsymbol{q}} \tilde{a}_{\boldsymbol{q}-\boldsymbol{k}} \tilde{a}_{\boldsymbol{k}} \rangle^c$. This expression may be further simplified by taking the limit $t_0 \to -\infty$. This approximation neglects the system's history but can be justified because I am interested in the asymptotic behavior of the system for long times. Finally, I get [54]

$$I^n_{\boldsymbol{k}} = \frac{2\pi}{N} \sum_{\boldsymbol{q}} \Bigg[\frac{1}{2} \delta\left(\epsilon_{\boldsymbol{k}} - \epsilon_{\boldsymbol{q}} - \epsilon_{\boldsymbol{k}-\boldsymbol{q}}\right) \mathrm{Re} \Bigg(\left|\Gamma^{\bar{a}aa}_{\boldsymbol{k};\boldsymbol{q},\boldsymbol{k}-\boldsymbol{q}}\right|^2 \left[n^c_{\boldsymbol{k}-\boldsymbol{q}} n^c_{\boldsymbol{q}} - n^c_{\boldsymbol{k}} \left(1 + n^c_{\boldsymbol{k}-\boldsymbol{q}} + n^c_{\boldsymbol{q}}\right)\right]$$
$$- \Gamma^{\bar{a}aa}_{\boldsymbol{k};\boldsymbol{q},\boldsymbol{k}-\boldsymbol{q}} \left(\Gamma^{\bar{a}aa}_{-\boldsymbol{q};\boldsymbol{k}-\boldsymbol{q},-\boldsymbol{k}}\right)^* \left[\tilde{p}^c_{\boldsymbol{k}} \left(\tilde{p}^c_{\boldsymbol{q}}\right)^* \right] - \Gamma^{\bar{a}aa}_{\boldsymbol{k};\boldsymbol{q},\boldsymbol{k}-\boldsymbol{q}} \left(\Gamma^{\bar{a}aa}_{\boldsymbol{q}-\boldsymbol{k};-\boldsymbol{k},\boldsymbol{q}}\right)^* \left[\tilde{p}^c_{\boldsymbol{k}} \left(\tilde{p}^c_{\boldsymbol{k}-\boldsymbol{q}}\right)^* \right] \Bigg) + \dots \Bigg]. \tag{3.62}$$

In the collision integrals for the off-diagonal distribution function (3.58b) the complex conjugated terms do not appear. Thus, the exponential function remains in the expression analogous to Eq. (3.61). When taking the limit $t_0 \to \infty$ I still retain the Dirac delta function but without the prefactor of 2.

It now becomes apparent that the contributions to the time evolution of three-point correlations that only contain the interaction vertex lead to terms of quadratic order in the interaction vertex for the collision integrals $I^n_{\boldsymbol{k}}$ and $I^p_{\boldsymbol{k}}$. If the contributions containing four-point correlations are taken into account as well, the time evolution of the four-point correlations needs to be derived in turn. If only the diagrams containing the interaction vertex are considered analogously to the above treatment of the three-point correlations, the resulting equations of motions have a similar structure compared to Eqs. (3.59). Therefore, the four-point correlations are of order of the interaction vertex. Inserting them into the equation of motion of the three-point correlation (3.59) thus leads to a term of quadratic order in the interaction vertex and subsequently inserting the three-point correlation into the collision integral (3.58a) leads to a term of quartic order. However, as all terms of order larger than quadratic in the interaction vertices should be neglected, the terms containing four-point correlations should be dropped from the equations of motion of the three-point correlations.

Finally, the collision integrals for the diagonal and the off-diagonal magnon distribution functions read [54]

$$I^n_{\boldsymbol{k}} = \frac{2\pi}{N} \sum_{\boldsymbol{q}} \mathrm{Re} \Bigg[\frac{1}{2} \delta\left(\epsilon_{\boldsymbol{k}} - \epsilon_{\boldsymbol{k}-\boldsymbol{q}} - \epsilon_{\boldsymbol{q}}\right)$$
$$\times \Bigg(\left|\Gamma^{\bar{a}aa}_{\boldsymbol{k};\boldsymbol{k}-\boldsymbol{q},\boldsymbol{q}}\right|^2 \left[n^c_{\boldsymbol{k}-\boldsymbol{q}} n^c_{\boldsymbol{q}} - n^c_{\boldsymbol{k}} \left(1 + n^c_{\boldsymbol{k}-\boldsymbol{q}} + n^c_{\boldsymbol{q}}\right)\right]$$
$$- \Gamma^{\bar{a}aa}_{\boldsymbol{k};\boldsymbol{q},\boldsymbol{k}-\boldsymbol{q}} \left(\Gamma^{\bar{a}aa}_{-\boldsymbol{q};\boldsymbol{k}-\boldsymbol{q},-\boldsymbol{k}}\right)^* \tilde{p}^c_{\boldsymbol{k}} \left(\tilde{p}^c_{\boldsymbol{q}}\right)^* - \Gamma^{\bar{a}aa}_{\boldsymbol{k};\boldsymbol{q},\boldsymbol{k}-\boldsymbol{q}} \left(\Gamma^{\bar{a}aa}_{\boldsymbol{q}-\boldsymbol{k};-\boldsymbol{k},\boldsymbol{q}}\right)^* \tilde{p}^c_{\boldsymbol{k}} \left(\tilde{p}^c_{\boldsymbol{k}-\boldsymbol{q}}\right)^* \Bigg)$$
$$+ \delta\left(\epsilon_{\boldsymbol{k}} + \epsilon_{\boldsymbol{q}-\boldsymbol{k}} - \epsilon_{\boldsymbol{q}}\right) \Bigg(\left|\Gamma^{\bar{a}aa}_{\boldsymbol{q};\boldsymbol{q}-\boldsymbol{k},\boldsymbol{k}}\right|^2 \left[n^c_{\boldsymbol{q}} \left(1 + n^c_{\boldsymbol{k}} + n^c_{\boldsymbol{q}-\boldsymbol{k}}\right) - n^c_{\boldsymbol{k}} n^c_{\boldsymbol{q}-\boldsymbol{k}} \right]$$
$$- \Gamma^{\bar{a}aa}_{-\boldsymbol{k};\boldsymbol{q}-\boldsymbol{k},-\boldsymbol{q}} \left(\Gamma^{\bar{a}aa}_{\boldsymbol{q};\boldsymbol{q}-\boldsymbol{k},\boldsymbol{k}}\right)^* \tilde{p}^c_{\boldsymbol{k}} \left(\tilde{p}^c_{\boldsymbol{q}}\right)^* - \Gamma^{\bar{a}aa}_{\boldsymbol{k}-\boldsymbol{q};\boldsymbol{k},-\boldsymbol{q}} \left(\Gamma^{\bar{a}aa}_{\boldsymbol{q};\boldsymbol{q}-\boldsymbol{k},\boldsymbol{k}}\right)^* \tilde{p}^c_{\boldsymbol{q}-\boldsymbol{k}} \left(\tilde{p}^c_{\boldsymbol{q}}\right)^* \Bigg) \Bigg], \tag{3.63}$$

and

$$I^p_{\boldsymbol{k}} = \frac{2\pi}{N}\sum_{\boldsymbol{q}}\Bigg[-\frac{1}{2}\delta\left(\epsilon_{-\boldsymbol{k}}-\epsilon_{\boldsymbol{q}}-\epsilon_{\boldsymbol{k}-\boldsymbol{q}}\right)$$
$$\times\Bigg(\left|\Gamma^{\bar{a}aa}_{\boldsymbol{k};\boldsymbol{k}-\boldsymbol{q},\boldsymbol{q}}\right|^2\tilde{p}^c_{\boldsymbol{k}}\left[1+n^c_{\boldsymbol{q}}+n^c_{\boldsymbol{k}-\boldsymbol{q}}\right]+\Gamma^{\bar{a}aa}_{\boldsymbol{q};\boldsymbol{k}-\boldsymbol{q},-\boldsymbol{k}}\left(\Gamma^{\bar{a}aa}_{\boldsymbol{k};\boldsymbol{k}-\boldsymbol{q},\boldsymbol{q}}\right)^*\tilde{p}^c_{\boldsymbol{q}}\left[1+n^c_{-\boldsymbol{k}}\right.$$
$$\left.+n^c_{\boldsymbol{k}-\boldsymbol{q}}\right]+\Gamma^{\bar{a}aa}_{\boldsymbol{q}-\boldsymbol{k};\boldsymbol{q},-\boldsymbol{k}}\left(\Gamma^{\bar{a}aa}_{\boldsymbol{k};\boldsymbol{k}-\boldsymbol{q},\boldsymbol{q}}\right)^*\tilde{p}^c_{\boldsymbol{k}-\boldsymbol{q}}\left[1+n^c_{-\boldsymbol{k}}+n^c_{\boldsymbol{q}}\right]\Bigg)$$
$$+\delta\left(\epsilon_{-\boldsymbol{k}}+\epsilon_{\boldsymbol{q}}-\epsilon_{\boldsymbol{k}-\boldsymbol{q}}\right)\Bigg(\Gamma^{\bar{a}aa}_{\boldsymbol{q};\boldsymbol{q}-\boldsymbol{k},\boldsymbol{k}}\left(\Gamma^{\bar{a}aa}_{-\boldsymbol{k};\boldsymbol{q}-\boldsymbol{k},-\boldsymbol{q}}\right)^*\tilde{p}^c_{\boldsymbol{q}}\left[n^c_{-\boldsymbol{k}}-n^c_{\boldsymbol{q}-\boldsymbol{k}}\right]$$
$$\left.-\Gamma^{\bar{a}aa}_{\boldsymbol{q};\boldsymbol{q}-\boldsymbol{k},\boldsymbol{k}}\left(\Gamma^{\bar{a}aa}_{\boldsymbol{q};\boldsymbol{q}-\boldsymbol{k},-\boldsymbol{k}}\right)^*\tilde{p}^c_{-\boldsymbol{k}}\left[n^c_{\boldsymbol{q}-\boldsymbol{k}}-n^c_{\boldsymbol{q}}\right]\Bigg)\right], \tag{3.64}$$

respectively. Note that I have neglected oscillating terms in the above equations. The collision integrals can be separated into an arrival (in-scattering) term and a departure (out-scattering) term,

$$I^n_{\boldsymbol{k}} = I^n_{\boldsymbol{k},\mathrm{in}} - I^n_{\boldsymbol{k},\mathrm{out}}, \tag{3.65a}$$
$$I^p_{\boldsymbol{k}} = I^p_{\boldsymbol{k},\mathrm{in}} - I^p_{\boldsymbol{k},\mathrm{out}}. \tag{3.65b}$$

The arrival terms describe scattering processes of particles which have the momentum $\boldsymbol{k}$ after the collision while the departure terms describe scattering processes of particles with momentum $\boldsymbol{k}$ into different states. For the above collision integrals the arrival and departure terms are

$$I^n_{\boldsymbol{k},\mathrm{in}} = \frac{2\pi}{N}\sum_{\boldsymbol{q}}\mathrm{Re}\Bigg[\frac{1}{2}\delta\left(\epsilon_{\boldsymbol{k}}-\epsilon_{\boldsymbol{k}-\boldsymbol{q}}-\epsilon_{\boldsymbol{q}}\right)\Bigg(\left|\Gamma^{\bar{a}aa}_{\boldsymbol{k};\boldsymbol{k}-\boldsymbol{q},\boldsymbol{q}}\right|^2 n^c_{\boldsymbol{k}-\boldsymbol{q}}n^c_{\boldsymbol{q}}$$
$$-\Gamma^{\bar{a}aa}_{\boldsymbol{k};\boldsymbol{q},\boldsymbol{k}-\boldsymbol{q}}\left(\Gamma^{\bar{a}aa}_{-\boldsymbol{q};\boldsymbol{k}-\boldsymbol{q},-\boldsymbol{k}}\right)^*\tilde{p}^c_{\boldsymbol{k}}\left(\tilde{p}^c_{\boldsymbol{q}}\right)^*-\Gamma^{\bar{a}aa}_{\boldsymbol{k};\boldsymbol{q},\boldsymbol{k}-\boldsymbol{q}}\left(\Gamma^{\bar{a}aa}_{\boldsymbol{q}-\boldsymbol{k};-\boldsymbol{k},\boldsymbol{q}}\right)^*\tilde{p}^c_{\boldsymbol{k}}\left(\tilde{p}^c_{\boldsymbol{k}-\boldsymbol{q}}\right)^*\Bigg)$$
$$+\delta\left(\epsilon_{\boldsymbol{k}}+\epsilon_{\boldsymbol{q}-\boldsymbol{k}}-\epsilon_{\boldsymbol{q}}\right)\Bigg(\left|\Gamma^{\bar{a}aa}_{\boldsymbol{q};\boldsymbol{q}-\boldsymbol{k},\boldsymbol{k}}\right|^2 n^c_{\boldsymbol{q}}\left[1+n^c_{\boldsymbol{q}-\boldsymbol{k}}\right]$$
$$\left.-\Gamma^{\bar{a}aa}_{-\boldsymbol{k};\boldsymbol{q}-\boldsymbol{k},-\boldsymbol{q}}\left(\Gamma^{\bar{a}aa}_{\boldsymbol{q};\boldsymbol{q}-\boldsymbol{k},\boldsymbol{k}}\right)^*\tilde{p}^c_{\boldsymbol{k}}\left(\tilde{p}^c_{\boldsymbol{q}}\right)^*-\Gamma^{\bar{a}aa}_{\boldsymbol{k}-\boldsymbol{q};\boldsymbol{k},-\boldsymbol{q}}\left(\Gamma^{\bar{a}aa}_{\boldsymbol{q};\boldsymbol{q}-\boldsymbol{k},\boldsymbol{k}}\right)^*\tilde{p}^c_{\boldsymbol{q}-\boldsymbol{k}}\left(\tilde{p}^c_{\boldsymbol{q}}\right)^*\Bigg)\Bigg], \tag{3.66a}$$

$$I^n_{\boldsymbol{k},\mathrm{out}} = \frac{2\pi}{N}\sum_{\boldsymbol{q}}\mathrm{Re}\Bigg[\frac{1}{2}\delta\left(\epsilon_{\boldsymbol{k}}-\epsilon_{\boldsymbol{k}-\boldsymbol{q}}-\epsilon_{\boldsymbol{q}}\right)\left|\Gamma^{\bar{a}aa}_{\boldsymbol{k};\boldsymbol{k}-\boldsymbol{q},\boldsymbol{q}}\right|^2 n^c_{\boldsymbol{k}}\left(1+n^c_{\boldsymbol{k}-\boldsymbol{q}}+n^c_{\boldsymbol{q}}\right)$$
$$+\delta\left(\epsilon_{\boldsymbol{k}}+\epsilon_{\boldsymbol{q}-\boldsymbol{k}}-\epsilon_{\boldsymbol{q}}\right)\left|\Gamma^{\bar{a}aa}_{\boldsymbol{q};\boldsymbol{q}-\boldsymbol{k},\boldsymbol{k}}\right|^2 n^c_{\boldsymbol{k}}\left(n^c_{\boldsymbol{q}-\boldsymbol{k}}-n^c_{\boldsymbol{q}}\right)\Bigg], \tag{3.66b}$$

$$I^p_{\boldsymbol{k},\mathrm{in}} = \frac{\pi}{N}\sum_{\boldsymbol{q}}\Bigg[-\frac{1}{2}\delta\left(\epsilon_{-\boldsymbol{k}}-\epsilon_{\boldsymbol{q}}-\epsilon_{\boldsymbol{k}-\boldsymbol{q}}\right)\Big(\Gamma^{\bar{a}aa}_{\boldsymbol{q};\boldsymbol{k}-\boldsymbol{q},-\boldsymbol{k}}\left(\Gamma^{\bar{a}aa}_{\boldsymbol{k};\boldsymbol{k}-\boldsymbol{q},\boldsymbol{q}}\right)^*\tilde{p}^c_{\boldsymbol{q}}\left[1+n^c_{-\boldsymbol{k}}+n^c_{\boldsymbol{k}-\boldsymbol{q}}\right] + \Gamma^{\bar{a}aa}_{\boldsymbol{q}-\boldsymbol{k};\boldsymbol{q},-\boldsymbol{k}}\left(\Gamma^{\bar{a}aa}_{\boldsymbol{k};\boldsymbol{k}-\boldsymbol{q},\boldsymbol{q}}\right)^*\tilde{p}^c_{\boldsymbol{k}-\boldsymbol{q}}\left[1+n^c_{-\boldsymbol{k}}+n^c_{\boldsymbol{q}}\right]\Big) + \delta\left(\epsilon_{-\boldsymbol{k}}+\epsilon_{\boldsymbol{q}}-\epsilon_{\boldsymbol{k}-\boldsymbol{q}}\right)\Big(\Gamma^{\bar{a}aa}_{\boldsymbol{q};\boldsymbol{q}-\boldsymbol{k},\boldsymbol{k}}\left(\Gamma^{\bar{a}aa}_{-\boldsymbol{k};\boldsymbol{q}-\boldsymbol{k},-\boldsymbol{q}}\right)^*\tilde{p}^c_{\boldsymbol{q}}\left[n^c_{-\boldsymbol{k}}-n^c_{\boldsymbol{q}-\boldsymbol{k}}\right]\Big)\Bigg], \tag{3.67a}$$

$$I^p_{\boldsymbol{k},\mathrm{out}} = -\frac{\pi}{N}\sum_{\boldsymbol{q}}\Bigg[\frac{1}{2}\delta\left(\epsilon_{-\boldsymbol{k}}-\epsilon_{\boldsymbol{q}}-\epsilon_{\boldsymbol{k}-\boldsymbol{q}}\right)\left|\Gamma^{\bar{a}aa}_{\boldsymbol{k};\boldsymbol{k}-\boldsymbol{q},\boldsymbol{q}}\right|^2\tilde{p}^c_{\boldsymbol{k}}\left[1+n^c_{\boldsymbol{q}}+n^c_{\boldsymbol{k}-\boldsymbol{q}}\right] + \delta\left(\epsilon_{-\boldsymbol{k}}+\epsilon_{\boldsymbol{q}}-\epsilon_{\boldsymbol{k}-\boldsymbol{q}}\right)\Gamma^{\bar{a}aa}_{\boldsymbol{q};\boldsymbol{q}-\boldsymbol{k},\boldsymbol{k}}\left(\Gamma^{\bar{a}aa}_{\boldsymbol{q};\boldsymbol{q}-\boldsymbol{k},-\boldsymbol{k}}\right)^*\tilde{p}^c_{-\boldsymbol{k}}\left[n^c_{\boldsymbol{q}-\boldsymbol{k}}-n^c_{\boldsymbol{q}}\right]\Bigg]. \tag{3.67b}$$

Furthermore, the departure terms can be written as

$$I^n_{\boldsymbol{k},\mathrm{out}} = \gamma^n_{\boldsymbol{k}} n^c_{\boldsymbol{k}}, \tag{3.68a}$$
$$I^p_{\boldsymbol{k},\mathrm{out}} = \gamma^p_{\boldsymbol{k}} \tilde{p}^c_{\boldsymbol{k}}, \tag{3.68b}$$

where $\gamma^n_{\boldsymbol{k}}$ and $\gamma^p_{\boldsymbol{k}}$ are time-dependent damping rates.

3.5 Confluence of magnons

Now that I have derived the kinetic equations, the next step is to investigate the effect of the collision integrals on the magnon dynamics. Considering the departure term of the diagonal collision integral given by Eq. (3.66b), the first line describes the damping due to confluence processes of magnons where two magnons are annihilated and one magnons is created [54],

$$\gamma^{n,\mathrm{con}}_{\boldsymbol{k}} = \frac{\pi}{N}\sum_{\boldsymbol{q}}\delta\left(\epsilon_{\boldsymbol{k}}-\epsilon_{\boldsymbol{k}-\boldsymbol{q}}-\epsilon_{\boldsymbol{q}}\right)\left|\Gamma^{\bar{a}aa}_{\boldsymbol{k};\boldsymbol{k}-\boldsymbol{q},\boldsymbol{q}}\right|^2\left(1+n^c_{\boldsymbol{k}-\boldsymbol{q}}+n^c_{\boldsymbol{q}}\right), \tag{3.69}$$

while the second line describes the damping due to splitting processes where one magnon is annihilated and two magnons are created,

$$\gamma^{n,\mathrm{split}}_{\boldsymbol{k}} = \frac{2\pi}{N}\sum_{\boldsymbol{q}}\delta\left(\epsilon_{\boldsymbol{k}}+\epsilon_{\boldsymbol{q}-\boldsymbol{k}}-\epsilon_{\boldsymbol{q}}\right)\left|\Gamma^{\bar{a}aa}_{\boldsymbol{q};\boldsymbol{q}-\boldsymbol{k},\boldsymbol{k}}\right|^2\left(n^c_{\boldsymbol{q}-\boldsymbol{k}}-n^c_{\boldsymbol{q}}\right). \tag{3.70}$$

In the diagrammatic language of Feynman diagrams the confluence processes are represented by particle-particle bubbles of magnon propagators while the splitting processes are represented by particle-hole bubbles.

3.5.1 Constant damping

Let us first assume that contributions originating from confluence and splitting processes dominate the above collision integrals and neglect the other terms. This approximation greatly simplifies the kinetic equations as the collision integrals can now be written in the form

$$I^n_{\boldsymbol{k}}(t) = \gamma^n_{\boldsymbol{k}}(t) n_{\boldsymbol{k}}(t), \tag{3.71a}$$
$$I^p_{\boldsymbol{k}}(t) = \gamma^p_{\boldsymbol{k}}(t) \tilde{p}_{\boldsymbol{k}}(t), \tag{3.71b}$$

where $\gamma^n_{\boldsymbol{k}}$ and $\gamma^p_{\boldsymbol{k}}$ are damping rates that, according to the above expressions for the collision integrals, explicitly depend on the magnon distribution function and are thus time-dependent. Let us assume for now that these damping rates are constant in order to investigate the relation of my kinetic theory with S-theory. It is easy to analytically derive the stationary non-equilibrium state within this approximation. In general, the damping rate $\gamma^p_{\boldsymbol{k}}$ can be complex valued. It is convenient to group together the imaginary part of $\gamma^p_{\boldsymbol{k}}$ with the magnon energy $E_{\boldsymbol{k}}$ so that [54]

$$\tilde{E}_{\boldsymbol{k}} = E_{\boldsymbol{k}} - \frac{1}{2}\mathrm{Im}\left[\gamma^p_{\boldsymbol{k}}\right] + \frac{1}{N}\sum_{\boldsymbol{q}} T_{\boldsymbol{k},\boldsymbol{q}} n_{\boldsymbol{q}}(t). \tag{3.72}$$

For $|V_{\boldsymbol{k}}| > \frac{1}{4}\gamma^n_{\boldsymbol{k}}\mathrm{Re}\left[\gamma^p_{\boldsymbol{k}}\right]$ there exists a stationary non-equilibrium state given by [54]

$$n^s_{\boldsymbol{k}} = \sqrt{\frac{\mathrm{Re}\left[\gamma^p_{\boldsymbol{k}}\right]}{\gamma^n_{\boldsymbol{k}}}}\,|\tilde{p}_{\boldsymbol{k}}|\,, \tag{3.73a}$$
$$\tilde{p}^s_{\boldsymbol{k}} = -\left(\sqrt{1 - \frac{\gamma^n_{\boldsymbol{k}}\mathrm{Re}\left[\gamma^p_{\boldsymbol{k}}\right]}{4\,|V_{\boldsymbol{k}}|^2}} + i\sqrt{\frac{\gamma^n_{\boldsymbol{k}}\mathrm{Re}\left[\gamma^p_{\boldsymbol{k}}\right]}{4\,|V_{\boldsymbol{k}}|^2}}\right)|\tilde{p}_{\boldsymbol{k}}|\,, \tag{3.73b}$$
$$|\tilde{p}^s_{\boldsymbol{k}}| = N\frac{\sqrt{|V_{\boldsymbol{k}}|^2 - \frac{1}{4}\gamma^n_{\boldsymbol{k}}\mathrm{Re}\left[\gamma^p_{\boldsymbol{k}}\right]} - |E_{\boldsymbol{k}} - \frac{1}{2}\mathrm{Im}\left[\gamma^p_{\boldsymbol{k}}\right]|\sqrt{\gamma^n_{\boldsymbol{k}}/\mathrm{Re}\left[\gamma^p_{\boldsymbol{k}}\right]}}{T_{\boldsymbol{k},\boldsymbol{k}} + \frac{1}{2}S_{\boldsymbol{k},\boldsymbol{k}}}. \tag{3.73c}$$

Note that for $\frac{1}{2}\gamma^n_{\boldsymbol{k}} = \frac{1}{2}\gamma^p_{\boldsymbol{k}} \equiv \gamma_{\boldsymbol{k}}$ the above expressions for the diagonal and off-diagonal distribution functions reduce to the conventional S-theory result (3.50). Furthermore, this expression is capable of describing the experimental findings in principle. The additional prefactor in Eq. (3.73a) can describe an enhancement of the magnon density if $\mathrm{Re}\left[\gamma^p_{\boldsymbol{k}}\right]$ becomes larger than $\gamma^n_{\boldsymbol{k}}$ while the damping rate

$$\gamma_{\boldsymbol{k}} = \frac{1}{2}\sqrt{\gamma^n_{\boldsymbol{k}}\mathrm{Re}\left[\gamma^p_{\boldsymbol{k}}\right]} \tag{3.74}$$

leads to a decrease of the magnon density.

The confluence magnetic field strength H^C is defined as the external magnetic field strength where confluence and splitting processes are allowed for parametrically pumped magnons with the same momenta. Due to the anisotropy of the magnon dispersion this field strength depends on the angle $\Theta_{\boldsymbol{k}}$ of the magnon wave vector (see Fig. 3.1). For

a YIG film of thickness $d = 22.8$ µm the confluence field strength for magnons with $\alpha_{\boldsymbol{k}} = \pi/2$ is $H^C_{\pi/2} = 94.68$ mT while for $\alpha_{\boldsymbol{k}} = 0$ I find $H^C_0 = 164.5$ mT. For instance, at the external field strength $H_0 = H^C_{\pi/2}$ energy and momentum conservation for confluence process are fulfilled for magnons with wave vectors $\boldsymbol{k}_0$ that fulfill the resonance condition $\epsilon_{\boldsymbol{k}_0} = \omega_0/2$ and $\boldsymbol{k}_0 \parallel \boldsymbol{e}_y$. The magnons that are created by this confluence process have the two times larger wave vector $2\boldsymbol{k}_0$ and the energy $\epsilon_{2\boldsymbol{k}_0} = \omega_0$. A significant dependence on the external magnetic field H_0 in this range of the magnetic field strength is expected. To see this, the two damping rates $\gamma^n_{\boldsymbol{k}}$ and $\gamma^p_{\boldsymbol{k}}$ should be calculated from the microscopic collision integrals (3.63) and (3.64).

3.5.2 Parametric and secondary magnon groups

Now, let us go beyond the approximation of setting the damping rates $\gamma^n_{\boldsymbol{k}}$ and $\gamma^p_{\boldsymbol{k}}$ to constant values. There are two interacting groups of magnons that are relevant to explain the observations of the experiment. They are characterized by distinct magnon energies. The first group is the parametric magnon group consisting of parametrically excited magnons which are generated by the oscillating microwave field. I use the previous result of S-theory that only magnons near the resonance surface characterized by $\epsilon_{\boldsymbol{k}} = \omega_0/2$ are generated by parametric pumping. Therefore, it is reasonable to assume that parametrically pumped magnons fulfill the resonance condition (3.51) [2, 5]. The second group is the secondary magnon group. Secondary magnons are created by confluence processes of parametric magnons where two magnons with energy $\omega_0/2$ are annihilated and one magnon with energy ω_0 is created. Therefore, secondary magnons posses the energy $\epsilon_{\boldsymbol{k}} = \omega_0$.

All other magnons are assumed to be in thermal equilibrium characterized by

$$n^{\mathrm{th}}_{\boldsymbol{k}} = \frac{1}{e^{\beta\epsilon_{\boldsymbol{k}}} - 1}, \tag{3.75a}$$

$$\tilde{p}^{\mathrm{th}}_{\boldsymbol{k}} = 0, \tag{3.75b}$$

and I include these contributions to the total magnon distribution functions for the numerical calculation of the collision integrals. The collision integrals in thermal equilibrium can be calculated numerically. For this purpose I approximate

$$\begin{aligned} \Gamma^{\bar{a}aa}_{\boldsymbol{k}_1;\boldsymbol{k}_2,\boldsymbol{k}_3} &= \Gamma^{\bar{b}bb}_{\boldsymbol{k}_1,\boldsymbol{k}_2,\boldsymbol{k}_3} = \sqrt{\frac{S}{2}}\left(D^{zy}_{\boldsymbol{k}_2} + D^{yz}_{\boldsymbol{k}_3}\right) \\ &\approx -\frac{\Delta}{\sqrt{2S}}\left(\frac{k_{2y}k_{2z}}{k_2^2} + \frac{k_{3y}k_{3z}}{k_3^2}\right). \end{aligned} \tag{3.76}$$

Furthermore, for large temperatures the magnon distribution function in thermal equilibrium may be approximated by

$$n_{\boldsymbol{q}} \approx T/\epsilon_{\boldsymbol{q}}, \tag{3.77a}$$

$$n_{\boldsymbol{k}-\boldsymbol{q}} \approx T/\epsilon_{\boldsymbol{k}-\boldsymbol{q}}, \tag{3.77b}$$

so that the contribution to the damping originating from confluence processes in thermal equilibrium can be approximated by [54]

$$\frac{\gamma_{\boldsymbol{k}}^{n,\mathrm{con}}}{\epsilon_{\boldsymbol{k}}} = \frac{T}{8J}\left(\frac{\Delta}{h_0 S}\right)^2 \Theta\left(|\boldsymbol{k}|-\kappa\right) F_{\mathrm{con}}\left(\boldsymbol{k}/\kappa\right), \tag{3.78}$$

with the threshold momentum

$$\kappa^2 = \frac{2h_0}{\rho}, \tag{3.79}$$

and

$$\begin{aligned} F_{\mathrm{con}}\left(\boldsymbol{p}\right) = \int_0^{2\pi} \frac{d\varphi}{2\pi} & \frac{1}{\left[1+\frac{1}{2}\left(\pm p+\hat{\boldsymbol{q}}_\varphi\sqrt{p^2-1}\right)^2\right]\left[1+\frac{1}{2}\left(\pm p-\hat{\boldsymbol{q}}_\varphi\sqrt{p^2-1}\right)^2\right]} \\ & \times\left[\frac{\left[p_y+\sqrt{p^2-1}\cos\varphi\right]\left[p_z+\sqrt{p^2-1}\sin\varphi\right]}{\left(\pm p+\hat{\boldsymbol{q}}_\varphi\sqrt{p^2-1}\right)^2}\right. \\ & \left.+\frac{\left[p_y-\sqrt{p^2-1}\cos\varphi\right]\left[p_z-\sqrt{p^2-1}\sin\varphi\right]}{\left(\pm p-\hat{\boldsymbol{q}}_\varphi\sqrt{p^2-1}\right)^2}\right]^2. \end{aligned} \tag{3.80}$$

For the contribution to the damping caused by splitting processes I find [54]

$$\begin{aligned} \frac{\gamma_{\boldsymbol{k}}^{n,\mathrm{split}}}{\epsilon_{\boldsymbol{k}}} = \frac{T}{8J}\left(\frac{\Delta}{h_0 S}\right)^2 \int_{-\infty}^{\infty}\frac{dq'}{\kappa} & \left[\frac{k_y k_z}{k^2}+\frac{\left(\frac{\kappa^2}{4|\boldsymbol{k}|}k_y+q'k_z\right)\left(\frac{\kappa^2}{4|\boldsymbol{k}|}k_z-q'k_y\right)}{\left(\frac{\kappa^2}{4|\boldsymbol{k}|}k_y+q'k_z\right)^2+\left(\frac{\kappa^2}{4|\boldsymbol{k}|}k_z-q'k_y\right)^2}\right]^2 \\ & \times\left[\frac{1}{1+2\frac{q'^2}{\kappa^2}}-\frac{1}{1+2\frac{|\boldsymbol{k}+\tilde{\boldsymbol{q}}'|^2}{\kappa^2}}\right], \end{aligned} \tag{3.81}$$

with $\tilde{\boldsymbol{q}}' = \frac{\kappa^2}{4|\boldsymbol{k}|}\mathbf{e}_\parallel + q'\mathbf{e}_\perp$ and $\mathbf{e}_\parallel \parallel \boldsymbol{k}$, $\mathbf{e}_\perp \perp \boldsymbol{k}$.

For the two magnon groups defined above the collision integrals greatly simplify because the arguments of the Dirac delta functions only vanish if two of the magnons of the three-body interactions are parametric magnons and the other magnon is a secondary magnon. $n_{\boldsymbol{k}}^{(0)}$ and $\tilde{p}_{\boldsymbol{k}}^{(0)}$ denote the parametric magnon distribution functions while $n_{\boldsymbol{k}}^{(1)}$ and $\tilde{p}_{\boldsymbol{k}}^{(1)}$ denote the secondary magnon distribution functions. These distribution functions do not contain contributions coming from thermal magnons but rather represent the deviation from the thermal magnon distribution functions due to the parametric

pumping. The collision integrals for parametric and secondary magnons read [54]

$$I_{\boldsymbol{k}}^{n0} = I_{\boldsymbol{k}}^{n,\mathrm{th}} + \frac{2\pi}{N} \sum_{\substack{\boldsymbol{q} \\ \epsilon_{\boldsymbol{q}}=\omega_0 \\ \epsilon_{\boldsymbol{q}-\boldsymbol{k}}=\omega_0/2}} \Bigg(\left|\Gamma^{\bar{a}aa}_{\boldsymbol{q};\boldsymbol{k},\boldsymbol{q}-\boldsymbol{k}}\right|^2 \left[n_{\boldsymbol{q}}^{(1)} \left(1 + n_{\boldsymbol{q}-\boldsymbol{k}}^{(0)}\right) - n_{\boldsymbol{k}}^{(0)} \left(n_{\boldsymbol{q}-\boldsymbol{k}}^{(0)} - n_{\boldsymbol{q}}^{(1)} \right) \right] - \mathrm{Re}\left[\Gamma^{\bar{a}aa}_{-\boldsymbol{k};\boldsymbol{q}-\boldsymbol{k},-\boldsymbol{q}} \left(\Gamma^{\bar{a}aa}_{\boldsymbol{q};\boldsymbol{q}-\boldsymbol{k},\boldsymbol{k}}\right)^* \tilde{p}_{\boldsymbol{k}}^{(0)} (\tilde{p}_{\boldsymbol{q}}^{(1)})^* + \Gamma^{\bar{a}aa}_{\boldsymbol{q}-\boldsymbol{k};\boldsymbol{k},\boldsymbol{q}} \left(\Gamma^{\bar{a}aa}_{\boldsymbol{q};\boldsymbol{q}-\boldsymbol{k},\boldsymbol{k}}\right)^* \tilde{p}_{\boldsymbol{q}-\boldsymbol{k}}^{(0)} (\tilde{p}_{\boldsymbol{q}}^{(1)})^* \right] \Bigg), \tag{3.82a}$$

$$I_{\boldsymbol{k}}^{n1} = I_{\boldsymbol{k}}^{n,\mathrm{th}} + \frac{2\pi}{N} \sum_{\substack{\boldsymbol{q} \\ \epsilon_{\boldsymbol{q}}=\omega_0/2 \\ \epsilon_{\boldsymbol{k}-\boldsymbol{q}}=\omega_0/2}} \Bigg(\frac{1}{2} \left|\Gamma^{\bar{a}aa}_{\boldsymbol{k};\boldsymbol{q},\boldsymbol{q}-\boldsymbol{k}}\right|^2 \left[n_{\boldsymbol{q}}^{(0)} n_{\boldsymbol{k}-\boldsymbol{q}}^{(0)} - n_{\boldsymbol{k}}^{(1)} \left(1 + n_{\boldsymbol{q}}^{(0)} + n_{\boldsymbol{k}-\boldsymbol{q}}^{(0)}\right) \right] - \mathrm{Re}\left[\Gamma^{\bar{a}aa}_{\boldsymbol{k};\boldsymbol{q},\boldsymbol{k}-\boldsymbol{q}} \left(\Gamma^{\bar{a}aa}_{\boldsymbol{q};\boldsymbol{k}-\boldsymbol{q},\boldsymbol{k}}\right)^* \tilde{p}_{\boldsymbol{k}}^{(1)} (\tilde{p}_{\boldsymbol{q}}^{(0)})^* + \Gamma^{\bar{a}aa}_{\boldsymbol{k}-\boldsymbol{q};\boldsymbol{k},\boldsymbol{q}} \left(\Gamma^{\bar{a}aa}_{\boldsymbol{k};\boldsymbol{q},\boldsymbol{q}-\boldsymbol{k}}\right)^* \tilde{p}_{\boldsymbol{k}}^{(1)} (\tilde{p}_{\boldsymbol{k}-\boldsymbol{q}}^{(0)})^* \right] \Bigg), \tag{3.82b}$$

$$I_{\boldsymbol{k}}^{p0} = I_{\boldsymbol{k}}^{p,\mathrm{th}} + \frac{\pi}{N} \sum_{\substack{\boldsymbol{q} \\ \epsilon_{\boldsymbol{q}}=\omega_0 \\ \epsilon_{\boldsymbol{q}-\boldsymbol{k}}=\omega_0/2}} \Bigg[- \left|\Gamma^{\bar{a}aa}_{\boldsymbol{q};\boldsymbol{q}-\boldsymbol{k},\boldsymbol{k}}\right|^2 \tilde{p}_{\boldsymbol{k}}^{(0)} \left(n_{\boldsymbol{q}-\boldsymbol{k}}^{(1)} - n_{\boldsymbol{q}}^{(0)} \right) + \Gamma^{\bar{a}aa}_{\boldsymbol{q};\boldsymbol{q}-\boldsymbol{k},\boldsymbol{k}} \left(\Gamma^{\bar{a}aa}_{-\boldsymbol{k};\boldsymbol{q}-\boldsymbol{k},-\boldsymbol{q}}\right)^* \tilde{p}_{\boldsymbol{q}}^{(0)} \left(n_{\boldsymbol{k}}^{(0)} - n_{\boldsymbol{q}-\boldsymbol{k}}^{(1)} \right) \Bigg], \tag{3.82c}$$

$$I_{\boldsymbol{k}}^{p1} = I_{\boldsymbol{k}}^{p,\mathrm{th}} + \frac{\pi}{N} \sum_{\substack{\boldsymbol{q} \\ \epsilon_{\boldsymbol{q}}=\omega_0/2 \\ \epsilon_{\boldsymbol{k}-\boldsymbol{q}}=\omega_0/2}} \Bigg[- \left|\Gamma^{\bar{a}aa}_{\boldsymbol{k};\boldsymbol{k}-\boldsymbol{q},\boldsymbol{q}}\right|^2 \tilde{p}_{\boldsymbol{k}}^{(1)} \left(1 + n_{\boldsymbol{q}}^{(0)} + n_{\boldsymbol{k}-\boldsymbol{q}}^{(0)}\right) + \Gamma^{\bar{a}aa}_{\boldsymbol{q};\boldsymbol{k}-\boldsymbol{q},-\boldsymbol{k}} \left(\Gamma^{\bar{a}aa}_{\boldsymbol{k};\boldsymbol{k}-\boldsymbol{q},\boldsymbol{q}}\right)^* \tilde{p}_{\boldsymbol{q}}^{(0)} \left(1 + n_{\boldsymbol{k}}^{(1)} + n_{\boldsymbol{k}-\boldsymbol{q}}^{(0)}\right) + \Gamma^{\bar{a}aa}_{\boldsymbol{q}-\boldsymbol{k};\boldsymbol{q},-\boldsymbol{k}} \left(\Gamma^{\bar{a}aa}_{\boldsymbol{k};\boldsymbol{k}-\boldsymbol{q},\boldsymbol{q}}\right)^* \tilde{p}_{\boldsymbol{k}-\boldsymbol{q}}^{(0)} \left(1 + n_{\boldsymbol{k}}^{(1)} + n_{\boldsymbol{q}}^{(0)}\right) \Bigg], \tag{3.82d}$$

where $I_{\boldsymbol{k}}^{n,\mathrm{th}}$ and $I_{\boldsymbol{k}}^{p,\mathrm{th}}$ are the collision integrals for the thermal magnon distribution and need to be calculated numerically. In the summation over the momenta $\boldsymbol{q}$ in the above equations (3.82) the condition $\epsilon_{\boldsymbol{k}} = \omega_0/2$, $\epsilon_{\boldsymbol{q}} = \omega_0$, $\epsilon_{\boldsymbol{q}-\boldsymbol{k}} = \omega_0/2$ has to be fulfilled for the parametric collision integrals (equations (3.82a) and (3.82c)) and $\epsilon_{\boldsymbol{k}} = \omega_0$, $\epsilon_{\boldsymbol{q}} = \omega_0/2$, $\epsilon_{\boldsymbol{k}-\boldsymbol{q}} = \omega_0/2$ has to be fulfilled for the secondary collision integrals (equations (3.82b) and (3.82d)). Each of these conditions is fulfilled on a curve in momentum space which

is approximately an ellipsis. For the parametric collision integrals $\boldsymbol{k}$ and $\boldsymbol{q}-\boldsymbol{k}$ lie on the same ellipsis and there is the additional condition that $\boldsymbol{q}$ must coincide with a point on a different ellipsis. Apparently, there is either only one wave vector $\boldsymbol{q}$ which can simultaneously fulfill all conditions or none in which case the collision integral vanishes for the given wave vector $\boldsymbol{k}$. Thus, in order to calculate the collision integrals numerically, it is necessary to find out which combinations of wave vectors fulfill the above conditions. I carry out the numerical calculations on a grid in momentum space and interpolate linearly between the values of the magnon distribution functions defined on the grid. Furthermore, I assume that all other magnons not included in one of the two magnon groups are in the thermal equilibrium state so that the contribution to the damping of magnons in thermal equilibrium $I_{\boldsymbol{k}}^{n,\mathrm{th}}$ and $I_{\boldsymbol{k}}^{p,\mathrm{th}}$ should be included by evaluating the collision integrals (3.63) and (3.64) for the thermal distribution.

Next, the magnon distribution functions in the stationary non-equilibrium state should be calculated in a self-consistent way. The initial values of the magnon distribution functions are set to the result within S-theory (3.50) where the initial damping rates are chosen as $\gamma_{\boldsymbol{k}}^n = \gamma_{\boldsymbol{k}}^p = 2\gamma_0 = 1.05 \times 10^{-4}$ K. Inserting the results into the expressions for the collision integrals (3.82) yields different values for the damping rates $\gamma_{\boldsymbol{k}}^n$ and $\gamma_{\boldsymbol{k}}^p$ which can be used to improve the guess of the stationary non-equilibrium state. I repeat this process iteratively to find the stationary non-equilibrium state self-consistently. The deviation of the magnon distribution functions from the true stationary non-equilibrium state can be estimated by evaluating the expressions for $\partial_t n_{\boldsymbol{k}}^c$ and $\partial_t \tilde{p}_{\boldsymbol{k}}^c$ according to the equations of motion (3.57) and taking the sum over their squared absolute values,

$$\frac{1}{N}\sum_{\boldsymbol{k}}\left(|\partial_t n_{\boldsymbol{k}}^c|^2 + |\partial_t \tilde{p}_{\boldsymbol{k}}^c|^2\right). \tag{3.83}$$

I use this expression to control the convergence of the algorithm. If it tends to zero the magnon distribution functions should converge to reasonable values.

The numerical calculations are carried out on a grid in momentum space so that the total magnon distribution function n is

$$n = \frac{1}{N_\Theta}\sum_{i=1}^{N_\Theta} n_i, \tag{3.84}$$

where the in-plane wave vector is parameterized by $N_\Theta = 40$ different angles Θ_i uniformly chosen in the interval $[0, \pi/2]$. The length of the wave vector for a given angle Θ_i is calculated for the parametric and the secondary magnon groups by solving numerically the equations $\epsilon_{\boldsymbol{k}_0} = \omega_0/2$ and $\epsilon_{\boldsymbol{k}_1} = \omega_0$ respectively where the magnon dispersions are given by Eq. (3.24). The grid in momentum space is shown in Fig. 3.13. Note that due to the symmetry of the problem it is only necessary to calculate the magnon distribution functions in one quadrant of momentum space.

Fig. 3.14 shows the numerically calculated magnon density for different pumping strengths in dependence of the external field H_0 for a YIG film of thickness $d = 22.8$ µm and the frequency of the microwave field $\omega_0 = 13.857$ GHz. The pumping strength is

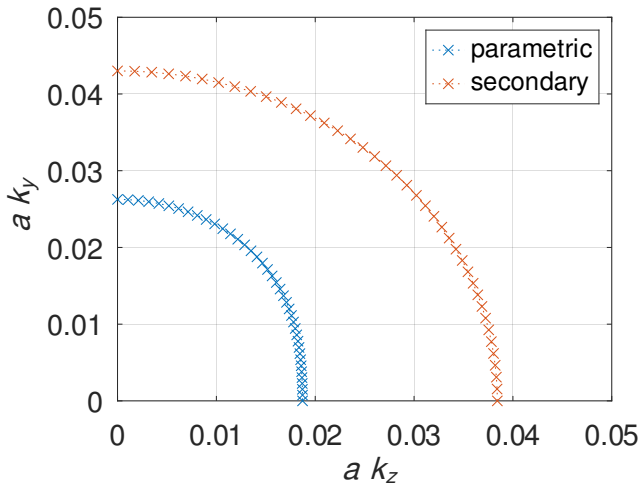

Figure 3.13: The grid in momentum space used for the numerical calculations in this chapter.

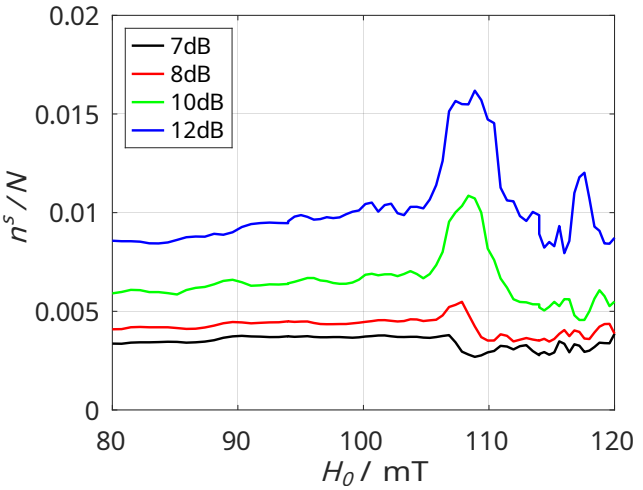

Figure 3.14: The total magnon density in the stationary non-equilibrium state in dependence of the external magnetic field H_0 for a YIG film of thickness $d = 22.8$ µm and pumping field frequency $\omega_0 = 13.857$ GHz for four different pumping strengths.

varied between 7dB and 12dB above the damping rate γ_0. The pumping strength is averaged over all momenta $\boldsymbol{k}_0$ of parametric magnons, i.e. the specification of the pumping strength is related to the expression

$$\frac{\langle V_{\boldsymbol{k}} \rangle_{\boldsymbol{k}_0} - \gamma_0}{\gamma_0}, \tag{3.85}$$

where $\langle \dots \rangle_{\boldsymbol{k}_0}$ denotes the average over all momenta that satisfy the resonance condition (3.51). It can be observed in Fig. 3.14 that the magnon density increases linearly until $H_0 \approx 100$ mT. Around $H_0 \approx 105$ mT peak structures appear which cannot be obtained within S-theory. For small pumping strengths dips can be seen while for large pumping strengths a peak appears instead. To understand this result we should take a look at the expression for the magnon distribution functions in the stationary state approximated by Eq. (3.73). The total damping rate appearing in Eq. (3.73c) is

$$\gamma_{\boldsymbol{k}} = \frac{1}{2}\sqrt{\gamma_{\boldsymbol{k}}^n \mathrm{Re}\left[\gamma_{\boldsymbol{k}}^p\right]}. \tag{3.86}$$

Increased damping strength leads to a lower saturation of the magnon density. With larger pumping strengths, however, this effect is suppressed. According to Eq. (3.73a) the magnon distribution function has an additional prefactor of $\sqrt{\mathrm{Re}\left[\gamma_{\boldsymbol{k}}^p\right]/\gamma_{\boldsymbol{k}}^n}$ compared to S-theory which can lead to an enhancement of the stationary magnon density. Fig. 3.15 shows the field dependence of the damping rate γ of parametric magnons as well as the prefactor $\sqrt{\mathrm{Re}\left[\gamma^p\right]/\gamma^n}$. Here, the missing $\boldsymbol{k}$ index indicates that the quantities have been averaged over all momenta on the resonance surface. The prefactor $\sqrt{\mathrm{Re}\left[\gamma^p\right]/\gamma^n}$ has indeed a peak near the confluence magnetic field strength. For low pumping strengths the enhanced damping leads to a reduced saturation of the magnon density. For large enough pumping strengths, however, the effect that enhances the saturation of the magnon density dominates. Physically, this effect is related to the enhanced coupling of the parametric and the secondary magnons near the confluence magnetic field strength. These interactions represent an additional relaxation channel which reduces the number of magnons for low pumping strengths. Given that the pumping strength is large enough to compensate the enhanced damping, however, the total number of magnons is increased instead [54].

As already mentioned, within S-theory the microscopic collision integrals are not included and instead a phenomenological damping rate describing magnon relaxation is introduced. However, without taking into account the dependence of the damping rate on the external field strength the above discussed mechanism cannot be reproduced. As a consequence, S-theory predicts an approximately linear dependence of the magnon density on the external field strength in the experimentally relevant parameter regime. From the fact that I only explicitly take into account parametric and secondary magnons and the experiment is well described by the theory it follows that the observed enhancement of the magnon density is caused by confluence and splitting processes of magnons. They are accounted for by the collision integrals (3.82) and they couple parametric magnons with certain wave vectors which depend on the external field strength. The confluence

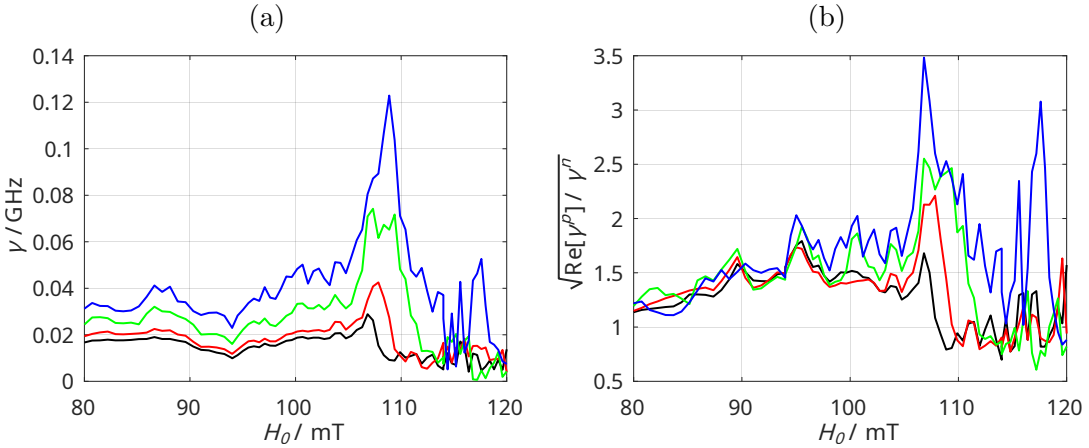

Figure 3.15: The damping rate $\gamma = \frac{1}{2}\sqrt{\mathrm{Re}\left[\gamma^p\right]\gamma^n}$ (a) and the square root of the ratio of the two damping rates $\sqrt{\mathrm{Re}\left[\gamma^p\right]/\gamma^n}$ (b) in dependence of the external field strength H_0. The parameters are the same as in Fig. 3.14.

magnetic field strength is defined as the external field strength H_0 where this coupling involves two parametric magnons with the same momenta. Near this field strength peak structures appear in the collision integrals in agreement with the experiment [46].

4 Accumulation of magnetoelastic modes in YIG

The material presented in this chapter is based on Ref. [55].

4.1 Introduction

While the theoretical investigation of magnon-phonon interactions has started 1952 with the work [20] by Abrahams and Kittel the interest has waned over the years. Often in the literature the effects of magnon-phonon interactions were not taken into account explicitly and phonons have merely been considered as a heat bath. Recently, the topic of magnon-phonon interactions has gained renewed interest because new methods to study phenomena that are dominated by magnon-phonon interactions and hybridization of magnons and phonons became available by now [21, 22, 23, 24, 25, 26, 27].

The formation of a magnon BEC in YIG has been observed earlier experimentally and theoretically [15, 17, 70]. The condensate forms in the minimum of the magnon dispersion which lies at a wave vector larger than zero. In a recent series of experiments [28, 47] the spontaneous accumulation of magnetoelastic bosons has been observed in an overpopulated magnon gas in YIG alongside the magnon BEC. It can be observed that the accumulated magnetoelastic bosons are nearly degenerate with the magnon BEC raising the question of the importance of the interaction between the magnetoelastic bosons and the magnons at the minimum of the magnon dispersion. Although the accumulation occurs in a narrow region in momentum space this is no prove that the accumulated magnetoelastic bosons are coherent. In fact, the numerical solution of the kinetic theory which is developed in this chapter shows that the accumulation is purely incoherent.

The aim of this chapter is to extend the theory developed in the previous chapter 3 to include the effects of magnon-phonon hybridization in order to be able to describe the accumulation process of magnetoelastic bosons. While the bottleneck accumulation effect already has been explained phenomenologically in Ref. [47] the results presented in this chapter are derived from the microscopical dynamics of the system. Furthermore, the method allows to investigate further questions regarding the accumulation process, e.g. the importance of the interaction between the accumulated magnetoelastic bosons and the magnon BEC or the coherence of the magnetoeslatic bosons.

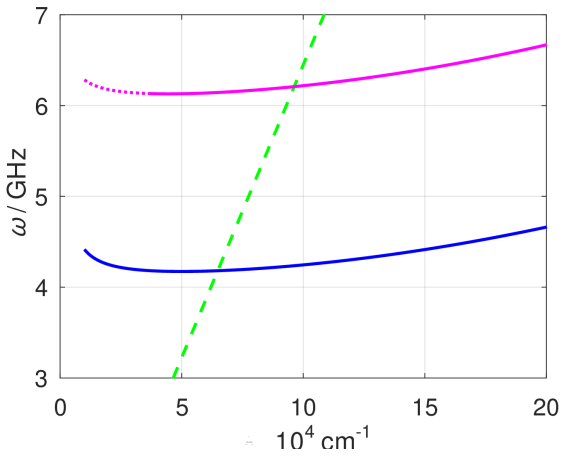

Figure 4.1: The dispersion $\epsilon_{\boldsymbol{k}}$ of magnons in YIG approximated by Eq. (3.24) is shown as a function of the wave vector $k = |\boldsymbol{k}|$ for momenta parallel (blue) and perpendicular (magenta) to the external magnetic field. The phonon dispersion of the transverse mode $\omega_{\boldsymbol{k}\perp} = c_\perp |\boldsymbol{k}|$ is also shown (dashes green). The parameters were chosen as $d = 6.7$ µm and $H = 145$ mT.

4.2 Effective magnon-phonon Hamiltonian

4.2.1 Magnon Hamiltonian

Until now, I have considered only the magnon part of the system. Comparing the dispersion relations for magnons and transversal phonons in YIG (see Fig. 4.1) the energies apparently have the same order of magnitude close to the minimum of the magnon dispersion so that hybridization of phonons and magnons is expected in this region. Therefore, magnon-phonon interactions should be included to the effective magnon Hamiltonian when investigating Bose-Einstein condensation of magnons in this parameter regime.

Because I investigate the system after the pumping field has been switched off the external driving does not have to be included in the description of the magnon subsystem. The quadratic part of the effective magnon Hamiltonian is now given by only the diagonal terms,

$$\mathcal{H}_m^{(2)} = \sum_{\boldsymbol{k}} \epsilon_{\boldsymbol{k}} b_{\boldsymbol{k}}^\dagger b_{\boldsymbol{k}}, \tag{4.1}$$

where in this chapter the symbols $b_{\boldsymbol{k}}^\dagger$ and $b_{\boldsymbol{k}}$ are used for the magnon creation and annihilation operators in place of $a_{\boldsymbol{k}}^\dagger$ and $a_{\boldsymbol{k}}$ in Eq. (3.28). Note that the transformation to the rotating reference frame carried out in chapter 3 to obtain Eq. (3.31) is not necessary here because no off-diagonal terms appear without the external driving. I only take into account the first term of the magnon-magnon interaction Hamiltonian (3.14) which contains two creation and two annihilation operators. The other terms can be

neglected. This is justified by the following arguments. In the long-wavelength regime that I am interested in, the magnon dispersion (3.24) is rather flat for YIG (see Fig. 4.1). Scattering processes which do not conserve the number of magnons need to involve high-energy magnons in order to fulfill the energy conservation law. In the thermal equilibrium state these modes are, however, very weakly occupied. Therefore, magnon-magnon scattering processes that conserve the number of magnons dominate, because they involve only low-energy magnons. As a result, for low-energy magnons there exists an approximate $U(1)$ symmetry due to the energy conservation law. Therefore, the relevant magnon-magnon interaction Hamiltonian is given by [55]

$$\mathcal{H}_m^{(4)} = \frac{1}{N} \sum_{\boldsymbol{k}_1,\ldots,\boldsymbol{k}_4} \delta_{\boldsymbol{k}_1+\cdots+\boldsymbol{k}_4,\boldsymbol{0}} \frac{1}{(2!)^2} \Gamma^{\bar{a}\bar{a}aa}_{1,2;3,4} b^\dagger_{-1} b^\dagger_{-2} b_3 b_4. \tag{4.2}$$

4.2.2 Phonon Hamiltonian

In order to include phonons into the effective Hamiltonian I start by introducing the quadratic phonon Hamiltonian

$$\mathcal{H}_p^{(2)} = \sum_{\boldsymbol{k},\lambda} \omega_{\boldsymbol{k},\lambda} \left(a^\dagger_{\boldsymbol{k},\lambda} a_{\boldsymbol{k},\lambda} + \frac{1}{2} \right), \tag{4.3}$$

which describes the phonon subsystem at long wave lengths. Here, λ denotes the three acoustic phonon branches. The longitudinal acoustic phonon branch is denoted by $\lambda = \parallel$ and the two transversal acoustic phonon branches are denoted by $\lambda = \perp 1, \perp 2$. $a^\dagger_{\boldsymbol{k},\lambda}$ is a creation operator for phonons of momentum $\boldsymbol{k}$ and polarization λ while $a_{\boldsymbol{k},\lambda}$ denote the phonon annihilation operators. There are three relevant acoustic phonon branches in YIG. Their energies are given by $\omega_{\boldsymbol{k},\lambda} = c_\lambda |\boldsymbol{k}|$, where c_λ is the phonon velocity. The phonon velocities are known from the literature [82], $c_\parallel = 7.209 \times 10^5$ cm/s for the longitudinal mode and $c_{\perp 1} = c_{\perp 2} = 3.843 \times 10^5$ cm/s for the two degenerate transverse modes. The transversal phonon dispersion $\omega_{\boldsymbol{k},\perp}$ is shown as dashed line in Fig. 4.1.

4.2.3 Phenomenological magnon-phonon Hamiltonian

There are two sources of magnon-phonon coupling: the dependence of the exchange coupling on the phonon displacements and relativistic effects related to the charge degrees of freedom. The prior effect can be taken into account by introducing phonon displacements $\boldsymbol{X}_i = X(\boldsymbol{R}_i)$ and taking into account that the positions $\boldsymbol{r}_i$ of the spins depend on the phonon displacements, $\boldsymbol{r}_i = \boldsymbol{R}_i + \boldsymbol{X}_i$. Therefore, the exchange couplings $J_{ij} = J(\boldsymbol{R}_i - \boldsymbol{R}_j + \boldsymbol{X}_i - \boldsymbol{X}_j)$ depend on the phonon displacements. This effect can be taken into account by expanding the above expression of the exchange couplings in powers of phonon displacements [21]. However, in collinear magnets the contribution of relativistic effects to the magnon-phonon coupling is usually dominant at low energies [82, 83]. Because these relativistic effects involve charge degrees of freedom they cannot be easily taken into account with an effective spin Hamiltonian. For this reason, I employ the strategy of quantizing a phenomenological expression for the classical

magnetoelastic energy. The method is based on a strategy pioneered by Abrahams and Kittel [20] and has been used in Ref. [21] to study magnetoelastic modes in YIG. The procedure is discussed in Ref. [21] in detail. The relevant contribution to the magnetoelastic energy at long wavelengths is

$$E_{\rm me} = \frac{n}{M_s^2} \int d^3r \sum_{\alpha,\beta} B_{\alpha\beta} M_\alpha \left(\boldsymbol{r}\right) M_\beta \left(\boldsymbol{r}\right) X_{\alpha\beta} \left(\boldsymbol{r}\right), \tag{4.4}$$

where $n = 1/a^3$ is the number density of magnetic ions, $\boldsymbol{M}\left(\boldsymbol{r}\right)$ is the magnetization, and $X_{\alpha\beta}\left(\boldsymbol{r}\right)$ is the symmetric strain tensor which can be written as

$$X_{\alpha\beta}\left(\boldsymbol{r}\right) = \frac{1}{2}\left(\frac{\partial X_\alpha\left(\boldsymbol{r}\right)}{\partial r_\beta} + \frac{\partial X_\beta\left(\boldsymbol{r}\right)}{\partial r_\alpha}\right), \tag{4.5}$$

where $X_\alpha\left(\boldsymbol{r}\right) = \boldsymbol{e}_\alpha \cdot \boldsymbol{X}\left(\boldsymbol{r}\right)$ and $\boldsymbol{X}\left(\boldsymbol{r}\right)$ is the phonon displacement field. $B_{\alpha\beta}$ are phenomenological magnetoelastic coupling constants which for a cubic lattice can be written as $B_{\alpha\beta} = \delta_{\alpha\beta} B_\parallel + \left(1 - \delta_{\alpha\beta}\right) B_\perp$. For YIG the two components of the coupling constant are $B_\parallel = 47.8$ K and $B_\perp = 95.6$ K [82, 84, 85]. At long wavelengths the largest contribution to these coupling constants originates from the spin-orbit coupling [82]. The Fourier transform of the above quantities can be introduced as

$$M_\alpha\left(\boldsymbol{k}\right) = \int d^3r e^{i\boldsymbol{k}\cdot\boldsymbol{r}} M_\alpha\left(\boldsymbol{r}\right), \tag{4.6}$$

$$X_\alpha\left(\boldsymbol{k}\right) = \int d^3r e^{i\boldsymbol{k}\cdot\boldsymbol{r}} X_\alpha\left(\boldsymbol{r}\right), \tag{4.7}$$

$$X_{\alpha\beta}\left(\boldsymbol{k}\right) = \int d^3r e^{i\boldsymbol{k}\cdot\boldsymbol{r}} X_{\alpha\beta}\left(\boldsymbol{r}\right) = \frac{i}{2}\left[X_\alpha\left(\boldsymbol{k}\right) k_\beta + X_\beta\left(\boldsymbol{k}\right) k_\alpha\right], \tag{4.8}$$

so that the magnetoelastic energy in momentum reads [21]

$$E_{\rm me} = \frac{n}{M_s^2} \int d^3k \int d^3k' \int d^3q\, \delta_{\boldsymbol{k}+\boldsymbol{k}'+\boldsymbol{q},\boldsymbol{0}} \sum_{\alpha\beta} B_{\alpha\beta} M_\alpha\left(\boldsymbol{k}\right) M_\beta\left(\boldsymbol{k}'\right) X_{\alpha\beta}\left(\boldsymbol{q}\right). \tag{4.9}$$

In order to quantize the above expression for the magnetoelastic energy the phonon displacement field $\boldsymbol{X}\left(\boldsymbol{k}\right)$ is replaced by $V/\sqrt{N}\boldsymbol{X}_{\boldsymbol{k}}$ and expanded in the phonon operators $a^\dagger_{\boldsymbol{k},\lambda}$ and $a_{\boldsymbol{k},\lambda}$, [21]

$$\boldsymbol{X}_{\boldsymbol{k}} = \sum_\lambda X_{\boldsymbol{k},\lambda} \boldsymbol{e}_{\boldsymbol{k},\lambda}, \tag{4.10}$$

$$X_{\boldsymbol{k},\lambda} = \frac{a_{\boldsymbol{k},\lambda} + a^\dagger_{-\boldsymbol{k},\lambda}}{\sqrt{2m\omega_{\lambda,\boldsymbol{k}}}}, \tag{4.11}$$

where $m = \rho a^3$ is the effective ionic mass of a unit cell and V is the volume of the system. $\boldsymbol{e}_{\boldsymbol{k},\lambda} = \boldsymbol{e}^*_{-\boldsymbol{k},\lambda}$ denotes the phonon polarization vectors which are orthogonal and

complete. They may be chosen as [21]

$$\boldsymbol{e}_{\boldsymbol{k},\parallel} = i\left[\cos\left(\theta_{\boldsymbol{k}}\right)\boldsymbol{e}_z + \sin\left(\theta_{\boldsymbol{k}}\right)\boldsymbol{e}_y\right], \tag{4.12a}$$

$$\boldsymbol{e}_{\boldsymbol{k},\perp 1} = i\left[\sin\left(\theta_{\boldsymbol{k}}\right)\boldsymbol{e}_z + \cos\left(\theta_{\boldsymbol{k}}\right)\boldsymbol{e}_y\right], \tag{4.12b}$$

$$\boldsymbol{e}_{\boldsymbol{k},\perp 2} = \boldsymbol{e}_x, \tag{4.12c}$$

which is convenient for the parametrization (3.17) of the wave vector $\boldsymbol{k}$. The magnetization in momentum space $\boldsymbol{M}(\boldsymbol{k})$ can be replaced by $g\mu_B\sqrt{N}\boldsymbol{S}_{\boldsymbol{k}} = g\mu_B\sum_i e^{-i\boldsymbol{k}\cdot\boldsymbol{r}_i}S_i$ [20, 86]. Furthermore, the spin operators can be expanded in bosonic operators via a Holstein-Primakoff transformation (3.3) as it has been done in chapter 3. Here, I take into account only the lowest order terms,

$$S^x_{\boldsymbol{k}} \approx \frac{\sqrt{2S}}{2}\left(b_{\boldsymbol{k}} + b^\dagger_{-\boldsymbol{k}}\right), \tag{4.13a}$$

$$S^y_{\boldsymbol{k}} \approx \frac{\sqrt{2S}}{2i}\left(b_{\boldsymbol{k}} - b^\dagger_{-\boldsymbol{k}}\right), \tag{4.13b}$$

$$S^z_{\boldsymbol{k}} \approx \sqrt{N}S\delta_{\boldsymbol{k},\boldsymbol{0}}. \tag{4.13c}$$

The magnon-phonon interaction Hamiltonian in lowest order in $1/S$ obtained via this method reads [21]

$$\mathcal{H}_{mp} = \frac{1}{2}\sum_{\boldsymbol{k},\lambda}\gamma_{\boldsymbol{k},\lambda}\left(a_{-\boldsymbol{k},\lambda} + a^\dagger_{\boldsymbol{k},\lambda}\right)b_{\boldsymbol{k}} + \text{h.c.}\,, \tag{4.14}$$

where h.c. refers to the hermitian conjugate and the hybridization vertices are given by

$$\gamma_{\boldsymbol{k}\parallel} = i\frac{B_\perp}{2\sqrt{S\rho n\omega_{\boldsymbol{k}}}}\frac{2k_yk_z}{|\boldsymbol{k}|} = i\frac{B_\perp}{2\sqrt{S\rho n\omega_{\boldsymbol{k}}}}|\boldsymbol{k}|\sin\left(2\theta_{\boldsymbol{k}}\right), \tag{4.15a}$$

$$\gamma_{\boldsymbol{k}\perp 1} = i\frac{B_\perp}{2\sqrt{S\rho n\omega_{\boldsymbol{k}}}}\frac{k_y^2 - k_z^2}{|\boldsymbol{k}|} = i\frac{B_\perp}{2\sqrt{S\rho n\omega_{\boldsymbol{k}}}}|\boldsymbol{k}|\cos\left(2\theta_{\boldsymbol{k}}\right), \tag{4.15b}$$

$$\gamma_{\boldsymbol{k}\perp 2} = -i\frac{B_\perp}{2\sqrt{S\rho n\omega_{\boldsymbol{k}}}}k_z = -i\frac{B_\perp}{2\sqrt{S\rho n\omega_{\boldsymbol{k}}}}|\boldsymbol{k}|\cos\left(\theta_{\boldsymbol{k}}\right), \tag{4.15c}$$

4.2.4 Hamiltonian for magnetoelastic bosons

I neglect the longitudinal phonon modes in the following because only the two transverse phonon modes hybridize with magnons in the experimentally relevant area [28] (see Fig. 4.1). Furthermore, I also neglect non-resonant terms in the magnon-phonon interaction Hamiltonian (4.14), i.e. terms that contain two annihilation or two creation operators, $a_{-\boldsymbol{k},\lambda}b_{\boldsymbol{k}}$ and $a^\dagger_{-\boldsymbol{k},\lambda}b^\dagger_{\boldsymbol{k}}$. This approximation is discussed in Refs. [47, 83] and is sufficient close to the hybridization region. The quadratic part of the Hamiltonian reads

$$\mathcal{H}^{(2)} = \mathcal{H}^{(2)}_m + \mathcal{H}^{(2)}_p + \mathcal{H}^{(2)}_{mp}, \tag{4.16}$$

and there are three relevant bosonic modes: magnons and the two degenerate transversal phonon modes. The quadratic Hamiltonian (4.16) can be diagonalized by the unitary transformation [55]

$$\begin{pmatrix} b_{\boldsymbol{k}} \\ a_{\boldsymbol{k}\perp 1} \\ a_{\boldsymbol{k}\perp 2} \end{pmatrix} = (\boldsymbol{\phi}_{\boldsymbol{k}+}, \boldsymbol{\phi}_{\boldsymbol{k}-}, \boldsymbol{\phi}_{\boldsymbol{k}p}) \begin{pmatrix} \psi_{\boldsymbol{k}+} \\ \psi_{\boldsymbol{k}-} \\ \psi_{\boldsymbol{k}p} \end{pmatrix}, \tag{4.17}$$

where $\psi_{\boldsymbol{k}+}$ and $\psi_{\boldsymbol{k}-}$ are canonical annihilation operators of magnetoelastic bosons with wave vector $\boldsymbol{k}$ and $\psi_{\boldsymbol{k}p}$ is a phonon annihilation operator. $\boldsymbol{\phi}_{\boldsymbol{k}+}$, $\boldsymbol{\phi}_{\boldsymbol{k}-}$, and $\boldsymbol{\phi}_{\boldsymbol{k}p}$ are given by

$$\boldsymbol{\phi}_{\boldsymbol{k}\pm} = \frac{\left(2\left[E_{\boldsymbol{k}\pm} - \omega_{\boldsymbol{k}\perp}\right], \gamma_{\boldsymbol{k}\perp 1}, \gamma_{\boldsymbol{k}\perp 2}\right)^T}{\sqrt{4\left(E_{\boldsymbol{k}\pm} - \omega_{\boldsymbol{k}\perp}\right)^2 + \left|\gamma_{\boldsymbol{k}\perp 1}\right|^2 + \left|\gamma_{\boldsymbol{k}\perp 2}\right|^2}}, \tag{4.18}$$

$$\boldsymbol{\phi}_{\boldsymbol{k}p} = \frac{\left(0, -\gamma^*_{\boldsymbol{k}\perp 2}, \gamma^*_{\boldsymbol{k}\perp 1}\right)^T}{\sqrt{\left|\gamma_{\boldsymbol{k}\perp 1}\right|^2 + \left|\gamma_{\boldsymbol{k}\perp 2}\right|^2}}, \tag{4.19}$$

where the dispersion $E_{\boldsymbol{k}\pm}$ of the two magnetoelastic modes is

$$E_{\boldsymbol{k}\pm} = \frac{1}{2}\left[\epsilon_{\boldsymbol{k}} + \omega_{\boldsymbol{k}\perp} \pm \sqrt{\left(\epsilon_{\boldsymbol{k}} - \omega_{\boldsymbol{k}\perp}\right)^2 + \left|\gamma_{\boldsymbol{k}\perp 1}\right|^2 + \left|\gamma_{\boldsymbol{k}\perp 2}\right|^2}\right]. \tag{4.20}$$

After applying the transformation the quadratic part of the Hamiltonian has the form

$$\mathcal{H}^{(2)} = \sum_{\boldsymbol{k}} \left[E_{\boldsymbol{k}+}\psi^\dagger_{\boldsymbol{k}+}\psi_{\boldsymbol{k}+} + E_{\boldsymbol{k}-}\psi^\dagger_{\boldsymbol{k}-}\psi_{\boldsymbol{k}-} + \omega_{\boldsymbol{k}\perp}\psi^\dagger_{\boldsymbol{k}p}\psi_{\boldsymbol{k}p}\right]. \tag{4.21}$$

I neglect the purely bosonic phonon mode because it is not relevant for the interaction between the two magnetoelastic modes. Fig. 4.2 shows the dispersions of the two magnetoelastic modes for a YIG film of thickness $d = 6.7$ µm.

Now, the magnon-magnon interaction Hamiltonian (4.2) needs to be expressed in terms of the magnetoelastic creation operators $\psi^\dagger_{\boldsymbol{k}\pm}$ and annihilation operators $\psi_{\boldsymbol{k}\pm}$. The quartic Hamiltonian has the form

$$\begin{aligned}
\mathcal{H}^{(4)}_m = \frac{1}{N}\sum_{\boldsymbol{k}_1,\ldots,\boldsymbol{k}_4} \delta_{\boldsymbol{k}_1+\cdots+\boldsymbol{k}_4,0}\frac{1}{(2!)^2} \\
\times\Big[\Gamma^{++++}_{1,2;3,4}\psi^\dagger_{-1+}\psi^\dagger_{-2+}\psi_{3+}\psi_{4+} + \Gamma^{----}_{1,2;3,4}\psi^\dagger_{-1-}\psi^\dagger_{-2-}\psi_{3-}\psi_{4-} \\
+\Gamma^{++--}_{1,2;3,4}\psi^\dagger_{-1+}\psi^\dagger_{-2+}\psi_{3-}\psi_{4-} + \Gamma^{--++}_{1,2;3,4}\psi^\dagger_{-1-}\psi^\dagger_{-2-}\psi_{3+}\psi_{4+} \\
+\Gamma^{+-+-}_{1,2;3,4}\psi^\dagger_{-1+}\psi^\dagger_{-2-}\psi_{3+}\psi_{4-} + \Gamma^{-+-+}_{1,2;3,4}\psi^\dagger_{-1-}\psi^\dagger_{-2+}\psi_{3-}\psi_{4+} \\
+\Gamma^{+++-}_{1,2;3,4}\psi^\dagger_{-1+}\psi^\dagger_{-2+}\psi_{3+}\psi_{4-} + \Gamma^{---+}_{1,2;3,4}\psi^\dagger_{-1-}\psi^\dagger_{-2-}\psi_{3-}\psi_{4+} \\
+\Gamma^{+-++}_{1,2;3,4}\psi^\dagger_{-1+}\psi^\dagger_{-2-}\psi_{3+}\psi_{4+} + \Gamma^{-+--}_{1,2;3,4}\psi^\dagger_{-1-}\psi^\dagger_{-2+}\psi_{3-}\psi_{4-}\Big].
\end{aligned} \tag{4.22}$$

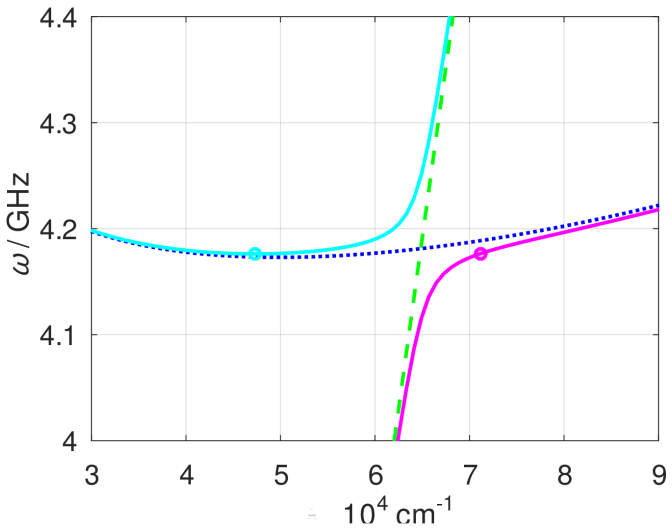

Figure 4.2: The dispersions of the the magnetoelastic modes are shown for the upper (+) branch (cyan) and the lower (−) branch (magenta) as a function of the wave vector. The cyan circle shows the minimum of the + branch dispersion and the magenta circle marks the point where the dispersion of the − branch is degenerate with the minimum of the + dispersion. The dispersions of magnons (dotted blue) and transverse phonons (dashed green) without hybridization are also shown. The parameters are the same as in Fig. 4.1.

The first line in Eq. (4.23) describes intramodal scattering events where the number of each type of magnetoelastic boson is conserved. The second line describes intermodal scattering events where the total number of magnetoelastic bosons is conserved but the number of magnetoelastic bosons in the upper (+) and lower (−) branch changes by two. The former processes are relevant for the thermalization within one magnetoelastic branch while the latter processes exchange energy and particles between the two magnetoelastic branches. In particular, they directly couple the region of the + mode close to the bottom of the magnon dispersion with the area of the − mode that lies energetically close to the hybridization area. Therefore, it is assumed that the intermodal processes are relevant for the appearance of the magnetoelastic accumulation [55].

The terms in the third line describe scattering processes that do not change the number of magnetoelastic bosons in both branches and the terms in the fourth and fifth line describe scattering processes where the number of magnetoelastic bosons change by one in each branch. The prior type of scattering events only redistribute magnetoelastic bosons within one of each branch. While it gives rise to additional thermalization channels it is not assumed that this type of scattering events qualitatively changes the stationary non-equilibrium state [47, 55]. The other type of scattering processes, on the other hand, lead to an exchange of magnetoelastic bosons between the two branches. In

principle, the magnetoelastic bosons of the upper (+) branch close to the bottom of the magnon dispersion and the bosons of the lower (−) branch close to the hybridization region can be coupled directly via the $+++- \Leftrightarrow ---+$ and $+-++ \Leftrightarrow -+--$ processes. However, as energy and momentum conservation have to be satisfied, it is necessary that high-energy magnons with large momenta far away from the hybridization region participate in the scattering events [55]. Therefore, following Ref. [47], these intermodal processes can be neglected as well. Thus, the Hamiltonian is approximated by [55]

$$\begin{aligned}\mathcal{H}_m^{(4)} \approx \frac{1}{N}\sum_{\boldsymbol{k}_1,\ldots,\boldsymbol{k}_4}\delta_{\boldsymbol{k}_1+\cdots+\boldsymbol{k}_4,0}\frac{1}{(2!)^2}\Big[&\Gamma^{++++}_{1,2;3,4}\psi^\dagger_{-1+}\psi^\dagger_{-2+}\psi_{3+}\psi_{4+}\\ &+\Gamma^{----}_{1,2;3,4}\psi^\dagger_{-1-}\psi^\dagger_{-2-}\psi_{3-}\psi_{4-}+\Gamma^{++--}_{1,2;3,4}\psi^\dagger_{-1+}\psi^\dagger_{-2+}\psi_{3-}\psi_{4-}\\ &+\Gamma^{--++}_{1,2;3,4}\psi^\dagger_{-1-}\psi^\dagger_{-2-}\psi_{3+}\psi_{4+}\Big],\end{aligned} \tag{4.23}$$

where the interaction vertices are given by

$$\Gamma^{\pm\pm\pm\pm}_{1,2;3,4} = \phi^*_{-1\pm}\phi^*_{-2\pm}\phi_{3\pm}\phi_{4\pm}\Gamma^{\bar{a}\bar{a}aa}_{1,2;3,4}, \tag{4.24}$$

$$\Gamma^{\pm\pm\mp\mp}_{1,2;3,4} = \phi^*_{-1\pm}\phi^*_{-2\pm}\phi_{3\mp}\phi_{4\mp}\Gamma^{\bar{a}\bar{a}aa}_{1,2;3,4}, \tag{4.25}$$

and $\phi_{\boldsymbol{k}\pm}$ is the magnonic component of $\boldsymbol{\phi}_{\boldsymbol{k}\pm}$,

$$\phi_{\boldsymbol{k}\pm} = \frac{2\left(E_{\boldsymbol{k}\pm}-\omega_{\boldsymbol{k}\perp}\right)}{\sqrt{4\left(E_{\boldsymbol{k}\pm}-\omega_{\boldsymbol{k}\perp}\right)^2+\left|\gamma_{\boldsymbol{k}\perp 1}\right|^2+\left|\gamma_{\boldsymbol{k}\perp 2}\right|^2}}. \tag{4.26}$$

4.3 Kinetic equations

The equations of motion of the magnetoelastic connected correlations,

$$n^c_{\boldsymbol{k}\pm} \equiv \langle\psi^\dagger_{\boldsymbol{k}\pm}\psi_{\boldsymbol{k}\pm}\rangle^c \equiv \langle\psi^\dagger_{\boldsymbol{k}\pm}\psi_{\boldsymbol{k}\pm}\rangle - \left|\Psi_{\boldsymbol{k}\pm}\right|^2, \tag{4.27}$$

can be derived the same way as in the previous chapter. Here, however, the condensate amplitude $\Psi_{\boldsymbol{k}\pm}$ has to be taken into account explicitly. The condensate amplitude $\Psi_{\boldsymbol{k}\pm}$ is defined as the vacuum expectation value of the magnetoelastic annihilation operators,

$$\Psi_{\boldsymbol{k}\pm} \equiv \langle\psi_{\boldsymbol{k}\pm}\rangle. \tag{4.28}$$

Here, the off-diagonal correlation functions vanish so that the equation of motion of the magnon correlation function is given by

$$\partial_t n^c_{\boldsymbol{k}\pm} = I_{\boldsymbol{k}\pm}, \tag{4.29}$$

where $I_{\boldsymbol{k}\pm}$ is the collision integral containing the contributions from the quartic interaction Hamiltonian (4.23). Furthermore, an equation of motion for the condensate

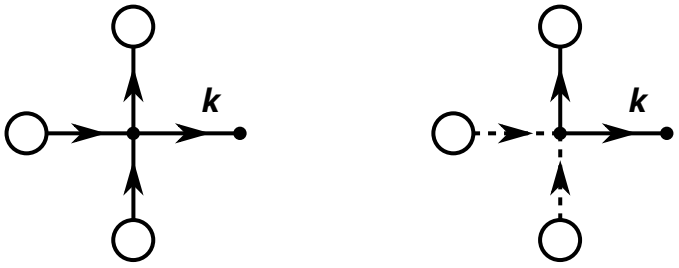

Figure 4.3: Diagrammatic representation of the contributions to the equations of motion of the condensate amplitude $\Psi_{\boldsymbol{k}+}$ corresponding to the Gross-Pitaevskii term. They contain the four-point interaction vertex and the product of three vacuum expectation values. Solid lines represent creation or annihilation operators for upper (+) branch magnetoelastic bosons while dashed lines represent the creation or annihilation operators of the lower (−) branch. Because there is a pair of equivalent lines a prefactor of 1/2 appears in the corresponding equation of motion. The diagrams for the equation of motion of the condensate amplitude $\Psi_{\boldsymbol{k}-}$ have the same form with $\Psi_{\boldsymbol{k}+} \leftrightarrow \Psi_{\boldsymbol{k}-}$.

amplitude $\Psi_{\boldsymbol{k}\pm}$ is necessary. Including the usual Gross-Pitaevskii term the equation of motion reads [55]

$$\partial_t \Psi_{\boldsymbol{k}\pm} + i\left(E_{\boldsymbol{k}\pm} - \mu_c\right)\Psi_{\boldsymbol{k}\pm} + \frac{i}{2N}\sum_{\boldsymbol{q}_1,\boldsymbol{q}_2,\boldsymbol{q}_3}\delta_{\boldsymbol{q}_1+\boldsymbol{q}_2+\boldsymbol{q}_3,\boldsymbol{k}}$$
$$\times\left[\Gamma^{\pm\pm\pm\pm}_{-\boldsymbol{k},1;2,3}\Psi^*_{-1\pm}\Psi_{2\pm}\Psi_{3\pm} + \Gamma^{\pm\pm\mp\mp}_{-\boldsymbol{k},1;2,3}\Psi^*_{-1\pm}\Psi_{2\mp}\Psi_{3\mp}\right] = \tilde{I}_{\boldsymbol{k}\pm}, \tag{4.30}$$

where μ_c is the chemical potential. It is required to describe the approximate magnon number conservation [55]. The chemical potential is an additional parameter characterizing the stationary non-equilibrium state and describes the effect of the pumping on the magnon condensate.

The Gross-Pitaevskii term in Eq. (4.30) can also be derived with the diagrammatic method. The corresponding diagrams are shown in Fig. 4.3. They simply contain the product of three vacuum expectation values and the four-point interaction vertex. Note that there is also a prefactor of 1/2 due to a pair of equivalent lines [55].

4.4 Collision integrals

The strategy for deriving the collision integrals is the same as in section 3.4. Fig. 4.4 show the diagrams contributing to the equation of motion of the magnon correlation function $n^c_{\boldsymbol{k}+}$. The diagrams for $n^c_{\boldsymbol{k}-}$ have the same form with $\Psi_{\boldsymbol{k}+}$ and $\Psi_{\boldsymbol{k}-}$ being

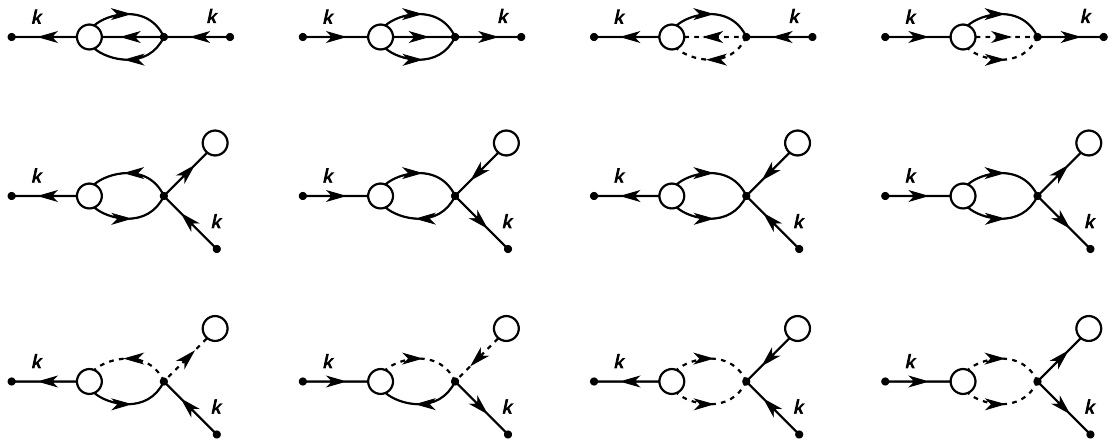

Figure 4.4: The diagrams which contain four-point interaction vertices and contribute to the equation of motion of the correlation functions $n^c_{\boldsymbol{k}+}$. Solid lines represent the bosonic operators of the + branch while dashed lines represent the − branch. The diagrams in the first line contain four-point correlations while the other diagrams contain three-point correlations and the condensate amplitude.

swapped. The (exact) collision integral evaluates to [55]

$$\begin{aligned} I_{\boldsymbol{k}\pm} = \frac{i}{2N} \sum_{\boldsymbol{q}_1,\boldsymbol{q}_2\boldsymbol{q}_3} \delta_{\boldsymbol{k}+\boldsymbol{q}_1,\boldsymbol{q}_2+\boldsymbol{q}_3} \Big[& \Gamma^{\pm\pm\pm\pm}_{-\boldsymbol{k},-\boldsymbol{q}_1;\boldsymbol{q}_2,\boldsymbol{q}_3} \langle \psi^\dagger_{2\pm} \psi^\dagger_{3\pm} \psi_{\boldsymbol{k}\pm} \psi_{1\pm} \rangle^c \\ & + \Gamma^{\pm\pm\mp\mp}_{-\boldsymbol{k},-\boldsymbol{q}_1;\boldsymbol{q}_2,\boldsymbol{q}_3} \langle \psi^\dagger_{2\mp} \psi^\dagger_{3\mp} \psi_{\boldsymbol{k}\pm} \psi_{1\pm} \rangle^c - \text{c.c.} \Big] \\ + \frac{i}{2N} \sum_{\boldsymbol{q}_1,\boldsymbol{q}_2,\boldsymbol{q}_3} \delta_{\boldsymbol{k}+\boldsymbol{q}_1,\boldsymbol{q}_2+\boldsymbol{q}_3} \Big[& \Gamma^{\pm\pm\pm\pm}_{-\boldsymbol{k},-\boldsymbol{q}_1;\boldsymbol{q}_2,\boldsymbol{q}_3} \Psi_{1\pm} \langle \psi^\dagger_{2\pm} \psi^\dagger_{3\pm} \psi_{\boldsymbol{k}\pm} \rangle^c \\ + 2\Gamma^{\pm\pm\pm\pm}_{-\boldsymbol{k},-\boldsymbol{q}_1;\boldsymbol{q}_2,\boldsymbol{q}_3} \Psi_{3\pm} \langle \psi^\dagger_{1\pm} \psi_{2\pm} \psi_{\boldsymbol{k}\pm} \rangle^c & + \Gamma^{\pm\pm\mp\mp}_{-\boldsymbol{k},-\boldsymbol{q}_1;\boldsymbol{q}_2,\boldsymbol{q}_3} \Psi_{1\pm} \langle \psi^\dagger_{2\mp} \psi^\dagger_{3\mp} \psi_{\boldsymbol{k}\pm} \rangle^c \\ & + 2\Gamma^{\pm\pm\mp\mp}_{-\boldsymbol{k},-\boldsymbol{q}_1;\boldsymbol{q}_2,\boldsymbol{q}_3} \Psi_{3\mp} \langle \psi^\dagger_{1\pm} \psi_{2\mp} \psi_{\boldsymbol{k}\pm} \rangle^c - \text{c.c.} \Big] \end{aligned} \tag{4.31}$$

where c.c. denotes the complex conjugate. At this point the collision integrals contain four-point and three-point correlations so that the equation of motion of the magnon correlation function (4.29) is not closed. I employ the same procedure as in section 3.4 and write down the equations of motion for these correlations in the lowest order in the interaction vertices. The diagrams for the relevant correlations for the collision integral of the + branch $I_{\boldsymbol{k}+}$ are shown in Fig. 4.5 and Fig. 4.6. The resulting equations of motion for the three-point and four-point correlations can be integrated and the result is inserted into the above Eq. (4.31). The collision integral $I_{\boldsymbol{k}-}$ can be calculated analogously. I

Figure 4.5: The lowest order diagrams contributing to the equation of motion of four-point correlations of the form $\langle \psi^\dagger_{\boldsymbol{q}_1+}\psi^\dagger_{\boldsymbol{q}_2+}\psi_{\boldsymbol{q}_3+}\psi_{\boldsymbol{q}_4+}\rangle^c$ (left) and $\langle \psi^\dagger_{\boldsymbol{q}_1+}\psi^\dagger_{\boldsymbol{q}_2+}\psi_{\boldsymbol{q}_3-}\psi_{\boldsymbol{q}_4-}\rangle^c$ (right). The diagrams contain only the four-point vertices and contractions.

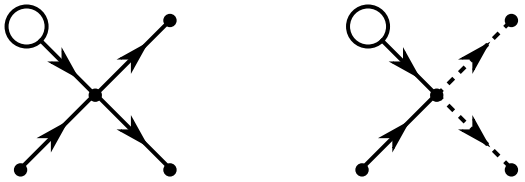

Figure 4.6: The lowest order diagrams contributing to the equation of motion of four-point correlations of the form $\langle \psi^\dagger_{\boldsymbol{q}_1+}\psi_{\boldsymbol{q}_2+}\psi_{\boldsymbol{q}_3+}\rangle^c$ (left) and $\langle \psi^\dagger_{\boldsymbol{q}_1+}\psi_{\boldsymbol{q}_2-}\psi_{\boldsymbol{q}_3-}\rangle^c$ (right). The diagrams contain the four-point vertices, the condensate amplitude $\Psi_{\boldsymbol{q}+}$, and contractions.

get [55]

$$
\begin{aligned}
I_{\boldsymbol{k}\pm} = \frac{\pi}{4N^2}\sum_{\boldsymbol{q}_1,\boldsymbol{q}_2,\boldsymbol{q}_3}\delta_{\boldsymbol{k}+\boldsymbol{q}_1,\boldsymbol{q}_2+\boldsymbol{q}_3}\sum_{r=\pm}\left|\Gamma^{\pm\pm rr}_{-\boldsymbol{k},-1;2,3}\right|^2\Bigg[\delta\left(E_{\boldsymbol{k}\pm}+E_{1\pm}-E_{2r}-E_{3r}\right)\\
\times\Big(\left[1+n_{\boldsymbol{k}\pm}\right]\left[1+n_{1\pm}\right]n_{2r}n_{3r}-n_{\boldsymbol{k}\pm}n_{1\pm}\left[1+n_{2r}\right]\left[1+n_{3r}\right]\Big)\\
-\frac{1}{2}\delta\left(E_{\boldsymbol{k}\pm}+\mu_c-E_{2r}-E_{3r}\right)\left|\Psi_{1\pm}\right|^2\Big(\left[1+n_{\boldsymbol{k}\pm}\right]n_{2r}n_{3r}-n_{\boldsymbol{k}\pm}\left[1+n_{2r}\right]\left[1+n_{3r}\right]\Big)\\
+\delta\left(E_{\boldsymbol{k}\pm}+E_{1\pm}-E_{2r}-\mu_c\right)\left|\Psi_{3r}\right|^2\Big(\left[1+n_{\boldsymbol{k}\pm}\right]\left[1+n_{1\pm}\right]n_{2r}-n_{\boldsymbol{k}\pm}n_{1\pm}\left[1+n_{2r}\right]\Big)\Bigg].
\end{aligned}
\tag{4.32}
$$

The same procedure has to be applied to the equations of motion of the condensate amplitudes $\Psi_{\boldsymbol{k}\pm}$ as well. The relevant diagrams contributing to the equation of motion of the condensate amplitude are shown in Fig. 4.7. The (exact) collision integral for the condensate amplitude is

$$
\tilde{I}_{\boldsymbol{k}\pm} = \frac{\pi}{2N}\sum_{\boldsymbol{q}_1,\boldsymbol{q}_2,\boldsymbol{q}_3}\delta_{\boldsymbol{k}+\boldsymbol{q}_1,\boldsymbol{q}_2+\boldsymbol{q}_3}\sum_{r=\pm}\left|\Gamma^{\pm\pm rr}_{-\boldsymbol{k},-\boldsymbol{q}_1;\boldsymbol{q}_2,\boldsymbol{q}_3}\right|^2\langle\psi^\dagger_{\boldsymbol{q}_1\pm}\psi_{\boldsymbol{q}_2 r}\psi_{\boldsymbol{q}_3 r}\rangle^c. \tag{4.33}
$$

Figure 4.7: Diagrams contributing to the condensate amplitude collision integral $\tilde{I}_{\boldsymbol{k}+}$. The diagrams contain a four-point vertex and a three-point correlation. Due to one pair of equivalent lines there is also a prefactor of 1/2.

The relevant diagrams contributing to the time evolution of the three-point correlations appearing in this equation are shown in Fig. 4.6. The approximate collision integrals for the condensate amplitude are given by [55]

$$\tilde{I}_{\boldsymbol{k}\pm} = \frac{\pi}{8N^2}\Psi_{\boldsymbol{k}\pm}\sum_{\boldsymbol{q}_1,\boldsymbol{q}_2,\boldsymbol{q}_3}\delta_{\boldsymbol{k}+\boldsymbol{q}_1,\boldsymbol{q}_2+\boldsymbol{q}_3}\sum_{r=\pm}\left|\Gamma^{\pm\pm rr}_{-\boldsymbol{k},-1;2,3}\right|^2\delta\left(E_{1\pm}+\mu_c-E_{2r}-E_{3r}\right)$$
$$\times\Big(n_{1\pm}\left[1+n_{2r}\right]\left[1+n_{3r}\right]-\left[1+n_{1\pm}\right]n_{2r}n_{3r}\Big). \quad (4.34)$$

Apparently, the form of the resulting kinetic equations for the correlation function of magnetoelastic modes and the condensate amplitude is the same as for the standard Boltzmann equations known from the literature [87]. Here, two magnetoelastic modes exist. In order to reproduce the Boltzmann equations two approximations have been used. The first approximation is the perturbative expansion so that only terms that are linear or quadratic in the interaction vertices appear. The second approximation is the Markovian type approximation applied to the collision integrals which is explained in section 3.4. This approximation neglects the history of the system and enforces energy conservation. Because I want to investigate the stationary-non equilibrium state in this chapter, applying the Markovian type approximation is justified.

4.5 Stationary non-equilibrium state

In order to properly simulate thermalization of the system a large region of momentum space has to be taken into account. The accumulation effect I investigate, however, occurs in a very small region of momentum space close to the hybridization region. While it is desirable to numerically calculate the time evolution of the system directly, it requires very much computation time due to the two scales in momentum space involved. For this reason I simulate only the accumulation process by carrying out the simulation on two non-uniform grids in momentum space for the lower (−) and upper (+) branches. The magnon-magnon interactions lead to a thermalization of the magnon gas to a quasi-equilibrium state. The magnons can be effectively described by a Bose distribution with an effective temperature T_m that may differs from the temperature T of phonons and a chemical potential μ_m. When the pumping is active and the magnon condensate has formed, the value of the chemical potential corresponds to the minimum of the magnon

dispersion [15, 16, 17, 78, 79, 80, 81]. After the pumping is turned off, the magnon condensate slowly decays due to magnon-phonon interactions and the chemical potential decreases. Thus, in presence of the magnon condensate the system is not in a true stationary state but a transient state. Nevertheless, because the spin-lattice relaxation time is much larger than the time scale on which the condensate forms the damping may be neglected. The system is then described by a thermal quasi-equilibrium state. I assume that the magnon gas is thermalized outside of the hybridization region while inside the hybridization region the magnon distribution function may differs from the Bose distribution. Neglecting magnon-phonon interactions the magnetoelastic distribution function can be written in the form [55]

$$n^c_{\boldsymbol{k}\pm} = |\phi_{\boldsymbol{k}\pm}|^2 \, n^c_{\boldsymbol{k}m} + \left(1 - |\phi_{\boldsymbol{k}\pm}|^2\right) n^c_{\boldsymbol{k}p}, \tag{4.35}$$

where $n^c_{\boldsymbol{k}m}$ and $n^c_{\boldsymbol{k}p}$ are the magnon and phonon distribution functions respectively. In the quasi-equilibrium state they are

$$n^c_{\boldsymbol{k}m} = \frac{1}{e^{(\epsilon_{\boldsymbol{k}}-\mu_m)/T_m} - 1}, \tag{4.36a}$$

$$n^c_{\boldsymbol{k}p} = \frac{1}{e^{\omega_{\boldsymbol{k}\perp}/T} - 1}. \tag{4.36b}$$

Note that the collision integrals (4.32) and (4.34) vanish almost everywhere if the above quasi-equilibrium distribution functions are inserted. They do not vanish, however, close to the hybridization region where we also expect deviations from the quasi-equilibrium state (4.35). The idea is thus to use Eq. (4.35) as initial condition of the magnetoelastic distribution functions and to calculate the deviation of the magnetoelastic distribution and the condensate amplitude near the hybridization region. Because near the bottom of the magnon dispersion the upper (+) branch is energetically degenerate with the hybridization region, this area also has to be included. I focus on finding a non-equilibrium stationary state rather than simulating the time evolution which is computationally demanding. In a stationary state the time derivatives of the distribution functions and the condensate amplitude should vanish,

$$\partial_t n^c_{\boldsymbol{k}\pm}(t) = 0, \tag{4.37a}$$

$$\partial_t \Psi_{\boldsymbol{k}\pm}(t) = 0. \tag{4.37b}$$

The initial magnetoelastic distribution $n^c_{\boldsymbol{k}\pm}(t_0)$ is the incoherent superposition of the quasi-equilibrium distribution (4.35). I assume that the condensate amplitude is only non-vanishing in the bottom of the magnon dispersion. To estimate the initial condensate density I consider only the Gross-Pitaevskii terms in Eq. (4.30) and neglect the collision integral at this point. From the condition that the time derivative vanishes it follows that [55]

$$|\Psi_{\boldsymbol{k}+}(t_0)| = \delta_{\boldsymbol{k},\boldsymbol{k}_{\min}} \sqrt{N \frac{|\mu_c - E_{\boldsymbol{k}+}|}{\left|\Gamma^{++++}_{-\boldsymbol{k},-\boldsymbol{k},\boldsymbol{k},\boldsymbol{k}}\right|}}, \tag{4.38a}$$

$$\Psi_{\boldsymbol{k}-}(t_0) = 0, \tag{4.38b}$$

where $\boldsymbol{k}_{\min}$ is the wave vector at the minimum of the magnon dispersion. Note that the quasi-equilibrium state is not exactly a stationary state. There are processes that lead to damping and a relaxation where the chemical potential decreases and the condensate vanishes. However, as the spin-lattice relaxation time is much larger than the time scale on which the magnon condensate forms these additional thermalization channels can be neglected here. Starting from these initial conditions, I use Eqs. (4.29) and (4.30) to find an estimate for the new values of the collision integrals so that the left-hand side of Eqs. (4.37) decreases. Furthermore, I determine the magnon temperature T_m and chemical potential μ_m self-consistently after each iteration starting with some guess for the initial values. Assuming that the phonons act as a thermal bath for the magnons I keep the phonon temperature T fixed at the room temperature value $T = 290$ K.

In order to carry out the numerical calculations I introduce two mesh grids in momentum space for the upper (+) and the lower (−) branch shown in Fig. 4.8. The meshes are constructed in the following way: the angle $\Theta_{\boldsymbol{k}} \in [0, \pi/2]$ of the wave vector $\boldsymbol{k}$ is chosen non-uniformly with N_Θ steps so that the density of grid points is larger at angles closer to $\pi/2$. For each angle $\Theta_{\boldsymbol{k}}$ the lengths $k = |\boldsymbol{k}|$ of the upper (+) mode wave vector are chosen are chosen uniformly from an interval centered around the minimum of the magnon dispersion. For the lower (−) mode the interval is centered around the wave vector where the dispersion is degenerate with the bottom of the magnon dispersion (see Fig. 4.2). In this case the lengths of the wave vectors are chosen non-uniformly so that the density of grid points is larger at smaller wave vectors. The mesh is chosen in this complicated way instead of a uniform grid in momentum space in order to reduce the number of grid points required to obtain accurate results. The density of grid points is larger in the relevant region of momentum space where the accumulation of magnetoelastic modes has been observed experimentally. Distribution functions outside the mesh are approximated by the quasi-equilibrium distribution (4.35). For the external magnetic field strength and the thickness of the YIG film I chose $H = 145$ mT and $d = 6.7$ µm in accordance to the experimental parameters. The initial magnon chemical potential is the to $\mu_m = 0.98\epsilon_{\boldsymbol{k}_{\min}}$ and the initial magnon temperature is set to the phonon temperature, $T_m = T$. The chemical potential of the condensate μ_c is set to the fixed value $\mu_c = 0.995\epsilon_{\boldsymbol{k}_{\min}}$. It is necessary to take into account that the chemical potential at the minimum of the magnon dispersion differs from that of the other magnon modes due to the presence of the magnon condensate. The magnon chemical potential μ_m and the magnon temperature T_m are determined self-consistently within the self-consistency iteration loop. Lastly, the system size N required for the estimation of the initial condensate density (4.38) is set to $N = 8.08 \times 10^6$.

The total magnon density $\rho_{\boldsymbol{k}m}$ is defined by

$$\rho_{\boldsymbol{k}m} \equiv \frac{1}{N}\langle b_{\boldsymbol{k}}^\dagger b_{\boldsymbol{k}}\rangle = \sum_{r=\pm} |\phi_{\boldsymbol{k}r}|^2 \left(n_{\boldsymbol{k}r}^c + |\Psi_{\boldsymbol{k}r}|^2\right). \tag{4.39}$$

The total magnon density in the self-consistent stationary state obtained numerically is shown in Fig. 4.9 and Fig. 4.10 in dependence of the wave vector component k_z parallel to the external magnetic field and the excitation frequency ω. Two sharp peaks

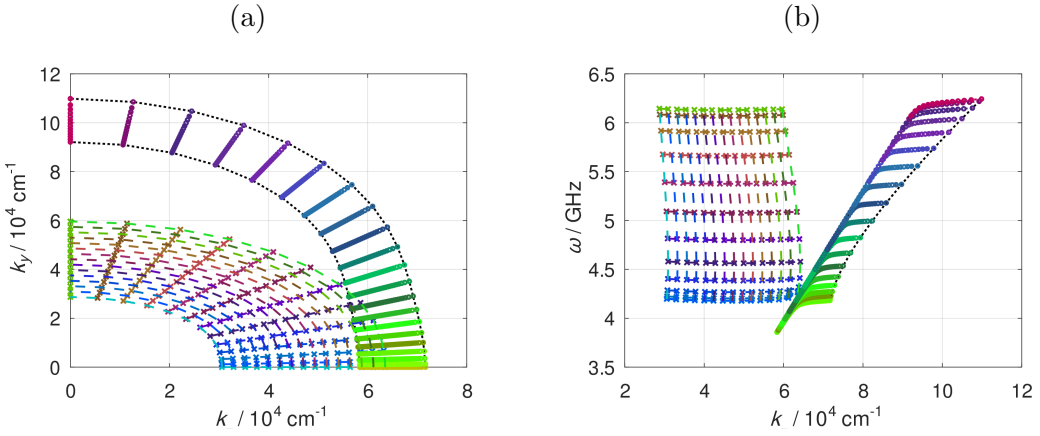

Figure 4.8: The wave vector mesh used for the numerical calculations in this section in momentum space (a) and in dependence of the length of the wave vector $k = |\boldsymbol{k}|$ and the excitation frequency ω (b). The color coding is the same for both plots with crosses for the upper (+) modes and circles for the lower (−) modes. The meshes consist of 790 grid points in total.

are visible: the condensate peak in the bottom of the magnon spectrum and another sharp peak in the lower (−) magnetoelastic mode within the hybridization region at a slightly lower excitation energy. My numerical results further reveal that this peak is completely incoherent, i.e. the peak appears in the incoherent distribution function $n^c_{\boldsymbol{k}-}$ while the condensate amplitude $\Psi_{\boldsymbol{k}-}$ tends to zero. The magnon temperature T_m and the magnon chemical potential μ_m deviate slightly from the initial values. I find $T_m = 289.6$ K and $\mu_m = 0.978\epsilon_{\boldsymbol{k}_{\min}}$. The fact that these values lie very close to the initial values is an indicator for the validity of the ansatz of the quasi-equilibrium state (4.35). Fig. 4.10 shows the total magnon density in momentum space. Apparently, the magnon density deviates from the quasi-equilibrium distribution only in two small regions in momentum space. I find no significant deviations away from the bottom of the magnon spectrum and the nearly degenerate hybridization region. This finding agrees well with the experiment [55]. Fig. 4.11 and Fig. 4.12 show experimental data from Ref. [55]. The experimentally measured total magnon density is shown analogously to Fig. 4.9 and Fig. 4.10. A comparison of the experimental and the theoretical plots shows that the location in the phase space and the amplitude of the observed peaks of the magnon density agree well.

In order to verify that the magnon condensate is important for the accumulation of the lower (−) magnetoelastic mode peak I repeat the simulation with a lower value of the chemical potential $\mu_c = 0.75\epsilon_{\boldsymbol{k}_{\min}}$ for the case where the magnon gas is not driven strong enough to form a magnon condensate. The corresponding plots are shown in Fig. 4.13 and 4.14. In Fig. 4.14 the peak of the lower (−) magnetoelastic mode is visible although much smaller than in the previous simulation. In fact, the peak has the order of magnitude of the thermal magnon distribution while in the case where the magnon

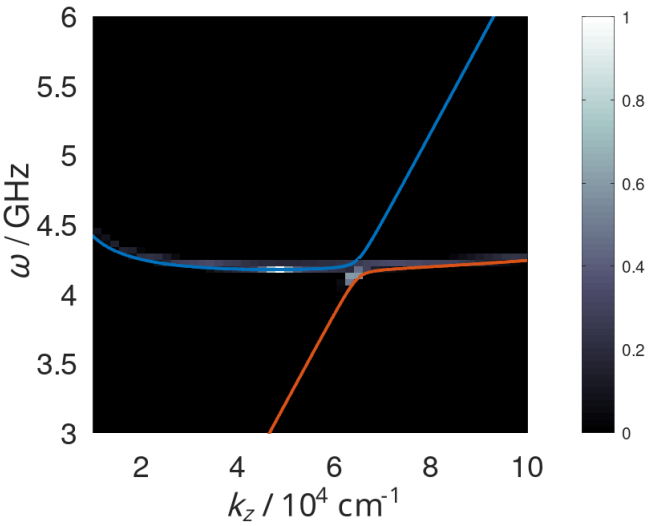

Figure 4.9: The total magnon density normalized to the condensate amplitude is shown in the phase space spanned by the wave vector in z direction and the excitation energy ω of magnons. The blue and red curve show the dispersions of the upper and lower magnetoelastic modes perpendicular to the external field respectively.

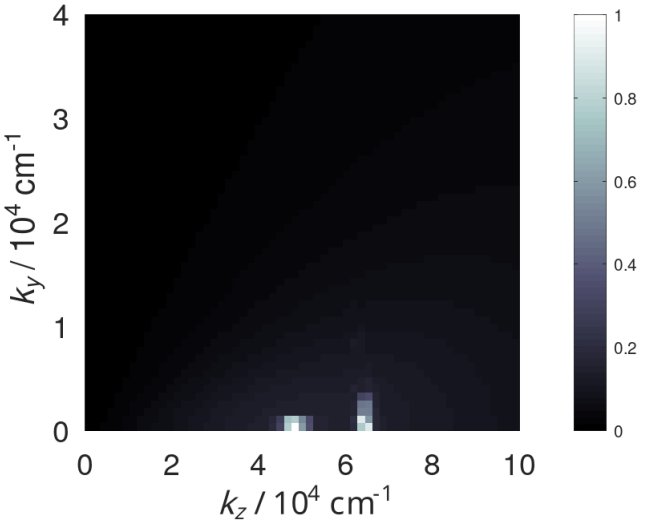

Figure 4.10: The total magnon density in momentum space normalized to the condensate amplitude. The left peak arises due to the magnon condensate while the right peak is the contribution from incoherent magnetoelastic modes. The magnon density is normalized the same way as in Fig. 4.9.

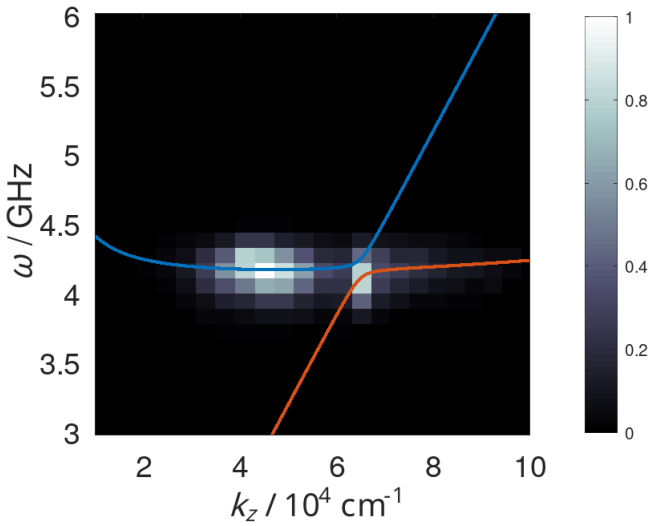

Figure 4.11: Experimental data from Ref. [55] of the total magnon density normalized to the condensate amplitude shown in the phase space spanned by the wave vector in z direction and the excitation energy ω of magnons. The blue and red curve show the dispersions of the upper and lower magnetoelastic modes perpendicular to the external field respectively.

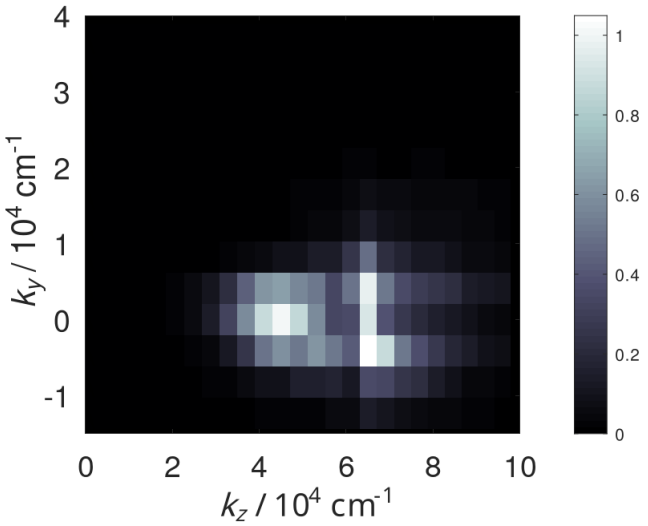

Figure 4.12: Experimental data from Ref. [55] of the total magnon density normalized to the condensate amplitude shown in momentum space. The left peak arises due to the magnon condensate while the right peak is the contribution from incoherent magnetoelastic modes.

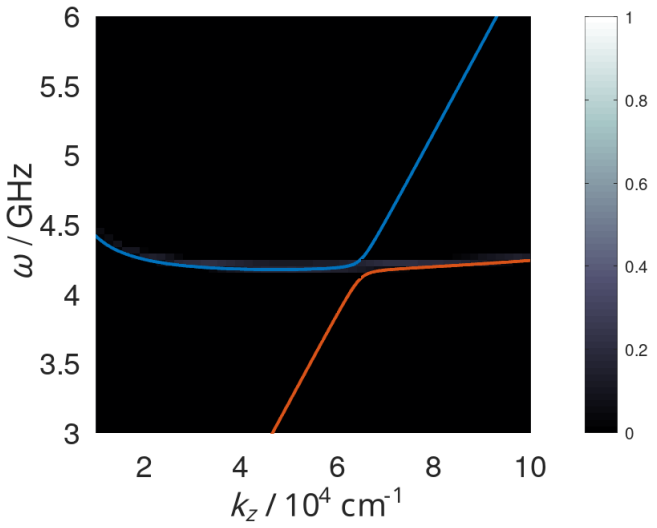

Figure 4.13: The total magnon density in absence of the magnon condensate is shown in the phase space spanned by the wave vector in z direction and the excitation energy ω of magnons. The magnon density is normalized in the same way as Fig. 4.9. The blue and red curve show the dispersions of the upper and lower magnetoelastic modes perpendicular to the external field respectively.

condensate is present the magnetoelastic peak has the same order of magnitude as the condensate peak. I conclude that the near-degeneracy of the lower $(-)$ magnetoelastic mode with the bottom of the magnon spectrum is necessary to observe the accumulation of magnetoelastic modes. The hybridization of magnons and phonons alone without this near-degeneracy is not sufficient. Only in presence of the magnon condensate the accumulation effect leads to a macroscopic occupation of magnetoelastic modes due to intermodal scattering of magnetoelastic modes with the magnon condensate. This finding agrees with the experimental data in Refs. [47, 55]. Furthermore, the formation of a small accumulation of magnetoelastic modes in the case when the pumping strength is too small for a magnon condensate to form can be reproduced by the theory as well. The theory also agrees with the discussion of the effect as a bottleneck accumulation effect due to intermodal scattering in Ref. [47]. While in Ref. [47] a phenomenological explanation of the accumulation effect is given, the kinetic theory derived in this chapter is obtained from the microscopic dynamics of the magnon-phonon system.

In summary, in this chapter I have included magnon-phonon interactions to the magnon subsystem in order to investigate an accumulation phenomenon of magnetoelastic bosons in an overpopulated magnon gas in YIG. Kinetic equations for the incoherent distribution functions and the condensate amplitude have been derived. The collision integrals describe the dominant scattering processes of the magnetoelastic bosons. I found an efficient strategy to obtain numerically the stationary state in a self-consistent way. The numerical solution confirms that only in a small region close to the magnon-phonon

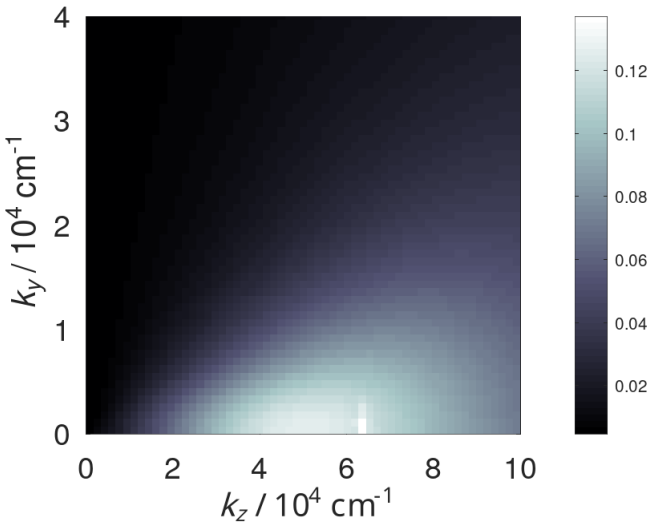

Figure 4.14: The total magnon density in absence of the magnon condensate is shown in momentum space. There is a barely visible peak originating from the contribution of incoherent lower magnetoelastic modes. The magnon density is normalized the same way as in Fig. 4.9 but the color coding is different to improve the visibility of the small peak.

hybridization region the magnetoelastic distribution function differs from the thermal quasi-equilibrium distribution. The numerical results agree well with the experimental data and confirm the importance of the magnon condensate; the interaction between the magnon condensate and the magnetoelastic bosons close to the hybridization region is necessary for the macroscopic accumulation of magnetoelastic bosons. Furthermore, it can be shown that this accumulation is purely incoherent. Therefore, the accumulation of magnetoleastic bosons is not associated with a coherent state.

5 Charge-density waves

In Ref. [37] a Gaussian theory has been introduced to describe charge-density waves (CDWs) in quasi-one-dimensional systems. Here, I go beyond this approximation and investigate the microscopic dynamics of CDW systems and the order parameter damping.

5.1 Introduction

In this chapter I consider a different type of system where charge-density waves arise due to a Peierls distortion. They are a collective phenomenon characterized by a spatial modulation of the charge density of the system [29]. CDWs are a good example for spontaneous symmetry breaking where the phase transition occurs due to the lower energy of the CDW ground state compared to the translationally invariant ground state. In the case where the charge-density wave vector is incommensurate with the lattice the order parameter associated with the CDW is complex. The collective modes can be described by an amplitude mode and a phase mode. Recently, progress in terahertz spectroscopy allowed for more detailed experimental investigations of the amplitude and phase modes in CDW materials [48, 50, 51].

The goal of this chapter is to understand the amplitude and phase mode spectra and the temperature dependence of the damping of amplitude and phase modes. For this purpose I formulate a kinetic theory using again the method of expansion in connected equal-time correlations which has been introduced in chapter 2. To make connection with to the mean-field approximation I apply a canonical transformation to the Fröhlich Hamiltonian which is capable of diagonalizing the electronic part of the Fröhlich Hamiltonian involving only interactions with $2k_F$ phonons. However, I explicitly take into account interactions with the entire phonon spectrum. Thus, the Hamiltonian cannot be diagonalized by the transformation and additional contributions to the microscopic collision integrals that are not contained within the Gaussian approximation [37] appear. This procedure allows me to linearize the kinetic equations around the thermal distribution obtained within the mean-field approximation and to compare the results with the Gaussian approximation or the equivalent random-phase approximation. We will see later that the contributions to the collision integrals coming from the additional interactions with non-$2k_F$ phonons lead to non-vanishing order parameter damping in the mean-field thermal equilibrium state. By expressing the order parameter in terms of phononic vacuum expectation values and calculating microscopic collision integrals I get coupled equations of motion for the order parameter and the phonon coordinates. The linearized equations of motion have the same form as the phenomenological Ginzburg-Landau equations [48, 50, 51].

5.2 Hamiltonian

5.2.1 Fröhlich Hamiltonian

I start from the Fröhlich Hamiltonian with multiple phonon bands labeled by the index λ, [30, 32]

$$\mathcal{H} = \sum_{\boldsymbol{k},\sigma} \epsilon_{\boldsymbol{k}} c^{\dagger}_{\boldsymbol{k},\sigma} c_{\boldsymbol{k},\sigma} + \sum_{\boldsymbol{q},\lambda} \omega_{\boldsymbol{q},\lambda} b^{\dagger}_{\boldsymbol{q},\lambda} b_{\boldsymbol{q},\lambda} + \frac{1}{\sqrt{\mathcal{V}}} \sum_{\lambda,\sigma,\boldsymbol{q},\boldsymbol{k}} \gamma_{\boldsymbol{q},\lambda} c^{\dagger}_{\boldsymbol{k}+\boldsymbol{q},\sigma} c_{\boldsymbol{k},\sigma} \left(b_{\boldsymbol{q},\lambda} + b^{\dagger}_{-\boldsymbol{q},\lambda} \right), \quad (5.1)$$

where σ denotes the spin of the electrons and $\boldsymbol{k}$ and $\boldsymbol{q}$ denote the wave vectors of electrons and phonons. This Hamiltonian has been used previously in the literature to investigate charge-density-wave systems. I consider transversal and longitudinal phonon modes which are both labeled by the indices λ. The phonon spectrum is considered to be three dimensional while the electrons are assumed to occupy a one dimensional band with flat Fermi surfaces. In quasi-one-dimensional materials this is realized by parallel one-dimensional chains. A more realistic treatment should involve interactions between the one-dimensional chains. For simplicity, this will not be done in this work.

5.2.2 Order parameter

The order parameter can be defined by

$$\Delta = \sum_{\lambda} \gamma_{\boldsymbol{Q},\lambda} \langle b_{\boldsymbol{Q},\lambda} + b^{\dagger}_{-\boldsymbol{Q},\lambda} \rangle, \quad (5.2)$$

where $\boldsymbol{Q} = (0, 0, 2k_F)$ is the charge-density wave vector and the order parameter Δ is complex in general. Assuming that the amplitude and phase fluctuations are decoupled, the order parameter can be written as

$$\Delta = (\Delta_0 + \delta)\, e^{i\phi}, \quad (5.3)$$

where Δ_0 is the equilibrium value of the order parameter and δ and ϕ are the amplitude and phase fluctuations. To the lowest order in δ and ϕ the relations [29]

$$\Delta_{\boldsymbol{Q}} + \Delta_{-\boldsymbol{Q}} \approx 2\Delta_0 + 2\delta, \quad (5.4)$$
$$\Delta_{\boldsymbol{Q}} - \Delta_{-\boldsymbol{Q}} \approx 2\Delta_0 \phi, \quad (5.5)$$

hold true. This is the motivation for introducing amplitude and phase mode annihilation operators $b^{(1)}_{\boldsymbol{q},\lambda}$ and $b^{(2)}_{\boldsymbol{q},\lambda}$ via the transformation [88]

$$\begin{pmatrix} b^{(1)}_{\boldsymbol{q},\lambda} \\ b^{(2)}_{\boldsymbol{q},\lambda} \end{pmatrix} = \frac{1}{\sqrt{2}} \begin{pmatrix} 1 & 1 \\ i & -i \end{pmatrix} \begin{pmatrix} b_{\boldsymbol{q}+\boldsymbol{Q},\lambda} \\ b_{\boldsymbol{q}-\boldsymbol{Q},\lambda} \end{pmatrix}, \quad (5.6)$$

corresponding to the expansion to lowest order in amplitude and phase fluctuations. The transformed Hamiltonian can be written as

$$\mathcal{H} = \sum_{\boldsymbol{k},\sigma} \epsilon_{\boldsymbol{k}} c^\dagger_{\boldsymbol{k},\sigma} c_{\boldsymbol{k},\sigma} + \sum_{\boldsymbol{q},\lambda} \omega_{\boldsymbol{q},\lambda} \left[\left(b^{(1)}_{\boldsymbol{q},\lambda} \right)^\dagger b^{(1)}_{\boldsymbol{q},\lambda} + \left(b^{(2)}_{\boldsymbol{q},\lambda} \right)^\dagger b^{(2)}_{\boldsymbol{q},\lambda} \right] + \frac{1}{\sqrt{\mathcal{V}}} \sum_{\lambda,\sigma,\boldsymbol{q},\boldsymbol{k}} \gamma_{\boldsymbol{q},\lambda} c^\dagger_{\boldsymbol{k}+\boldsymbol{q},\sigma} c_{\boldsymbol{k},\sigma} \left[X^{(1)}_{\boldsymbol{q},\lambda} + X^{(2)}_{\boldsymbol{q},\lambda} \right], \tag{5.7}$$

with the phonon displacement fields

$$X^{(1)}_{\boldsymbol{q},\lambda} = \frac{b^{(1)}_{\boldsymbol{q},\lambda} + \left(b^{(1)}_{-\boldsymbol{q},\lambda} \right)^\dagger}{\sqrt{2\omega_{\boldsymbol{q},\lambda}}}, \tag{5.8a}$$

$$X^{(2)}_{\boldsymbol{q},\lambda} = \frac{-i b^{(2)}_{\boldsymbol{q},\lambda} + i \left(b^{(2)}_{-\boldsymbol{q},\lambda} \right)^\dagger}{\sqrt{2\omega_{\boldsymbol{q},\lambda}}}. \tag{5.8b}$$

5.2.3 Mean-field approximation

Let us consider a CDW with wave vector $\boldsymbol{Q}$ within mean-field approximation. To study the CDW instability I replace the phonon displacement operators with their expectation values assuming finite expectation values only for the wave vectors $\pm\boldsymbol{Q}$ and $\boldsymbol{0}$ [37],

$$X^\alpha_{\boldsymbol{q},\lambda} \to X^{0,\alpha}_{\boldsymbol{q},\lambda} = \sqrt{\mathcal{V}} \left[\delta_{\boldsymbol{q},\boldsymbol{0}} X^{0,\alpha}_{\lambda,\boldsymbol{0}} + \delta_{\boldsymbol{q},\boldsymbol{Q}} X^{0,\alpha}_{\boldsymbol{Q},\lambda} + \delta_{\boldsymbol{q},-\boldsymbol{Q}} X^{0,\alpha}_{-\boldsymbol{Q},\lambda} \right], \tag{5.9}$$

for $\alpha = 1, 2$. The fermionic and interaction parts of the Hamiltonian now read

$$\mathcal{H}_F + \mathcal{H}_I = \sum_{\boldsymbol{k},\sigma} \left[\epsilon_{\boldsymbol{k}} + \sum_{\lambda,\alpha=1,2} \gamma_{\boldsymbol{0},\lambda} X^{0,\alpha}_{\boldsymbol{0},\lambda} \right] c^\dagger_{\boldsymbol{k},\sigma} c_{\boldsymbol{k},\sigma} + \sum_{\boldsymbol{k},\sigma,\lambda,\alpha=1,2} \left[\gamma_{\boldsymbol{Q},\lambda} X^{0,\alpha}_{\boldsymbol{Q},\lambda} c^\dagger_{\boldsymbol{k}+\boldsymbol{Q},\sigma} c_{\boldsymbol{k},\sigma} + \gamma_{-\boldsymbol{Q},\lambda} X^{0,\alpha}_{-\boldsymbol{Q},\lambda} c^\dagger_{\boldsymbol{k}-\boldsymbol{Q},\sigma} c_{\boldsymbol{k},\sigma} \right]. \tag{5.10}$$

By introducing

$$U_{\boldsymbol{0}} = \sum_{\lambda,\alpha=1,2} \gamma_{\lambda,\boldsymbol{0}} X^{0,\alpha}_{\lambda,\boldsymbol{0}}, \tag{5.11}$$

$$U_{\boldsymbol{Q}} = \sum_{\lambda,\alpha=1,2} \gamma_{\boldsymbol{Q},\lambda} X^{0,\alpha}_{\boldsymbol{Q},\lambda}, \tag{5.12}$$

$$U_{-\boldsymbol{Q}} = \sum_{\lambda,\alpha=1,2} \gamma_{-\boldsymbol{Q},\lambda} X^{0,\alpha}_{-\boldsymbol{Q},\lambda} = U^*_{\boldsymbol{Q}}, \tag{5.13}$$

and shifting the momentum labels the fermionic part of the Hamiltonian can be written as

$$\mathcal{H}_F = \sum_{\boldsymbol{k},\sigma} \begin{pmatrix} c^\dagger_{\boldsymbol{k}+\frac{\boldsymbol{Q}}{2},\sigma}, & c^\dagger_{\boldsymbol{k}-\frac{\boldsymbol{Q}}{2},\sigma} \end{pmatrix} \begin{pmatrix} \epsilon_{\boldsymbol{k}+\frac{\boldsymbol{Q}}{2}} + U_{\boldsymbol{0}} & U_{\boldsymbol{Q}} \\ U_{-\boldsymbol{Q}} & \epsilon_{\boldsymbol{k}-\frac{\boldsymbol{Q}}{2}} + U_{\boldsymbol{0}} \end{pmatrix} \begin{pmatrix} c_{\boldsymbol{k}+\frac{\boldsymbol{Q}}{2},\sigma} \\ c_{\boldsymbol{k}-\frac{\boldsymbol{Q}}{2},\sigma} \end{pmatrix}. \tag{5.14}$$

This expression can be diagonalized via an unitary transformation by introducing new fermionic operators $d^+_{\boldsymbol{k},\sigma}$ and $d^-_{\boldsymbol{k},\sigma}$. This transformation is defined by

$$\begin{pmatrix} c_{\boldsymbol{k}+\frac{\boldsymbol{Q}}{2},\sigma} \\ c_{\boldsymbol{k}-\frac{\boldsymbol{Q}}{2},\sigma} \end{pmatrix} = \mathcal{U}_{\boldsymbol{k}} \begin{pmatrix} d^+_{\boldsymbol{k},\sigma} \\ d^-_{\boldsymbol{k},\sigma} \end{pmatrix} = \begin{pmatrix} u_{\boldsymbol{k}} & -v_{\boldsymbol{k}} \\ v^*_{\boldsymbol{k}} & u^*_{\boldsymbol{k}} \end{pmatrix} \begin{pmatrix} d^+_{\boldsymbol{k},\sigma} \\ d^-_{\boldsymbol{k},\sigma} \end{pmatrix}, \tag{5.15}$$

with

$$\Delta = U_{\boldsymbol{Q}}, \quad \Delta^* = U_{-\boldsymbol{Q}}, \tag{5.16}$$

$$u_{\boldsymbol{k}} = \frac{\Delta}{|\Delta|}\sqrt{\frac{E_{\boldsymbol{k}}+\xi_{\boldsymbol{k}}}{2E_{\boldsymbol{k}}}}, \tag{5.17}$$

$$v_{\boldsymbol{k}} = \sqrt{\frac{E_{\boldsymbol{k}}-\xi_{\boldsymbol{k}}}{2E_{\boldsymbol{k}}}}, \tag{5.18}$$

$$E_{\boldsymbol{k}} = \sqrt{\xi^2_{\boldsymbol{k}}+|\Delta|^2}, \tag{5.19}$$

$$\xi_{\boldsymbol{k}} = \frac{\epsilon_{\boldsymbol{k}+\frac{\boldsymbol{Q}}{2}} - \epsilon_{\boldsymbol{k}-\frac{\boldsymbol{Q}}{2}}}{2}. \tag{5.20}$$

Note that for the new fermionic operators there is the restriction $|k_z| \leq k_F$ to avoid double counting. This restriction also ensures that the new operators $d^+_{\boldsymbol{k},\sigma}$ and $d^-_{\boldsymbol{k},\sigma}$ satisfy fermionic anti-commutator relations,

$$\left\{ d^\alpha_{\boldsymbol{k},\sigma}, d^\beta_{\boldsymbol{q},\sigma} \right\} = 0, \tag{5.21a}$$

$$\left\{ \left(d^\alpha_{\boldsymbol{k},\sigma}\right)^\dagger, d^\beta_{\boldsymbol{q},\sigma} \right\} = \delta_{\alpha,\beta}\delta_{\boldsymbol{k},\boldsymbol{q}}. \tag{5.21b}$$

If the restriction $|k_z| \leq k_F$ is not enforced, additional complex valued terms that involve the Kronecker delta $\delta_{\boldsymbol{k}\pm\boldsymbol{Q},\boldsymbol{q}}$ appear in the above commutator relation (5.21b). After this transformation the fermionic Hamiltonian has the diagonal form

$$\mathcal{H}_F = \sum_{\boldsymbol{k},\sigma,\alpha=\pm} E^\alpha_{\boldsymbol{k}} \left(d^\alpha_{\boldsymbol{k},\sigma}\right)^\dagger d^\alpha_{\boldsymbol{k},\sigma}, \tag{5.22}$$

with [37]

$$E^\pm_{\boldsymbol{k}} = \pm E_{\boldsymbol{k}} + \frac{\epsilon_{\boldsymbol{k}+\frac{\boldsymbol{Q}}{2}} + \epsilon_{\boldsymbol{k}-\frac{\boldsymbol{Q}}{2}}}{2} + U_{\boldsymbol{0}}. \tag{5.23}$$

This expression can be further simplified if the electronic dispersion is linearized around $\boldsymbol{k}_F$. With the CDW wave vector $\boldsymbol{Q} = (0, 0, 2k_F)$ the electronic dispersion can be approximated by

$$\epsilon_{\boldsymbol{k}} \approx v_F \left(|k_z| - k_F\right). \tag{5.24}$$

The electronic energy $E^\pm_{\boldsymbol{k}}$ is then given by

$$E^\pm_{\boldsymbol{k}} \approx \pm\sqrt{v_F^2 k_z^2 + |\Delta|^2} + U_{\boldsymbol{0}}. \tag{5.25}$$

The constant $U_{\mathbf{0}}$ may be absorbed into the chemical potential. From the form of the new dispersion (5.25) it is apparent that the new operators $d^{+}_{\boldsymbol{k},\sigma}$ and $d^{-}_{\boldsymbol{k},\sigma}$ describe a conductance band and a valence band respectively. In the CDW phase the system behaves effectively like a semiconductor.

In order to go beyond the mean-field approximation the entire Fröhlich Hamiltonian should be taken into account. Therefore, I apply the unitary transformation (5.15) to the full Hamiltonian (5.7). For the interaction part of the Hamiltonian I find

$$\mathcal{H}_I = \frac{1}{\sqrt{\mathcal{V}}} \sum_{\lambda,\sigma,\boldsymbol{k},\boldsymbol{q}} \Bigg[\gamma^{++}_{\boldsymbol{q},\boldsymbol{k},\lambda} \left(d^{+}_{\boldsymbol{k},\sigma}\right)^{\dagger} d^{+}_{\boldsymbol{k}-\boldsymbol{q}+\boldsymbol{Q},\sigma} X_{\boldsymbol{q},\lambda} - \gamma^{--}_{\boldsymbol{q},\boldsymbol{k},\lambda} \left(d^{-}_{\boldsymbol{k},\sigma}\right)^{\dagger} d^{-}_{\boldsymbol{k}-\boldsymbol{q}+\boldsymbol{Q},\sigma} X_{\boldsymbol{q},\lambda} + \gamma^{+-}_{\boldsymbol{q},\boldsymbol{k},\lambda} \left(d^{+}_{\boldsymbol{k},\sigma}\right)^{\dagger} d^{-}_{\boldsymbol{k}-\boldsymbol{q}+\boldsymbol{Q},\sigma} X_{\boldsymbol{q},\lambda} - \gamma^{-+}_{\boldsymbol{q},\boldsymbol{k},\lambda} \left(d^{-}_{\boldsymbol{k},\sigma}\right)^{\dagger} d^{+}_{\boldsymbol{k}-\boldsymbol{q}+\boldsymbol{Q},\sigma} X_{\boldsymbol{q},\lambda} + \text{h.c.} \Bigg], \tag{5.26}$$

with

$$X_{\boldsymbol{q},\lambda} = \sum_{\alpha=1,2} \left[X^{(\alpha)}_{\boldsymbol{q},\lambda} - \delta_{\boldsymbol{q},\mathbf{0}} X^{0,\alpha}_{\mathbf{0},\lambda} - \delta_{\boldsymbol{q},\boldsymbol{Q}} X^{0,\alpha}_{\boldsymbol{Q},\lambda} - \delta_{\boldsymbol{q},-\boldsymbol{Q}} X^{0,\alpha}_{-\boldsymbol{Q},\lambda} \right]. \tag{5.27}$$

and

$$\gamma^{++}_{\boldsymbol{q},\boldsymbol{k},\lambda} = u^{*}_{\boldsymbol{k}} v^{*}_{\boldsymbol{k}-\boldsymbol{q}+\boldsymbol{Q}} \gamma_{\boldsymbol{q},\lambda}, \tag{5.28a}$$

$$\gamma^{--}_{\boldsymbol{q},\boldsymbol{k},\lambda} = v^{*}_{\boldsymbol{k}} u^{*}_{\boldsymbol{k}-\boldsymbol{q}+\boldsymbol{Q}} \gamma_{\boldsymbol{q},\lambda}, \tag{5.28b}$$

$$\gamma^{+-}_{\boldsymbol{q},\boldsymbol{k},\lambda} = u^{*}_{\boldsymbol{k}} u^{*}_{\boldsymbol{k}-\boldsymbol{q}+\boldsymbol{Q}} \gamma_{\boldsymbol{q},\lambda}, \tag{5.28c}$$

$$\gamma^{-+}_{\boldsymbol{q},\boldsymbol{k},\lambda} = v^{*}_{\boldsymbol{k}} v^{*}_{\boldsymbol{k}-\boldsymbol{q}+\boldsymbol{Q}} \gamma_{\boldsymbol{q},\lambda}. \tag{5.28d}$$

Apparently, the transformation (5.15) is not capable of diagonalizing the entire Hamiltonian (5.7). There still appear interaction terms containing phonons with wave vectors $\boldsymbol{q}$ that are not equal to $\pm\boldsymbol{Q}$ or $\mathbf{0}$. When formulating the kinetic equations these terms need to be included into the collision integrals so that the exact collision integrals contain all electron-phonon interactions which are neglected within mean-field approximation. The effect of interactions between electrons and phonons with wave vectors $\pm\boldsymbol{Q}$ and $\mathbf{0}$ are effectively included into the electronic dispersions (5.25) which explicitly depend on the order parameter. As a result of this effect the system behaves effectively as a semiconductor. In order to investigate the effect of the non-$2k_F$ phonons on the system the microscopic collision integrals should to be calculated.

5.3 Kinetic equations

The connected distribution functions for the electrons, the amplitude phonons, and the phase phonons are defined as

$$f^{\pm}_{\boldsymbol{k},\sigma} \equiv \langle \left(d^{\pm}_{\boldsymbol{k},\sigma}\right)^{\dagger} d^{\pm}_{\boldsymbol{k},\sigma} \rangle^{c} = \langle \left(d^{\pm}_{\boldsymbol{k},\sigma}\right)^{\dagger} d^{\pm}_{\boldsymbol{k},\sigma} \rangle, \tag{5.29a}$$

$$\tilde{f}^{\pm}_{\boldsymbol{k},\sigma} \equiv \langle \left(d^{\pm}_{\boldsymbol{k},\sigma}\right)^{\dagger} d^{\mp}_{\boldsymbol{k},\sigma} \rangle^{c} = \langle \left(d^{\pm}_{\boldsymbol{k},\sigma}\right)^{\dagger} d^{\mp}_{\boldsymbol{k},\sigma} \rangle, \tag{5.29b}$$

$$n^{(1,2)}_{\boldsymbol{q},\lambda} \equiv \langle \left(b^{(1,2)}_{\boldsymbol{q},\lambda}\right)^{\dagger} b^{(1,2)}_{\boldsymbol{q},\lambda} \rangle^{c} = \langle \left(b^{(1,2)}_{\boldsymbol{q},\lambda}\right)^{\dagger} b^{(1,2)}_{\boldsymbol{q},\lambda} \rangle - \langle \left(b^{(1,2)}_{\boldsymbol{q},\lambda}\right)^{\dagger} \rangle \langle b^{(1,2)}_{\boldsymbol{q},\lambda} \rangle. \tag{5.29c}$$

Note that the electronic distribution functions $f^{\pm}_{\boldsymbol{k},\sigma}$ and $\tilde{f}^{\pm}_{\boldsymbol{k},\sigma}$ are only defined for $-k_F \leq k_z \leq k_F$ due to the restriction of the fermionic operators $d^{\pm}_{\boldsymbol{k},\sigma}$ explained in the previous section. Furthermore, I define the vacuum expectation values for amplitude and phase phonons as

$$\psi^{(1)}_{\boldsymbol{q},\lambda} \equiv \langle b^{(1)}_{\boldsymbol{q},\lambda} \rangle, \tag{5.30a}$$

$$\psi^{(2)}_{\boldsymbol{q},\lambda} \equiv \langle b^{(2)}_{\boldsymbol{q},\lambda} \rangle. \tag{5.30b}$$

Using the Heisenberg equations of motion,

$$i\partial_t d^{\pm}_{\boldsymbol{k},\sigma} = \left[d^{\pm}_{\boldsymbol{k},\sigma}, H\right], \tag{5.31a}$$

$$i\partial_t \left(d^{\pm}_{\boldsymbol{k},\sigma}\right)^{\dagger} = \left[\left(d^{\pm}_{\boldsymbol{k},\sigma}\right)^{\dagger}, H\right], \tag{5.31b}$$

$$i\partial_t b^{(1,2)}_{\lambda,\boldsymbol{k}} = \left[b^{(1,2)}_{\lambda,\boldsymbol{k}}, H\right], \tag{5.31c}$$

$$i\partial_t \left(b^{(1,2)}_{\lambda,\boldsymbol{k}}\right)^{\dagger} = \left[\left(b^{(1,2)}_{\lambda,\boldsymbol{k}}\right)^{\dagger}, H\right], \tag{5.31d}$$

and only explicitly considering the quadratic terms of the Hamiltonian (5.7) the equations of motion for the distribution functions (5.29) and the phonon vacuum expectation values (5.30) can be derived. The contributions of the interaction terms can be included to the equations of motion by introducing collision integrals on their right-hand side, leading to the equations

$$\frac{d}{dt} f^{\pm}_{\boldsymbol{k},\sigma} = I^{\pm}_{\boldsymbol{k},\sigma}, \tag{5.32a}$$

$$\frac{d}{dt} \tilde{f}^{\pm}_{\boldsymbol{k},\sigma} = \tilde{I}^{\pm}_{\boldsymbol{k},\sigma}, \tag{5.32b}$$

$$\frac{d}{dt} n^{(1,2)}_{\boldsymbol{q},\lambda} = I^{(1,2)}_{\boldsymbol{q},\lambda}, \tag{5.32c}$$

$$\frac{d}{dt} \psi^{(1,2)}_{\boldsymbol{q},\lambda} + i\omega_{\boldsymbol{q},\lambda} \psi^{(1,2)}_{\boldsymbol{q},\lambda} = J^{(1,2)}_{\boldsymbol{q},\lambda}. \tag{5.32d}$$

Using the same diagrammatic method as in the previous two chapters 3 and 4, I apply a perturbative expansion in orders of the electron-phonon coupling constant and take into account collision terms that are of linear or quadratic order. Furthermore, I make a Markovian approximation for the collision integrals neglecting the history of the system. This procedure is the same as in the previous two chapters. Due to this approximation the imaginary parts of the collision integrals vanish which contain information about frequency renormalizations. It is shown below that in the exact expressions for the collision integrals $J^{(1,2)}_{\boldsymbol{q},\lambda}$ only two-point correlations appear so that they can be used without further approximations. The collision integrals $I^{\pm}_{\boldsymbol{k},\sigma}$ and $I^{(1,2)}_{\boldsymbol{q},\lambda}$ are real; the imaginary parts drop out exactly. Therefore, applying the Markovian approximation to these three types of collision integrals is viable. The collision integrals $\tilde{I}^{\pm}_{\boldsymbol{k},\sigma}$, however, are complex

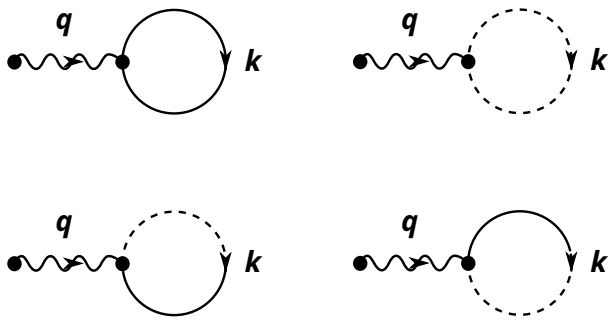

Figure 5.1: Diagrams representing the contributions to the collision integral $J^{(1)}_{\boldsymbol{q},\lambda}$ in the equation of motion of $\psi^{(1)}_{\boldsymbol{q},\lambda}(t)$. The wavy lines represent the annihilation operators for amplitude phonons $b^{(1)}_{\boldsymbol{q},\lambda}$ and the solid and dashed lines represent the fermionic operators $d^{+}_{\boldsymbol{k},\sigma}$ and $d^{-}_{\boldsymbol{k},\sigma}$ respectively. The dots represent interaction vertices and external vertices. The diagrams for the phase phonons have the same form.

valued. Applying the Markovian approximation here drops frequency renormalizations which are important to properly describe the collective modes. In order to be able take them into account I also calculate the purely imaginary valued principal values of the collision integrals $\tilde{I}^{\pm}_{\boldsymbol{k},\sigma}$.

5.3.1 Collision integrals for vacuum expectation values

From the diagrams shown in Fig. 5.1 I obtain the collision integrals

$$\begin{aligned} J^{(1)}_{\boldsymbol{q},\lambda} = \frac{i}{\sqrt{2\omega_{\boldsymbol{q},\lambda}\mathcal{V}}} \sum_{\boldsymbol{k},\sigma} \Bigg(& -\delta_{\boldsymbol{q},\boldsymbol{Q}} \Big[\left(\gamma^{++}_{\boldsymbol{q},\boldsymbol{k},\lambda}\right)^{*} f^{+}_{\boldsymbol{k},\sigma} - \left(\gamma^{--}_{\boldsymbol{q},\boldsymbol{k},\lambda}\right)^{*} f^{-}_{\boldsymbol{k},\sigma} \\ & + \left(\gamma^{+-}_{\boldsymbol{q},\boldsymbol{k},\lambda}\right)^{*} \tilde{f}^{+}_{\boldsymbol{k},\sigma} - \left(\gamma^{-+}_{\boldsymbol{q},\boldsymbol{k},\lambda}\right)^{*} \tilde{f}^{-}_{\boldsymbol{k},\sigma} \Big] \\ & + \delta_{\boldsymbol{q},-\boldsymbol{Q}} \Big[\left(\gamma^{++}_{-\boldsymbol{q},\boldsymbol{k},\lambda}\right)^{*} f^{+}_{\boldsymbol{k},\sigma} - \left(\gamma^{--}_{-\boldsymbol{q},\boldsymbol{k},\lambda}\right)^{*} f^{-}_{\boldsymbol{k},\sigma} \\ & + \left(\gamma^{+-}_{-\boldsymbol{q},\boldsymbol{k},\lambda}\right)^{*} \tilde{f}^{+}_{\boldsymbol{k},\sigma} - \left(\gamma^{-+}_{-\boldsymbol{q},\boldsymbol{k},\lambda}\right)^{*} \tilde{f}^{-}_{\boldsymbol{k},\sigma} \Big] \Bigg), \end{aligned} \tag{5.33a}$$

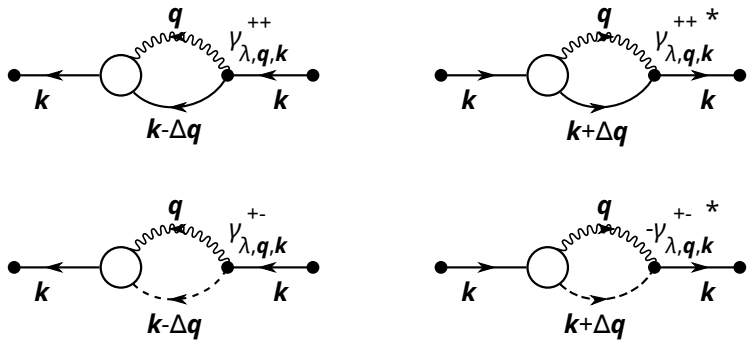

Figure 5.2: Diagrams representing the contributions to the collision integral $I^{+}_{\boldsymbol{k}}$. The symbols have the same meaning as in Fig. 5.1. The terms containing annihilation or creation operators for phase phonons have the same form and were thus left out. The diagrams contain three-point vertices represented by dots and three-point correlations represented by circles.

and

$$J^{(2)}_{\boldsymbol{q},\lambda} = \frac{1}{\sqrt{2\omega_{\boldsymbol{q},\lambda}\mathcal{V}}} \sum_{\boldsymbol{k},\sigma} \Bigg(-\delta_{\boldsymbol{q},\boldsymbol{Q}} \Big[\left(\gamma^{++}_{\boldsymbol{q},\boldsymbol{k},\lambda}\right)^{*} f^{+}_{\boldsymbol{k},\sigma} - \left(\gamma^{--}_{\boldsymbol{q},\boldsymbol{k},\lambda}\right)^{*} f^{-}_{\boldsymbol{k},\sigma} + \left(\gamma^{+-}_{\boldsymbol{q},\boldsymbol{k},\lambda}\right)^{*} \tilde{f}^{+}_{\boldsymbol{k},\sigma} - \left(\gamma^{-+}_{\boldsymbol{q},\boldsymbol{k},\lambda}\right)^{*} \tilde{f}^{-}_{\boldsymbol{k},\sigma} \Big] - \delta_{\boldsymbol{q},-\boldsymbol{Q}} \Big[\left(\gamma^{++}_{-\boldsymbol{q},\boldsymbol{k},\lambda}\right)^{*} f^{+}_{\boldsymbol{k},\sigma} - \left(\gamma^{--}_{-\boldsymbol{q},\boldsymbol{k},\lambda}\right)^{*} f^{-}_{\boldsymbol{k},\sigma} + \left(\gamma^{+-}_{-\boldsymbol{q},\boldsymbol{k},\lambda}\right)^{*} \tilde{f}^{+}_{\boldsymbol{k},\sigma} - \left(\gamma^{-+}_{-\boldsymbol{q},\boldsymbol{k},\lambda}\right)^{*} \tilde{f}^{-}_{\boldsymbol{k},\sigma} \Big] \Bigg). \tag{5.33b}$$

Note that these contributions can also be directly obtained from the Heisenberg equations of motion because the collision integrals contain only fermionic two-point correlations which coincide with two-point distribution functions for fermions.

5.3.2 Collision integrals for single-particle correlation functions

For the collision integrals contributing to the equations of motion of the distribution functions $f^{\pm}_{\boldsymbol{k}}$, $\tilde{f}^{\pm}_{\boldsymbol{k}}$, and $n^{(1/2)}_{\boldsymbol{k}}$ I obtain from the diagrams shown in Fig. 5.2, 5.3, and 5.4 the expressions

$$I^{\pm}_{\boldsymbol{k},\sigma} = \pm\frac{i}{\sqrt{\mathcal{V}}} \sum_{\boldsymbol{q},\lambda} \Big[\gamma^{\pm\pm}_{\boldsymbol{q},\boldsymbol{k},\lambda} \langle \left(d^{\pm}_{\boldsymbol{k}-\boldsymbol{q}+\boldsymbol{Q},\sigma}\right)^{\dagger} d^{\pm}_{\boldsymbol{k},\sigma} X_{\boldsymbol{q},\lambda} \rangle^{c} + \gamma^{\pm\mp}_{\boldsymbol{q},\boldsymbol{k},\lambda} \langle \left(d^{\mp}_{\boldsymbol{k}-\boldsymbol{q}+\boldsymbol{Q},\sigma}\right)^{\dagger} d^{\pm}_{\boldsymbol{k},\sigma} X_{\boldsymbol{q},\lambda} \rangle^{c} - \text{c.c.} \Big], \tag{5.34a}$$

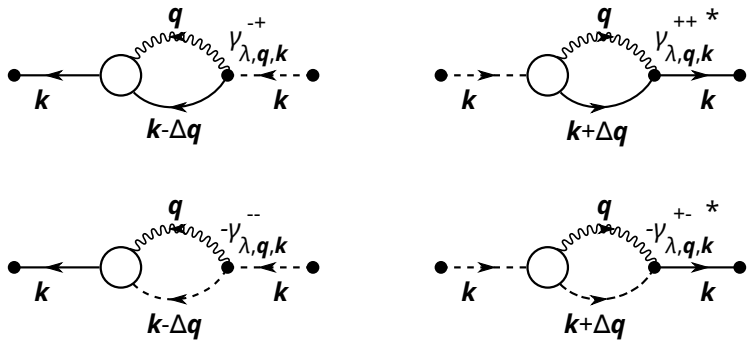

Figure 5.3: Diagrams representing the contributions to the collision integral $\tilde{I}^{+}_{\boldsymbol{k}}$. The symbols have the same meaning as in Fig. 5.1. The terms containing annihilation or creation operators for phase phonons have the same form and were thus left out. The diagrams contain three-point vertices represented by dots and three-point correlations represented by circles.

$$\tilde{I}^{\pm}_{\boldsymbol{k},\sigma} = \mp\frac{i}{\sqrt{\mathcal{V}}}\sum_{\boldsymbol{q},\lambda}\Big[\left(\gamma^{\pm\mp}_{\boldsymbol{q},\boldsymbol{k},\lambda}\right)^{*}\langle\left(d^{\mp}_{\boldsymbol{k},\sigma}\right)^{\dagger}d^{\mp}_{\boldsymbol{k}-\boldsymbol{q}+\boldsymbol{Q},\sigma}X_{\boldsymbol{q},\lambda}\rangle^{c} + \left(\gamma^{\pm\pm}_{\boldsymbol{q},\boldsymbol{k},\lambda}\right)^{*}\langle\left(d^{\mp}_{\boldsymbol{k},\sigma}\right)^{\dagger}d^{\pm}_{\boldsymbol{k}-\boldsymbol{q}+\boldsymbol{Q},\sigma}X_{\boldsymbol{q},\lambda}\rangle^{c}$$
$$+\gamma^{\mp\mp}_{\boldsymbol{q},\boldsymbol{k},\lambda}\langle\left(d^{\mp}_{\boldsymbol{k}-\boldsymbol{q}+\boldsymbol{Q},\sigma}\right)^{\dagger}d^{\pm}_{\boldsymbol{k},\sigma}X_{\boldsymbol{q},\lambda}\rangle^{c} + \gamma^{\mp\pm}_{\boldsymbol{q},\boldsymbol{k},\lambda}\langle\left(d^{\pm}_{\boldsymbol{k}-\boldsymbol{q}+\boldsymbol{Q},\sigma}\right)^{\dagger}d^{\pm}_{\boldsymbol{k},\sigma}X_{\boldsymbol{q},\lambda}\rangle^{c}\Big], \tag{5.34b}$$

$$I^{(1/2)}_{\boldsymbol{q},\lambda} = \frac{i}{\sqrt{V}}\sum_{\boldsymbol{k},\sigma,\alpha=\pm,\beta=\pm}\left[\alpha\left(\gamma^{\alpha\beta}_{\boldsymbol{q},\boldsymbol{k},\lambda}\right)^{*}\langle\left(d^{\beta}_{\boldsymbol{k},\sigma}\right)^{\dagger}d^{\alpha}_{\boldsymbol{k}-\boldsymbol{q}+\boldsymbol{Q},\sigma}b^{(1/2)}_{\boldsymbol{q},\lambda}\rangle^{c} - \text{c.c.}\right] \tag{5.34c}$$

These expressions contain three-point correlations so that it is necessary to derive the collision integrals for the three-point correlations appearing in the above collision integrals.

In order to obtain closed kinetic equations, the equations of motion of the three-point correlations represented by the diagrams shown in Fig. 5.5 are formally integrated and inserted into the collision integrals (5.34). To further simplify the collision integrals a Markovian approximation is applied neglecting the system's history. Note that the exact expressions for the three-point correlations have non-vanishing imaginary principal values. If the exact expressions are inserted into the collision integrals $I^{\pm}_{\boldsymbol{k},\sigma}$ and $I^{(1,2)}_{\boldsymbol{q},\lambda}$ the imaginary parts drop out. For the other two collision integrals $\tilde{I}^{\pm}_{\boldsymbol{k},\sigma}$ I calculate the principal values because these contributions represent the real part of the self-energy and are relevant for the frequency renormalization of the order parameter. The final result for the collision integrals can be obtained by inserting the three-point correlation functions into the collision integrals given by Eqs. (5.34). These expressions are lengthy and cumbersome to handle. They greatly simplify when they are linearized around the

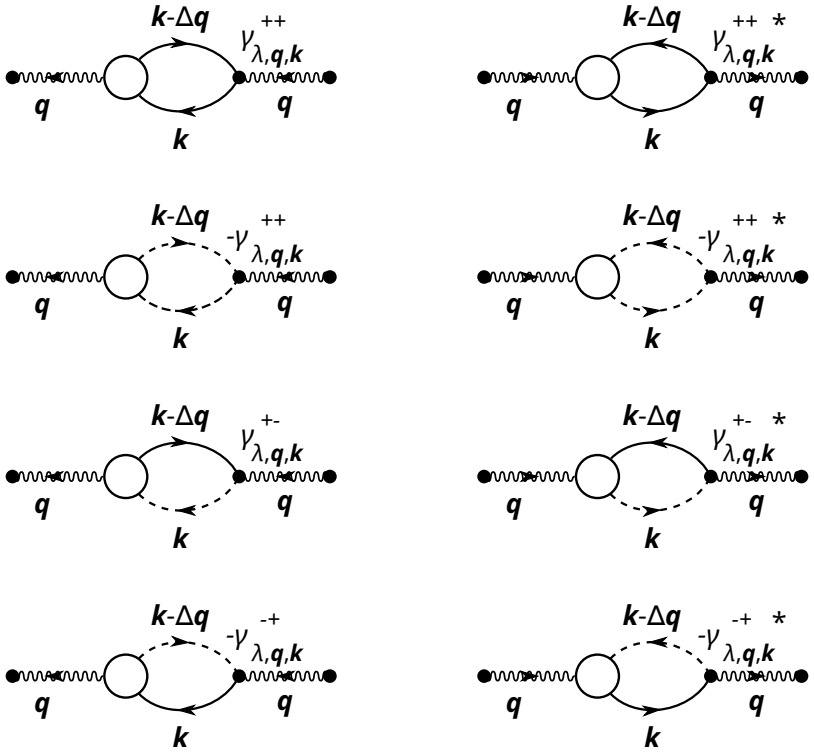

Figure 5.4: Diagrams representing the contributions to the amplitude mode collision integral $I^{(1)}_{\boldsymbol{q},\lambda}$. The symbols have the same meaning as in Fig. 5.1. Note that a prefactor of 2 appears because for each diagram there are two contributions that both lead to the same terms in the collision integral. The contributions to the phase mode collision integral $I^{(2)}_{\boldsymbol{q},\lambda}$ have the same form.

mean-field thermal equilibrium state which is done in section 5.5. The collision integrals

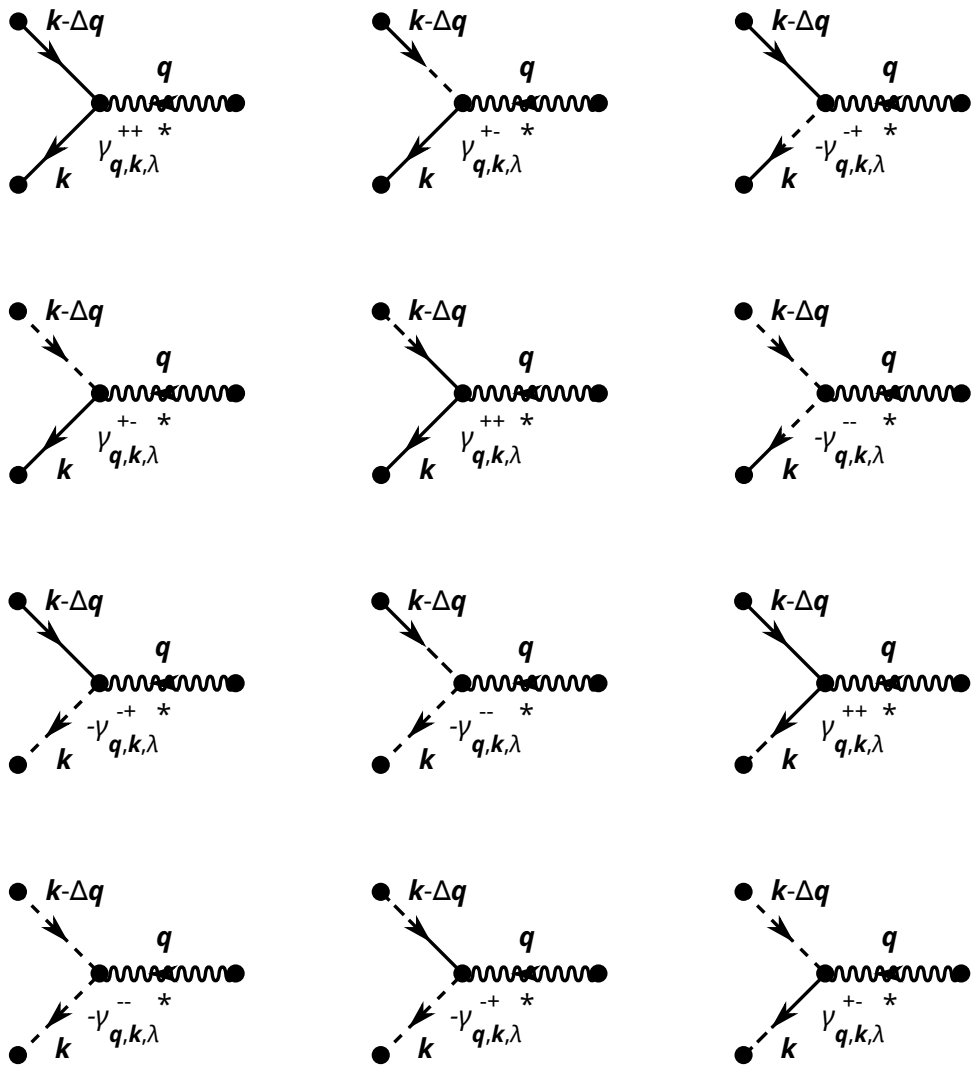

Figure 5.5: Diagrams contributing to the equation of motion of the three-point correlations $\langle\left(d^{+}_{\boldsymbol{k}-\boldsymbol{q}+\boldsymbol{Q},\sigma}\right)^{\dagger} d^{+}_{\boldsymbol{k},\sigma} b^{(1)}_{\boldsymbol{q},\lambda}\rangle^{c}$ (first line), $\langle\left(d^{-}_{\boldsymbol{k}-\boldsymbol{q}+\boldsymbol{Q},\sigma}\right)^{\dagger} d^{+}_{\boldsymbol{k},\sigma} b^{(1)}_{\boldsymbol{q},\lambda}\rangle^{c}$ (second line), $\langle\left(d^{+}_{\boldsymbol{k}-\boldsymbol{q}+\boldsymbol{Q},\sigma}\right)^{\dagger} d^{-}_{\boldsymbol{k},\sigma} b^{(1)}_{\boldsymbol{q},\lambda}\rangle^{c}$ (third line), and $\langle\left(d^{-}_{\boldsymbol{k}-\boldsymbol{q}+\boldsymbol{Q},\sigma}\right)^{\dagger} d^{-}_{\boldsymbol{k},\sigma} b^{(1)}_{\boldsymbol{q},\lambda}\rangle^{c}$ (fourth line). Here, I neglect diagrams that contain correlation bubbles because they lead to terms of higher order in the interaction vertices.

for the two fermionic distribution functions $f^{\pm}_{\boldsymbol{k},\sigma}$ and $\tilde{f}^{\pm}_{\boldsymbol{k},\sigma}$ are given by

$$
\begin{aligned}
I^{\pm}_{\boldsymbol{k},\sigma} = \pm\frac{\pi}{\mathcal{V}}\sum_{\boldsymbol{q},\lambda}\frac{|\gamma_{\boldsymbol{q},\lambda}|^2}{E_{\boldsymbol{k}}E_{\boldsymbol{k}-\boldsymbol{q}+\boldsymbol{Q}}}\mathrm{Re}\Bigg[&\delta\left(E_{\boldsymbol{k}-\boldsymbol{q}+\boldsymbol{Q}}-E_{\boldsymbol{k}}-\omega_{\boldsymbol{q},\lambda}\right)\\
&\times\Bigg(\left[E_{\boldsymbol{k}}+\xi_{\boldsymbol{k}}\right]\left[E_{\boldsymbol{k}-\boldsymbol{q}+\boldsymbol{Q}}-\xi_{\boldsymbol{k}-\boldsymbol{q}+\boldsymbol{Q}}\right]\\
&\times\left[\left(1-f^{\pm}_{\boldsymbol{k}-\boldsymbol{q}+\boldsymbol{Q},\sigma}\right)f^{\pm}_{\boldsymbol{k},\sigma}n_{\boldsymbol{q},\lambda}-f^{\pm}_{\boldsymbol{k}-\boldsymbol{q}+\boldsymbol{Q},\sigma}\left(1-f^{\pm}_{\boldsymbol{k},\sigma}\right)\left(1+n_{\boldsymbol{q},\lambda}\right)\right]\\
&+\Delta\left[E_{\boldsymbol{k}}+\xi_{\boldsymbol{k}}\right]\tilde{f}^{\pm}_{\boldsymbol{k}-\boldsymbol{q}+\boldsymbol{Q},\sigma}\left[f^{\pm}_{\boldsymbol{k},\sigma}n_{\boldsymbol{q},\lambda}+\left(1-f^{\pm}_{\boldsymbol{k},\sigma}\right)\left(1+n_{\boldsymbol{q},\lambda}\right)\right]\\
&-\Delta^{*}\left[E_{\boldsymbol{k}-\boldsymbol{q}+\boldsymbol{Q}}-\xi_{\boldsymbol{k}-\boldsymbol{q}+\boldsymbol{Q}}\right]\tilde{f}^{\mp}_{\boldsymbol{k},\sigma}\left[\left(1-f^{\pm}_{\boldsymbol{k}-\boldsymbol{q}+\boldsymbol{Q},\sigma}\right)n_{\boldsymbol{q},\lambda}+f^{\pm}_{\boldsymbol{k}-\boldsymbol{q}+\boldsymbol{Q},\sigma}\left(1+n_{\boldsymbol{q},\lambda}\right)\right]\Bigg)\\
&-\delta\left(E_{\boldsymbol{k}-\boldsymbol{q}+\boldsymbol{Q}}-E_{\boldsymbol{k}}+\omega_{\boldsymbol{q},\lambda}\right)\Bigg(\left[E_{\boldsymbol{k}}+\xi_{\boldsymbol{k}}\right]\left[E_{\boldsymbol{k}-\boldsymbol{q}+\boldsymbol{Q}}-\xi_{\boldsymbol{k}-\boldsymbol{q}+\boldsymbol{Q}}\right]\\
&\times\left[\left(1-f^{\pm}_{\boldsymbol{k}-\boldsymbol{q}+\boldsymbol{Q},\sigma}\right)f^{\pm}_{\boldsymbol{k},\sigma}\left(1+n_{-\boldsymbol{q},\lambda}\right)-f^{\pm}_{\boldsymbol{k}-\boldsymbol{q}+\boldsymbol{Q},\sigma}\left(1-f^{\pm}_{\boldsymbol{k},\sigma}\right)n_{-\boldsymbol{q},\lambda}\right]\\
&+\Delta\left[E_{\boldsymbol{k}}+\xi_{\boldsymbol{k}}\right]\tilde{f}^{\pm}_{\boldsymbol{k}-\boldsymbol{q}+\boldsymbol{Q},\sigma}\left[f^{\pm}_{\boldsymbol{k},\sigma}\left(1+n_{-\boldsymbol{q},\lambda}\right)+\left(1-f^{\pm}_{\boldsymbol{k},\sigma}\right)n_{-\boldsymbol{q},\lambda}\right]\\
&-\Delta^{*}\left[E_{\boldsymbol{k}-\boldsymbol{q}+\boldsymbol{Q}}-\xi_{\boldsymbol{k}-\boldsymbol{q}+\boldsymbol{Q}}\right]\tilde{f}^{\mp}_{\boldsymbol{k},\sigma}\left[\left(1-f^{\pm}_{\boldsymbol{k}-\boldsymbol{q}+\boldsymbol{Q},\sigma}\right)\left(1+n_{-\boldsymbol{q},\lambda}\right)+f^{\pm}_{\boldsymbol{k}-\boldsymbol{q}+\boldsymbol{Q},\sigma}n_{-\boldsymbol{q},\lambda}\right]\Bigg)\\
&-\delta\left(E_{\boldsymbol{k}-\boldsymbol{q}+\boldsymbol{Q}}+E_{\boldsymbol{k}}-\omega_{\boldsymbol{q},\lambda}\right)\Bigg(\left[E_{\boldsymbol{k}}+\xi_{\boldsymbol{k}}\right]\left[E_{\boldsymbol{k}-\boldsymbol{q}+\boldsymbol{Q}}+\xi_{\boldsymbol{k}-\boldsymbol{q}+\boldsymbol{Q}}\right]\\
&\times\left[\left(1-f^{\mp}_{\boldsymbol{k}-\boldsymbol{q}+\boldsymbol{Q},\sigma}\right)f^{\pm}_{\boldsymbol{k},\sigma}\left(1+n_{-\boldsymbol{q},\lambda}\right)-f^{\mp}_{\boldsymbol{k}-\boldsymbol{q}+\boldsymbol{Q},\sigma}\left(1-f^{\pm}_{\boldsymbol{k},\sigma}\right)n_{-\boldsymbol{q},\lambda}\right]\\
&+\Delta^{*}\left[E_{\boldsymbol{k}}+\xi_{\boldsymbol{k}}\right]\tilde{f}^{\mp}_{\boldsymbol{k}-\boldsymbol{q}+\boldsymbol{Q},\sigma}\left[f^{\pm}_{\boldsymbol{k},\sigma}\left(1+n_{-\boldsymbol{q},\lambda}\right)+\left(1-f^{\pm}_{\boldsymbol{k},\sigma}\right)n_{-\boldsymbol{q},\lambda}\right]\\
&-\Delta^{*}\left[E_{\boldsymbol{k}-\boldsymbol{q}+\boldsymbol{Q}}+\xi_{\boldsymbol{k}-\boldsymbol{q}+\boldsymbol{Q}}\right]\tilde{f}^{\mp}_{\boldsymbol{k},\sigma}\left[\left(1-f^{\mp}_{\boldsymbol{k}-\boldsymbol{q}+\boldsymbol{Q},\sigma}\right)\left(1+n_{-\boldsymbol{q},\lambda}\right)+f^{\mp}_{\boldsymbol{k}-\boldsymbol{q}+\boldsymbol{Q},\sigma}n_{-\boldsymbol{q},\lambda}\right]\Bigg)\Bigg],
\end{aligned}
\tag{5.35a}
$$

$$
\begin{aligned}
\tilde{I}^{\pm}_{\boldsymbol{k},\sigma} = \frac{\pi}{N}\sum_{\boldsymbol{q},\lambda}\left|\gamma_{\boldsymbol{q},\lambda}\right|^2 \frac{1}{E_{\boldsymbol{k}}E_{\boldsymbol{k}-\boldsymbol{q}+\boldsymbol{Q}}}\Bigg[\delta\left(E_{\boldsymbol{k}-\boldsymbol{q}+\boldsymbol{Q}}-E_{\boldsymbol{k}}+\omega_{\boldsymbol{q},\lambda}\right)\Bigg(\Delta^{\pm}\left[E_{\boldsymbol{k}-\boldsymbol{q}+\boldsymbol{Q}}+\xi_{\boldsymbol{k}-\boldsymbol{q}+\boldsymbol{Q}}\right] \\
\times\left[\left(1-f^{\mp}_{\boldsymbol{k}-\boldsymbol{q}+\boldsymbol{Q},\sigma}\right)f^{\mp}_{\boldsymbol{k},\sigma}n_{\boldsymbol{q},\lambda}-f^{\mp}_{\boldsymbol{k}-\boldsymbol{q}+\boldsymbol{Q},\sigma}\left(1-f^{\mp}_{\boldsymbol{k},\sigma}\right)\left(1+n_{\boldsymbol{q},\lambda}\right)\right] \\
+\left(\Delta^{\pm}\right)^2\left(\tilde{f}^{\mp}_{\boldsymbol{k}-\boldsymbol{q}+\boldsymbol{Q},\sigma}\right)^*\left[f^{\mp}_{\boldsymbol{k},\sigma}n_{\boldsymbol{q},\lambda}+\left(1-f^{\mp}_{\boldsymbol{k},\sigma}\right)\left(1+n_{\boldsymbol{q},\lambda}\right)\right] \\
-\left[E_{\boldsymbol{k}}+\xi_{\boldsymbol{k}}\right]\left[E_{\boldsymbol{k}-\boldsymbol{q}+\boldsymbol{Q}}+\xi_{\boldsymbol{k}-\boldsymbol{q}+\boldsymbol{Q}}\right]\left(\tilde{f}^{\pm}_{\boldsymbol{k},\sigma}\right)^*\left[\left(1-f^{\mp}_{\boldsymbol{k}-\boldsymbol{q}+\boldsymbol{Q},\sigma}\right)n_{\boldsymbol{q},\lambda}+f^{\mp}_{\boldsymbol{k}-\boldsymbol{q}+\boldsymbol{Q},\sigma}\left(1+n_{\boldsymbol{q},\lambda}\right)\right] \\
+\Delta^{\pm}\left[E_{\boldsymbol{k}-\boldsymbol{q}+\boldsymbol{Q}}-\xi_{\boldsymbol{k}-\boldsymbol{q}+\boldsymbol{Q}}\right]\left[\left(1-f^{\pm}_{\boldsymbol{k}-\boldsymbol{q}+\boldsymbol{Q},\sigma}\right)f^{\pm}_{\boldsymbol{k},\sigma}\left(1+n_{-\boldsymbol{q},\lambda}\right)-f^{\pm}_{\boldsymbol{k}-\boldsymbol{q}+\boldsymbol{Q},\sigma}\left(1-f^{\pm}_{\boldsymbol{k},\sigma}\right)n_{-\boldsymbol{q},\lambda}\right] \\
+\left(\Delta^{\pm}\right)^2\tilde{f}^{\pm}_{\boldsymbol{k}-\boldsymbol{q}+\boldsymbol{Q},\sigma}\left[f^{\pm}_{\boldsymbol{k},\sigma}\left(1+n_{-\boldsymbol{q},\lambda}\right)+\left(1-f^{\pm}_{\boldsymbol{k},\sigma}\right)n_{-\boldsymbol{q},\lambda}\right] \\
-\left[E_{\boldsymbol{k}}-\xi_{\boldsymbol{k}}\right]\left[E_{\boldsymbol{k}-\boldsymbol{q}+\boldsymbol{Q}}-\xi_{\boldsymbol{k}-\boldsymbol{q}+\boldsymbol{Q}}\right]\tilde{f}^{\mp}_{\boldsymbol{k},\sigma}\left[\left(1-f^{\pm}_{\boldsymbol{k}-\boldsymbol{q}+\boldsymbol{Q},\sigma}\right)\left(1+n_{-\boldsymbol{q},\lambda}\right)+f^{\pm}_{\boldsymbol{k}-\boldsymbol{q}+\boldsymbol{Q},\sigma}n_{-\boldsymbol{q},\lambda}\right]\Bigg) \\
-\delta\left(E_{\boldsymbol{k}-\boldsymbol{q}+\boldsymbol{Q}}-E_{\boldsymbol{k}}-\omega_{\boldsymbol{q},\lambda}\right)\Bigg(\Delta^{\pm}\left[E_{\boldsymbol{k}-\boldsymbol{q}+\boldsymbol{Q}}+\xi_{\boldsymbol{k}-\boldsymbol{q}+\boldsymbol{Q}}\right] \\
\times\left[\left(1-f^{\mp}_{\boldsymbol{k}-\boldsymbol{q}+\boldsymbol{Q},\sigma}\right)f^{\mp}_{\boldsymbol{k},\sigma}\left(1+n_{-\boldsymbol{q},\lambda}\right)-f^{\mp}_{\boldsymbol{k}-\boldsymbol{q}+\boldsymbol{Q},\sigma}\left(1-f^{\mp}_{\boldsymbol{k},\sigma}\right)n_{-\boldsymbol{q},\lambda}\right] \\
+\left(\Delta^{\pm}\right)^2\left(\tilde{f}^{\mp}_{\boldsymbol{k}-\boldsymbol{q}+\boldsymbol{Q},\sigma}\right)^*\left[f^{\mp}_{\boldsymbol{k},\sigma}\left(1+n_{-\boldsymbol{q},\lambda}\right)+\left(1-f^{\mp}_{\boldsymbol{k},\sigma}\right)n_{-\boldsymbol{q},\lambda}\right] \\
-\left[E_{\boldsymbol{k}}+\xi_{\boldsymbol{k}}\right]\left[E_{\boldsymbol{k}-\boldsymbol{q}+\boldsymbol{Q}}+\xi_{\boldsymbol{k}-\boldsymbol{q}+\boldsymbol{Q}}\right]\left(\tilde{f}^{\pm}\right)^*\left[\left(1-f^{\mp}_{\boldsymbol{k}-\boldsymbol{q}+\boldsymbol{Q},\sigma}\right)\left(1+n_{-\boldsymbol{q},\lambda}\right)+f^{\mp}_{\boldsymbol{k}-\boldsymbol{q}+\boldsymbol{Q},\sigma}n_{-\boldsymbol{q},\lambda}\right] \\
+\Delta^{\pm}\left[E_{\boldsymbol{k}-\boldsymbol{q}+\boldsymbol{Q}}-\xi_{\boldsymbol{k}-\boldsymbol{q}+\boldsymbol{Q}}\right]\left[\left(1-f^{\pm}_{\boldsymbol{k}-\boldsymbol{q}+\boldsymbol{Q},\sigma}\right)f^{\pm}_{\boldsymbol{k},\sigma}n_{\boldsymbol{q},\lambda}-f^{\pm}_{\boldsymbol{k}-\boldsymbol{q}+\boldsymbol{Q},\sigma}\left(1-f^{\pm}_{\boldsymbol{k},\sigma}\right)\left(1+n_{\boldsymbol{q},\lambda}\right)\right] \\
+\left(\Delta^{\pm}\right)^2\tilde{f}^{\pm}_{\boldsymbol{k}-\boldsymbol{q}+\boldsymbol{Q},\sigma}\left[f^{\pm}_{\boldsymbol{k},\sigma}n_{\boldsymbol{q},\lambda}+\left(1-f^{\pm}_{\boldsymbol{k},\sigma}\right)\left(1+n_{\boldsymbol{q},\lambda}\right)\right] \\
-\left[E_{\boldsymbol{k}}-\xi_{\boldsymbol{k}}\right]\left[E_{\boldsymbol{k}-\boldsymbol{q}+\boldsymbol{Q}}-\xi_{\boldsymbol{k}-\boldsymbol{q}+\boldsymbol{Q}}\right]\tilde{f}^{\mp}_{\boldsymbol{k},\sigma}\left[\left(1-f^{\pm}_{\boldsymbol{k}-\boldsymbol{q}+\boldsymbol{Q},\sigma}\right)n_{\boldsymbol{q},\lambda}+f^{\pm}_{\boldsymbol{k}-\boldsymbol{q}+\boldsymbol{Q},\sigma}\left(1+n_{\boldsymbol{q},\lambda}\right)\right]\Bigg) \\
+\delta\left(E_{\boldsymbol{k}-\boldsymbol{q}+\boldsymbol{Q}}+E_{\boldsymbol{k}}-\omega_{\boldsymbol{q},\lambda}\right)\Bigg(\Delta^{\pm}\left[E_{\boldsymbol{k}-\boldsymbol{q}+\boldsymbol{Q}}+\xi_{\boldsymbol{k}-\boldsymbol{q}+\boldsymbol{Q}}\right] \\
\times\left[\left(1-f^{\mp}_{\boldsymbol{k}-\boldsymbol{q}+\boldsymbol{Q},\sigma}\right)f^{\pm}_{\boldsymbol{k},\sigma}\left(1+n_{-\boldsymbol{q},\lambda}\right)-f^{\mp}_{\boldsymbol{k}-\boldsymbol{q}+\boldsymbol{Q},\sigma}\left(1-f^{\pm}_{\boldsymbol{k},\sigma}\right)n_{-\boldsymbol{q},\lambda}\right] \\
+\left|\Delta\right|^2\tilde{f}^{\mp}_{\boldsymbol{k}-\boldsymbol{q}+\boldsymbol{Q},\sigma}\left[f^{\pm}_{\boldsymbol{k},\sigma}\left(1+n_{\boldsymbol{q},\lambda}\right)+\left(1-f^{\pm}_{\boldsymbol{k},\sigma}\right)n_{-\boldsymbol{q},\lambda}\right] \\
-\left[E_{\boldsymbol{k}}-\xi_{\boldsymbol{k}}\right]\left[E_{\boldsymbol{k}-\boldsymbol{q}+\boldsymbol{Q}}+\xi_{\boldsymbol{k}-\boldsymbol{q}+\boldsymbol{Q}}\right]\tilde{f}^{\mp}_{\boldsymbol{k},\sigma}\left[\left(1-f^{\mp}_{\boldsymbol{k}-\boldsymbol{q}+\boldsymbol{Q},\sigma}\right)\left(1+n_{-\boldsymbol{q},\lambda}\right)+f^{\mp}_{\boldsymbol{k}-\boldsymbol{q}+\boldsymbol{Q},\sigma}n_{-\boldsymbol{q},\lambda}\right] \\
+\Delta^{\pm}\left[E_{\boldsymbol{k}-\boldsymbol{q}+\boldsymbol{Q}}-\xi_{\boldsymbol{k}-\boldsymbol{q}+\boldsymbol{Q}}\right]\left[\left(1-f^{\pm}_{\boldsymbol{k}-\boldsymbol{q}+\boldsymbol{Q},\sigma}\right)f^{\mp}_{\boldsymbol{k},\sigma}n_{\boldsymbol{q},\lambda}-f^{\pm}_{\boldsymbol{k}-\boldsymbol{q}+\boldsymbol{Q},\sigma}\left(1-f^{\mp}_{\boldsymbol{k},\sigma}\right)\left(1+n_{\boldsymbol{q},\lambda}\right)\right] \\
+\left|\Delta\right|^2\left(\tilde{f}^{\pm}_{\boldsymbol{k}-\boldsymbol{q}+\boldsymbol{Q},\sigma}\right)^*\left[f^{\mp}_{\boldsymbol{k},\sigma}n_{\boldsymbol{q},\lambda}+\left(1-f^{\mp}_{\boldsymbol{k},\sigma}\right)\left(1+n_{\boldsymbol{q},\lambda}\right)\right] \\
-\left[E_{\boldsymbol{k}}+\xi_{\boldsymbol{k}}\right]\left[E_{\boldsymbol{k}-\boldsymbol{q}+\boldsymbol{Q}}-\xi_{\boldsymbol{k}-\boldsymbol{q}+\boldsymbol{Q}}\right]\left(\tilde{f}^{\pm}_{\boldsymbol{k},\sigma}\right)^*\left[\left(1-f^{\pm}_{\boldsymbol{k}-\boldsymbol{q}+\boldsymbol{Q},\sigma}\right)n_{\boldsymbol{q},\lambda}\right. \\
\left.+f^{\pm}_{\boldsymbol{k}-\boldsymbol{q}+\boldsymbol{Q},\sigma}\left(1+n_{\boldsymbol{q},\lambda}\right)\right]\Bigg)\Bigg],
\end{aligned}
\tag{5.35b}
$$

with

$$n_{\boldsymbol{q},\lambda} = \frac{1}{2}\left(n^{(1)}_{\boldsymbol{q},\lambda} + n^{(2)}_{\boldsymbol{q},\lambda}\right), \tag{5.36}$$

and

$$\Delta^{+} = \Delta; \quad \Delta^{-} = \Delta^{*}. \tag{5.37}$$

For the bosonic distribution functions I get

$$\begin{aligned}
I^{(1/2)}_{\boldsymbol{q},\lambda} = \frac{\pi}{N}\sum_{\boldsymbol{k},\sigma}\frac{|\gamma_{\boldsymbol{q},\lambda}|^2}{E_{\boldsymbol{k}}E_{\boldsymbol{k}-\boldsymbol{q}+\boldsymbol{Q}}}\mathrm{Re}\Bigg[\delta\left(E_{\boldsymbol{k}-\boldsymbol{q}+\boldsymbol{Q}} - E_{\boldsymbol{k}} - \omega_{\boldsymbol{q},\lambda}\right)\Bigg(\left[E_{\boldsymbol{k}} - \xi_{\boldsymbol{k}}\right]\left[E_{\boldsymbol{k}-\boldsymbol{q}+\boldsymbol{Q}} + \xi_{\boldsymbol{k}-\boldsymbol{q}+\boldsymbol{Q}}\right] \\
\times\left[\left(1 - f^{-}_{\boldsymbol{k}-\boldsymbol{q}+\boldsymbol{Q},\sigma}\right)f^{-}_{\boldsymbol{k},\sigma}\left(1 + n^{(1/2)}_{-\boldsymbol{q},\lambda}\right) - f^{-}_{\boldsymbol{k}-\boldsymbol{q}+\boldsymbol{Q},\sigma}\left(1 - f^{-}_{\boldsymbol{k},\sigma}\right)n^{(1/2)}_{-\boldsymbol{q},\lambda}\right] \\
+\Delta\left[E_{\boldsymbol{k}} - \xi_{\boldsymbol{k}}\right]\tilde{f}^{-}_{\boldsymbol{k}-\boldsymbol{q}+\boldsymbol{Q},\sigma}\left[f^{-}_{\boldsymbol{k},\sigma}\left(1 + n^{(1/2)}_{-\boldsymbol{q},\lambda}\right) + \left(1 - f^{-}_{\boldsymbol{k},\sigma}\right)n^{(1/2)}_{-\boldsymbol{q},\lambda}\right] \\
-\Delta^{*}\left[E_{\boldsymbol{k}-\boldsymbol{q}+\boldsymbol{Q}} + \xi_{\boldsymbol{k}-\boldsymbol{q}+\boldsymbol{Q}}\right]\tilde{f}^{+}_{\boldsymbol{k},\sigma}\left[\left(1 - f^{-}_{\boldsymbol{k}-\boldsymbol{q}+\boldsymbol{Q},\sigma}\right)\left(1 + n^{(1/2)}_{-\boldsymbol{q},\lambda}\right) + f^{-}_{\boldsymbol{k}-\boldsymbol{q}+\boldsymbol{Q},\sigma}n^{(1/2)}_{-\boldsymbol{q},\lambda}\right] \\
-\left|\Delta\right|^2\tilde{f}^{-}_{\boldsymbol{k}-\boldsymbol{q}+\boldsymbol{Q},\sigma}\tilde{f}^{+}_{\boldsymbol{k},\sigma}\Bigg) - \delta\left(E_{\boldsymbol{k}-\boldsymbol{q}+\boldsymbol{Q}} - E_{\boldsymbol{k}} + \omega_{\boldsymbol{q},\lambda}\right)\Bigg(\left[E_{\boldsymbol{k}} + \xi_{\boldsymbol{k}}\right]\left[E_{\boldsymbol{k}-\boldsymbol{q}+\boldsymbol{Q}} - \xi_{\boldsymbol{k}-\boldsymbol{q}+\boldsymbol{Q}}\right] \\
\times\left[\left(1 - f^{+}_{\boldsymbol{k}-\boldsymbol{q}+\boldsymbol{Q},\sigma}\right)f^{+}_{\boldsymbol{k},\sigma}\left(1 + n^{(1/2)}_{-\boldsymbol{q},\lambda}\right) - f^{+}_{\boldsymbol{k}-\boldsymbol{q}+\boldsymbol{Q},\sigma}\left(1 - f^{+}_{\boldsymbol{k},\sigma}\right)n^{(1/2)}_{-\boldsymbol{q},\lambda}\right] \\
+\Delta\left[E_{\boldsymbol{k}} + \xi_{\boldsymbol{k}}\right]\tilde{f}^{+}_{\boldsymbol{k}-\boldsymbol{q}+\boldsymbol{Q},\sigma}\left[f^{+}_{\boldsymbol{k},\sigma}\left(1 + n^{(1/2)}_{-\boldsymbol{q},\lambda}\right) + \left(1 - f^{+}_{\boldsymbol{k},\sigma}\right)n^{(1/2)}_{-\boldsymbol{q},\lambda}\right] \\
-\Delta^{*}\left[E_{\boldsymbol{k}-\boldsymbol{q}+\boldsymbol{Q}} - \xi_{\boldsymbol{k}-\boldsymbol{q}+\boldsymbol{Q}}\right]\tilde{f}^{-}_{\boldsymbol{k},\sigma}\left[\left(1 - f^{+}_{\boldsymbol{k}-\boldsymbol{q}+\boldsymbol{Q},\sigma}\right)\left(1 + n^{(1/2)}_{-\boldsymbol{q},\lambda}\right) + f^{+}_{\boldsymbol{k}-\boldsymbol{q}+\boldsymbol{Q},\sigma}n^{(1/2)}_{-\boldsymbol{q},\lambda}\right] \\
-\left|\Delta\right|^2\tilde{f}^{+}_{\boldsymbol{k}-\boldsymbol{q}+\boldsymbol{Q},\sigma}\tilde{f}^{-}_{\boldsymbol{k},\sigma}\Bigg) - \delta\left(E_{\boldsymbol{k}-\boldsymbol{q}+\boldsymbol{Q}} + E_{\boldsymbol{k}} - \omega_{\boldsymbol{q},\lambda}\right) \\
\times\Bigg(\Delta^2\left[\left(1 - f^{-}_{\boldsymbol{k}-\boldsymbol{q}+\boldsymbol{Q},\sigma}\right)f^{+}_{\boldsymbol{k},\sigma}\left(1 + n^{(1/2)}_{-\boldsymbol{q},\lambda}\right) - f^{-}_{\boldsymbol{k}-\boldsymbol{q}+\boldsymbol{Q},\sigma}\left(1 - f^{+}_{\boldsymbol{k},\sigma}\right)n^{(1/2)}_{-\boldsymbol{q},\lambda}\right] \\
+\Delta\left[E_{\boldsymbol{k}} - \xi_{\boldsymbol{k}}\right]\tilde{f}^{-}_{\boldsymbol{k}-\boldsymbol{q}+\boldsymbol{Q},\sigma}\left[f^{+}_{\boldsymbol{k},\sigma}\left(1 + n^{(1/2)}_{-\boldsymbol{q},\lambda}\right) + \left(1 - f^{+}_{\boldsymbol{k},\sigma}\right)n^{(1/2)}_{-\boldsymbol{q},\lambda}\right] \\
-\Delta\left[E_{\boldsymbol{k}-\boldsymbol{q}+\boldsymbol{Q}} - \xi_{\boldsymbol{k}-\boldsymbol{q}+\boldsymbol{Q}}\right]\tilde{f}^{-}_{\boldsymbol{k},\sigma}\left[\left(1 - f^{-}_{\boldsymbol{k}-\boldsymbol{q}+\boldsymbol{Q},\sigma}\right)\left(1 + n^{(1/2)}_{-\boldsymbol{q},\lambda}\right) + f^{-}_{\boldsymbol{k}-\boldsymbol{q}+\boldsymbol{Q},\sigma}n^{(1/2)}_{-\boldsymbol{q},\lambda}\right] \\
-\left[E_{\boldsymbol{k}} - \xi_{\boldsymbol{k}}\right]\left[E_{\boldsymbol{k}-\boldsymbol{q}+\boldsymbol{Q}} - \xi_{\boldsymbol{k}-\boldsymbol{q}+\boldsymbol{Q}}\right]\tilde{f}^{-}_{\boldsymbol{k}-\boldsymbol{q}+\boldsymbol{Q},\sigma}\tilde{f}^{-}_{\boldsymbol{k},\sigma}\Bigg)\Bigg].
\end{aligned} \tag{5.38}$$

Now, the principal values of the three-point correlations need to be calculated. Note that the principal values of the three-point correlations are real valued. When inserted into the collision integrals $\tilde{I}^{+}_{\boldsymbol{k},\sigma}$ and $\tilde{I}^{-}_{\boldsymbol{k},\sigma}$ purely imaginary terms are generated. They are

given by

$$
\begin{aligned}
\mathrm{pV}\tilde{I}^{\pm}_{\boldsymbol{k},\sigma} = \frac{i}{4N}\sum_{\boldsymbol{q},\lambda}|\gamma_{\boldsymbol{q},\lambda}|^2\Bigg[&\frac{1}{E_{\boldsymbol{k}-\boldsymbol{q}+\boldsymbol{Q}}+E_{\boldsymbol{k}}+\omega_{\boldsymbol{q},\lambda}}\Bigg(-\frac{\Delta^{\pm}}{E_{\boldsymbol{k}}}\frac{E_{\boldsymbol{k}-\boldsymbol{q}+\boldsymbol{Q}}-\xi_{\boldsymbol{k}-\boldsymbol{q}+\boldsymbol{Q}}}{E_{\boldsymbol{k}-\boldsymbol{q}+\boldsymbol{Q}}}\\
&\times\Big[\big(1-f^{\pm}_{\boldsymbol{k}-\boldsymbol{q}+\boldsymbol{Q},\sigma}\big)f^{\mp}_{\boldsymbol{k},\sigma}\big(1+n_{-\boldsymbol{q},\lambda}\big)-f^{\pm}_{\boldsymbol{k}-\boldsymbol{q}+\boldsymbol{Q},\sigma}\big(1-f^{\mp}_{\boldsymbol{k},\sigma}\big)n_{-\boldsymbol{q},\lambda}\Big]\\
&-\frac{|\Delta|^2}{E_{\boldsymbol{k}}E_{\boldsymbol{k}-\boldsymbol{q}+\boldsymbol{Q}}}\left(\tilde{f}^{\pm}_{\boldsymbol{k}-\boldsymbol{q}+\boldsymbol{Q},\sigma}\right)^*\Big[f^{\mp}_{\boldsymbol{k},\sigma}\left(1+n_{-\boldsymbol{q},\lambda}\right)+\left(1-f^{\mp}_{\boldsymbol{k},\sigma}\right)n_{-\boldsymbol{q},\lambda}\Big]\\
&+\frac{E_{\boldsymbol{k}}+\xi_{\boldsymbol{k}}}{E_{\boldsymbol{k}}}\frac{E_{\boldsymbol{k}-\boldsymbol{q}+\boldsymbol{Q}}-\xi_{\boldsymbol{k}-\boldsymbol{q}+\boldsymbol{Q}}}{E_{\boldsymbol{k}-\boldsymbol{q}+\boldsymbol{Q}}}\left(\tilde{f}^{\pm}_{\boldsymbol{k},\sigma}\right)^*\Big[\left(1-f^{\pm}_{\boldsymbol{k}-\boldsymbol{q}+\boldsymbol{Q},\sigma}\right)\left(1+n_{-\boldsymbol{q},\lambda}\right)+f^{\pm}_{\boldsymbol{k}-\boldsymbol{q}+\boldsymbol{Q},\sigma}n_{-\boldsymbol{q},\lambda}\Big]\\
&-\frac{E_{\boldsymbol{k}}+\xi_{\boldsymbol{k}}}{E_{\boldsymbol{k}}}\frac{\Delta^{\mp}}{E_{\boldsymbol{k}-\boldsymbol{q}+\boldsymbol{Q}}}\left(\tilde{f}^{\pm}_{\boldsymbol{k}-\boldsymbol{q}+\boldsymbol{Q},\sigma}\right)^*\left(\tilde{f}^{\pm}_{\boldsymbol{k},\sigma}\right)^*\\
&+\frac{\Delta^{\pm}}{E_{\boldsymbol{k}}}\frac{E_{\boldsymbol{k}-\boldsymbol{q}+\boldsymbol{Q}}+\xi_{\boldsymbol{k}-\boldsymbol{q}+\boldsymbol{Q}}}{E_{\boldsymbol{k}-\boldsymbol{q}+\boldsymbol{Q}}}\Big[\big(1-f^{\mp}_{\boldsymbol{k}-\boldsymbol{q}+\boldsymbol{Q},\sigma}\big)f^{\pm}_{\boldsymbol{k},\sigma}n_{\boldsymbol{q},\lambda}-f^{\mp}_{\boldsymbol{k}-\boldsymbol{q}+\boldsymbol{Q},\sigma}\big(1-f^{\pm}_{\boldsymbol{k},\sigma}\big)\big(1+n_{\boldsymbol{q},\lambda}\big)\Big]\\
&+\frac{|\Delta|^2}{E_{\boldsymbol{k}}E_{\boldsymbol{k}-\boldsymbol{q}+\boldsymbol{Q}}}\tilde{f}^{\mp}_{\boldsymbol{k}-\boldsymbol{q}+\boldsymbol{Q},\sigma}\Big[f^{\pm}_{\boldsymbol{k},\sigma}n_{\boldsymbol{q},\lambda}-\left(1-f^{\pm}_{\boldsymbol{k},\sigma}\right)\left(1+n_{\boldsymbol{q},\lambda}\right)\Big]\\
&-\frac{E_{\boldsymbol{k}}-\xi_{\boldsymbol{k}}}{E_{\boldsymbol{k}}}\frac{E_{\boldsymbol{k}-\boldsymbol{q}+\boldsymbol{Q}}+\xi_{\boldsymbol{k}-\boldsymbol{q}+\boldsymbol{Q}}}{E_{\boldsymbol{k}-\boldsymbol{q}+\boldsymbol{Q}}}\tilde{f}^{\mp}_{\boldsymbol{k},\sigma}\Big[\left(1-f^{\mp}_{\boldsymbol{k}-\boldsymbol{q}+\boldsymbol{Q},\sigma}\right)n_{\boldsymbol{q},\lambda}-f^{\mp}_{\boldsymbol{k}-\boldsymbol{q}+\boldsymbol{Q},\sigma}\left(1+n_{\boldsymbol{q},\lambda}\right)\Big]\\
&-\frac{E_{\boldsymbol{k}}-\xi_{\boldsymbol{k}}}{E_{\boldsymbol{k}}}\frac{\Delta^{\mp}}{E_{\boldsymbol{k}-\boldsymbol{q}+\boldsymbol{Q}}}\tilde{f}^{\mp}_{\boldsymbol{k}-\boldsymbol{q}+\boldsymbol{Q},\sigma}\tilde{f}^{\mp}_{\boldsymbol{k},\sigma}\Bigg)\\
&+\frac{1}{E_{\boldsymbol{k}-\boldsymbol{q}+\boldsymbol{Q}}+E_{\boldsymbol{k}}-\omega_{\boldsymbol{q},\lambda}}\Bigg(\frac{\Delta^{\pm}}{E_{\boldsymbol{k}}}\frac{E_{\boldsymbol{k}-\boldsymbol{q}+\boldsymbol{Q}}-\xi_{\boldsymbol{k}-\boldsymbol{q}+\boldsymbol{Q}}}{E_{\boldsymbol{k}-\boldsymbol{q}+\boldsymbol{Q}}}\\
&\times\Big[\big(1-f^{\pm}_{\boldsymbol{k}-\boldsymbol{q}+\boldsymbol{Q},\sigma}\big)f^{\mp}_{\boldsymbol{k},\sigma}n_{\boldsymbol{q},\lambda}-f^{\pm}_{\boldsymbol{k}-\boldsymbol{q}+\boldsymbol{Q},\sigma}\big(1-f^{\mp}_{\boldsymbol{k},\sigma}\big)\big(1+n_{\boldsymbol{q},\lambda}\big)\Big]\\
&+\frac{|\Delta|^2}{E_{\boldsymbol{k}}E_{\boldsymbol{k}-\boldsymbol{q}+\boldsymbol{Q}}}\left(\tilde{f}^{\pm}_{\boldsymbol{k}-\boldsymbol{q}+\boldsymbol{Q},\sigma}\right)^*\Big[f^{\mp}_{\boldsymbol{k},\sigma}\left(1+n_{-\boldsymbol{q},\lambda}\right)-\left(1-f^{\mp}_{\boldsymbol{k},\sigma}\right)n_{-\boldsymbol{q},\lambda}\Big]\Bigg)\\
&-\frac{E_{\boldsymbol{k}}+\xi_{\boldsymbol{k}}}{E_{\boldsymbol{k}}}\frac{E_{\boldsymbol{k}-\boldsymbol{q}+\boldsymbol{Q}}-\xi_{\boldsymbol{k}-\boldsymbol{q}+\boldsymbol{Q}}}{E_{\boldsymbol{k}-\boldsymbol{q}+\boldsymbol{Q}}}\left(\tilde{f}^{\pm}_{\boldsymbol{k},\sigma}\right)^*\Big[\left(1-f^{\pm}_{\boldsymbol{k}-\boldsymbol{q}+\boldsymbol{Q}}\right)n_{\boldsymbol{q},\lambda}-f^{\pm}_{\boldsymbol{k}-\boldsymbol{q}+\boldsymbol{Q},\sigma}\left(1+n_{\boldsymbol{q},\lambda}\right)\Big]\\
&-\frac{E_{\boldsymbol{k}}+\xi_{\boldsymbol{k}}}{E_{\boldsymbol{k}}}\frac{\Delta^{\mp}}{E_{\boldsymbol{k}-\boldsymbol{q}+\boldsymbol{Q}}}\left(\tilde{f}^{\pm}_{\boldsymbol{k}-\boldsymbol{q}+\boldsymbol{Q},\sigma}\right)^*\left(\tilde{f}^{\pm}_{\boldsymbol{k},\sigma}\right)^*\\
&-\frac{\Delta^{\pm}}{E_{\boldsymbol{k}}}\frac{E_{\boldsymbol{k}-\boldsymbol{q}+\boldsymbol{Q}}+\xi_{\boldsymbol{k}-\boldsymbol{q}+\boldsymbol{Q}}}{E_{\boldsymbol{k}-\boldsymbol{q}+\boldsymbol{Q}}}\Big[\big(1-f^{\mp}_{\boldsymbol{k}-\boldsymbol{q}+\boldsymbol{Q},\sigma}\big)f^{\pm}_{\boldsymbol{k},\sigma}\big(1+n_{-\boldsymbol{q},\lambda}\big)-f^{\mp}_{\boldsymbol{k}-\boldsymbol{q}+\boldsymbol{Q},\sigma}\big(1-f^{\pm}_{\boldsymbol{k},\sigma}\big)n_{-\boldsymbol{q},\lambda}\Big]\\
&-\frac{|\Delta|^2}{E_{\boldsymbol{k}}E_{\boldsymbol{k}-\boldsymbol{q}+\boldsymbol{Q}}}\tilde{f}^{\mp}_{\boldsymbol{k}-\boldsymbol{q}+\boldsymbol{Q},\sigma}\Big[f^{\pm}_{\boldsymbol{k},\sigma}\left(1+n_{-\boldsymbol{q},\lambda}\right)-\left(1-f^{\pm}_{\boldsymbol{k}-\boldsymbol{q}+\boldsymbol{Q},\sigma}\right)n_{-\boldsymbol{q},\lambda}\Big]\\
&+\frac{E_{\boldsymbol{k}}-\xi_{\boldsymbol{k}}}{E_{\boldsymbol{k}}}\frac{E_{\boldsymbol{k}-\boldsymbol{q}+\boldsymbol{Q}}+\xi_{\boldsymbol{k}-\boldsymbol{q}+\boldsymbol{Q}}}{E_{\boldsymbol{k}-\boldsymbol{q}+\boldsymbol{Q}}}\tilde{f}^{\mp}_{\boldsymbol{k},\sigma}\Big[\left(1-f^{\mp}_{\boldsymbol{k}-\boldsymbol{q}+\boldsymbol{Q},\sigma}\right)\left(1+n_{-\boldsymbol{q},\lambda}\right)-f^{\mp}_{\boldsymbol{k}-\boldsymbol{q}+\boldsymbol{Q},\sigma}n_{-\boldsymbol{q},\lambda}\Big]\\
&-\frac{E_{\boldsymbol{k}}-\xi_{\boldsymbol{k}}}{E_{\boldsymbol{k}}}\frac{\Delta^{\mp}}{E_{\boldsymbol{k}-\boldsymbol{q}+\boldsymbol{Q}}}\tilde{f}^{\mp}_{\boldsymbol{k}-\boldsymbol{q}+\boldsymbol{Q},\sigma}\tilde{f}^{\mp}_{\boldsymbol{k},\sigma}\Bigg)
\end{aligned}
$$

$$
\begin{aligned}
&+\frac{1}{E_{\boldsymbol{k}-\boldsymbol{q}+\boldsymbol{Q}}-E_{\boldsymbol{k}}+\omega_{\boldsymbol{q},\lambda}}\Bigg(-\frac{\Delta^{\pm}}{E_{\boldsymbol{k}}}\frac{E_{\boldsymbol{k}-\boldsymbol{q}+\boldsymbol{Q}}+\xi_{\boldsymbol{k}-\boldsymbol{q}+\boldsymbol{Q}}}{E_{\boldsymbol{k}-\boldsymbol{q}+\boldsymbol{Q}}}\\
&\times\Big[\big(1-f^{\mp}_{\boldsymbol{k}-\boldsymbol{q}+\boldsymbol{Q},\sigma}\big)f^{\mp}_{\boldsymbol{k},\sigma}n_{\boldsymbol{q},\lambda}-f^{\mp}_{\boldsymbol{k}-\boldsymbol{q}+\boldsymbol{Q},\sigma}\big(1-f^{\mp}_{\boldsymbol{k},\sigma}\big)\big(1+n_{\boldsymbol{q},\lambda}\big)\Big]\\
&-\frac{\left(\Delta^{\pm}\right)^2}{E_{\boldsymbol{k}}E_{\boldsymbol{k}-\boldsymbol{q}+\boldsymbol{Q}}}\left(\tilde{f}^{\mp}_{\boldsymbol{k}-\boldsymbol{q}+\boldsymbol{Q},\sigma}\right)^{*}\Big[f^{\mp}_{\boldsymbol{k},\sigma}n_{\boldsymbol{q},\lambda}-\left(1-f^{\mp}_{\boldsymbol{k},\sigma}\right)\left(1+n_{\boldsymbol{q},\lambda}\right)\Big]\\
&+\frac{E_{\boldsymbol{k}}+\xi_{\boldsymbol{k}}}{E_{\boldsymbol{k}}}\frac{E_{\boldsymbol{k}-\boldsymbol{q}+\boldsymbol{Q}}+\xi_{\boldsymbol{k}-\boldsymbol{q}+\boldsymbol{Q}}}{E_{\boldsymbol{k}-\boldsymbol{q}+\boldsymbol{Q}}}\left(\tilde{f}^{\pm}_{\boldsymbol{k},\sigma}\right)^{*}\Big[\left(1-f^{\mp}_{\boldsymbol{k}-\boldsymbol{q}+\boldsymbol{Q},\sigma}\right)n_{\boldsymbol{q},\lambda}-f^{\mp}_{\boldsymbol{k}-\boldsymbol{q}+\boldsymbol{Q},\sigma}\left(1+n_{\boldsymbol{q},\lambda}\right)\Big]\\
&-\frac{E_{\boldsymbol{k}}+\xi_{\boldsymbol{k}}}{E_{\boldsymbol{k}}}\frac{\Delta^{\pm}}{E_{\boldsymbol{k}-\boldsymbol{q}+\boldsymbol{Q}}}\left(\tilde{f}^{\mp}_{\boldsymbol{k}-\boldsymbol{q}+\boldsymbol{Q},\sigma}\right)^{*}\left(\tilde{f}^{\pm}_{\boldsymbol{k},\sigma}\right)^{*}\\
&+\frac{\Delta^{\pm}}{E_{\boldsymbol{k}}}\frac{E_{\boldsymbol{k}-\boldsymbol{q}+\boldsymbol{Q}}-\xi_{\boldsymbol{k}-\boldsymbol{q}+\boldsymbol{Q}}}{E_{\boldsymbol{k}-\boldsymbol{q}+\boldsymbol{Q}}}\Big[\big(1-f^{\pm}_{\boldsymbol{k}-\boldsymbol{q}+\boldsymbol{Q},\sigma}\big)f^{\pm}_{\boldsymbol{k},\sigma}\big(1+n_{-\boldsymbol{q},\lambda}\big)-f^{\pm}_{\boldsymbol{k}-\boldsymbol{q}+\boldsymbol{Q},\sigma}\big(1-f^{\pm}_{\boldsymbol{k},\sigma}\big)n_{-\boldsymbol{q},\lambda}\Big]\\
&+\frac{\left(\Delta^{\pm}\right)^2}{E_{\boldsymbol{k}}E_{\boldsymbol{k}-\boldsymbol{q}+\boldsymbol{Q}}}\tilde{f}^{\pm}_{\boldsymbol{k}-\boldsymbol{q}+\boldsymbol{Q},\sigma}\Big[f^{\pm}_{\boldsymbol{k},\sigma}\left(1+n_{-\boldsymbol{q},\lambda}\right)-\left(1-f^{\pm}_{\boldsymbol{k},\sigma}\right)n_{-\boldsymbol{q},\lambda}\Big]\\
&-\frac{E_{\boldsymbol{k}}-\xi_{\boldsymbol{k}}}{E_{\boldsymbol{k}}}\frac{E_{\boldsymbol{k}-\boldsymbol{q}+\boldsymbol{Q}}-\xi_{\boldsymbol{k}-\boldsymbol{q}+\boldsymbol{Q}}}{E_{\boldsymbol{k}-\boldsymbol{q}+\boldsymbol{Q}}}\tilde{f}^{\mp}_{\boldsymbol{k},\sigma}\Big[\left(1-f^{\pm}_{\boldsymbol{k}-\boldsymbol{q}+\boldsymbol{Q},\sigma}\right)\left(1+n_{-\boldsymbol{q},\lambda}\right)-f^{\pm}_{\boldsymbol{k}-\boldsymbol{q}+\boldsymbol{Q},\sigma}n_{-\boldsymbol{q},\lambda}\Big]\\
&-\frac{E_{\boldsymbol{k}}-\xi_{\boldsymbol{k}}}{E_{\boldsymbol{k}}}\frac{\Delta^{\pm}}{E_{\boldsymbol{k}-\boldsymbol{q}+\boldsymbol{Q}}}\tilde{f}^{\pm}_{\boldsymbol{k}-\boldsymbol{q}+\boldsymbol{Q},\sigma}\tilde{f}^{\mp}_{\boldsymbol{k},\sigma}\Bigg)\\
&+\frac{1}{E_{\boldsymbol{k}-\boldsymbol{q}+\boldsymbol{Q}}-E_{\boldsymbol{k}}-\omega_{\boldsymbol{q},\lambda}}\Bigg(\frac{\Delta^{\pm}}{E_{\boldsymbol{k}}}\frac{E_{\boldsymbol{k}-\boldsymbol{q}+\boldsymbol{Q}}+\xi_{\boldsymbol{k}-\boldsymbol{q}+\boldsymbol{Q}}}{E_{\boldsymbol{k}-\boldsymbol{q}+\boldsymbol{Q}}}\\
&\times\Big[\big(1-f^{\mp}_{\boldsymbol{k}-\boldsymbol{q}+\boldsymbol{Q},\sigma}\big)f^{\mp}_{\boldsymbol{k},\sigma}\big(1+n_{-\boldsymbol{q},\lambda}\big)-f^{\mp}_{\boldsymbol{k}-\boldsymbol{q}+\boldsymbol{Q},\sigma}\big(1-f^{\mp}_{\boldsymbol{k},\sigma}\big)n_{-\boldsymbol{q},\lambda}\Big]\\
&+\frac{\left(\Delta^{\pm}\right)^2}{E_{\boldsymbol{k}}E_{\boldsymbol{k}-\boldsymbol{q}+\boldsymbol{Q}}}\left(f^{\mp}_{\boldsymbol{k}-\boldsymbol{q}+\boldsymbol{Q},\sigma}\right)^{*}\Big[f^{\mp}_{\boldsymbol{k},\sigma}\left(1+n_{\boldsymbol{q},\lambda}\right)-\left(1-f^{\mp}_{\boldsymbol{k},\sigma}\right)n_{-\boldsymbol{q},\lambda}\Big]\\
&-\frac{E_{\boldsymbol{k}}+\xi_{\boldsymbol{k}}}{E_{\boldsymbol{k}}}\frac{E_{\boldsymbol{k}-\boldsymbol{q}+\boldsymbol{Q}}+\xi_{\boldsymbol{k}-\boldsymbol{q}+\boldsymbol{Q}}}{E_{\boldsymbol{k}-\boldsymbol{q}+\boldsymbol{Q}}}\left(\tilde{f}^{\pm}_{\boldsymbol{k},\sigma}\right)^{*}\Big[\left(1-f^{\mp}_{\boldsymbol{k}-\boldsymbol{q}+\boldsymbol{Q},\sigma}\right)\left(1+n_{-\boldsymbol{q},\lambda}\right)-f^{\mp}_{\boldsymbol{k}-\boldsymbol{q}+\boldsymbol{Q},\sigma}n_{-\boldsymbol{q},\lambda}\Big]\\
&-\frac{E_{\boldsymbol{k}}+\xi_{\boldsymbol{k}}}{E_{\boldsymbol{k}}}\frac{\Delta^{\pm}}{E_{\boldsymbol{k}-\boldsymbol{q}+\boldsymbol{Q}}}\left(f^{\mp}_{\boldsymbol{k}-\boldsymbol{q}+\boldsymbol{Q},\sigma}\right)^{*}\left(\tilde{f}^{\pm}_{\boldsymbol{k},\sigma}\right)^{*}\\
&-\frac{\Delta^{\pm}}{E_{\boldsymbol{k}}}\frac{E_{\boldsymbol{k}-\boldsymbol{q}+\boldsymbol{Q}}-\xi_{\boldsymbol{k}-\boldsymbol{q}+\boldsymbol{Q}}}{E_{\boldsymbol{k}-\boldsymbol{q}+\boldsymbol{Q}}}\Big[\big(1-f^{\pm}_{\boldsymbol{k}-\boldsymbol{q}+\boldsymbol{Q},\sigma}\big)f^{\pm}_{\boldsymbol{k},\sigma}n_{\boldsymbol{q},\lambda}-f^{\pm}_{\boldsymbol{k}-\boldsymbol{q}+\boldsymbol{Q},\sigma}\big(1-f^{\pm}_{\boldsymbol{k},\sigma}\big)\big(1+n_{\boldsymbol{q},\lambda}\big)\Big]\\
&-\frac{\left(\Delta^{\pm}\right)^2}{E_{\boldsymbol{k}}E_{\boldsymbol{k}-\boldsymbol{q}+\boldsymbol{Q}}}\tilde{f}^{\pm}_{\boldsymbol{k}-\boldsymbol{q}+\boldsymbol{Q},\sigma}\Big[f^{\pm}_{\boldsymbol{k},\sigma}n_{\boldsymbol{q},\lambda}-\left(1-f_{\boldsymbol{k},\sigma}\right)\left(1+n_{\boldsymbol{q},\lambda}\right)\Big]\\
&+\frac{E_{\boldsymbol{k}}-\xi_{\boldsymbol{k}}}{E_{\boldsymbol{k}}}\frac{E_{\boldsymbol{k}-\boldsymbol{q}+\boldsymbol{Q}}-\xi_{\boldsymbol{k}-\boldsymbol{q}+\boldsymbol{Q}}}{E_{\boldsymbol{k}-\boldsymbol{q}+\boldsymbol{Q}}}\tilde{f}^{\mp}_{\boldsymbol{k},\sigma}\Big[\left(1-f^{\pm}_{\boldsymbol{k}-\boldsymbol{q}+\boldsymbol{Q},\sigma}\right)n_{\boldsymbol{q},\lambda}-f^{\pm}_{\boldsymbol{k}-\boldsymbol{q}+\boldsymbol{Q},\sigma}\left(1+n_{\boldsymbol{q},\lambda}\right)\Big]\\
&-\frac{E_{\boldsymbol{k}}-\xi_{\boldsymbol{k}}}{E_{\boldsymbol{k}}}\frac{\Delta^{\pm}}{E_{\boldsymbol{k}-\boldsymbol{q}+\boldsymbol{Q}}}\tilde{f}^{\pm}_{\boldsymbol{k}-\boldsymbol{q}+\boldsymbol{Q},\sigma}\tilde{f}^{\mp}_{\boldsymbol{k},\sigma}\Big)\Bigg].
\end{aligned}
\tag{5.39}
$$

5.4 Mean-field order parameter

From here on, the index $\boldsymbol{Q}$ for the electron-phonon coupling constant and the phonon frequency is dropped, i.e. I set

$$\gamma_\lambda \equiv \gamma_{\boldsymbol{Q},\lambda}, \tag{5.40a}$$
$$\omega_\lambda \equiv \omega_{\boldsymbol{Q},\lambda}. \tag{5.40b}$$

Within the kinetic theory presented in this chapter the order parameter is obtained from the vacuum expectation values of the amplitude and phase phonons as

$$\Delta = \sum_\lambda \frac{\gamma_\lambda}{\sqrt{2\mathcal{V}\omega_\lambda}} \left[\psi^{(1)}_{\boldsymbol{Q},\lambda} + \left(\psi^{(1)}_{-\boldsymbol{Q},\lambda}\right)^* - i\psi^{(2)}_{\boldsymbol{Q},\lambda} + i\left(\psi^{(2)}_{-\boldsymbol{Q},\lambda}\right)^* \right]. \tag{5.41}$$

The order parameter enters the equations of motion of the fermionic and bosonic distribution functions via the dispersions $E^\pm_{\boldsymbol{k}}$. By applying a partial derivative with respect to the time t on the above equation (5.41) and inserting the equation of motion of the vacuum expectation values,

$$\frac{d}{dt}\psi^{(\alpha)}_{\boldsymbol{Q},\lambda} = -i\omega_\lambda \psi^{(\alpha)}_{\boldsymbol{Q},\lambda} + J^{(\alpha)}_{\boldsymbol{Q},\lambda}, \tag{5.42}$$

I get an equation of motion for the order parameter,

$$\begin{aligned} \frac{d}{dt}\Delta = &-\sum_\lambda \omega_\lambda \xi_\lambda - i\left[\sum_\lambda \frac{|\gamma_\lambda|^2}{\omega_\lambda}\right]\frac{1}{\mathcal{V}}\left[\sum_{\boldsymbol{k},\sigma}\frac{\Delta}{2E_{\boldsymbol{k}}}\left(f^+_{\boldsymbol{k},\sigma} - f^-_{\boldsymbol{k},\sigma}\right)\right. \\ &\left. + \sum_{\boldsymbol{k},\sigma}\left(\frac{\Delta^2}{|\Delta|^2}\frac{E_{\boldsymbol{k}}+\xi_{\boldsymbol{k}}}{2E_{\boldsymbol{k}}}\left[\tilde{f}^+_{\boldsymbol{k},\sigma}\right]^* - \frac{E_{\boldsymbol{k}}-\xi_{\boldsymbol{k}}}{2E_{\boldsymbol{k}}}\left[\tilde{f}^-_{\boldsymbol{k},\sigma}\right]^*\right)\right], \end{aligned} \tag{5.43}$$

where ξ_λ are the phonon coordinates defined as

$$\xi_\lambda = \frac{\gamma_\lambda}{\sqrt{2\mathcal{V}\omega_\lambda}}\left[i\psi^{(1)}_{\boldsymbol{Q},\lambda} - i\left(\psi^{(1)}_{-\boldsymbol{Q},\lambda}\right)^* + \psi^{(2)}_{\boldsymbol{Q},\lambda} + \left(\psi^{(2)}_{-\boldsymbol{Q},\lambda}\right)^* \right]. \tag{5.44}$$

Eq. (5.43) is a rather complicated integral differential equation coupled to the electronic distribution functions. The equation may be linearized around a stationary state to obtain a simpler set of equations of motion which allows the investigation of the collective modes. For this purpose I investigate the mean-field thermal equilibrium state in the following.

From the condition that the time derivative of $\psi^{(\alpha)}_{\boldsymbol{q},\lambda}$ vanishes,

$$\frac{d}{dt}\psi^{(\alpha)}_{\boldsymbol{q},\lambda} \stackrel{!}{=} 0, \tag{5.45}$$

it follows that in the stationary state the vacuum expectation values of amplitude and phase phonons satisfy the relations

$$\psi^{(1)}_{\pm\boldsymbol{Q},\lambda} = \mp\frac{\gamma^*_{\pm\boldsymbol{Q},\lambda}}{\sqrt{2\omega_\lambda \mathcal{V}\omega_\lambda}} \sum_{\boldsymbol{k},\sigma}\left[u^*_{\boldsymbol{k}}v^*_{\boldsymbol{k}}f^+_{\boldsymbol{k},\sigma} - u^*_{\boldsymbol{k}}v^*_{\boldsymbol{k}}f^-_{\boldsymbol{k},\sigma} + \left(u^*_{\boldsymbol{k}}\right)^2\tilde{f}^+_{\boldsymbol{k},\sigma} - \left(v^*_{\boldsymbol{k}}\right)^2\tilde{f}^-_{\boldsymbol{k},\sigma}\right], \tag{5.46a}$$

$$\psi^{(2)}_{\pm\boldsymbol{Q},\lambda} = i\frac{\gamma^*_{\pm\boldsymbol{Q},\lambda}}{\sqrt{2\omega_\lambda \mathcal{V}\omega_\lambda}} \sum_{\boldsymbol{k},\sigma}\left[u^*_{\boldsymbol{k}}v^*_{\boldsymbol{k}}f^+_{\boldsymbol{k},\sigma} - u^*_{\boldsymbol{k}}v^*_{\boldsymbol{k}}f^-_{\boldsymbol{k},\sigma} + \left(u^*_{\boldsymbol{k}}\right)^2\tilde{f}^+_{\boldsymbol{k},\sigma} - \left(v^*_{\boldsymbol{k}}\right)^2\tilde{f}^-_{\boldsymbol{k},\sigma}\right]. \tag{5.46b}$$

$$\psi^{(1,2)}_{\boldsymbol{q}\neq\pm\boldsymbol{Q},\lambda} = 0, \tag{5.46c}$$

By inserting the above expressions into the definition of the order parameter (5.41) I get the self-consistency equation

$$\Delta = \left[\sum_\lambda \frac{|\gamma_\lambda|^2}{\omega_\lambda^2}\right]\frac{1}{\mathcal{V}}\sum_{\boldsymbol{k},\sigma}\left[\frac{\Delta}{2E_{\boldsymbol{k}}}\left(f^-_{\boldsymbol{k},\sigma} - f^+_{\boldsymbol{k},\sigma}\right) - \frac{\Delta^2}{|\Delta|^2}\frac{E_{\boldsymbol{k}}+\xi_{\boldsymbol{k}}}{2E_{\boldsymbol{k}}}\left(\tilde{f}^+_{\boldsymbol{k},\sigma}\right)^* + \frac{E_{\boldsymbol{k}}-\xi_{\boldsymbol{k}}}{2E_{\boldsymbol{k}}}\left(\tilde{f}^-_{\boldsymbol{k},\sigma}\right)^*\right]. \tag{5.47}$$

The form of this self-consistency equation differs from the usual mean-field self-consistency equation. It can be seen, however, that they coincide in the mean-field thermal equilibrium state. The fermionic distribution functions in the mean-field thermal equilibrium state are given by

$$f^\pm_{\boldsymbol{k}} = \frac{1}{e^{\beta\left(E^\pm_{\boldsymbol{k}}\mp\mu\right)}+1}, \tag{5.48a}$$

$$\tilde{f}^\pm_{\boldsymbol{k}} = 0. \tag{5.48b}$$

It is easy to see that the collision integrals $I^\pm_{\boldsymbol{k}}$ vanish exactly for these distribution functions. However, the collision integrals $\tilde{I}^\pm_{\boldsymbol{k}}$ do not vanish. It will be shown later that these collision integrals lead to non-vanishing order parameter damping in the mean-field thermal equilibrium state. Using Eqs. (5.48) and the linearized electronic dispersion (5.25) the above self-consistency equation (5.47) reduces to the mean-field self-consistency equation

$$1 = \frac{g_0}{\mathcal{V}}\sum_{\boldsymbol{k}}\frac{1}{2E_{\boldsymbol{k}}}\tanh\left(\frac{\beta E_{\boldsymbol{k}}}{2}\right), \tag{5.49}$$

with

$$g_0 \equiv (2S+1)\sum_\lambda \frac{|\gamma_\lambda|^2}{\omega_\lambda^2}, \tag{5.50}$$

and

$$E_{\boldsymbol{k}} \equiv E^+_{\boldsymbol{k}} = \sqrt{v_F^2 k_z^2 + |\Delta|^2}. \tag{5.51}$$

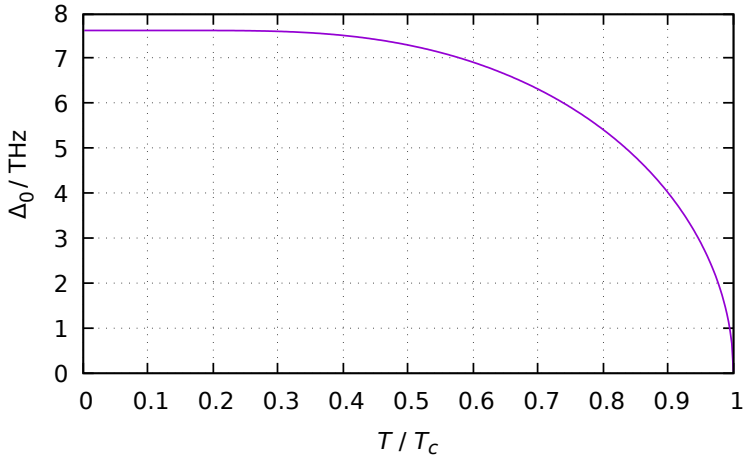

Figure 5.6: The mean-field order parameter Δ_0 obtained from the numerical solution of the self-consistency equation (5.49) is plotted over the temperature T. The Fermi energy was chosen as $\epsilon_F = v_F k_F = 58.36$ GHz and the density of states was approximated by Eq. (5.53).

Eq. (5.49) can be solved by finding the roots of the function

$$F(\Delta) = \frac{g_0}{\mathcal{V}} \sum_{\boldsymbol{k}} \frac{1}{2E_{\boldsymbol{k}}} \tanh\left(\frac{\beta E_{\boldsymbol{k}}}{2}\right) - 1, \tag{5.52}$$

which is a function of the order parameter Δ. This task can be easily done numerically. The temperature dependence of the mean-field order parameter is shown in Fig. 5.6. Here, the density of states is approximated by

$$\nu_0 = \frac{1}{\pi v_F}. \tag{5.53}$$

Eq. (5.47) is more general than the mean-field self-consistency equation (5.49) and is also valid for any stationary state outside of thermal equilibrium.

Fig. 5.7 shows the time evolution of the ratio $\Delta(t)/\Delta_0$ of the order parameter $\Delta(t)$ to the mean-field order parameter Δ_0 after a small initial excitation close to thermal equilibrium. The initial condition is $\Delta(0) = 1.01 \times \Delta_0$ where the mean-field order parameter Δ_0 was obtained from the numerical solution of Eq. (5.49). The initial values of the fermionic distribution functions were chosen as their equilibrium value given by (5.48) and the initial phonon distribution functions were set to the Bose distribution function

$$n_{\boldsymbol{q},\lambda} = \frac{1}{e^{\beta\omega_{\boldsymbol{q},\lambda}} - 1}. \tag{5.54}$$

The parameters were chosen as $\epsilon_F = v_F k_F = 58.36$ GHz and $\mu = 7.135$ THz. The phonon frequencies and electron-phonon coupling constants were chosen according to Tab. 5.5.1.

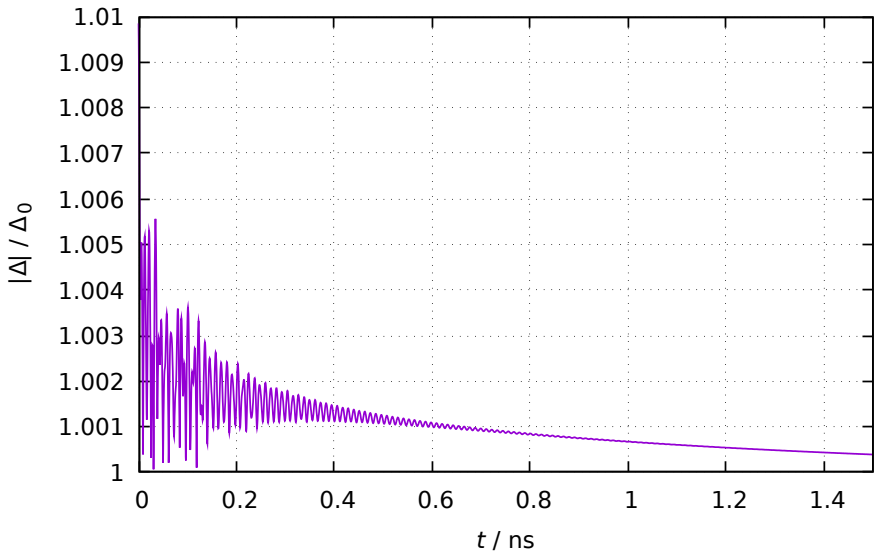

Figure 5.7: The ratio of the order parameter $\Delta(t)$ to the mean-field order parameter Δ_0 is plotted over the time t after a small initial excitation with $\Delta(0) = 1.01 \times \Delta_0$. The mean-field order parameter was obtained from the numerical solution of Eq. (5.49). The parameters were chosen as $\epsilon_F = 58.36$ GHz, $\mu = 7.135$ THz, and $T = 100$ K. The phonon frequencies and the electron-phonon coupling constants are given by Tab. 5.5.1.

These values have been obtained from fits to experimental data which is explained in the next section. The order parameter shown in Fig. 5.7 shows an oscillatory behavior with fast damped oscillations around a certain time-dependent mean value which slowly converges to the mean-field order parameter value.

5.5 Linearized kinetic equations

The equation of motion of the order parameter (5.43) is a complicated integral differential equation; note that the fermionic dispersion $E_{\boldsymbol{k}}$ depends non-linearly on the order parameter. In this work, I am particularly interested in the phonon frequencies of amplitude and phase modes as they are experimentally accessible. While it is possible to obtain these information from the numerical solution of the equation of motion of the order parameter (5.43) by calculating the spectral density, it is also possible to extract the frequency and the damping by linearizing the kinetic equations around the mean-field thermal equilibrium state.

Furthermore, by linearizing the kinetic equations I am able to compare the method presented in this chapter with existing methods, namely the Gaussian approximation [37] (which is equivalent to the random-phase approximation [30, 31, 32]) and the phenomenological, time-dependent Ginzburg-Landau approach [48, 50, 51].

5.5.1 Order parameter equation of motion

The time-dependent order parameter can be written as

$$\Delta(t) = \Delta_0 + \delta(t), \tag{5.55}$$

where Δ_0 is the mean-field order parameter obtained from the solution of the mean-field self-consistency equation (5.49) and $\delta(t)$ is a small, time-dependent fluctuation. I only take into account terms of first order in $\delta(t)$ and drop higher order terms. Furthermore, I consider the fermionic and bosonic distribution functions in lowest order, replacing them by the mean-field thermal distributions (5.48) and (5.54). Applying a partial derivative with respect to the time t to the equation of motion of the order parameter (5.43) and using the self-consistency condition (5.49) for the thermal equilibrium state I get

$$\begin{aligned}\frac{d^2}{dt^2}\delta(t) = &-\sum_\lambda \omega_\lambda^2 \delta_\lambda(t) - \frac{\sum_\lambda |\gamma_\lambda|^2}{\sum_\lambda \frac{|\gamma_\lambda|^2}{\omega_\lambda^2}}\delta(t) + iD\frac{d}{dt}\delta(t) \\ -i\frac{(2S+1)}{\mathcal{V}}&\left[\sum_\lambda \frac{|\gamma_\lambda|^2}{\omega_\lambda}\right]\sum_{\boldsymbol{k}}\left[\frac{\Delta^2}{|\Delta|^2}\frac{E_{\boldsymbol{k}}+\xi_{\boldsymbol{k}}}{2E_{\boldsymbol{k}}}\left(\tilde{I}_{\boldsymbol{k}}^{+}\right)^* - \frac{E_{\boldsymbol{k}}-\xi_{\boldsymbol{k}}}{2E_{\boldsymbol{k}}}\left(\tilde{I}_{\boldsymbol{k}}^{-}\right)^*\right],\end{aligned} \tag{5.56}$$

with

$$\delta_\lambda(t) = \frac{\gamma_\lambda}{\sqrt{2\mathcal{V}\omega_\lambda}}\left(\delta\psi^{(1)}_{\boldsymbol{Q},\lambda}(t) + \left(\delta\psi^{(1)}_{-\boldsymbol{Q},\lambda}(t)\right)^* - i\delta\psi^{(2)}_{\boldsymbol{Q},\lambda}(t) + i\left(\delta\psi^{(2)}_{-\boldsymbol{Q},\lambda}(t)\right)^*\right), \tag{5.57}$$

$$\delta(t) = \sum_\lambda \delta_\lambda(t), \tag{5.58}$$

and

$$D = \frac{2S+1}{2}\left[\sum_\lambda \frac{|\gamma_\lambda|^2}{\omega_\lambda}\right]\frac{1}{\mathcal{V}}\sum_{\boldsymbol{k}}\left[\frac{1}{E_{\boldsymbol{k}}}\tanh\left(\frac{\beta E_{\boldsymbol{k}}}{2}\right)\right]. \tag{5.59}$$

Inserting the collision integrals (5.34b) into Eq. (5.56) the equation can be written in the form

$$\frac{d^2}{dt^2}\delta(t) = -\sum_\lambda \omega_\lambda^2\delta_\lambda(t) - \frac{\sum_\lambda |\gamma_\lambda|^2}{\sum_\lambda \frac{|\gamma_\lambda|^2}{\omega_\lambda^2}}\delta(t) + iD\frac{d}{dt}\delta(t) - i\left(\Delta_0+\delta(t)\right)\sum_\lambda \frac{|\gamma_\lambda|^2}{\omega_\lambda}\left(\tilde{\Gamma}+i\tilde{F}\right), \tag{5.60}$$

with

$$\tilde{\Gamma} = \frac{\pi\left(2S+1\right)}{N^2}\sum_{\boldsymbol{k},\boldsymbol{q},\mu}\frac{\left|\gamma_{\boldsymbol{q},\mu}\right|^2}{E_{\boldsymbol{k}}}\Bigg[\Bigg(\delta\left(E_{\boldsymbol{k}-\boldsymbol{q}+\boldsymbol{Q}}-E_{\boldsymbol{k}}-\omega_{\boldsymbol{q},\mu}\right)-\delta\left(E_{\boldsymbol{k}-\boldsymbol{q}+\boldsymbol{Q}}-E_{\boldsymbol{k}}+\omega_{\boldsymbol{q},\mu}\right)\Bigg)$$
$$\times\Bigg(\left[\tanh\left(\frac{\beta E_{\boldsymbol{k}}}{2}\right)-\tanh\left(\frac{\beta E_{\boldsymbol{k}-\boldsymbol{q}+\boldsymbol{Q}}}{2}\right)\right]\left[1+2n_{\boldsymbol{q},\mu}\right]$$
$$+\frac{\xi_{\boldsymbol{k}}}{E_{\boldsymbol{k}}}\left[1-\tanh\left(\frac{\beta E_{\boldsymbol{k}}}{2}\right)\tanh\left(\frac{\beta E_{\boldsymbol{k}-\boldsymbol{q}+\boldsymbol{Q}}}{2}\right)\right]\Bigg)$$
$$+\delta\left(E_{\boldsymbol{k}-\boldsymbol{q}+\boldsymbol{Q}}+E_{\boldsymbol{k}}-\omega_{\boldsymbol{q},\mu}\right)\Bigg(\left[\tanh\left(\frac{\beta E_{\boldsymbol{k}}}{2}\right)+\tanh\left(\frac{\beta E_{\boldsymbol{k}-\boldsymbol{q}+\boldsymbol{Q}}}{2}\right)\right]\left[1+2n_{\boldsymbol{q},\mu}\right]$$
$$+\frac{\xi_{\boldsymbol{k}}}{E_{\boldsymbol{k}}}\left[1+\tanh\left(\frac{\beta E_{\boldsymbol{k}}}{2}\right)\tanh\left(\frac{\beta E_{\boldsymbol{k}-\boldsymbol{q}+\boldsymbol{Q}}}{2}\right)\right]\Bigg)\Bigg], \tag{5.61}$$

and

$$\tilde{F} = \frac{2S+1}{2N^2}\sum_{\boldsymbol{k},\boldsymbol{q},\mu}\frac{\left|\gamma_{\boldsymbol{q},\mu}\right|^2}{E_{\boldsymbol{k}}}\Bigg(-\frac{E_{\boldsymbol{k}}+E_{\boldsymbol{k}-\boldsymbol{q}+\boldsymbol{Q}}}{\left(E_{\boldsymbol{k}-\boldsymbol{q}+\boldsymbol{Q}}+E_{\boldsymbol{k}}\right)^2-\omega_{\boldsymbol{q},\mu}^2}$$
$$\times\left[\tanh\left(\frac{\beta E_{\boldsymbol{k}}}{2}\right)+\tanh\left(\frac{\beta E_{\boldsymbol{k}-\boldsymbol{q}+\boldsymbol{Q}}}{2}\right)\right]\left[1+2n_{\boldsymbol{q},\mu}\right]$$
$$-\frac{\omega_{\boldsymbol{q},\mu}}{\left(E_{\boldsymbol{k}-\boldsymbol{q}+\boldsymbol{Q}}-E_{\boldsymbol{k}}\right)^2-\omega_{\boldsymbol{q},\mu}^2}\left[\tanh\left(\frac{\beta E_{\boldsymbol{k}}}{2}\right)-\tanh\left(\frac{\beta E_{\boldsymbol{k}-\boldsymbol{q}+\boldsymbol{Q}}}{2}\right)\right]\left[1+2n_{\boldsymbol{q},\mu}\right]$$
$$-\frac{\xi_{\boldsymbol{k}}}{E_{\boldsymbol{k}}}\frac{E_{\boldsymbol{k}-\boldsymbol{q}+\boldsymbol{Q}}+E_{\boldsymbol{k}}}{\left[\left(E_{\boldsymbol{k}-\boldsymbol{q}+\boldsymbol{Q}}+E_{\boldsymbol{k}}\right)^2-\omega_{\boldsymbol{q},\mu}^2\right]}\left[1+\tanh\left(\frac{\beta E_{\boldsymbol{k}}}{2}\right)\tanh\left(\frac{\beta E_{\boldsymbol{k}-\boldsymbol{q}+\boldsymbol{Q}}}{2}\right)\right]$$
$$+\frac{\xi_{\boldsymbol{k}}}{E_{\boldsymbol{k}}}\frac{E_{\boldsymbol{k}-\boldsymbol{q}+\boldsymbol{Q}}-E_{\boldsymbol{k}}}{\left[\left(E_{\boldsymbol{k}-\boldsymbol{q}+\boldsymbol{Q}}-E_{\boldsymbol{k}}\right)^2-\omega_{\boldsymbol{q},\mu}^2\right]}\left[1-\tanh\left(\frac{\beta E_{\boldsymbol{k}}}{2}\right)\tanh\left(\frac{\beta E_{\boldsymbol{k}-\boldsymbol{q}+\boldsymbol{Q}}}{2}\right)\right]\Bigg). \tag{5.62}$$

Note that I have dropped terms involving the distribution functions $\tilde{f}^{+}_{\boldsymbol{k},\sigma}$ and $\tilde{f}^{-}_{\boldsymbol{k},\sigma}$ in the above expressions because they are assumed to vanish in the mean-field thermal equilibrium state (5.48). The order parameter equation of motion (5.43) may be used to get rid of the the terms involving imaginary valued prefactors appearing in Eq. (5.60). Using the definition (5.44) the order parameter equation of motion can be reformulated in terms of coupled equations of motion for the order parameter and the phonon coordinates,

$$\frac{d^2}{dt^2}\delta(t) = -\sum_{\lambda}\omega_{\lambda}^2\delta_{\lambda}(t)-\sum_{\lambda}\left|\gamma_{\lambda}\right|^2\tilde{F}\delta(t)-C\tilde{\Gamma}\left[\frac{d}{dt}\delta(t)+\sum_{\lambda}\omega_{\lambda}\delta\xi_{\lambda}(t)\right], \tag{5.63a}$$

$$\frac{d^2}{dt^2}\delta\xi_{\lambda}(t) = -\omega_{\lambda}^2\delta\xi_{\lambda}(t)+\frac{\frac{\left|\gamma_{\lambda}\right|^2}{\omega_{\lambda}}}{\sum_{\mu}\frac{\left|\gamma_{\mu}\right|^2}{\omega_{\mu}^2}}\sum_{\mu}\omega_{\mu}\delta\xi_{\mu}(t)+\left|\gamma_{\lambda}\right|^2\tilde{\Gamma}\delta(t)-C\tilde{F}\frac{\partial}{\partial t}\delta(t), \tag{5.63b}$$

with

$$C = \sum_{\lambda} \frac{|\gamma_\lambda|^2}{\omega_\lambda}. \tag{5.64}$$

A numerical evaluation of the order parameter damping and the frequency renormalization,

$$\Gamma = C\tilde{\Gamma}, \tag{5.65a}$$
$$F = C\tilde{F}, \tag{5.65b}$$

in dependence of the temperature T are shown in Fig. 5.8. For $T \to T_c$ the damping diverges as $\sqrt{T_c/(T_c - T)}$ while for low temperatures I obtain a rather low damping rate. This finding shows that the mean-field approximation breaks down at the critical temperature T_c. The source of the order parameter damping are the collision integrals $\tilde{I}^{\pm}_{\boldsymbol{k}}$ that do not vanish in the mean-field thermal equilibrium state. These non-vanishing contributions originate from the interaction terms involving non-$2k_F$ phonons that are neglected within the mean-field approximation and show that the mean-field thermal equilibrium state is not stable. However, due to the large order parameter this state is stabilized and the damping rate remains small. The strong temperature dependence of the order parameter damping is due to the fact that close to T_c the order parameter vanishes and the electronic dispersion becomes gapless. Without this stabilizing effect the mean-field solution is not capable of describing the system reasonably well so that the linearization around this solution is not reasonable. Thus, the results presented in this section become inaccurate close to the critical temperature. Note that the momentum dependence of the electron-phonon coupling constants $\gamma_{\boldsymbol{q},\lambda}$ has been neglected within the integrals (5.61) and (5.62). I set $\gamma_{\boldsymbol{q},\lambda} = \gamma_\lambda$ to evaluate these integrals.

The set of equations of motion (5.63) can be solved numerically to investigate the linearized dynamics of the collective modes. The time evolution of $\delta(t)$ and $\delta\xi(t)$ after a small excitation at $t_0 = 0$ is shown in Fig. 5.9. Furthermore, Fig. 5.10 shows the spectral density calculated from the numerical solution for $\delta(t)$ and $\delta\xi(t)$. The comparison with the time evolution of the non-linearized order parameter equation of motion shown in Fig. 5.7 reveals that the time evolution of the linearized equation of motion is simpler. There are only damped oscillations around the mean-field order-parameter value while in Fig. 5.7 it can be observed that the damped oscillations occur around a slowly decaying order-parameter value converging to the mean-field order-parameter value.

From Eqs. (5.63) the amplitude and phase mode frequencies can be read off if the mode coupling can be neglected. For the amplitude mode they are given by

$$\tilde{\omega}_\lambda^2 = \omega_\lambda^2 + |\gamma_\lambda|^2 \tilde{F}, \tag{5.66}$$

while the phase mode frequencies $\tilde{\nu}_\lambda$ can be obtained by diagonalizing Eq. (5.63b). However, the damping leads to coupling of all modes and subsequently to hybridization of amplitude and phase modes. This effect leads to shifts of the amplitude and phase mode frequencies and thus needs to be explicitly taken into account. After diagonalizing

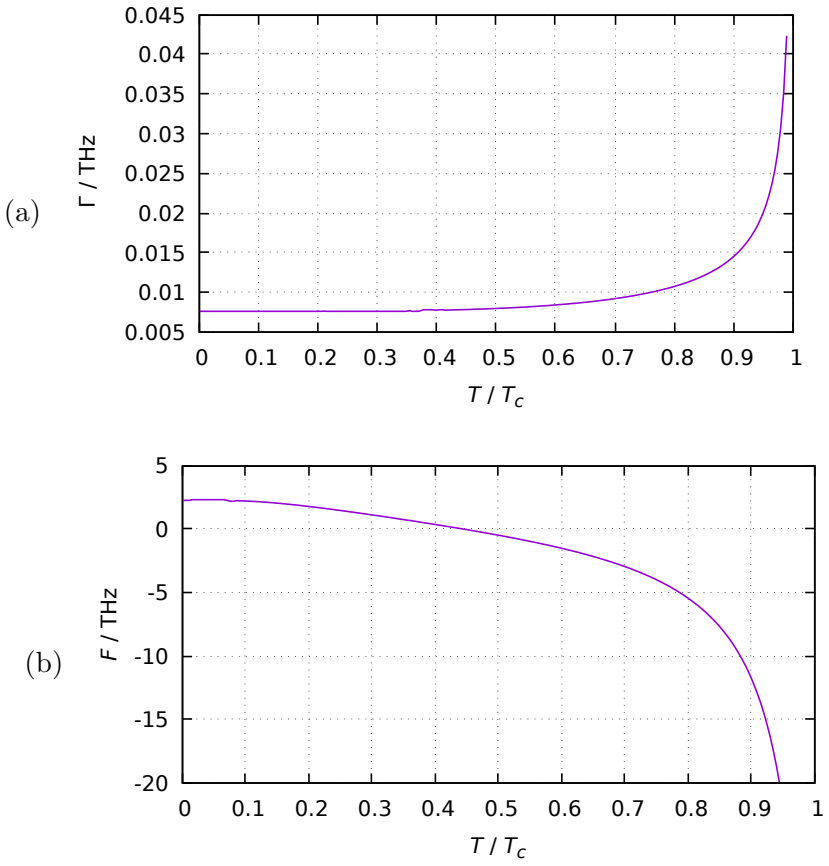

Figure 5.8: Numerical evaluation of the order parameter damping coefficient Γ (a) and the contribution to the frequency renormalization originating form the principal values of the collision integrals F (b) plotted over the temperature T. The parameters are chosen according to table 5.5.1.

Eq. (5.63b) the set of equations of motion (5.63) can be solved by the ansatz

$$\delta_\lambda(t) = A_\lambda e^{\alpha_\lambda t}, \tag{5.67a}$$
$$\delta\xi_\lambda(t) = B_\lambda e^{\beta_\lambda t}. \tag{5.67b}$$

I find the self-consistency condition

$$\left[\sum_\lambda \frac{C\tilde{\Gamma}}{\alpha_\lambda^2+\omega_\lambda^2}\right]\left[\sum_\lambda \frac{\omega_\lambda |\gamma_\lambda|^2 \tilde{\Gamma} + \omega_\lambda C\tilde{F}\sum_\mu \alpha_\mu}{\beta_\lambda^2+\tilde{\nu}_\lambda^2}\right] - \sum_\lambda \frac{|\gamma_\lambda|^2 \tilde{F} + C\tilde{\Gamma}\sum_\mu \alpha_\mu}{\alpha_\lambda^2+\omega_\lambda^2} - 1 = 0, \tag{5.68}$$

where $\tilde{\nu}_\lambda$ are the phonon frequencies of the diagonalized Eq. (5.63b). To find the coefficients α_λ and β_λ the roots of the above equation have to be found numerically. That

(a)

(b)

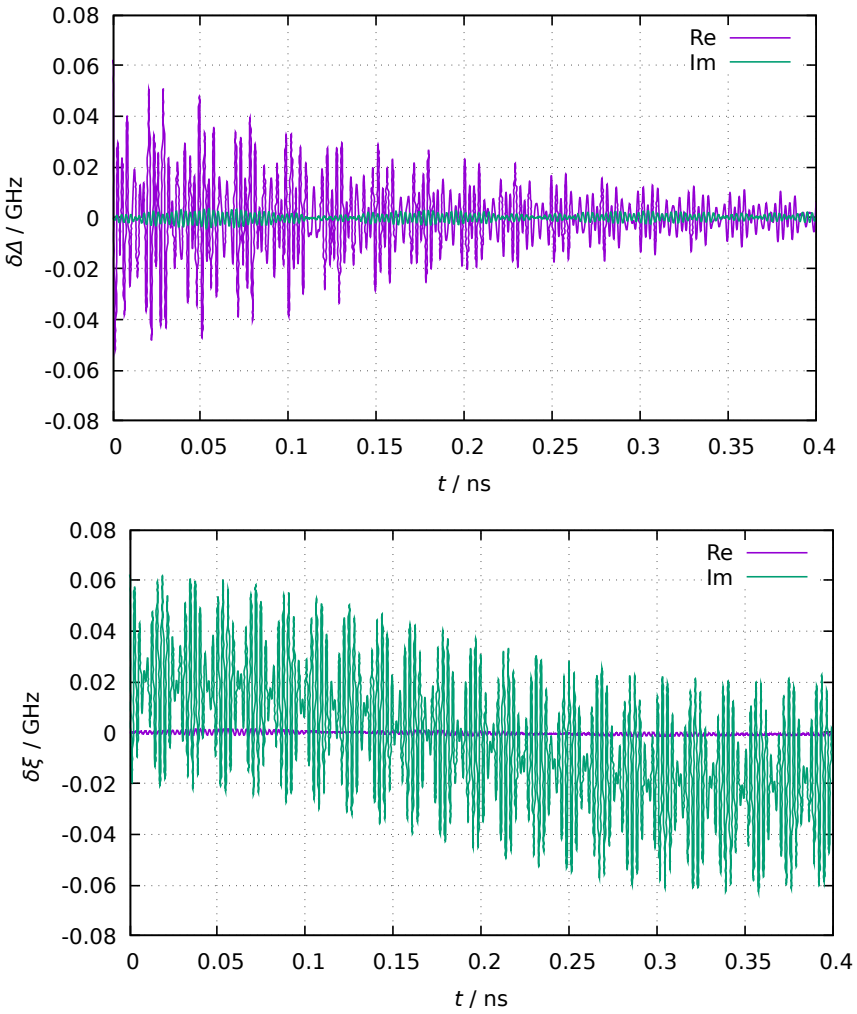

Figure 5.9: Time evolution of $\delta\Delta(t) = \Delta(t) - \Delta_0$ (a) and the phonon coordinates $\delta\xi(t) = \sum_\lambda \delta\xi_\lambda(t)$ (b) obtained by solving numerically the set of linearized equations of motion (5.63) for $T = 100$ K. Here, three phonon modes have been used with $\omega_1 = 1.69$ THz, $\omega_2 = 2.23$ THz, $\omega_3 = 2.56$ THz, $\gamma_1 = 0.108$ GHz, $\gamma_2 = 0.0906$ GHz, and $\gamma_3 = 0.161$ GHz.

(a)

(b)

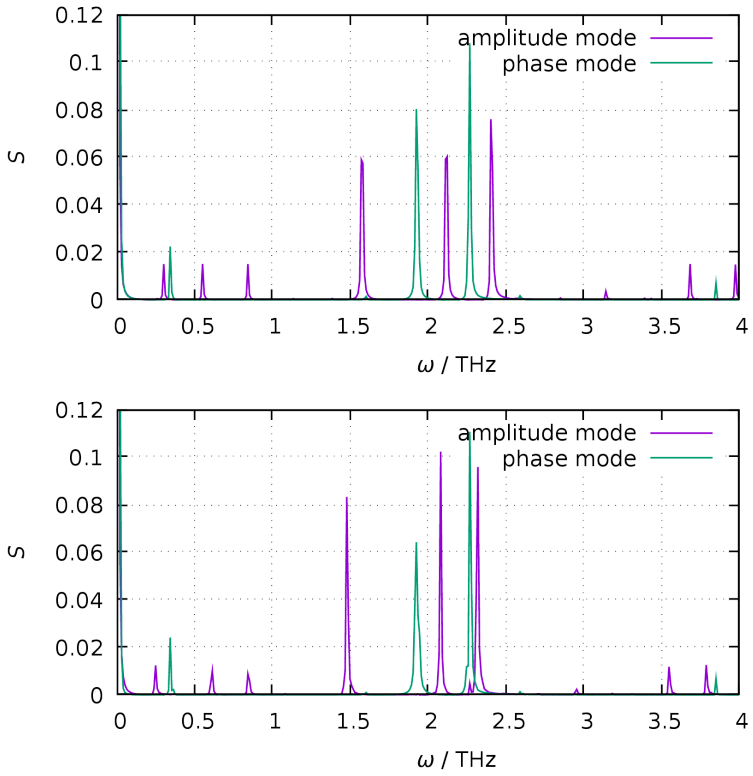

Figure 5.10: The spectral density normalized to one has been calculated from the numerical solution of the linearized order parameter equation of motion (5.63) (see also Fig. 5.9) for two different temperatures, $T = 50$ K (a) and $T = 100$ K (b). The parameters are the same as in Fig. 5.9. Note that the small peaks at small and large frequencies originate from the application of the discrete Fourier transformation on $\delta(t) = \sum_\lambda \delta_\lambda(t)$ and $\delta\xi(t) = \sum_\lambda \delta\xi_\lambda(t)$. For example, peaks with frequencies $\tilde{\omega}_\lambda - \tilde{\omega}_\mu$ and $\tilde{\omega}_\lambda + \tilde{\omega}_\mu$ appear where $\tilde{\omega}_\lambda$ are the mode frequencies.

requires some initial values. To obtain the initial values, the coupling between different amplitude modes and different phase modes is neglected, i.e. I only consider terms that couple the λ-th amplitude mode and the λ-th pase mode. I get

$$\alpha_\lambda = -\frac{C\tilde{\Gamma}}{2} \pm \sqrt{\frac{C^2\tilde{\Gamma}^2}{4} - \omega_\lambda^2 + |\gamma_\lambda|^2\,\tilde{\Gamma}}, \tag{5.69a}$$

$$\beta_\lambda = \pm\sqrt{\omega_\lambda C\tilde{\Gamma} - \tilde{\nu}_\lambda^2}. \tag{5.69b}$$

Starting from these initial conditions I use the self-consistency condition (5.68) to iteratively obtain a self-consistent solution. The algorithm converges fast. After 16 iterations the left-hand side of Eq. (5.68) is about 10^{-12}. Writing the constants α_λ and β_λ in the

n	1	2	3	4	5
ω_n / THz	1.64	2.21	2.52	2.58	2.73
γ_n / GHz	0.918	0.181	0.118	0.057	0.059

Table 5.1: The table shows the bare phonon frequencies ω_n and the bare electron-phonon coupling constants γ_n for the first five phonon modes obtained by fits of Eq. (5.68) to experimental data from Ref. [49].

form $-\gamma_\lambda + i\Omega_\lambda$ frequencies and damping constants can be obtained from the numerical solution of the self-consistency equation (5.68). Discarding solutions with negative frequencies or damping, M solutions are obtained from each of the equations (5.67) where M is the number of bare phonon modes.

Now, let us evaluate the order parameter damping numerically and calculate the frequencies and damping constants of amplitude and phase modes. I chose the chemical potential μ in such a way that the system is close to quarter-filling. In order to be incommensurate with the lattice it should not be exactly half filled or quarter filled. I set the filling factor to $0.16\pi/2 \approx 0.2513$ as π is incommensurate with 1. I consider 5 phonon modes and fit the frequencies and coupling constants to the experimental data from Ref. [49]. From the experiments it is not known whether the phonon modes are longitudinal or transversal phonon modes. Therefore, I assume that all phonon modes are longitudinal phonon modes. Within the method introduced in this chapter longitudinal as well as transversal phonon modes can be explicitly taken into account. In order to calculate the integral appearing in the expression of the order parameter damping constant (5.61), the roots of the arguments of the Dirac delta functions need to be computed. This can be done analytically for both, longitudinal and transversal phonon modes. Therefore, calculating the damping constant (5.61) can easily be done numerically. Because evaluating the damping coefficients (5.61) numerically still requires too much computational time I evaluate the damping only once for the initial values and do the fitting for this fixed value of the damping. After the fitting I re-evaluate the damping coefficients with the new parameter values. The Fermi velocity v_F is fine-tuned so that the critical temperature $T_c = 183$ K of blue bronze is reproduced. This procedure has to be repeated in each iteration step during the fitting process. The numerical values for the bare phonon frequencies and the bare electron-phonon coupling constants are shown in Tab. 5.5.1.

The numerical results for the frequencies and damping rates are shown in Fig. 5.11. Note that I ignore the lowest phase mode for the fit as well as the damping of the lowest amplitude and phase modes. I explicitly take into account the other frequencies and damping rates for the fit so that there are 10 parameters, the bare phonon frequencies ω_λ and the bare electron-phonon coupling constants γ_λ for $\lambda = 1, \ldots, 5$, and 17 constraints. From the Gaussian approximation it is expected that the lowest phase mode has the frequency zero [37]. Here, I find frequencies larger than zero which is possible due to phonon mixing. This effect is not present in the Gaussian theory because it originates from higher order diagrams or order parameter damping which requires to include vertex

corrections within the Gaussian approximation. My result for the lowest phase mode is, however, not reliable. When the number of fitted phonon modes is changed, the frequency of the lowest phase mode shifts up or down. Apparently, the lowest phase mode is more sensitive for phonon mixing than the higher order phase modes and the amplitude modes. Furthermore, I find that the electron-phonon coupling constant γ_λ has the largest value for the lowest phonon mode and decreases for the second and third phonon mode but starts to increase for the fifth phonon mode (see Fig. 5.12). This finding agrees with Ref. [49]. As a result of this behavior, higher order phonon modes cannot be neglected when evaluating the self-consistency equation (5.68) for the lowest phase mode. The numerical results for the lowest phase mode presented in this section are thus unreliable.

5.5.2 Comparison with other methods

Now, let us investigate how the above results are related to the Gaussian approximation (which is equivalent to the random-phase approximation) and the phenomenological Ginzburg-Landau approach.

Random-phase/Gaussian approximation

As damping is not present within the Gaussian approximation the damping shall be neglected for now. The equation of motion of the order parameter and the phonon coordinates simplify in this case to

$$\frac{d^2}{dt^2}\delta_\lambda(t) = -\omega_\lambda^2\delta_\lambda(t) - |\gamma_\lambda|^2\,\tilde{F}\sum_\mu \delta_\mu(t), \tag{5.70a}$$

$$\frac{d^2}{dt^2}\delta\xi_\lambda(t) = -\omega_\lambda^2\delta\xi_\lambda(t) + \frac{\frac{|\gamma_\lambda|^2}{\omega_\lambda}}{\sum_\mu \frac{|\gamma_\mu|^2}{\omega_\mu^2}}\sum_\mu \omega_\mu\delta\xi_\mu(t). \tag{5.70b}$$

Note that these two equations are decoupled because the coupling of amplitude and phase modes is proportional to the order parameter damping constant $\tilde{\Gamma}$.

Let us first consider the frequencies of amplitude modes. The solution of the order parameter equation of motion (5.70a) can be found by using the ansatz

$$\delta_\lambda(t) = A_\lambda e^{i\nu_\lambda t}. \tag{5.71}$$

The resulting self-consistency equation reads

$$\left[\sum_\lambda \frac{|\gamma_\lambda|^2}{\omega_\lambda^2 - \nu_\lambda^2}\right]^{-1} + \tilde{F} = 0. \tag{5.72}$$

This equation has the same form as the self-consistency equation within Gaussian approximation where a polarization function appears instead of $\tilde{F}$ [37]. Here, this function

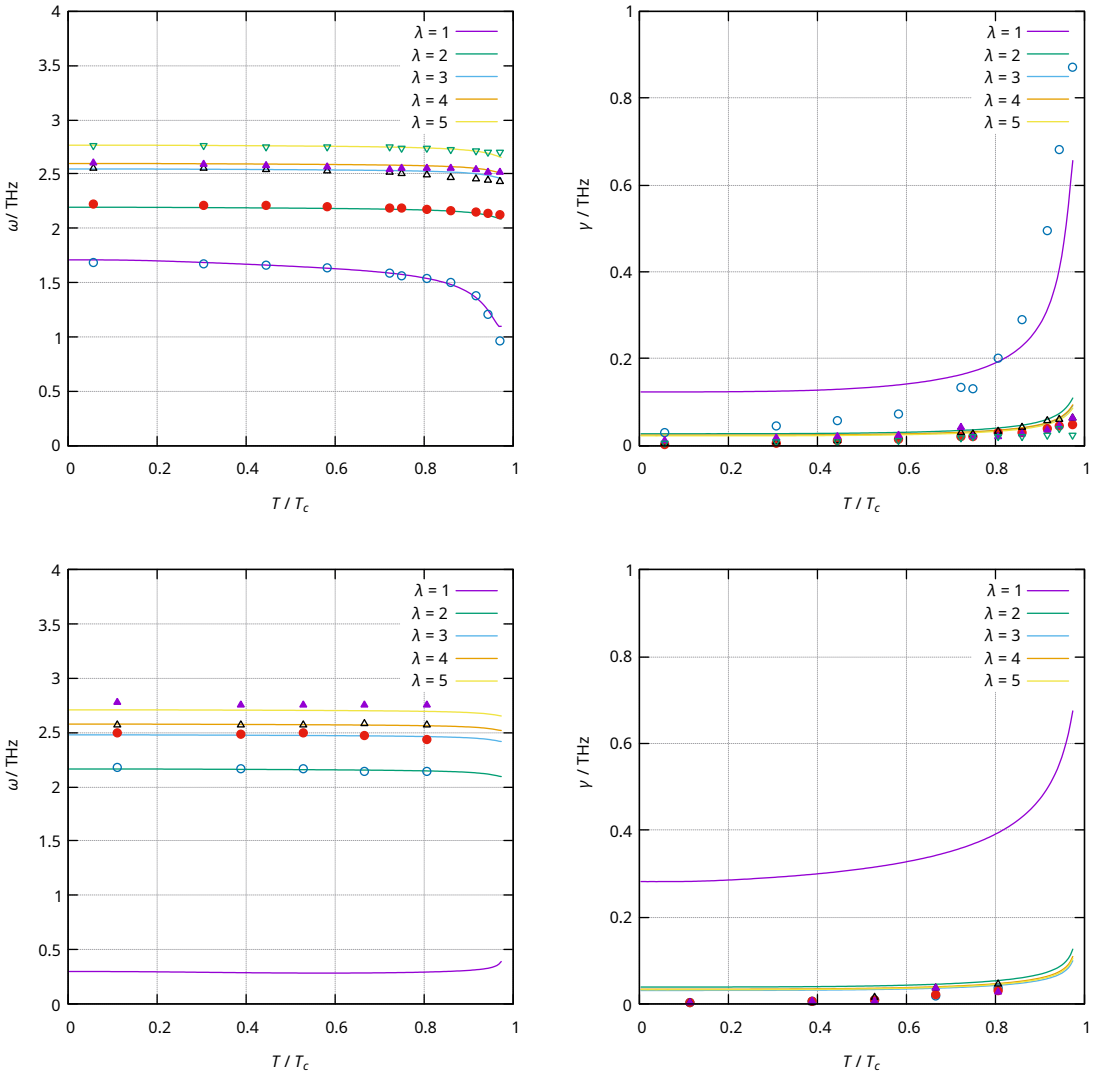

Figure 5.11: Numerical evaluation of the frequencies and damping coefficient of amplitude and phase modes obtained by solving the self-consistency equation (5.68) numerically while fitting the bare phonon frequencies and bare electron-phonon coupling constants to the experimental data from Ref. [49]. The dots represent the experimental data. Note that I have ignored the lowest phase mode when fitting the parameters.

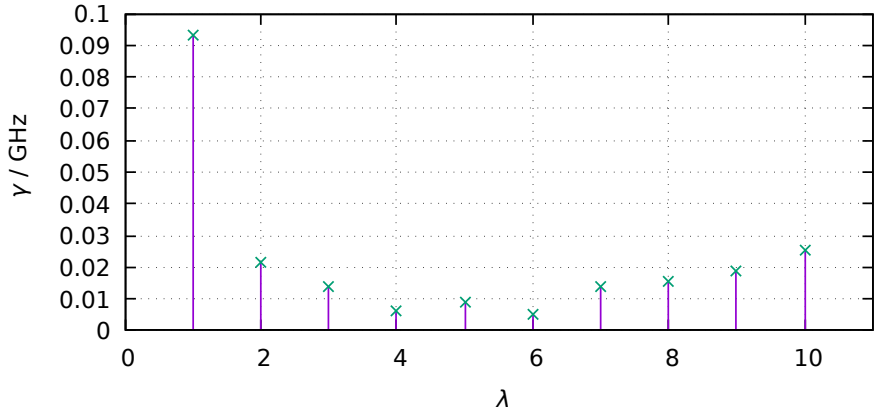

Figure 5.12: The values obtained for the bare electron-phonon coupling constants γ_λ by fitting the experimental data are shown for each mode label λ. The lowest mode has the largest coupling constant and the coupling constants become smaller for the next few modes but starting at the fifth mode the values increase.

is given by Eq. (5.62). For $\boldsymbol{q} = \boldsymbol{Q}$ it simplifies to

$$\tilde{F} = -\frac{2\,(2S+1)}{N} \sum_{\boldsymbol{k},\lambda} |\gamma_\lambda|^2 \, \frac{\tanh\left(\frac{\beta E_{\boldsymbol{k}}}{2}\right)}{(2E_{\boldsymbol{k}})^2 - \omega_\lambda^2} \, (1 + 2n_{\boldsymbol{Q},\lambda}) \,. \tag{5.73}$$

For small temperatures the phonon distribution function $n_{\boldsymbol{q},\lambda}$ can be neglected. In the case of $T = 0$ the above equation reduces to

$$\tilde{F} = -\frac{2\,(2S+1)}{N} \sum_{\boldsymbol{k},\lambda} |\gamma_\lambda|^2 \, \frac{1}{(2E_{\boldsymbol{k}})^2 - \omega_\lambda^2}. \tag{5.74}$$

In Ref. [37] the function $\tilde{F}$ was approximated for $T = 0$, $\boldsymbol{q} = \boldsymbol{Q}$ and small frequencies by

$$\tilde{F} \approx -\frac{2S+1}{2\mathcal{V}} \sum_{\boldsymbol{k},\lambda} \frac{\omega_\lambda^2}{E_{\boldsymbol{k}} \left[(2E_{\boldsymbol{k}})^2 - \omega_\lambda^2\right]} - \frac{2S+1}{2\mathcal{V}} \sum_{\boldsymbol{k}} \frac{1}{E_{\boldsymbol{k}}}. \tag{5.75}$$

These two equations are not equal. Apparently, Eq. (5.74) contains only terms that are proportional to $|\gamma_\lambda|^2$ while the above equation does not. Note that Eq. (5.49) can be used to relate the sum $\sum_\lambda \frac{|\gamma_\lambda|^2}{\omega_\lambda^2}$ with an integral over $1/(2E_{\boldsymbol{k}})$,

$$\frac{2S+1}{\mathcal{V}} \sum_{\boldsymbol{k}} \frac{1}{2E_{\boldsymbol{k}}} = \left[\sum_\lambda \frac{|\gamma_\lambda|^2}{\omega_\lambda^2}\right]^{-1}. \tag{5.76}$$

Thus, the factor of $|\gamma_\lambda|^2$ can be hidden in the mean-field order parameter self-consistency equation. Still, these two results for $\tilde{F}$ differ quantitatively. The reason is that additional

vertex corrections are included within the kinetic theory which are not present within the Gaussian theory. Furthermore, for $\boldsymbol{q} \neq \boldsymbol{Q}$ additional terms for $\tilde{F}$ appear within my formalism. This is related to the fact that I include contributions with $\boldsymbol{q} \neq \boldsymbol{Q}$ in the electron-phonon interaction Hamiltonian. These additional terms are given by the last two lines of Eq. (5.62). For $\boldsymbol{q} = \boldsymbol{Q}$ these terms become antisymmetric in $\boldsymbol{k}$ and thus vanish when carrying out the integral over $\boldsymbol{k}$.

For the phase modes I also use an exponential ansatz,

$$\delta\xi_\lambda(t) = B_\lambda e^{i\tilde{\nu}_\lambda t}, \tag{5.77}$$

leading to the self-consistency equation

$$\left[\sum_\lambda \frac{|\gamma_\lambda|^2}{\omega_\lambda^2 - \tilde{\nu}_\lambda^2}\right]^{-1} - \left[\sum_\lambda \frac{|\gamma_\lambda|^2}{\omega_\lambda^2}\right]^{-1} = 0. \tag{5.78}$$

This equation corresponds to the self-consistency equation of the phase mode frequency within Gaussian approximation at zero temperature. Within the Gaussian approximation an additional temperature dependent term appears in the self-consistency equation [37]. However, this additional term leads to a very small temperature dependence of the phase mode frequencies and can usually be neglected even for large temperatures.

In summary, if damping is neglected the same result for the phase mode frequencies as in Gaussian approximation is retained at zero temperature. For the amplitude mode the form of the self-consistency equation (5.72) is the same as for the Gaussian approximation but the frequency renormalization term $\tilde{F}$ differs quantitatively. The reason is that in the kinetic theory some vertex corrections are summed up alongside the bubble diagrams which appear in the Gaussian approximation. Let us consider one of the diagrams of Fig. 5.2. The diagram contributing to the equation of motion of the two-point correlation function contains a three-point correlation function. In order to obtain a closed result I integrate the equation of motion of the three-point correlation and substitute the three-point correlation appearing in the equation of motion of the two-point correlation function. This procedure of inserting the diagrams iteratively into each other produces not only the contribution of a single bubble diagram but accounts for summing up all orders of bubble diagrams and also includes some vertex corrections. It is, however, non-trivial to figure out which additional vertex corrections the method of kinetic equations includes. The reason is the different treatment of the collision terms within the method developed in this work and the Green's functions approach - an expansion of the collision integrals in terms of connected correlations within the method of expansion in connected correlations compared to a perturbative expansion in terms of one-particle functions within the Green's functions approach. The classification of collision terms into contributions that renormalize the energies and vertex corrections originates from the Green's functions approach and does not exist within the method of expansion in connected correlations. Therefore, it is not trivial to compare the two methods directly.

Time-dependent Ginzburg-Landau equations

First, let us briefly introduce the time-dependent Ginzburg-Landau approach. The starting point is a phenomenological potential that contains a quadratic term and a quartic term. For multiple phonon modes the potential is given by [50, 51]

$$\begin{aligned}\phi = \phi_0 + \frac{1}{2}\alpha\left(T - T_c\right)\left(\Delta_1^2 + \Delta_2^2\right) + \frac{1}{4}\beta\left(\Delta_1^2 + \Delta_2^2\right)^2 \\ + \sum_\lambda \frac{\omega_\lambda^2}{2}\left(\xi_{\lambda,1}^2 + \xi_{\lambda,2}^2\right) - \sum_\lambda m_\lambda\left(\Delta_1\xi_{\lambda,1} + \Delta_2\xi_{\lambda,2}\right),\end{aligned} \tag{5.79}$$

where the index 1 refers to the real part and the index 2 refers to the imaginary part, e.g.

$$\Delta = \Delta_1 + i\Delta_2. \tag{5.80}$$

α and β are the phenomenological Ginzburg-Landau constants and ω_λ is - as in the previous sections - the bare frequency of the $2k_F$ phonon of the λ phonon mode above the critical temperature. From the above effective potential (5.79) linearized equations of motion can be derived. In thermal equilibrium the stationary solution is [50, 51]

$$\Delta_0 = \sqrt{\frac{\alpha}{\beta}\left(\tilde{T}_c - T\right)}, \tag{5.81a}$$

$$\xi_{0,\lambda} = \frac{m_\lambda}{\omega_\lambda^2}\Delta_0, \tag{5.81b}$$

where $\tilde{T}_c$ is the renormalized critical temperature,

$$\tilde{T}_c = T_c + \frac{1}{\alpha}\sum_\lambda \frac{m_\lambda^2}{\omega_\lambda^2}. \tag{5.82}$$

The equilibrium solution (5.81a) is the motivation why the phenomenological potential is chosen in this specific way. It can be considered as an approximation to the solution of the mean-field self-consistency equation (5.49) for temperatures close to T_c. For comparison, Fig. 5.13 shows the numerical solution of the mean-field order parameter self-consistency equation and the phenomenological expression (5.81a). The linearized equations of motion can be formulated as [48, 51]

$$\partial_t^2\delta\Delta_1(t) = -\left[2\alpha\left(\tilde{T}_c - T\right) + \sum_\lambda \frac{m_\lambda^2}{\omega_\lambda^2}\right]\delta\Delta_1(t) + \sum_\lambda m_\lambda\delta\xi_{\lambda,1}(t) - \gamma_1\partial_t\delta\Delta_1, \tag{5.83}$$

$$\partial_t^2\delta\Delta_2(t) = -\sum_\lambda \frac{m_\lambda^2}{\omega_\lambda^2}\delta\Delta_2(t) + \sum_\lambda m_\lambda\delta\xi_{\lambda,2}(t) - \gamma_2\partial_t\delta\Delta_2 \tag{5.84}$$

$$\partial_t^2\delta\xi_{\lambda,1}(t) = -\omega_\lambda^2\delta\xi_{\lambda,1} + m_\lambda\delta\Delta_1 \tag{5.85}$$

$$\partial_t^2\delta\xi_{\lambda,2}(t) = -\omega_\lambda^2\delta\xi_{\lambda,2} + m_\lambda\delta\Delta_2, \tag{5.86}$$

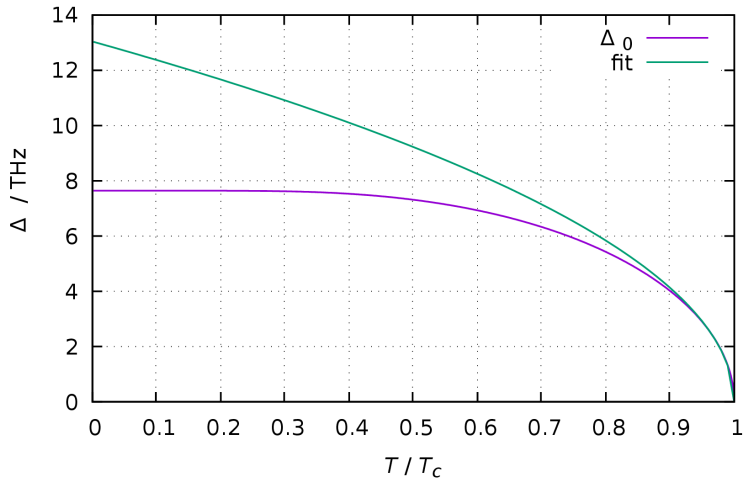

Figure 5.13: The temperature dependence of the mean-field order parameter (purple) and a fit of the form (5.81a) fitted in the temperature range from $0.95T_c$ to T_c (green).

where here the index 1 denotes the amplitude and the index 2 denotes the phase of the complex order parameter and phonon coordinates. The free parameters α, m_λ, ω_λ, γ_1, and γ_2 are usually fitted to experimental data. Comparing this set of equations of motion with the linearized kinetic equations (5.63) I find that the only difference is an additional term in the equation of motion of the phonon coordinates (5.63b) proportional to $\partial_t \delta(t)$. However, I find that the prefactor of $C\tilde{F}$ is small so that this term can be neglected and the linearized kinetic equations have the same form as the time-dependent Ginzburg-Landau equations.

There are two major differences between the kinetic equations and the time-dependent Ginzburg-Landau equations. The first one is the approximation of the order parameter by Eq. (5.81a). This approximation is valid only close to the critical temperature while at low temperature there is a large deviation from the mean-field order parameter (see Fig. 5.13). However, the mean-field order parameter enters the equations of motion explicitly only via Eq. (5.83) where the frequency renormalization term can be identified as $2\beta\Delta_0^2 = 2\alpha\left(\tilde{T}_c - T\right)$. This frequency renormalization is assumed to be linear in the temperature within the Ginzburg-Landau approach. The frequency renormalization $\tilde{F}$ obtained from the collision integral (5.62) numerically is shown in Fig. 5.14 together with a linear fit of the form $a\,(T_c - T) + b$. Apparently, a linear fit is viable in a wide temperature range up to 80% of the critical temperature. While the mean-field order parameter is well approximated close to the critical temperature, the frequency renormalization is reasonably well approximated at low and medium temperatures. This finding is surprising because the Ginzburg-Landau approximation is usually assumed to describe the system well close to the critical temperature. However, the frequency renormalization is

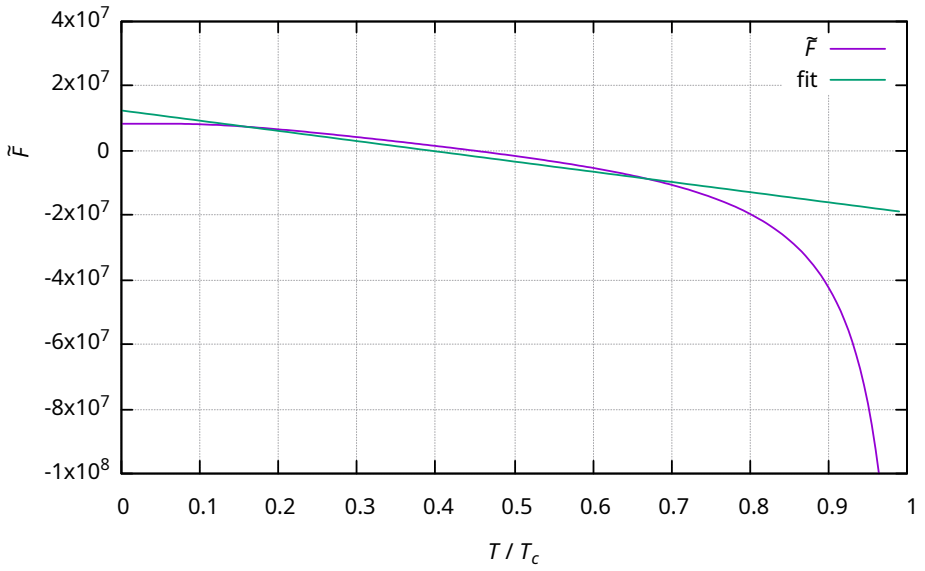

Figure 5.14: The frequency renormalization term $\tilde{F}$ is plotted over the temperature (purple) together with a linear fit (green).

approximated by only one term that is proportional to Δ_0^2. This approximation is only reasonable at low temperatures which causes an inconsistency. Ultimately, the temperature dependence of the frequency renormalization is a linear function and a linear function can be fitted sufficiently well to the frequency renormalization term $\tilde{F}$ obtained from the numerical calculation of the collision integrals (see Fig. 5.14). I conclude that the Ginzburg-Landau equations are capable of describing the system well at low and medium temperatures. As the mean-field order parameter does not enter the linearized equations of motion explicitly it is not relevant that the approximation for the mean-field order parameter is only valid close to the critical temperature T_c.

The second difference is the replacement of the damping by two phenomenological parameters which are usually fitted to experimental data. In my approach the damping is calculated from the microscopic dynamics with the relevant parameters being the bare phonon dispersions and the bare electron-phonon coupling constants. Furthermore, in the time-dependent Ginzburg-Landau approach the amplitude and phase damping, γ_1 and γ_2, can be chosen completely independent of each other. In my numerical calculations I found that the ratio of these two damping rates usually lies between 0.05 and 0.1 for blue bronze. Furthermore, the damping constants are assumed to have no temperature dependence. At low temperatures up to 70% of the critical temperature T_c neglecting the temperature dependence is a reasonable approximation (see Fig. 5.8(a)). The strong temperature dependence of the damping rate $\tilde{\Gamma}$ given by Eq. (5.61) originates, however, from the breakdown of the mean-field approximation at the critical temperature. Thus, the temperature dependence of the order parameter damping is

overestimated within the kinetic theory.

5.6 Coulomb interaction

In section 5.2 the Coulomb interaction has been neglected so far. Here, I take it into account by adding to the Fröhlich Hamiltonian (5.1) the Coulomb Hamiltonian

$$\mathcal{H}_C = \frac{1}{2\mathcal{V}} \sum_{\boldsymbol{k}} V_{\boldsymbol{k}} \rho_{\boldsymbol{k}} \rho_{-\boldsymbol{k}}, \tag{5.87}$$

with the Coulomb vertex $V_{\boldsymbol{k}}$ which for small wave vectors (without screening) is approximately

$$V_{\boldsymbol{k}} \approx \frac{4\pi e^2}{\boldsymbol{k}^2}, \tag{5.88}$$

and the density operator

$$\rho_{\boldsymbol{k}} = \rho^e_{\boldsymbol{k}} - \rho^i_{\boldsymbol{k}}, \tag{5.89}$$

where $\rho^e_{\boldsymbol{k}}$ is the electronic density operator and $\rho^i_{\boldsymbol{k}}$ is the ionic density operator defined as

$$\rho^e_{\boldsymbol{k}} = \sum_{\boldsymbol{q}} c^\dagger_{\boldsymbol{q}} c_{\boldsymbol{q}+\boldsymbol{k}}, \tag{5.90}$$

$$\rho^i_{\boldsymbol{k}} = -\sqrt{\mathcal{V}} \alpha_{\boldsymbol{k}} \sum_{\lambda} \left(b_{\lambda,\boldsymbol{k}} + b^\dagger_{\lambda,-\boldsymbol{k}} \right). \tag{5.91}$$

The resulting Hamiltonian can be written as

$$\begin{aligned} \mathcal{H} = & \sum_{\boldsymbol{k}} \epsilon_{\boldsymbol{k}} c^\dagger_{\boldsymbol{k}} c_{\boldsymbol{k}} + \sum_{\boldsymbol{q},\lambda} \left(\frac{1}{2} + \omega_{\boldsymbol{q},\lambda} + V_{\boldsymbol{q}} \alpha^2_{\boldsymbol{q}} \right) b^\dagger_{\boldsymbol{q},\lambda} b_{\boldsymbol{q},\lambda} \\ & + \frac{1}{\sqrt{\mathcal{V}}} \sum_{\lambda,\boldsymbol{k},\boldsymbol{q}} \left(\gamma_{\boldsymbol{q},\lambda} + V_{\boldsymbol{q}} \alpha_{\boldsymbol{q}} \right) c^\dagger_{\boldsymbol{k}+\boldsymbol{q}} c_{\boldsymbol{k}} \left(b_{\boldsymbol{q},\lambda} + b^\dagger_{-\boldsymbol{q},\lambda} \right) \\ & + \frac{1}{2\mathcal{V}} \sum_{\boldsymbol{k}} V_{\boldsymbol{k}} \rho^e_{\boldsymbol{k}} \rho^e_{-\boldsymbol{k}} + \frac{1}{2\mathcal{V}} \sum_{\boldsymbol{q},\lambda} V_{\boldsymbol{q}} \alpha^2_{\boldsymbol{q}} \left(1 + b_{\boldsymbol{q},\lambda} b_{-\boldsymbol{q},\lambda} + b^\dagger_{-\boldsymbol{q},\lambda} b^\dagger_{\boldsymbol{q},\lambda} \right). \end{aligned} \tag{5.92}$$

The additional contribution in the first line can be reabsorbed into a renormalized phonon frequency and the same can be done for the electron-phonon coupling constant so that the renormalized quantities are

$$\tilde{\omega}_{\boldsymbol{q},\lambda} = \omega_{\boldsymbol{q},\lambda} + V_{\boldsymbol{q}} \alpha^2_{\boldsymbol{q}}, \tag{5.93a}$$

$$\tilde{\gamma}_{\boldsymbol{q},\lambda} = \gamma_{\boldsymbol{q},\lambda} + V_{\boldsymbol{q}} \alpha_{\boldsymbol{q}}. \tag{5.93b}$$

5.6.1 Off-diagonal phonon distribution function

The new contributions in the last line of the above Hamiltonian (5.92) lead to non-vanishing off-diagonal phonon distribution functions which are defined by

$$p_{\boldsymbol{q},\lambda} \equiv \langle b_{-\boldsymbol{q},\lambda} b_{\boldsymbol{q},\lambda} \rangle. \tag{5.94}$$

If only one phonon mode exists the phononic part of the Hamiltonian (5.92) may be diagonalized via a canonical transformation. This can be done by applying to the Hamiltonian (5.92) a Bogoliubov transformation of the form

$$\begin{pmatrix} \tilde{b}_{\boldsymbol{q}} \\ \tilde{b}^{\dagger}_{-\boldsymbol{q}} \end{pmatrix} = \begin{pmatrix} \tilde{u}_{\boldsymbol{q}} & -\tilde{v}_{\boldsymbol{q}} \\ -\tilde{v}^{*}_{\boldsymbol{q}} & \tilde{u}_{\boldsymbol{q}} \end{pmatrix} \begin{pmatrix} b_{\boldsymbol{q}} \\ b^{\dagger}_{-\boldsymbol{q}} \end{pmatrix}, \tag{5.95}$$

with

$$\tilde{u}_{\boldsymbol{q}} = \sqrt{\frac{\Omega_{\boldsymbol{q}} + \tilde{\omega}_{\boldsymbol{q}}}{2\Omega_{\boldsymbol{q}}}}, \tag{5.96a}$$

$$\tilde{v}_{\boldsymbol{q}} = \frac{V_{\boldsymbol{q}} \alpha^2_{\boldsymbol{q}}}{|V_{\boldsymbol{q}} \alpha^2_{\boldsymbol{q}}|} \sqrt{\frac{\Omega_{\boldsymbol{q}} - \tilde{\omega}_{\boldsymbol{q}}}{2\Omega_{\boldsymbol{q}}}}, \tag{5.96b}$$

$$\Omega_{\boldsymbol{q},\lambda} = \sqrt{\tilde{\omega}^2_{\boldsymbol{q}} - \left(V_{\boldsymbol{q}} \alpha^2_{\boldsymbol{q}}\right)^2} = \omega_{\boldsymbol{q},\lambda} \sqrt{1 + \frac{2 V_{\boldsymbol{q}} \alpha^2_{\boldsymbol{q}}}{\omega_{\boldsymbol{q}}}}. \tag{5.96c}$$

The electron-phonon interaction vertex becomes under this transformation

$$\Gamma_{\boldsymbol{q}} = \tilde{\gamma}_{\boldsymbol{q}} \frac{\sqrt{\Omega_{\boldsymbol{q}} + \tilde{\omega}_{\boldsymbol{q}}} + \sqrt{\Omega_{\boldsymbol{q}} - \tilde{\omega}_{\boldsymbol{q}}}}{\sqrt{2\Omega_{\boldsymbol{q}}}}. \tag{5.97}$$

However, for the experimentally relevant materials many phonon modes exist which makes the diagonalization of the phononic part of the Hamiltonian (5.92) not feasible. An alternative is to explicitly take into account the off-diagonal phonon distribution function. The corresponding equation of motion for the non-interacting system can be obtained from the Heisenberg equations of motion by only taking into account the quadratic parts of the Hamiltonian (5.92). Introducing a collision integral that describes the effects of interactions on the right-hand side of the equation of motion and defining the off-diagonal phonon correlation function as

$$p^c_{\boldsymbol{q},\lambda} = \langle b_{-\boldsymbol{q},\lambda} b_{\boldsymbol{q},\lambda} \rangle^c = p^c_{\boldsymbol{q},\lambda} - |\psi_{\boldsymbol{q},\lambda}|^2, \tag{5.98}$$

the equation of motion of the off-diagonal phonon correlations reads

$$\frac{d}{dt} p^c_{\boldsymbol{q},\lambda} + i\tilde{\omega}_{\boldsymbol{q},\lambda} \left(p^c_{\boldsymbol{q},\lambda} + p^c_{-\boldsymbol{q},\lambda}\right) + 2i V_{\boldsymbol{q}} \alpha^2_{\boldsymbol{q}} \left(1 + n^c_{\boldsymbol{q},\lambda} + n^c_{-\boldsymbol{q},\lambda}\right) = \tilde{I}^n_{\boldsymbol{q},\lambda}. \tag{5.99}$$

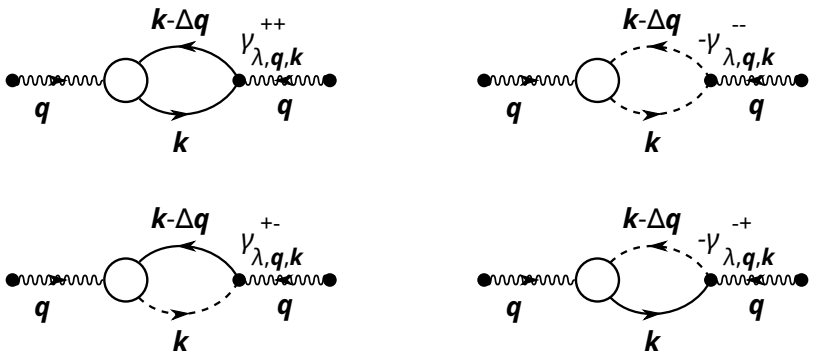

Figure 5.15: Diagrams representing the contributions to the collision integral $\tilde{I}^n_{\boldsymbol{q},\lambda}$ of the off-diagonal phonon distribution function $p^c_{\boldsymbol{q},\lambda}$. The symbols have the same meaning as in Fig. 5.1. Note that a prefactor of 2 appears because for each diagram there are two contributions that both lead to the same terms in the collision integral.

The diagrams that contribute to the collision integral $\tilde{I}^n_{\boldsymbol{q},\lambda}$ are shown in Fig. 5.15. They give

$$\tilde{I}^n_{\boldsymbol{q},\lambda} = -\frac{i}{\sqrt{\mathcal{V}}} \sum_{\boldsymbol{k},\sigma,\alpha=\pm,\beta=\pm} \left[\alpha \tilde{\gamma}^{\alpha\beta}_{\lambda,\boldsymbol{q},\boldsymbol{k}} \langle d^{\beta}_{\boldsymbol{k},\sigma} \left(d^{\alpha}_{\boldsymbol{k}-\boldsymbol{q}+\boldsymbol{Q},\sigma} \right)^{\dagger} b^{\dagger}_{\boldsymbol{q},\lambda} \rangle^c \right]. \tag{5.100}$$

Comparing the above equation with Eq. (5.34c) the similarity of these two expressions becomes apparent. The above equation (5.100) has a prefactor of 1/2 and here the imaginary part also contributes to the expression while it drops out in Eq. (5.34c). For this reason the principal value of the collision integral $\tilde{I}^n_{\boldsymbol{q},\lambda}$ needs to be calculated as well if the Markovian approximation that has been used to derive the collision integral $I^{(1/2)}_{\boldsymbol{q},\lambda}$ is applied here.

The off-diagonal collision integral reads

$$\begin{aligned}\tilde{I}^{n}_{\boldsymbol{q},\lambda} = \frac{\pi}{\mathcal{V}} \sum_{\boldsymbol{k},\sigma} \frac{|\gamma_{\boldsymbol{q},\lambda}|^2}{E_{\boldsymbol{k}} E_{\boldsymbol{k}-\boldsymbol{q}+\boldsymbol{Q}}} \Bigg[\delta\left(E_{\boldsymbol{k}-\boldsymbol{q}+\boldsymbol{Q}} - E_{\boldsymbol{k}} - \omega_{\boldsymbol{q},\lambda}\right) \Bigg(\left[E_{\boldsymbol{k}} - \xi_{\boldsymbol{k}}\right] \left[E_{\boldsymbol{k}-\boldsymbol{q}+\boldsymbol{Q}} + \xi_{\boldsymbol{k}-\boldsymbol{q}+\boldsymbol{Q}}\right] \\ \times \left[\left(1 - f^{-}_{\boldsymbol{k}-\boldsymbol{q}+\boldsymbol{Q},\sigma}\right) f^{-}_{\boldsymbol{k},\sigma} \left(1 + n^{c}_{-\boldsymbol{q},\lambda}\right) - f^{-}_{\boldsymbol{k}-\boldsymbol{q}+\boldsymbol{Q},\sigma} \left(1 - f^{-}_{\boldsymbol{k},\sigma}\right) n^{c}_{-\boldsymbol{q},\lambda} \right] \\ + \Delta\left[E_{\boldsymbol{k}} - \xi_{\boldsymbol{k}}\right] \tilde{f}^{-}_{\boldsymbol{k}-\boldsymbol{q}+\boldsymbol{Q},\sigma} \left[f^{-}_{\boldsymbol{k},\sigma} \left(1 + n^{c}_{-\boldsymbol{q},\lambda}\right) + \left(1 - f^{-}_{\boldsymbol{k},\sigma}\right) n^{c}_{-\boldsymbol{q},\lambda} + p^{c}_{-\boldsymbol{q},\lambda} \right] \\ - \Delta^{*}\left[E_{\boldsymbol{k}-\boldsymbol{q}+\boldsymbol{Q}} + \xi_{\boldsymbol{k}-\boldsymbol{q}+\boldsymbol{Q}}\right] \tilde{f}^{+}_{\boldsymbol{k},\sigma} \left[\left(1 - f^{-}_{\boldsymbol{k}-\boldsymbol{q}+\boldsymbol{Q},\sigma}\right) \left(1 + n^{c}_{-\boldsymbol{q},\lambda}\right) + f^{-}_{\boldsymbol{k}-\boldsymbol{q}+\boldsymbol{Q},\sigma} n^{c}_{-\boldsymbol{q},\lambda} + p^{c}_{-\boldsymbol{q},\lambda} \right] \\ - |\Delta|^2 \tilde{f}^{-}_{\boldsymbol{k}-\boldsymbol{q}+\boldsymbol{Q},\sigma} \tilde{f}^{+}_{\boldsymbol{k},\sigma} \Bigg) - \delta\left(E_{\boldsymbol{k}-\boldsymbol{q}+\boldsymbol{Q}} - E_{\boldsymbol{k}} + \omega_{\boldsymbol{q},\lambda}\right) \Bigg(\left[E_{\boldsymbol{k}} + \xi_{\boldsymbol{k}}\right] \left[E_{\boldsymbol{k}-\boldsymbol{q}+\boldsymbol{Q}} - \xi_{\boldsymbol{k}-\boldsymbol{q}+\boldsymbol{Q}}\right] \\ \times \left[\left(1 - f^{+}_{\boldsymbol{k}-\boldsymbol{q}+\boldsymbol{Q},\sigma}\right) f^{+}_{\boldsymbol{k},\sigma} \left(1 + n^{c}_{-\boldsymbol{q},\lambda}\right) - f^{+}_{\boldsymbol{k}-\boldsymbol{q}+\boldsymbol{Q},\sigma} \left(1 - f^{+}_{\boldsymbol{k},\sigma}\right) n^{c}_{-\boldsymbol{q},\lambda} \right] \\ + \Delta\left[E_{\boldsymbol{k}} + \xi_{\boldsymbol{k}}\right] \tilde{f}^{+}_{\boldsymbol{k}-\boldsymbol{q}+\boldsymbol{Q},\sigma} \left[f^{+}_{\boldsymbol{k},\sigma} \left(1 + n^{c}_{-\boldsymbol{q},\lambda}\right) + \left(1 - f^{+}_{\boldsymbol{k},\sigma}\right) n^{c}_{-\boldsymbol{q},\lambda} + p^{c}_{-\boldsymbol{q},\lambda} \right] \\ - \Delta^{*}\left[E_{\boldsymbol{k}-\boldsymbol{q}+\boldsymbol{Q}} - \xi_{\boldsymbol{k}-\boldsymbol{q}+\boldsymbol{Q}}\right] \tilde{f}^{-}_{\boldsymbol{k},\sigma} \left[\left(1 - f^{+}_{\boldsymbol{k}-\boldsymbol{q}+\boldsymbol{Q},\sigma}\right) \left(1 + n^{c}_{-\boldsymbol{q},\lambda}\right) + f^{+}_{\boldsymbol{k}-\boldsymbol{q}+\boldsymbol{Q},\sigma} n^{c}_{-\boldsymbol{q},\lambda} + p^{c}_{-\boldsymbol{q},\lambda} \right] \\ - |\Delta|^2 \tilde{f}^{+}_{\boldsymbol{k}-\boldsymbol{q}+\boldsymbol{Q},\sigma} \tilde{f}^{-}_{\boldsymbol{k},\sigma} \Bigg) - \delta\left(E_{\boldsymbol{k}-\boldsymbol{q}+\boldsymbol{Q}} + E_{\boldsymbol{k}} - \omega_{\boldsymbol{q},\lambda}\right) \\ \times \Bigg(\Delta^2 \left[\left(1 - f^{-}_{\boldsymbol{k}-\boldsymbol{q}+\boldsymbol{Q},\sigma}\right) f^{+}_{\boldsymbol{k},\sigma} \left(1 + n^{c}_{-\boldsymbol{q},\lambda}\right) - f^{-}_{\boldsymbol{k}-\boldsymbol{q}+\boldsymbol{Q},\sigma} \left(1 - f^{+}_{\boldsymbol{k},\sigma}\right) n^{c}_{-\boldsymbol{q},\lambda} \right] \\ + \Delta\left[E_{\boldsymbol{k}} - \xi_{\boldsymbol{k}}\right] \tilde{f}^{-}_{\boldsymbol{k}-\boldsymbol{q}+\boldsymbol{Q},\sigma} \left[f^{+}_{\boldsymbol{k},\sigma} \left(1 + n^{c}_{-\boldsymbol{q},\lambda}\right) + \left(1 - f^{+}_{\boldsymbol{k},\sigma}\right) n^{c}_{-\boldsymbol{q},\lambda} + p^{c}_{-\boldsymbol{q},\lambda} \right] \\ - \Delta\left[E_{\boldsymbol{k}-\boldsymbol{q}+\boldsymbol{Q}} - \xi_{\boldsymbol{k}-\boldsymbol{q}+\boldsymbol{Q}}\right] \tilde{f}^{-}_{\boldsymbol{k},\sigma} \left[\left(1 - f^{-}_{\boldsymbol{k}-\boldsymbol{q}+\boldsymbol{Q},\sigma}\right) \left(1 + n^{c}_{-\boldsymbol{q},\lambda}\right) + f^{-}_{\boldsymbol{k}-\boldsymbol{q}+\boldsymbol{Q},\sigma} n^{c}_{-\boldsymbol{q},\lambda} + p^{c}_{-\boldsymbol{q},\lambda} \right] \\ - \left[E_{\boldsymbol{k}} - \xi_{\boldsymbol{k}}\right] \left[E_{\boldsymbol{k}-\boldsymbol{q}+\boldsymbol{Q}} - \xi_{\boldsymbol{k}-\boldsymbol{q}+\boldsymbol{Q}}\right] \tilde{f}^{-}_{\boldsymbol{k}-\boldsymbol{q}+\boldsymbol{Q},\sigma} \tilde{f}^{-}_{\boldsymbol{k},\sigma} \Bigg) \Bigg].\end{aligned} \tag{5.101}$$

Furthermore, the off-diagonal distribution functions $p^{c}_{\boldsymbol{q},\lambda}$ appear in the other collision integrals $I^{\pm}_{\boldsymbol{k},\sigma}$, $\tilde{I}^{\pm}_{\boldsymbol{k},\sigma}$, and $I^{(1/2)}_{\boldsymbol{q},\lambda}$. Analogous to the above collision integral an additional $p^{c}_{\boldsymbol{q},\lambda}$ term appears in the contributions where one off-diagonal electronic distribution function $\tilde{f}^{\pm}_{\boldsymbol{k},\sigma}$ is present. The principal value of the off-diagonal collision integrals is

given by

$$
\begin{aligned}
\mathrm{pV}\tilde{I}^{n}_{\boldsymbol{q},\lambda} = \frac{i}{\mathcal{V}}\sum_{\boldsymbol{k},\sigma}\frac{|\gamma_{\boldsymbol{q},\lambda}|^2}{E_{\boldsymbol{k}}E_{\boldsymbol{k}-\boldsymbol{q}+\boldsymbol{Q}}}\Bigg[&\frac{1}{E_{\boldsymbol{k}-\boldsymbol{q}+\boldsymbol{Q}}-E_{\boldsymbol{k}}-\omega_{\boldsymbol{q},\lambda}}\Bigg([E_{\boldsymbol{k}}-\xi_{\boldsymbol{k}}]\left[E_{\boldsymbol{k}-\boldsymbol{q}+\boldsymbol{Q}}+\xi_{\boldsymbol{k}-\boldsymbol{q}+\boldsymbol{Q}}\right]\\
&\times\left[\left(1-f^{-}_{\boldsymbol{k}-\boldsymbol{q}+\boldsymbol{Q},\sigma}\right)f^{-}_{\boldsymbol{k},\sigma}\left(1+n^{c}_{-\boldsymbol{q},\lambda}\right)-f^{-}_{\boldsymbol{k}-\boldsymbol{q}+\boldsymbol{Q},\sigma}\left(1-f^{-}_{\boldsymbol{k},\sigma}\right)n^{c}_{-\boldsymbol{q},\lambda}\right]\\
&+\Delta\left[E_{\boldsymbol{k}}-\xi_{\boldsymbol{k}}\right]\tilde{f}^{-}_{\boldsymbol{k}-\boldsymbol{q}+\boldsymbol{Q},\sigma}\left[f^{-}_{\boldsymbol{k},\sigma}\left(1+n^{c}_{-\boldsymbol{q},\lambda}\right)+\left(1-f^{-}_{\boldsymbol{k},\sigma}\right)n^{c}_{-\boldsymbol{q},\lambda}+p^{c}_{-\boldsymbol{q},\lambda}\right]\\
&-\Delta^{*}\left[E_{\boldsymbol{k}-\boldsymbol{q}+\boldsymbol{Q}}+\xi_{\boldsymbol{k}-\boldsymbol{q}+\boldsymbol{Q}}\right]\tilde{f}^{+}_{\boldsymbol{k},\sigma}\left[\left(1-f^{-}_{\boldsymbol{k}-\boldsymbol{q}+\boldsymbol{Q},\sigma}\right)\left(1+n^{c}_{-\boldsymbol{q},\lambda}\right)+f^{-}_{\boldsymbol{k}-\boldsymbol{q}+\boldsymbol{Q},\sigma}n^{c}_{-\boldsymbol{q},\lambda}+p^{c}_{-\boldsymbol{q},\lambda}\right]\\
&-|\Delta|^2\,\tilde{f}^{-}_{\boldsymbol{k}-\boldsymbol{q}+\boldsymbol{Q},\sigma}\tilde{f}^{+}_{\boldsymbol{k},\sigma}\Bigg)-\frac{1}{E_{\boldsymbol{k}-\boldsymbol{q}+\boldsymbol{Q}}-E_{\boldsymbol{k}}+\omega_{\boldsymbol{q},\lambda}}\Bigg([E_{\boldsymbol{k}}+\xi_{\boldsymbol{k}}]\left[E_{\boldsymbol{k}-\boldsymbol{q}+\boldsymbol{Q}}-\xi_{\boldsymbol{k}-\boldsymbol{q}+\boldsymbol{Q}}\right]\\
&\times\left[\left(1-f^{+}_{\boldsymbol{k}-\boldsymbol{q}+\boldsymbol{Q},\sigma}\right)f^{+}_{\boldsymbol{k},\sigma}\left(1+n^{c}_{-\boldsymbol{q},\lambda}\right)-f^{+}_{\boldsymbol{k}-\boldsymbol{q}+\boldsymbol{Q},\sigma}\left(1-f^{+}_{\boldsymbol{k},\sigma}\right)n^{c}_{-\boldsymbol{q},\lambda}\right]\\
&+\Delta\left[E_{\boldsymbol{k}}+\xi_{\boldsymbol{k}}\right]\tilde{f}^{+}_{\boldsymbol{k}-\boldsymbol{q}+\boldsymbol{Q},\sigma}\left[f^{+}_{\boldsymbol{k},\sigma}\left(1+n^{c}_{-\boldsymbol{q},\lambda}\right)+\left(1-f^{+}_{\boldsymbol{k},\sigma}\right)n^{c}_{-\boldsymbol{q},\lambda}+p^{c}_{-\boldsymbol{q},\lambda}\right]\\
&-\Delta^{*}\left[E_{\boldsymbol{k}-\boldsymbol{q}+\boldsymbol{Q}}-\xi_{\boldsymbol{k}-\boldsymbol{q}+\boldsymbol{Q}}\right]\tilde{f}^{-}_{\boldsymbol{k},\sigma}\left[\left(1-f^{+}_{\boldsymbol{k}-\boldsymbol{q}+\boldsymbol{Q},\sigma}\right)\left(1+n^{c}_{-\boldsymbol{q},\lambda}\right)+f^{+}_{\boldsymbol{k}-\boldsymbol{q}+\boldsymbol{Q},\sigma}n^{c}_{-\boldsymbol{q},\lambda}+p^{c}_{-\boldsymbol{q},\lambda}\right]\\
&-|\Delta|^2\,\tilde{f}^{+}_{\boldsymbol{k}-\boldsymbol{q}+\boldsymbol{Q},\sigma}\tilde{f}^{-}_{\boldsymbol{k},\sigma}\Bigg)-\frac{1}{E_{\boldsymbol{k}-\boldsymbol{q}+\boldsymbol{Q}}+E_{\boldsymbol{k}}-\omega_{\boldsymbol{q},\lambda}}\\
&\times\Bigg(\Delta^2\left[\left(1-f^{-}_{\boldsymbol{k}-\boldsymbol{q}+\boldsymbol{Q},\sigma}\right)f^{+}_{\boldsymbol{k},\sigma}\left(1+n^{c}_{-\boldsymbol{q},\lambda}\right)-f^{-}_{\boldsymbol{k}-\boldsymbol{q}+\boldsymbol{Q},\sigma}\left(1-f^{+}_{\boldsymbol{k},\sigma}\right)n^{c}_{-\boldsymbol{q},\lambda}\right]\\
&+\Delta\left[E_{\boldsymbol{k}}-\xi_{\boldsymbol{k}}\right]\tilde{f}^{-}_{\boldsymbol{k}-\boldsymbol{q}+\boldsymbol{Q},\sigma}\left[f^{+}_{\boldsymbol{k},\sigma}\left(1+n^{c}_{-\boldsymbol{q},\lambda}\right)+\left(1-f^{+}_{\boldsymbol{k},\sigma}\right)n^{c}_{-\boldsymbol{q},\lambda}+p^{c}_{-\boldsymbol{q},\lambda}\right]\\
&-\Delta\left[E_{\boldsymbol{k}-\boldsymbol{q}+\boldsymbol{Q}}-\xi_{\boldsymbol{k}-\boldsymbol{q}+\boldsymbol{Q}}\right]\tilde{f}^{-}_{\boldsymbol{k},\sigma}\left[\left(1-f^{-}_{\boldsymbol{k}-\boldsymbol{q}+\boldsymbol{Q},\sigma}\right)\left(1+n^{c}_{-\boldsymbol{q},\lambda}\right)+f^{-}_{\boldsymbol{k}-\boldsymbol{q}+\boldsymbol{Q},\sigma}n^{c}_{-\boldsymbol{q},\lambda}+p^{c}_{-\boldsymbol{q},\lambda}\right]\\
&-\left[E_{\boldsymbol{k}}-\xi_{\boldsymbol{k}}\right]\left[E_{\boldsymbol{k}-\boldsymbol{q}+\boldsymbol{Q}}-\xi_{\boldsymbol{k}-\boldsymbol{q}+\boldsymbol{Q}}\right]\tilde{f}^{-}_{\boldsymbol{k}-\boldsymbol{q}+\boldsymbol{Q},\sigma}\tilde{f}^{-}_{\boldsymbol{k},\sigma}\Bigg)\Bigg].
\end{aligned}
\tag{5.102}
$$

5.6.2 Relation to mean-field approximation

Now, repeating the same procedure as in section 5.2 the canonical transformation (5.15) introduced in section 5.2.3 has to be applied to the electronic part of the Coulomb Hamiltonian. I get

$$
V_{\boldsymbol{k}}\rho^{e}_{\boldsymbol{k}}\rho^{e}_{-\boldsymbol{k}} = \sum_{\substack{\boldsymbol{q}_1,\,\boldsymbol{q}_2,\\ r_1,r_2,r_3,r_4=\pm}}\left[r_2r_3\tilde{\gamma}^{r_1\bar{r}_2r_3\bar{r}_4}_{\boldsymbol{k},\boldsymbol{q}_1,\boldsymbol{q}_2}\left(d^{(r_1)}_{\boldsymbol{q}_1-\Delta\boldsymbol{k}}\right)^{\dagger}d^{(r_2)}_{\boldsymbol{q}_1+\Delta\boldsymbol{k}}\left(d^{(r_3)}_{\boldsymbol{q}_2+\Delta\boldsymbol{k}}\right)^{\dagger}d^{(r_4)}_{\boldsymbol{q}_2-\Delta\boldsymbol{k}}+\mathrm{h.c.}\right],
\tag{5.103}
$$

with $\Delta\boldsymbol{k} = \frac{\boldsymbol{k}}{2} - \frac{\boldsymbol{Q}}{2}$ and

$$\bar{r} = -r. \tag{5.104}$$

The four-point vertices are given by

$$\Gamma^{r_1 r_2 r_3 r_4}_{\boldsymbol{k},\boldsymbol{q}_1,\boldsymbol{q}_2} = V_{\boldsymbol{k}} \tilde{u}^{r_1}_{\boldsymbol{q}_1+\Delta\boldsymbol{k}} \tilde{u}^{r_2}_{\boldsymbol{q}_1-\Delta\boldsymbol{k}} \left(\tilde{u}^{r_3}_{\boldsymbol{q}_2+\Delta\boldsymbol{k}}\right)^* \left(\tilde{u}^{r_4}_{\boldsymbol{q}_2-\Delta\boldsymbol{k}}\right)^*, \tag{5.105}$$

where $r_1, r_2, r_3, r_4 = \pm$ and

$$\tilde{u}^{+}_{\boldsymbol{q}} = \tilde{u}_{\boldsymbol{q}}, \tag{5.106a}$$

$$\tilde{u}^{-}_{\boldsymbol{q}} = \tilde{v}_{\boldsymbol{q}}. \tag{5.106b}$$

5.6.3 Collision integrals

Additional contributions originating from the Coulomb interaction appear in the collision integrals of the fermionic correlation functions $f^{\pm}_{\boldsymbol{k},\sigma}$ and $\tilde{f}^{\pm}_{\boldsymbol{k},\sigma}$. These contributions are shown diagrammatically in Fig. 5.16 and 5.17. They evaluate to

$$I^{C\pm}_{\boldsymbol{k},\sigma} = \frac{i}{\mathcal{V}} \sum_{\substack{\boldsymbol{q} \\ r_1, r_2, r_3 = \pm}} \mathrm{Re}\left[r_1 r_3 \tilde{\gamma}^{\pm \bar{r}_1 r_2 \bar{r}_3}_{\boldsymbol{k},\boldsymbol{k}-\Delta\boldsymbol{k},\boldsymbol{q}} \langle \left(d^{\pm}_{\boldsymbol{k},\sigma}\right)^\dagger \left(d^{(r_3)}_{\boldsymbol{q}-\Delta\boldsymbol{k},\sigma}\right)^\dagger d^{(r_1)}_{\boldsymbol{k}-2\Delta\boldsymbol{k},\sigma} d^{(r_2)}_{\boldsymbol{q}+\Delta\boldsymbol{k},\sigma} \rangle^c \right], \tag{5.107a}$$

$$\tilde{I}^{C\pm}_{\boldsymbol{k},\sigma} = \frac{i}{\mathcal{V}} \sum_{\substack{\boldsymbol{q} \\ r_1, r_2, r_3 = \pm}} \mathrm{Re}\left[r_1 r_3 \tilde{\gamma}^{\pm \bar{r}_1 r_2 \bar{r}_3}_{\boldsymbol{k},\boldsymbol{k}-\Delta\boldsymbol{k},\boldsymbol{q}} \langle \left(d^{\mp}_{\boldsymbol{k},\sigma}\right)^\dagger \left(d^{(r_3)}_{\boldsymbol{q}-\Delta\boldsymbol{k},\sigma}\right)^\dagger d^{(r_1)}_{\boldsymbol{k}-2\Delta\boldsymbol{k},\sigma} d^{(r_2)}_{\boldsymbol{q}+\Delta\boldsymbol{k},\sigma} \rangle^c \right], \tag{5.107b}$$

Four-point correlations appear in the above collision integrals. Therefore, the lowest order diagrams for these four-point correlations need to be evaluated. They are shown in Fig. 5.18. Analogously to the procedure in the previous chapters, the resulting equations of motion are formally integrated and a Markovian approximation is applied. Neglecting

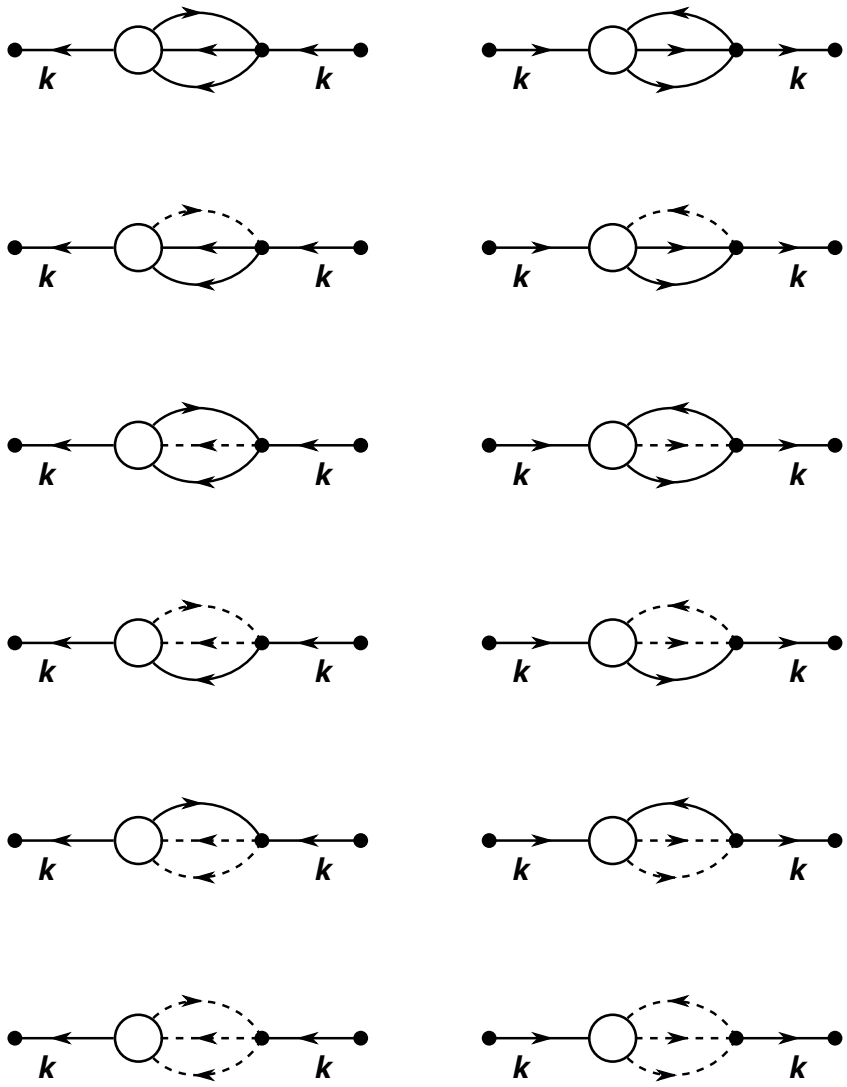

Figure 5.16: The diagrams representing the contributions to the time evolution of the electronic distribution function $f^{+}_{\boldsymbol{k},\sigma}$ that originate from Coulomb interactions. They contain the Coulomb vertex and a four-point correlation. The diagrams contributing to the time evolution of $f^{-}_{\boldsymbol{k},\sigma}$ have the same form.

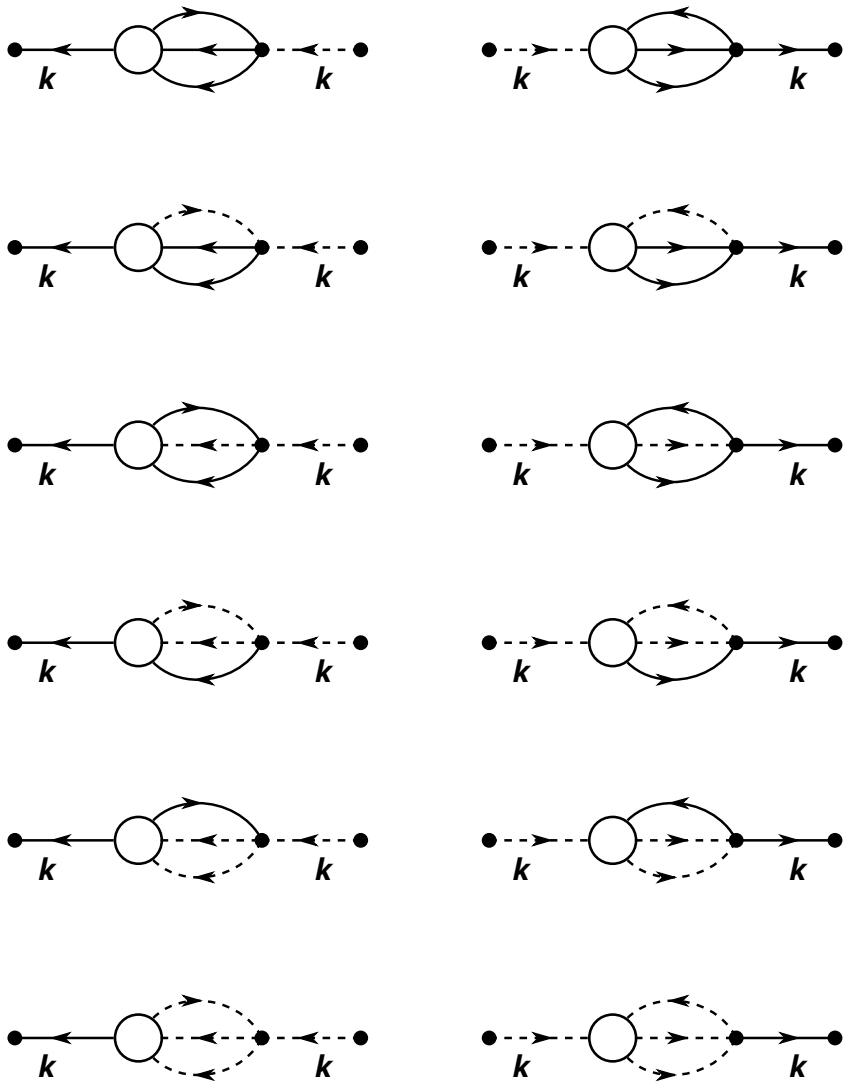

Figure 5.17: The diagrams representing the contributions to the time evolution of the electronic distribution function $\tilde{f}^{+}_{\boldsymbol{k},\sigma}$ that originate from Coulomb interactions. They contain the Coulomb vertex and a four-point correlation. The diagrams contributing to the time evolution of $\tilde{f}^{-}_{\boldsymbol{k},\sigma}$ have the same form.

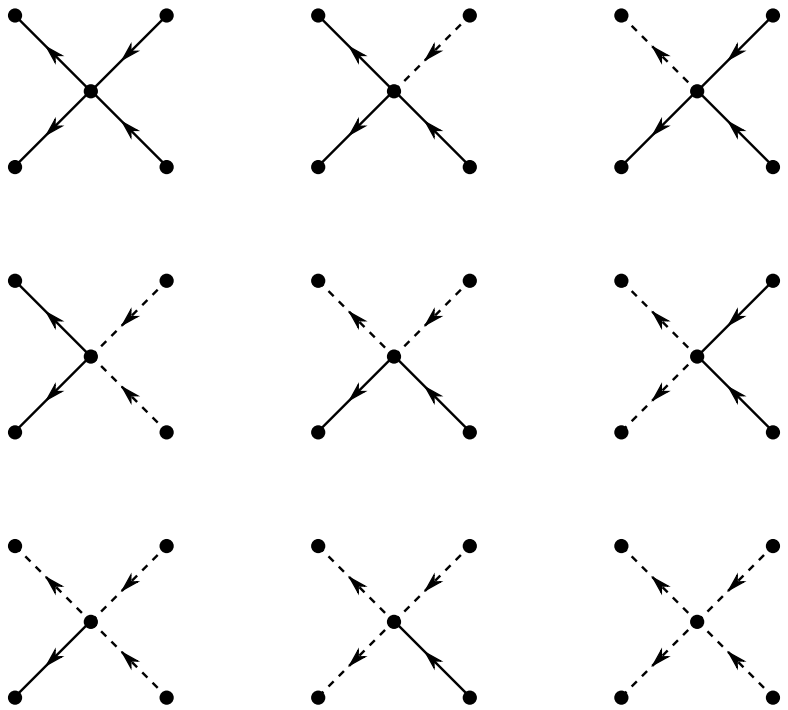

Figure 5.18: The diagrams representing the contributions to the time evolution of the four-point correlation functions appearing in the collision integrals of the electronic distribution functions. They contain the Coulomb vertex and contractions.

the off-diagonal electronic distribution function $\tilde{f}_{\boldsymbol{k},\sigma}$ I get

$$
\begin{aligned}
I^{C\pm}_{\boldsymbol{k},\sigma} = \frac{\pi}{2\mathcal{V}^2} \sum_{\substack{\boldsymbol{q} \\ r_1,r_2,r_3=\pm}} \mathrm{Re}\Bigg[& r_1 r_3 \delta\left(\pm E_{\boldsymbol{k}} + r_3 E_{\boldsymbol{q}-\Delta\boldsymbol{k}} - r_1 E_{\boldsymbol{k}-2\Delta\boldsymbol{k}} - r_2 E_{\boldsymbol{q}+\Delta\boldsymbol{k}}\right) \\
& \times \Bigg(\left|\tilde{\gamma}^{\pm\bar{r}_1 r_2 \bar{r}_3}_{\boldsymbol{k},\boldsymbol{k}-\Delta\boldsymbol{k},\boldsymbol{q}}\right|^2 \Bigg[\left(1 - f^{(r_1)}_{\boldsymbol{k}-2\Delta\boldsymbol{k},\sigma}\right)\left(1 - f^{(r_2)}_{\boldsymbol{q}+\Delta\boldsymbol{k},\sigma}\right) f^{\pm}_{\boldsymbol{k},\sigma} f^{(r_3)}_{\boldsymbol{q}-\Delta\boldsymbol{k},\sigma} \\
& \qquad - f^{(r_1)}_{\boldsymbol{k}-2\Delta\boldsymbol{k},\sigma} f^{(r_2)}_{\boldsymbol{q}+\Delta\boldsymbol{k},\sigma}\left(1 - f^{\pm}_{\boldsymbol{k},\sigma}\right)\left(1 - f^{(r_3)}_{\boldsymbol{q}-\Delta\boldsymbol{k},\sigma}\right)\Bigg] \\
& + \tilde{\gamma}^{\pm\bar{r}_1 r_2 \bar{r}_3}_{\boldsymbol{k},\boldsymbol{k}-\Delta\boldsymbol{k},\boldsymbol{q}} \left(\tilde{\gamma}^{\pm r_1 r_2 \bar{r}_3}_{\boldsymbol{k},\boldsymbol{k}-\Delta\boldsymbol{k},\boldsymbol{q}}\right)^* \tilde{f}^{(r_1)}_{\boldsymbol{k}-2\Delta\boldsymbol{k},\sigma} \Bigg[\left(1 - f^{(r_2)}_{\boldsymbol{q}+\Delta\boldsymbol{k},\sigma}\right) f^{\pm}_{\boldsymbol{k},\sigma} f^{(r_3)}_{\boldsymbol{q}-\Delta\boldsymbol{k},\sigma} \\
& \qquad - f^{(r_2)}_{\boldsymbol{q}+\Delta\boldsymbol{k},\sigma}\left(1 - f^{\pm}_{\boldsymbol{k},\sigma}\right)\left(1 - f^{(r_3)}_{\boldsymbol{q}-\Delta\boldsymbol{k},\sigma}\right)\Bigg] \\
& + \tilde{\gamma}^{\pm\bar{r}_1 r_2 \bar{r}_3}_{\boldsymbol{k},\boldsymbol{k}-\Delta\boldsymbol{k},\boldsymbol{q}} \left(\tilde{\gamma}^{\pm\bar{r}_1 \bar{r}_2 \bar{r}_3}_{\boldsymbol{k},\boldsymbol{k}-\Delta\boldsymbol{k},\boldsymbol{q}}\right)^* \tilde{f}^{(r_2)}_{\boldsymbol{q}+\Delta\boldsymbol{k},\sigma} \Bigg[\left(1 - f^{(r_1)}_{\boldsymbol{k}-2\Delta\boldsymbol{k},\sigma}\right) f^{\pm}_{\boldsymbol{k},\sigma} f^{(r_3)}_{\boldsymbol{q}-\Delta\boldsymbol{k},\sigma} \\
& \qquad - f^{(r_1)}_{\boldsymbol{k}-2\Delta\boldsymbol{k},\sigma}\left(1 - f^{\pm}_{\boldsymbol{k},\sigma}\right)\left(1 - f^{(r_3)}_{\boldsymbol{q}-\Delta\boldsymbol{k},\sigma}\right)\Bigg]
\end{aligned}
$$

$$
\begin{aligned}
&-\tilde{\gamma}^{\pm\bar{r}_1 r_2 \bar{r}_3}_{\boldsymbol{k},\boldsymbol{k}-\Delta\boldsymbol{k},\boldsymbol{q}} \left(\tilde{\gamma}^{\mp\bar{r}_1 r_2 \bar{r}_3}_{\boldsymbol{k},\boldsymbol{k}-\Delta\boldsymbol{k},\boldsymbol{q}}\right)^* \tilde{f}^{\mp}_{\boldsymbol{k},\sigma} \Big[\left(1 - f^{(r_1)}_{\boldsymbol{k}-2\Delta\boldsymbol{k},\sigma}\right) \left(1 - f^{(r_2)}_{\boldsymbol{q}+\Delta\boldsymbol{k},\sigma}\right) f^{(r_3)}_{\boldsymbol{q}-\Delta\boldsymbol{k},\sigma} \\
&\qquad - f^{(r_1)}_{\boldsymbol{k}-2\Delta\boldsymbol{k},\sigma} f^{(r_2)}_{\boldsymbol{q}+\Delta\boldsymbol{k},\sigma} \left(1 - f^{(r_3)}_{\boldsymbol{q}-\Delta\boldsymbol{k},\sigma}\right) \Big] \\
&-\tilde{\gamma}^{\pm\bar{r}_1 r_2 \bar{r}_3}_{\boldsymbol{k},\boldsymbol{k}-\Delta\boldsymbol{k},\boldsymbol{q}} \left(\tilde{\gamma}^{\pm\bar{r}_1 r_2 r_3}_{\boldsymbol{k},\boldsymbol{k}-\Delta\boldsymbol{k},\boldsymbol{q}}\right)^* \tilde{f}^{(-r_3)}_{\boldsymbol{q}-\Delta\boldsymbol{k},\sigma} \Big[\left(1 - f^{(r_1)}_{\boldsymbol{k}-2\Delta\boldsymbol{k},\sigma}\right) \left(1 - f^{(r_2)}_{\boldsymbol{q}+\Delta\boldsymbol{k},\sigma}\right) f^{\pm}_{\boldsymbol{k},\sigma} \\
&\qquad - f^{(r_1)}_{\boldsymbol{k}-2\Delta\boldsymbol{k},\sigma} f^{(r_2)}_{\boldsymbol{q}+\Delta\boldsymbol{k},\sigma} \left(1 - f^{\pm}_{\boldsymbol{k},\sigma}\right) \Big] \\
&+\tilde{\gamma}^{\pm\bar{r}_1 r_2 \bar{r}_3}_{\boldsymbol{k},\boldsymbol{k}-\Delta\boldsymbol{k},\boldsymbol{q}} \left(\tilde{\gamma}^{\pm r_1 \bar{r}_2 \bar{r}_3}_{\boldsymbol{k},\boldsymbol{k}-\Delta\boldsymbol{k},\boldsymbol{q}}\right)^* \tilde{f}^{(r_1)}_{\boldsymbol{k}-2\Delta\boldsymbol{k},\sigma} \tilde{f}^{(r_2)}_{\boldsymbol{q}+\Delta\boldsymbol{k},\sigma} \Big[f^{\pm}_{\boldsymbol{k},\sigma} f^{(r_3)}_{\boldsymbol{q}-\Delta\boldsymbol{k},\sigma} \\
&\qquad - \left(1 - f^{\pm}_{\boldsymbol{k},\sigma}\right) \left(1 - f^{(r_3)}_{\boldsymbol{q}-\Delta\boldsymbol{k},\sigma}\right) \Big] \\
&-\tilde{\gamma}^{\pm\bar{r}_1 r_2 \bar{r}_3}_{\boldsymbol{k},\boldsymbol{k}-\Delta\boldsymbol{k},\boldsymbol{q}} \left(\tilde{\gamma}^{\pm r_1 r_2 r_3}_{\boldsymbol{k},\boldsymbol{k}-\Delta\boldsymbol{k},\boldsymbol{q}}\right)^* \tilde{f}^{(r_1)}_{\boldsymbol{k}-2\Delta\boldsymbol{k},\sigma} \tilde{f}^{(-r_3)}_{\boldsymbol{q}-\Delta\boldsymbol{k},\sigma} \Big[\left(1 - f^{(r_2)}_{\boldsymbol{q}+\Delta\boldsymbol{k},\sigma}\right) f^{\pm}_{\boldsymbol{k},\sigma} \\
&\qquad - f^{(r_2)}_{\boldsymbol{q}+\Delta\boldsymbol{k},\sigma} \left(1 - f^{\pm}_{\boldsymbol{k},\sigma}\right) \Big] \\
&-\tilde{\gamma}^{\pm\bar{r}_1 r_2 \bar{r}_3}_{\boldsymbol{k},\boldsymbol{k}-\Delta\boldsymbol{k},\boldsymbol{q}} \left(\tilde{\gamma}^{\mp r_1 r_2 \bar{r}_3}_{\boldsymbol{k},\boldsymbol{k}-\Delta\boldsymbol{k},\boldsymbol{q}}\right)^* \tilde{f}^{(r_1)}_{\boldsymbol{k}-2\Delta\boldsymbol{k},\sigma} \tilde{f}^{\mp}_{\boldsymbol{k},\sigma} \Big[\left(1 - f^{(r_2)}_{\boldsymbol{q}+\Delta\boldsymbol{k},\sigma}\right) f^{(r_3)}_{\boldsymbol{q}-\Delta\boldsymbol{k},\sigma} \\
&\qquad - f^{(r_2)}_{\boldsymbol{q}+\Delta\boldsymbol{k},\sigma} \left(1 - f^{(r_3)}_{\boldsymbol{q}-\Delta\boldsymbol{k},\sigma}\right) \Big] \\
&-\tilde{\gamma}^{\pm\bar{r}_1 r_2 \bar{r}_3}_{\boldsymbol{k},\boldsymbol{k}-\Delta\boldsymbol{k},\boldsymbol{q}} \left(\tilde{\gamma}^{\pm\bar{r}_1 \bar{r}_2 r_3}_{\boldsymbol{k},\boldsymbol{k}-\Delta\boldsymbol{k},\boldsymbol{q}}\right)^* \tilde{f}^{(r_2)}_{\boldsymbol{q}+\Delta\boldsymbol{k},\sigma} \tilde{f}^{(-r_3)}_{\boldsymbol{q}-\Delta\boldsymbol{k},\sigma} \Big[\left(1 - f^{(r_1)}_{\boldsymbol{k}-2\Delta\boldsymbol{k},\sigma}\right) f^{\pm}_{\boldsymbol{k},\sigma} \\
&\qquad - f^{(r_1)}_{\boldsymbol{k}-2\Delta\boldsymbol{k},\sigma} \left(1 - f^{\pm}_{\boldsymbol{k},\sigma}\right) \Big] \\
&-\tilde{\gamma}^{\pm\bar{r}_1 r_2 \bar{r}_3}_{\boldsymbol{k},\boldsymbol{k}-\Delta\boldsymbol{k},\boldsymbol{q}} \left(\tilde{\gamma}^{\mp\bar{r}_1 \bar{r}_2 \bar{r}_3}_{\boldsymbol{k},\boldsymbol{k}-\Delta\boldsymbol{k},\boldsymbol{q}}\right)^* \tilde{f}^{(r_2)}_{\boldsymbol{q}+\Delta\boldsymbol{k},\sigma} \tilde{f}^{\mp}_{\boldsymbol{k},\sigma} \Big[\left(1 - f^{(r_1)}_{\boldsymbol{k}-2\Delta\boldsymbol{k},\sigma}\right) f^{(r_3)}_{\boldsymbol{q}-\Delta\boldsymbol{k},\sigma} \\
&\qquad - f^{(r_1)}_{\boldsymbol{k}-2\Delta\boldsymbol{k},\sigma} \left(1 - f^{(r_3)}_{\boldsymbol{q}-\Delta\boldsymbol{k},\sigma}\right) \Big] \\
&+\tilde{\gamma}^{\pm\bar{r}_1 r_2 \bar{r}_3}_{\boldsymbol{k},\boldsymbol{k}-\Delta\boldsymbol{k},\boldsymbol{q}} \left(\tilde{\gamma}^{\mp\bar{r}_1 r_2 r_3}_{\boldsymbol{k},\boldsymbol{k}-\Delta\boldsymbol{k},\boldsymbol{q}}\right)^* \tilde{f}^{(-r_3)}_{\boldsymbol{q}-\Delta\boldsymbol{k},\sigma} \tilde{f}^{\mp}_{\boldsymbol{k},\sigma} \Big[\left(1 - f^{(r_1)}_{\boldsymbol{k}-2\Delta\boldsymbol{k},\sigma}\right) \left(1 - f^{(r_2)}_{\boldsymbol{q}+\Delta\boldsymbol{k},\sigma}\right) \\
&\qquad - f^{(r_1)}_{\boldsymbol{k}-2\Delta\boldsymbol{k},\sigma} f^{(r_2)}_{\boldsymbol{q}+\Delta\boldsymbol{k},\sigma} \Big] \\
&-\tilde{\gamma}^{\pm\bar{r}_1 r_2 \bar{r}_3}_{\boldsymbol{k},\boldsymbol{k}-\Delta\boldsymbol{k},\boldsymbol{q}} \left(\tilde{\gamma}^{\pm r_1 \bar{r}_2 r_3}_{\boldsymbol{k},\boldsymbol{k}-\Delta\boldsymbol{k},\boldsymbol{q}}\right)^* \tilde{f}^{(r_1)}_{\boldsymbol{k}-2\Delta\boldsymbol{k},\sigma} \tilde{f}^{(r_2)}_{\boldsymbol{q}+\Delta\boldsymbol{k},\sigma} \tilde{f}^{(-r_3)}_{\boldsymbol{q}-\Delta\boldsymbol{k},\sigma} \\
&-\tilde{\gamma}^{\pm\bar{r}_1 r_2 \bar{r}_3}_{\boldsymbol{k},\boldsymbol{k}-\Delta\boldsymbol{k},\boldsymbol{q}} \left(\tilde{\gamma}^{\mp r_1 \bar{r}_2 \bar{r}_3}_{\boldsymbol{k},\boldsymbol{k}-\Delta\boldsymbol{k},\boldsymbol{q}}\right)^* \tilde{f}^{(r_1)}_{\boldsymbol{k}-2\Delta\boldsymbol{k},\sigma} \tilde{f}^{(r_2)}_{\boldsymbol{q}+\Delta\boldsymbol{k},\sigma} \tilde{f}^{\mp}_{\boldsymbol{k},\sigma} \\
&+\tilde{\gamma}^{\pm\bar{r}_1 r_2 \bar{r}_3}_{\boldsymbol{k},\boldsymbol{k}-\Delta\boldsymbol{k},\boldsymbol{q}} \left(\tilde{\gamma}^{\mp\bar{r}_1 \bar{r}_2 r_3}_{\boldsymbol{k},\boldsymbol{k}-\Delta\boldsymbol{k},\boldsymbol{q}}\right)^* \tilde{f}^{(r_2)}_{\boldsymbol{q}+\Delta\boldsymbol{k},\sigma} \tilde{f}^{(-r_3)}_{\boldsymbol{q}-\Delta\boldsymbol{k},\sigma} \tilde{f}^{\mp}_{\boldsymbol{k},\sigma} \\
&+\tilde{\gamma}^{\pm\bar{r}_1 r_2 \bar{r}_3}_{\boldsymbol{k},\boldsymbol{k}-\Delta\boldsymbol{k},\boldsymbol{q}} \left(\tilde{\gamma}^{\mp r_1 r_2 r_3}_{\boldsymbol{k},\boldsymbol{k}-\Delta\boldsymbol{k},\boldsymbol{q}}\right)^* \tilde{f}^{(r_1)}_{\boldsymbol{k}-2\Delta\boldsymbol{k},\sigma} \tilde{f}^{(-r_3)}_{\boldsymbol{q}-\Delta\boldsymbol{k},\sigma} \tilde{f}^{\mp}_{\boldsymbol{k},\sigma} \Big) \Big], \qquad (5.108a)
\end{aligned}
$$

$$\tilde{I}^{C\pm}_{\boldsymbol{k},\sigma} = \frac{\pi}{2\mathcal{V}^2} \sum_{\substack{\boldsymbol{q} \\ r_1,r_2,r_3=\pm}} \mathrm{Re}\Bigg[r_1 r_3 \delta\left(\pm E_{\boldsymbol{k}} + r_3 E_{\boldsymbol{q}-\Delta\boldsymbol{k}} - r_1 E_{\boldsymbol{k}-2\Delta\boldsymbol{k}} - r_2 E_{\boldsymbol{q}+\Delta\boldsymbol{k}}\right)$$
$$\times \Bigg(\tilde{\gamma}^{\pm \bar{r}_1 r_2 \bar{r}_3}_{\boldsymbol{k},\boldsymbol{k}-\Delta\boldsymbol{k},\boldsymbol{q}} \left(\tilde{\gamma}^{\mp \bar{r}_1 r_2 \bar{r}_3}_{\boldsymbol{k},\boldsymbol{k}-\Delta\boldsymbol{k},\boldsymbol{q}}\right)^* \Bigg[\left(1 - f^{(r_1)}_{\boldsymbol{k}-2\Delta\boldsymbol{k},\sigma}\right)\left(1 - f^{(r_2)}_{\boldsymbol{q}+\Delta\boldsymbol{k},\sigma}\right) f^{\mp}_{\boldsymbol{k},\sigma} f^{(r_3)}_{\boldsymbol{q}-\Delta\boldsymbol{k},\sigma}$$
$$- f^{(r_1)}_{\boldsymbol{k}-2\Delta\boldsymbol{k},\sigma} f^{(r_2)}_{\boldsymbol{q}+\Delta\boldsymbol{k},\sigma}\left(1 - f^{\mp}_{\boldsymbol{k},\sigma}\right)\left(1 - f^{(r_3)}_{\boldsymbol{q}-\Delta\boldsymbol{k},\sigma}\right) \Bigg]$$
$$+ \tilde{\gamma}^{\pm \bar{r}_1 r_2 \bar{r}_3}_{\boldsymbol{k},\boldsymbol{k}-\Delta\boldsymbol{k},\boldsymbol{q}} \left(\tilde{\gamma}^{\mp r_1 r_2 \bar{r}_3}_{\boldsymbol{k},\boldsymbol{k}-\Delta\boldsymbol{k},\boldsymbol{q}}\right)^* \tilde{f}^{(r_1)}_{\boldsymbol{k}-2\Delta\boldsymbol{k},\sigma} \Bigg[\left(1 - f^{(r_2)}_{\boldsymbol{q}+\Delta\boldsymbol{k},\sigma}\right) f^{\mp}_{\boldsymbol{k},\sigma} f^{(r_3)}_{\boldsymbol{q}-\Delta\boldsymbol{k},\sigma}$$
$$- f^{(r_2)}_{\boldsymbol{q}+\Delta\boldsymbol{k},\sigma}\left(1 - f^{\mp}_{\boldsymbol{k},\sigma}\right)\left(1 - f^{(r_3)}_{\boldsymbol{q}-\Delta\boldsymbol{k},\sigma}\right) \Bigg]$$
$$+ \tilde{\gamma}^{\pm \bar{r}_1 r_2 \bar{r}_3}_{\boldsymbol{k},\boldsymbol{k}-\Delta\boldsymbol{k},\boldsymbol{q}} \left(\tilde{\gamma}^{\mp \bar{r}_1 \bar{r}_2 \bar{r}_3}_{\boldsymbol{k},\boldsymbol{k}-\Delta\boldsymbol{k},\boldsymbol{q}}\right)^* \tilde{f}^{(r_2)}_{\boldsymbol{q}+\Delta\boldsymbol{k},\sigma} \Bigg[\left(1 - f^{(r_1)}_{\boldsymbol{k}-2\Delta\boldsymbol{k},\sigma}\right) f^{\mp}_{\boldsymbol{k},\sigma} f^{(r_3)}_{\boldsymbol{q}-\Delta\boldsymbol{k},\sigma}$$
$$- f^{(r_1)}_{\boldsymbol{k}-2\Delta\boldsymbol{k},\sigma}\left(1 - f^{\mp}_{\boldsymbol{k},\sigma}\right)\left(1 - f^{(r_3)}_{\boldsymbol{q}-\Delta\boldsymbol{k},\sigma}\right) \Bigg]$$
$$- \tilde{\gamma}^{\pm \bar{r}_1 r_2 \bar{r}_3}_{\boldsymbol{k},\boldsymbol{k}-\Delta\boldsymbol{k},\boldsymbol{q}} \left(\tilde{\gamma}^{\pm \bar{r}_1 r_2 \bar{r}_3}_{\boldsymbol{k},\boldsymbol{k}-\Delta\boldsymbol{k},\boldsymbol{q}}\right)^* \tilde{f}^{\pm}_{\boldsymbol{k},\sigma} \Bigg[\left(1 - f^{(r_1)}_{\boldsymbol{k}-2\Delta\boldsymbol{k},\sigma}\right)\left(1 - f^{(r_2)}_{\boldsymbol{q}+\Delta\boldsymbol{k},\sigma}\right) f^{(r_3)}_{\boldsymbol{q}-\Delta\boldsymbol{k},\sigma}$$
$$- f^{(r_1)}_{\boldsymbol{k}-2\Delta\boldsymbol{k},\sigma} f^{(r_2)}_{\boldsymbol{q}+\Delta\boldsymbol{k},\sigma}\left(1 - f^{(r_3)}_{\boldsymbol{q}-\Delta\boldsymbol{k},\sigma}\right) \Bigg]$$
$$- \tilde{\gamma}^{\pm \bar{r}_1 r_2 \bar{r}_3}_{\boldsymbol{k},\boldsymbol{k}-\Delta\boldsymbol{k},\boldsymbol{q}} \left(\tilde{\gamma}^{\mp \bar{r}_1 r_2 r_3}_{\boldsymbol{k},\boldsymbol{k}-\Delta\boldsymbol{k},\boldsymbol{q}}\right)^* \tilde{f}^{(-r_3)}_{\boldsymbol{q}-\Delta\boldsymbol{k},\sigma} \Bigg[\left(1 - f^{(r_1)}_{\boldsymbol{k}-2\Delta\boldsymbol{k},\sigma}\right)\left(1 - f^{(r_2)}_{\boldsymbol{q}+\Delta\boldsymbol{k},\sigma}\right) f^{\mp}_{\boldsymbol{k},\sigma}$$
$$- f^{(r_1)}_{\boldsymbol{k}-2\Delta\boldsymbol{k},\sigma} f^{(r_2)}_{\boldsymbol{q}+\Delta\boldsymbol{k},\sigma}\left(1 - f^{\mp}_{\boldsymbol{k},\sigma}\right) \Bigg]$$
$$+ \tilde{\gamma}^{\pm \bar{r}_1 r_2 \bar{r}_3}_{\boldsymbol{k},\boldsymbol{k}-\Delta\boldsymbol{k},\boldsymbol{q}} \left(\tilde{\gamma}^{\mp r_1 \bar{r}_2 \bar{r}_3}_{\boldsymbol{k},\boldsymbol{k}-\Delta\boldsymbol{k},\boldsymbol{q}}\right)^* \tilde{f}^{(r_1)}_{\boldsymbol{k}-2\Delta\boldsymbol{k},\sigma} \tilde{f}^{(r_2)}_{\boldsymbol{q}+\Delta\boldsymbol{k},\sigma} \Bigg[f^{\mp}_{\boldsymbol{k},\sigma} f^{(r_3)}_{\boldsymbol{q}-\Delta\boldsymbol{k},\sigma}$$
$$- \left(1 - f^{\mp}_{\boldsymbol{k},\sigma}\right)\left(1 - f^{(r_3)}_{\boldsymbol{q}-\Delta\boldsymbol{k},\sigma}\right) \Bigg]$$
$$- \tilde{\gamma}^{\pm \bar{r}_1 r_2 \bar{r}_3}_{\boldsymbol{k},\boldsymbol{k}-\Delta\boldsymbol{k},\boldsymbol{q}} \left(\tilde{\gamma}^{\mp r_1 r_2 r_3}_{\boldsymbol{k},\boldsymbol{k}-\Delta\boldsymbol{k},\boldsymbol{q}}\right)^* \tilde{f}^{(r_1)}_{\boldsymbol{k}-2\Delta\boldsymbol{k},\sigma} \tilde{f}^{(-r_3)}_{\boldsymbol{q}-\Delta\boldsymbol{k},\sigma} \Bigg[\left(1 - f^{(r_2)}_{\boldsymbol{q}+\Delta\boldsymbol{k},\sigma}\right) f^{\mp}_{\boldsymbol{k},\sigma}$$
$$- f^{(r_2)}_{\boldsymbol{q}+\Delta\boldsymbol{k},\sigma}\left(1 - f^{\mp}_{\boldsymbol{k},\sigma}\right) \Bigg]$$
$$- \tilde{\gamma}^{\pm \bar{r}_1 r_2 \bar{r}_3}_{\boldsymbol{k},\boldsymbol{k}-\Delta\boldsymbol{k},\boldsymbol{q}} \left(\tilde{\gamma}^{\pm r_1 r_2 \bar{r}_3}_{\boldsymbol{k},\boldsymbol{k}-\Delta\boldsymbol{k},\boldsymbol{q}}\right)^* \tilde{f}^{(r_1)}_{\boldsymbol{k}-2\Delta\boldsymbol{k},\sigma} \tilde{f}^{\pm}_{\boldsymbol{k},\sigma} \Bigg[\left(1 - f^{(r_2)}_{\boldsymbol{q}+\Delta\boldsymbol{k},\sigma}\right) f^{(r_3)}_{\boldsymbol{q}-\Delta\boldsymbol{k},\sigma}$$
$$- f^{(r_2)}_{\boldsymbol{q}+\Delta\boldsymbol{k},\sigma}\left(1 - f^{(r_3)}_{\boldsymbol{q}-\Delta\boldsymbol{k},\sigma}\right) \Bigg]$$
$$- \tilde{\gamma}^{\pm \bar{r}_1 r_2 \bar{r}_3}_{\boldsymbol{k},\boldsymbol{k}-\Delta\boldsymbol{k},\boldsymbol{q}} \left(\tilde{\gamma}^{\mp \bar{r}_1 \bar{r}_2 r_3}_{\boldsymbol{k},\boldsymbol{k}-\Delta\boldsymbol{k},\boldsymbol{q}}\right)^* \tilde{f}^{(r_2)}_{\boldsymbol{q}+\Delta\boldsymbol{k},\sigma} \tilde{f}^{(-r_3)}_{\boldsymbol{q}-\Delta\boldsymbol{k},\sigma} \Bigg[\left(1 - f^{(r_1)}_{\boldsymbol{k}-2\Delta\boldsymbol{k},\sigma}\right) f^{\mp}_{\boldsymbol{k},\sigma}$$
$$- f^{(r_1)}_{\boldsymbol{k}-2\Delta\boldsymbol{k},\sigma}\left(1 - f^{\mp}_{\boldsymbol{k},\sigma}\right) \Bigg]$$

$$
\begin{aligned}
&-\tilde{\gamma}^{\pm\bar{r}_1 r_2 \bar{r}_3}_{\boldsymbol{k},\boldsymbol{k}-\Delta\boldsymbol{k},\boldsymbol{q}} \left(\tilde{\gamma}^{\pm\bar{r}_1 \bar{r}_2 \bar{r}_3}_{\boldsymbol{k},\boldsymbol{k}-\Delta\boldsymbol{k},\boldsymbol{q}}\right)^* \tilde{f}^{(r_2)}_{\boldsymbol{q}+\Delta\boldsymbol{k},\sigma} \tilde{f}^{\pm}_{\boldsymbol{k},\sigma} \Big[\left(1 - f^{(r_1)}_{\boldsymbol{k}-2\Delta\boldsymbol{k},\sigma}\right) f^{(r_3)}_{\boldsymbol{q}-\Delta\boldsymbol{k},\sigma} \\
&\qquad - f^{(r_1)}_{\boldsymbol{k}-2\Delta\boldsymbol{k},\sigma} \left(1 - f^{(r_3)}_{\boldsymbol{q}-\Delta\boldsymbol{k},\sigma}\right) \Big] \\
&+\tilde{\gamma}^{\pm\bar{r}_1 r_2 \bar{r}_3}_{\boldsymbol{k},\boldsymbol{k}-\Delta\boldsymbol{k},\boldsymbol{q}} \left(\tilde{\gamma}^{\pm\bar{r}_1 r_2 r_3}_{\boldsymbol{k},\boldsymbol{k}-\Delta\boldsymbol{k},\boldsymbol{q}}\right)^* \tilde{f}^{(-r_3)}_{\boldsymbol{q}-\Delta\boldsymbol{k},\sigma} \tilde{f}^{\pm}_{\boldsymbol{k},\sigma} \Big[\left(1 - f^{(r_1)}_{\boldsymbol{k}-2\Delta\boldsymbol{k},\sigma}\right) \left(1 - f^{(r_2)}_{\boldsymbol{q}+\Delta\boldsymbol{k},\sigma}\right) \\
&\qquad - f^{(r_1)}_{\boldsymbol{k}-2\Delta\boldsymbol{k},\sigma} f^{(r_2)}_{\boldsymbol{q}+\Delta\boldsymbol{k},\sigma} \Big] \\
&-\tilde{\gamma}^{\pm\bar{r}_1 r_2 \bar{r}_3}_{\boldsymbol{k},\boldsymbol{k}-\Delta\boldsymbol{k},\boldsymbol{q}} \left(\tilde{\gamma}^{\mp r_1 \bar{r}_2 r_3}_{\boldsymbol{k},\boldsymbol{k}-\Delta\boldsymbol{k},\boldsymbol{q}}\right)^* \tilde{f}^{(r_1)}_{\boldsymbol{k}-2\Delta\boldsymbol{k},\sigma} \tilde{f}^{(r_2)}_{\boldsymbol{q}+\Delta\boldsymbol{k},\sigma} \tilde{f}^{(-r_3)}_{\boldsymbol{q}-\Delta\boldsymbol{k},\sigma} \\
&-\tilde{\gamma}^{\pm\bar{r}_1 r_2 \bar{r}_3}_{\boldsymbol{k},\boldsymbol{k}-\Delta\boldsymbol{k},\boldsymbol{q}} \left(\tilde{\gamma}^{\pm r_1 \bar{r}_2 \bar{r}_3}_{\boldsymbol{k},\boldsymbol{k}-\Delta\boldsymbol{k},\boldsymbol{q}}\right)^* \tilde{f}^{(r_1)}_{\boldsymbol{k}-2\Delta\boldsymbol{k},\sigma} \tilde{f}^{(r_2)}_{\boldsymbol{q}+\Delta\boldsymbol{k},\sigma} \tilde{f}^{\mp}_{\boldsymbol{k},\sigma} \\
&+\tilde{\gamma}^{\pm\bar{r}_1 r_2 \bar{r}_3}_{\boldsymbol{k},\boldsymbol{k}-\Delta\boldsymbol{k},\boldsymbol{q}} \left(\tilde{\gamma}^{\pm\bar{r}_1 \bar{r}_2 r_3}_{\boldsymbol{k},\boldsymbol{k}-\Delta\boldsymbol{k},\boldsymbol{q}}\right)^* \tilde{f}^{(r_2)}_{\boldsymbol{q}+\Delta\boldsymbol{k},\sigma} \tilde{f}^{(-r_3)}_{\boldsymbol{q}-\Delta\boldsymbol{k},\sigma} \tilde{f}^{\pm}_{\boldsymbol{k},\sigma} \\
&+\tilde{\gamma}^{\pm\bar{r}_1 r_2 \bar{r}_3}_{\boldsymbol{k},\boldsymbol{k}-\Delta\boldsymbol{k},\boldsymbol{q}} \left(\tilde{\gamma}^{\pm r_1 r_2 r_3}_{\boldsymbol{k},\boldsymbol{k}-\Delta\boldsymbol{k},\boldsymbol{q}}\right)^* \tilde{f}^{(r_1)}_{\boldsymbol{k}-2\Delta\boldsymbol{k},\sigma} \tilde{f}^{(-r_3)}_{\boldsymbol{q}-\Delta\boldsymbol{k},\sigma} \tilde{f}^{\pm}_{\boldsymbol{k},\sigma} \Big) \Big]. \qquad (5.108b)
\end{aligned}
$$

Note that the two factors in the two above collision integrals containing four-point vertices can be evaluated as

$$
\left|\tilde{\gamma}^{r_1 r_2 r_3 r_4}_{\boldsymbol{k},\boldsymbol{k}-\Delta\boldsymbol{k},\boldsymbol{q}}\right|^2 = \frac{|V_{\boldsymbol{k}}|^2}{16} \frac{E_{\boldsymbol{k}} + r_1 \xi_{\boldsymbol{k}}}{E_{\boldsymbol{k}}} \frac{E_{\boldsymbol{Q}} + r_2 \xi_{\boldsymbol{Q}}}{E_{\boldsymbol{Q}}} \frac{E_{\boldsymbol{q}+\Delta\boldsymbol{k}} + r_3 \xi_{\boldsymbol{q}+\Delta\boldsymbol{k}}}{E_{\boldsymbol{q}+\Delta\boldsymbol{k}}} \frac{E_{\boldsymbol{q}-\Delta\boldsymbol{k}} + r_4 \xi_{\boldsymbol{q}-\Delta\boldsymbol{k}}}{E_{\boldsymbol{q}-\Delta\boldsymbol{k}}} \qquad (5.109a)
$$

and

$$
\tilde{\gamma}^{r_1 r_2 r_3 r_4}_{\boldsymbol{k},\boldsymbol{k}-\Delta\boldsymbol{k},\boldsymbol{q}} \left(\tilde{\gamma}^{\bar{r}_1 r_2 r_3 r_4}_{\boldsymbol{k},\boldsymbol{k}-\Delta\boldsymbol{k},\boldsymbol{q}}\right)^* = \frac{|V_{\boldsymbol{k}}|^2}{16} \frac{\Delta}{E_{\boldsymbol{k}}} \frac{E_{\boldsymbol{Q}} + r_2 \xi_{\boldsymbol{Q}}}{E_{\boldsymbol{Q}}} \frac{E_{\boldsymbol{q}+\Delta\boldsymbol{k}} + r_3 \xi_{\boldsymbol{q}+\Delta\boldsymbol{k}}}{E_{\boldsymbol{q}+\Delta\boldsymbol{k}}} \frac{E_{\boldsymbol{q}-\Delta\boldsymbol{k}} + r_4 \xi_{\boldsymbol{q}-\Delta\boldsymbol{k}}}{E_{\boldsymbol{q}-\Delta\boldsymbol{k}}}. \qquad (5.109b)
$$

Furthermore, in this case the collision integral of the off-diagonal electronic distribution function $\tilde{f}^{\pm}_{\boldsymbol{k},\sigma}$ is real so that I do not need to calculate the principal value of the collision integral.

To compute the above collision integrals it is necessary to find the roots of the arguments of the delta functions. It is easy to see that for some terms there is a solution,

$$
q_z = \pm \left(\frac{k_z}{2} + k_F\right), \qquad (5.110)
$$

and for the other terms there is no real solution for the wave vector q_z. Furthermore, by inserting the mean-field thermal equilibrium state (5.48) into the collision integrals $I^{C\pm}_{\boldsymbol{k},\sigma}$ and $\tilde{I}^{C\pm}_{\boldsymbol{k},\sigma}$ given by Eqs. (5.108) it is easy to see that they vanish in thermal equilibrium. Therefore, I conclude that Coulomb interactions do not contribute to the order parameter damping directly. Coulomb interactions lead to renormalizations of the phonon frequencies as well as the electron-phonon coupling constants, though. This can be taken into account by diagonalizing the phonon part of the Hamiltonian or, in the case of an arbitrary amount of phonon modes, including the off-diagonal phonon distribution

function $p^c_{\boldsymbol{q},\lambda}$. In both cases, in order to determine the effect on the order parameter damping it is, however, necessary to include the effect of screening.

5.6.4 Screening

In this section I investigate the screening of the Coulomb interaction. Within random-phase approximation the screened Coulomb interaction can be written as [89]

$$V^r_{s,\boldsymbol{q}}(t_1,t_2) = V_{\boldsymbol{q}}\delta(t_1-t_2) + V_{\boldsymbol{q}}\int_{t_2}^{t_1} dt_3 L^r_{\boldsymbol{q}}(t_1,t_3)V^r_{s,\boldsymbol{q}}(t_3,t_2), \tag{5.111}$$

where

$$L^r_{\boldsymbol{q}}(t_1,t_2) = -2i\sum_{\boldsymbol{k}} G^r_{\boldsymbol{k}+\boldsymbol{q}}(t_1,t_2)G^a_{\boldsymbol{k}}(t_2,t_1)\big[f_{\boldsymbol{k}}(t_2) - f_{\boldsymbol{k}+\boldsymbol{q}}(t_2)\big] \tag{5.112}$$

does only contain the contribution from polarization bubbles. In thermal equilibrium Eq. (5.112) can be written as [89]

$$L^r_{\boldsymbol{q}}(t_1,t_2) = -2i\theta(t_1-t_2)\sum_{\boldsymbol{k}} e^{i(\epsilon_{\boldsymbol{k}}-\epsilon_{\boldsymbol{k}+\boldsymbol{q}})(t_1-t_2)}\big[f_{\boldsymbol{k}}(t_2) - f_{\boldsymbol{k}+\boldsymbol{q}}(t_2)\big]. \tag{5.113}$$

Within the plasmon pole approximation the screened Coulomb interaction is given by [89]

$$V^r_{s,\boldsymbol{q}}(t_1,t_2) = V_{\boldsymbol{q}}\left[\delta(t_1-t_2) + S_{\boldsymbol{q}}(t_1,t_2)e^{-2\gamma(t_1-t_2)}\right], \tag{5.114}$$

where γ is the Landau damping (introduced by hand) and $S_{\boldsymbol{q}}(t_1,t_2)$ is the density-density correlation function. The Landau damping arises due to the curvature of the Fermi surface and is important for the convergence of the above expression. In this chapter the Fermi surface is assumed to be flat for quasi-one-dimensional systems. Apparently, this approximation is not suitable for long times causing problems with the convergence of the screening. A simple way to correct this issue is to include by hand the Landau damping constant into Eq. (5.114). Withing RPA the density-density correlation function can be calculated from particle-hole bubbles and is given by [89]

$$S_{\boldsymbol{q}}(t_1,t_2) = V_{\boldsymbol{q}}L^r_{\boldsymbol{q}}(t_1,t_2) + V_{\boldsymbol{q}}\int_{t_2}^{t_1} dt_3 L^r_{\boldsymbol{q}}(t_1,t_3)S_{\boldsymbol{q}}(t_3,t_2). \tag{5.115}$$

In order to obtain equal-time quantities the generalized Kadanoff-Baym ansatz [63] may be employed. It can be shown that Eqs. (5.113) and (5.115) reduce to

$$\partial_t V^r_{s,\boldsymbol{q}}(t) = -2V_{\boldsymbol{q}}\sum_{\boldsymbol{k}}\int_{t_0}^{t} dt' e^{-i\left(\epsilon_{\boldsymbol{k}}-\epsilon_{\boldsymbol{k}+\boldsymbol{q}}-2i\gamma\right)(t-t')}V^r_{s,\boldsymbol{q}}(t')\Big[f_{\boldsymbol{k}}(t') - f_{\boldsymbol{k}+\boldsymbol{q}}(t')\Big]. \tag{5.116}$$

This is a closed equation if the electrons are assumed to be in thermal equilibrium so that the electronic distribution functions $f_{\boldsymbol{k}}$ are given by the Fermi-Dirac distribution function. The screened Coulomb interaction $V^r_{s,\boldsymbol{q}}$ can be related to the screening length κ via

$$V^r_{s,\boldsymbol{q}}(t) = \frac{4\pi e^2}{\boldsymbol{q}^2 + \kappa(t)^2}. \tag{5.117}$$

In general, the screening length κ depends on the wave vector $\boldsymbol{q}$ and is time-dependent. Now, I integrate Eq. (5.116) numerically. I chose $V^r_{s,\boldsymbol{q}}(t_0) = V_{\boldsymbol{q}}$ for all $\boldsymbol{k}$ as initial condition corresponding to $\kappa = 0$, i.e. the case without screening. I assume that the system is in thermal equilibrium,

$$f_{\boldsymbol{k}} = \frac{1}{e^{\beta\epsilon_{\boldsymbol{k}}} + 1}, \tag{5.118}$$

where $\epsilon_{\boldsymbol{k}}$ is the electronic dispersion. If the Landau damping is set to zero, $\gamma = 0$, the numerical solution of the equation of motion of the screened Coulomb interaction shows an oscillatory behavior with a decreasing amplitude for short times. However, for long times the amplitude increases exponentially. The Landau damping is necessary to solve this issue [89]. The reason is that I assume that the quasi-one-dimensional material has a one-dimensional electronic dispersion. However, the true electronic dispersion may be three-dimensional, i.e. the Fermi surface has a finite curvature. This opens up an additional dissipation channel which is qualitatively described by the additional damping rate γ. This damping rate is essential for the time evolution for long times. The numerical results for the electronic dispersion of free electrons $\epsilon_{\boldsymbol{k}} = \frac{\boldsymbol{k}^2}{2m}$ at temperature $T = 20$ K are shown in Fig. 5.19 where

$$n_{\boldsymbol{k}}(t) \equiv \frac{V^r_{s,\boldsymbol{k}}(t)}{V_{\boldsymbol{k}}}. \tag{5.119}$$

5.6.5 Time evolution of the order parameter

Fig. 5.20 shows the time evolution of the order parameter $\Delta(t)$ with (green) and without (purple) Coulomb interaction. The ration $\Delta(t)/\Delta_0$ is plotted over the time where Δ_0 denotes the mean-field order parameter. The initial condition is $\Delta(0) = 1.1 \times \Delta_0$. The initial values for the distribution functions were chosen as the mean-field thermal equilibrium distributions. The parameters were chosen the same way as for the previous Fig. 5.7. To obtain these results the kinetic equations for the case with and without the contributions of Coulomb interaction to the collision integrals have been solved numerically. For the case with Coulomb interaction the screening length was set to the fixed value $\kappa^2 = 0.06\ k_F^2$ which has been found to be the value that the screening length converges to when solving Eq. (5.116) numerically for the thermal equilibrium state. In principle, it is possible to obtain the time-dependent screening length by numerically integrating Eq. (5.116). However, the relevant time scale is smaller by two orders of magnitude compared to the time scale of the order parameter dynamics. Therefore, this

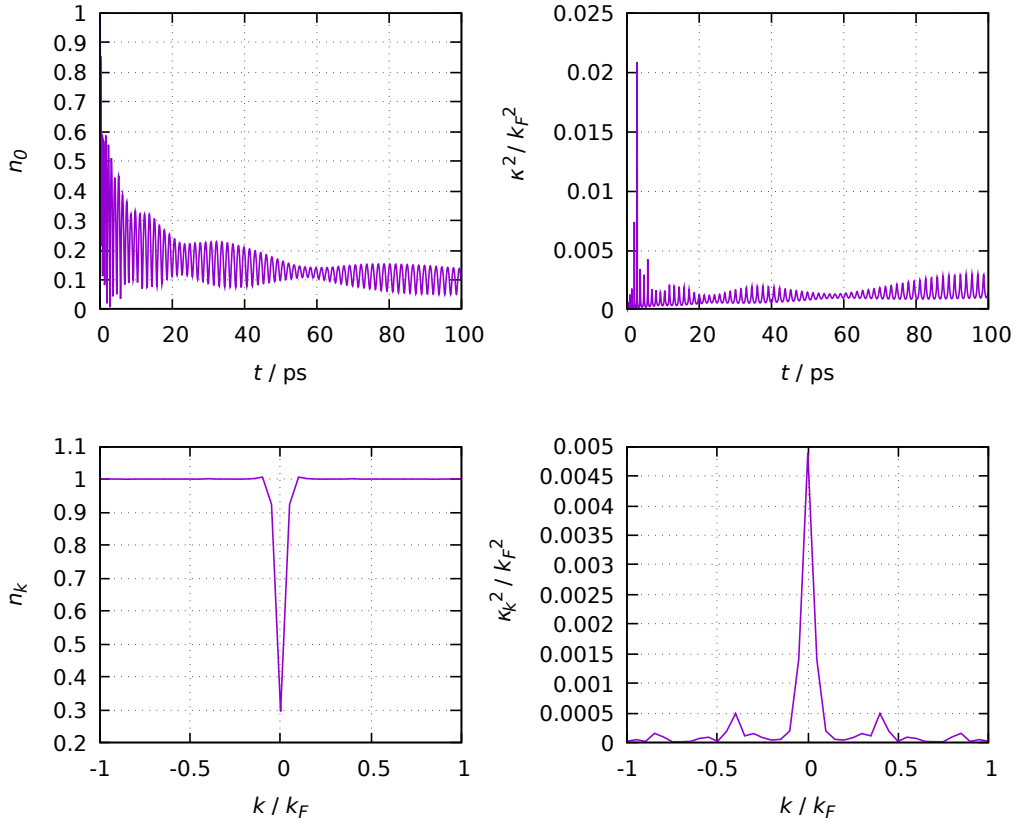

Figure 5.19: Time dependence (a) of the dimensionless function $n_{\mathbf{0}}(t)$ for zero momentum defined by Eq. (5.119) and $n_{\boldsymbol{k}}(t_f)$ in dependence of the wave vector after convergence has been reached at time t_f (b). (c) and (d) show the same for the screening length κ^2.

procedure is inconvenient, because the time step for the numerical integration needs to be chosen smaller.

Fig. 5.20 shows that there is only a small difference between the curves for the time dependence of the order parameter with and without Coulomb interaction. It can be observed that the damping is slightly larger when the effects of Coulomb interaction are included. Note that here the initial deviation of the order parameter from the mean-field order parameter was chosen to be larger compared to Fig. 5.7. The effects of the Coulomb interaction are stronger further away from the thermal equilibrium state, because the collision integrals (5.108) vanish exactly in the thermal equilibrium state. Therefore, the effects of Coulomb interaction on the time evolution of the order parameter are stronger further away from thermal equilibrium. Close to the thermal equilibrium the effect of Coulomb interaction is to renormalize the phonon frequencies and electron-

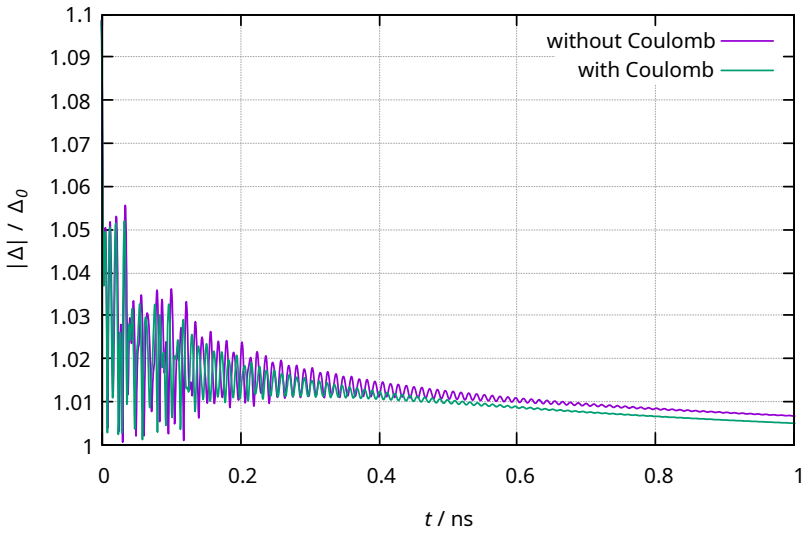

Figure 5.20: The ratio of the order parameter $\Delta(t)$ to the mean-field order parameter Δ_0 with (green) and without (purple) the effect of the Coulomb interaction is plotted over the time t after a small initial excitation with $\Delta(0) = 1.1 \times \Delta_0$. The mean-field order parameter was obtained from the numerical solution of Eq. (5.49). The parameters are the same as in Fig. (5.7).

phonon coupling constants. In Fig. 5.20 this effect is low, however, leading to a slightly increased damping of the order parameter. As a result, the effect of Coulomb interaction is very difficult to observe experimentally close to thermal equilibrium. Far away from thermal equilibrium the collision integrals do not vanish so that additional effects of the Coulomb interaction emerge. Therefore, far away from thermal equilibrium there is a chance to observe experimentally effects that can only be explained by including Coulomb interactions.

I conclude that the Coulomb interaction is not important to understand the results of the experiments carried out in Refs. [48, 49]. Close to the thermal equilibrium state the Coulomb interaction is not relevant for the time evolution of the order parameter and for the frequencies of amplitude and phase modes. An exception is the lowest phase mode. It is assumed that the Coulomb interaction is important for the damping of the lowest phase mode. However, I have encountered a problem with the description of the lowest phase mode within my theory which makes it difficult to accurately compute its frequency and damping rate. This problem is related to phonon mixing; For the lowest phase mode all other phonon modes are relevant so that high-energy phonon modes cannot be neglected. Due to the large unit cell of blue bronze and subsequently the large number of phonon modes it is challenging to take into account all phonon modes.

6 Summary and conclusion

In this work I have investigated different systems by employing the method of kinetic equations. The set of equations of motion contains complicated collision integrals that were derived from Hamiltonians describing the microscopic dynamics of those systems. The method in turn has been derived with the use of generating functionals of equal-time connected correlations analogously to Ref. [52]. The diagrammatic formalism that I have obtained this way is the same one that has been introduced in Ref. [44] with the use of the cluster expansion. The derivation in terms of generating functionals is a mathematically simpler approach. The advantages of the method of expansion in connected correlations is the fact that it directly yields a hierarchy of equations of motion of equal-time correlations and a scheme that allows to systematically decouple the infinite hierarchy at arbitrary order. The truncation of the infinite hierarchy results in a closed set of equations of motion and allows to solve this set of equations numerically.

The damping of parametrically pumped magnons in YIG has been calculated via the microscopic collision integrals for the stationary non-equilibrium state. These collision integrals have a complicated structure and lead to a non-monotonous dependence of the damping on the static external magnetic field with a sharp peak at a certain field strength. This peak lies close to the confluence field strength where confluence processes of parametric magnons with the same momenta become kinematically possible. Due to the non-linear nature of magnons this peak in the damping strength leads either to a decrease or increase of the saturation magnon density depending on the pumping strength [54].

By taking into account magnon-phonon interactions I was able to observe the formation of an incoherent macroscopic accumulation of magnetoelastic modes close to the magnon-phonon hybridization region in the numerical solution of the corresponding kinetic equations. This result agrees with experimental observations for YIG [55]. Often in the literature the effects of magnon-phonon interactions are not taken into account explicitly and phonons are merely considered as a heat bath for the magnons. This can be justified by the fact that the magnon-phonon interaction is very weak. In the experimental situation investigated here, however, the magnon-phonon interactions are responsible for the observed macroscopic accumulation of magnetoelastic modes [55]. The important feature is the hybridization of magnons and phonons. There is a point on the dispersion of the lower magnetoelastic mode that is degenerate with the minimum of the magnon dispersion where the magnon condensate forms during the thermalization process. Due to the interactions between the magnon condensate and the energetically degenerate magnetoelastic mode a macroscopic accumulation arises even though magnon-phonon interactions are weak.

Regarding charge-density waves there is the possibility to investigate the time evolu-

tion of the order parameter far from equilibrium with the usage of the kinetic theory developed in this work. This possibility has not been fully exhausted yet and there is also little experimental data available on that matter. Here, I have focused on the stationary thermal equilibrium state to be able to compare my results with data from recent experiments [49]. The temperature dependence of the amplitude and phase mode frequencies and damping rates obtained from the linearized kinetic equations agrees well with the experiments. In particular, there is a strong temperature dependence of the damping rates close to the critical temperature. The lowest phase mode is an exception, however. It couples to all other phonon modes and taking into account only the low energy modes is not sufficient to produce accurate results for the frequency and the damping rate of the lowest phase mode. Furthermore, I am able to confirm that the experimental results can be understood with the use of the phenomenological Ginzburg-Landau approach [48, 50, 51] because the resulting linearized order parameter equations of motion coincide with the linearized kinetic equations. While the order parameter damping is obtained within the phenomenological approach by fits to experimental data, within the kinetic theory the damping is calculated from the microscopic dynamics of the system and is evaluated from the collision integrals. The advantage of the kinetic theory developed in this work over the Gaussian approximation is the fact that it includes damping and that the time evolution of the order parameter as well as the time evolution of electron and phonon distribution functions can be calculated. The non-vanishing damping leads to mode mixing for amplitude and phase phonons. This in turn leads to a non-zero frequency of the lowest phase mode which is a gapless mode within the Gaussian approximation [37].

Furthermore, I have included the effect of Coulomb interactions. However, it becomes evident that the system does not behave qualitatively different with or without Coulomb interactions close to the thermal equilibrium state. The dominant effect of the Coulomb interaction on the order parameter is slightly increased damping. The method introduced in this work, however, allows to investigate the time evolution of the system far from equilibrium and is possibly helpful to understand future experiments where the system is driven far away from thermal equilibrium.

7 Bibliography

[1] V. Cherepanov, I. Kolokolov, and V. L'vov, *The saga of YIG: spectra, thermodynamics, interaction and relaxation of magnons in a complex magnet*, Phys. Rept. **229**, 81 (1993).

[2] V. E. Zakharov, V. S. L'vov, and S. S. Starobinets, *Stationary nonlinear theory of parametric excitation of waves*, Zh. Eksp. Teor. Fiz. **59**, 1200 (1970) [Sov. Phys. JETP **32**, 656 (1971)].

[3] H. Suhl, *The theory of ferromagnetic resonance at high signal powers*, J. Phys. Chem. Solids **1**, 209 (1957).

[4] E. Schlömann, J. J. Green, and U. Milano, *Recent Developments in Ferromagnetic Resonance at High Power Levels*, J. Appl. Phys. **31**, 386S (1960); E. Schlömann and R. I. Joseph, *Instability of Spin Waves and Magnetostatic Modes in a Microwave Magnetic Field Applied Parallel to the dc Field*, *ibid.* **32**, 1006 (1961); E. Schlömann and J. J. Green, *Spin-Wave Growth Under Parallel Pumping*, *ibid.* **34**, 1291 (1963).

[5] V. E. Zakharov, V. S. L'vov, and S. S. Starobinets, *Spin-wave turbulence beyond the parametric excitation threshold*, Usp. Fiz. Nauk **114**, 609 (1974) [Sov. Phys.-Usp. **17**, 896 (1975)].

[6] C. B. Araujo, *Quantum-statistical theory of the nonlinear excitation of magnons in parallel pumping experiments*, Phys. Rev. B **10**, 3961 (1974).

[7] V. M. Tsukernik and R. P. Yankelevich, *Stationary distribution of magnons following parametric excitation in ferromagnetic substance*, Zh. Eksp. Teor. Fiz. **68**, 2116 (1975) [Sov. Phys. JETP **41**, 1059 (1976)].

[8] I. A. Vinikovetskii, A. M. Frishman, and V. M. Tsukernik, *Kinetic equation for a system of parametrically excited spin waves*, Zh. Eksp. Teor. Fiz. **76**, 2110 (1979) [Sov. Phys. JETP **49**, 1067 (1979)].

[9] S. P. Lim and D. L. Huber, *Microscopic theory of spin-wave instabilities in parallel-pumped easy-plane ferromagnets*, Phys. Rev. B **37**, 5426 (1988); *Possible mechanism for limiting the number of modes in spin-wave instabilities in parallel pumping*, *ibid.* **41**, 9283 (1990).

[10] Yu. D. Kalafati and V. L. Safanov, *Thermodynamic approach in the theory of paramagnetic resonance of magnons*, Zh. Eksp. Teor. Fiz. **95**, 2009 (1989) [Sov. Phys. JETP **68**, 1162 (1989)].

[11] V. S. L'vov, *Wave Turbulence Under Parametric Excitations* (Springer, Berlin, 1994).

[12] S. M. Rezende, *Theory of microwave superradiance from a Bose-Einstein condensate of magnons*, Phys. Rev. B **79**, 060410(R) (2009); *Theory of coherence in Bose-Einstein condensation phenomena in a microwave-driven interacting magnon gas*, *ibid.*, 174411 (2009).

[13] T. Kloss, A. Kreisel, and P. Kopietz, *Parametric pumping and kinetics of magnons in dipolar ferromagnets*, Phys. Rev. B **81**, 104308 (2010).

[14] V. L. Safonov, *Nonequilibrium Magnons* (Wiley-VCH, Weinheim, Germany, 2013).

[15] S. O. Demokritov, V. E. Demidov, O. Dzyapko, G. A. Melkov, A. A. Serga, B. Hillebrands, and A. N. Slavin, *Bose–Einstein condensation of quasi-equilibrium magnons at room temperature under pumping*, Nature **443**, 430 (2006).

[16] O. Dzyapko, V. E. Demidov, S. O. Demokritov, G. A. Melkov, and A. N. Slavin, *Direct observation of Bose–Einstein condensation in a parametrically driven gas of magnons*, New J. Phys. **9**, 64 (2007).

[17] A. A. Serga, V. S. Tiberkevich, C. W. Sandweg, V. I. Vasyuchka, D. A. Bozhko, A. V. Chumak, T. Neumann, B. Obry, G. A. Melkov, A. N. Slavin, and B. Hillebrands, *Bose–Einstein condensation in an ultra-hot gas of pumped magnons*, Nat. Commun. **5**, 3452 (2014).

[18] V. V. Kruglyak, S. O. Demokritov, and D. Grundler, *Magnonics*, J. Phys. D: Appl. Phys. **43**, 264001 (2010).

[19] A. V. Chumak, V. I. Vasyuchka, A. A. Serga, and B. Hillebrands, *Magnon spintronics*, Nat. Phys. **11**, 453 (2015).

[20] E. Abrahams and C. Kittel, *Spin-Lattice Relaxation in Ferromagnets*, Phys. Rev. **88**, 1200 (1952); *Relaxation Process in Ferromagnetism*, Rev. Mod. Phys. **25**, 233 (1953).

[21] A. Rückriegel, P. Kopietz, D. A. Bozhko, A. A. Serga, and B. Hillebrands, *Magnetoelastic modes and lifetime of magnons in thin yttrium iron garnet films*, Phys. Rev. B **89**, 184413 (2014).

[22] A. Kamra and G. E. W. Bauer, *Actuation, propagation, and detection of transverse magnetoelastic waves in ferromagnets*, Solid State Commun. **198**, 35 (2014).

[23] N. Ogawa, W. Koshibae, A. J. Beekman, N. Nagaosa, M. Kubota, M. Kawasaki, and Y. Tokura, *Photodrive of magnetic bubbles via magnetoelastic waves*, Proc. Natl. Acad. Sci. USA **112**, 8977 (2015)

[24] T. Kikkawa, K. Shen, B. Flebus, R. A. Duine, K. Uchida, Z. Qiu, G. E. W. Bauer, and E. Saitoh, *Magnon polarons in the spin Seebeck effect*, Phys. Rev. Lett. **117**, 207203 (2016).

[25] V. G. Baryakhtar and A. G. Danilevich, *Magnetoelastic oscillations in ferromagnets with cubic symmetry*, Low Temp. Phys. **43**, 351 (2017).

[26] R. Ramos, T. Hioki, Y. Hashimoto, T. Kikkawa, P. Frey, A. J. E. Kreil, V. I. Vasyuchka, A. A. Serga, B. Hillebrands, and E. Saitoh, *Room temperature and low-field resonant enhancement of spin Seebeck effect in partially compensated magnets*, Nat. Commun. **10**, 5162 (2019).

[27] A. Rückriegel and R. A. Duine, *Long-range phonon spin transport in ferromagnet-nonmagnetic insulator heterostructures*, Phys. Rev. Lett. **124**, 117201 (2020).

[28] P. Frey, D. A. Bozhko, V. S. L'vov, B. Hillebrands, and A. A. Serga, *Double accumulation and anisotropic transport of magneto-elastic bosons in yttrium iron garnet films*, Phys. Rev. B **104**, 014420 (2021).

[29] G. Grüner, *The dynamics of charge-density waves*, Rev. Mod. Phys. **60**, 1129 (1988).

[30] P. A. Lee, T. M. Rice, and P. W. Anderson, *Conductivity from charge or spin density waves*, Solid State Commun. **14**, 703 (1974).

[31] M. J. Rice, *Organic Linear Conductors as Systems for the Study of Electron-Phonon Interactions in the Organic Solid State*, Phys. Rev. Lett. **37**, 36 (1976).

[32] M. J. Rice, *Dynamical Properties of the Peierls-Fröhlich State on the Many-Phonon-Coupling Model*, Solid State Commun. **25**, 1083 (1978).

[33] H. Fröhlich, *On the theory of superconductivity: the one-dimensional case*, Proc. R. Soc. Lond. A **223**, 296 (1954).

[34] P. A. Lee and H. Fukuyama, *Dynamics of the charge-density wave. II. Long-range Coulomb effects in an array of chains*, Phys. Rev. B **17**, 542 (1978).

[35] K. Y. M. Wong and S. Takada, *Effects of quasiparticle screening on collective modes: Incommensurate charge-density-wave systems*, Phys. Rev. B **36**, 5476 (1987).

[36] A. Virosztek and K. Maki, *Collective modes in charge-density waves and long-range Coulomb interactions*, Phys. Rev. B **48**, 1368 (1993).

[37] M. O. Hansen, Y. Palan, V. Hahn, M. D. Thomson, K. Warawa, H. G. Roskos, J. Demsar, F. Pientka, O. Tsyplyatyev, and P. Kopietz, *Collective modes in the charge-density wave state of $K_{0.3}MoO_3$: The role of long-range Coulomb interactions revisited*, arXiv:2303.08580 (2023).

[38] J. Chang, E. Blackburn, A. T. Holmes, N. B. Christensen, J. Larsen, J. Mesot, R. Liang, D. A. Bonn, W. N. Hardy, A. Watenphul, M. v. Zimmermann, E. M. Forgan, and S. M. Hayden, *Direct observation of competition between superconductivity and charge density wave order in* $YBa_2Cu_3O_{6.67}$, Nat. Phys. **8**, 871 (2012).

[39] S. Lee, G. de la Peña, S. X.-L. Sun, M. Mitrano, Y. Fang, H. Jang, J.-S. Lee, C. Eckberg, D. Campbell, J. Collini, J. Paglione, F. M. F. de Groot, and P. Abbamonte, *Unconventional Charge Density Wave Order in the Pnictide Superconductor* $Ba(Ni_{1-x}\ Co_x)_2\ As_2$, Phys. Rev. Lett. **112**, 147601 (2019).

[40] B. R. Ortiz, S. M. L. Teicher, Y. Hu, J. L. Zuo, P. M. Sarte, E. C. Schueller, A. M. M. Abeykoon, M. J. Krogstad, S. Rosenkranz, R. Osborn, R. Seshadri, L. Balents, J. He, and S. D. Wilson, CsV_3Sb_5 *: A* $\mathbb{Z}_2$ *Topological Kagome Metal with a Superconducting Ground State*, Phys. Rev. Lett. **125**, 247002 (2020).

[41] S. Raghu, X.-L. Qi, C. Honerkamp, and S.-C. Zhang, *Topological mott insulators*, Phys. Rev. Lett. **100**, 156401 (2008).

[42] T. Zhang, M. Y. Sun, Z. Wang, W. Shi, and P. Sheng, *Crossover from Peierls distortion to one-dimensional superconductivity in arrays of (5,0) carbon nanotubes*, Phys. Rev. B **84**, 245449 (2011).

[43] R. Shimizu et al., *Charge-density wave in Ca-intercalated bilayer graphene induced by commensurate lattice matching*, Phys. Rev. Lett. **114**, 146103 (2015).

[44] J. Fricke, PhD thesis of Jens Fricke (Sarker Verlag, Göttingen, 1997); J. Fricke, *Transport Equations Including Many-Particle Correlations for an Arbitrary Quantum System: A General Formalism*, Ann. Phys. **252**, 479 (1996).

[45] C. Wetterich, *Time Evolution of Nonequilibrium Effective Action*, Phys. Rev. Lett. **78**, 3598 (1997).

[46] T. B. Noack, V. I. Vasyuchka, D. A. Bozhko, B. Heinz, P. Frey, D. V. Slobodianiuk, O. V. Prokopenko, G. A. Melkov, P. Kopietz, B. Hillebrands, and A. A. Serga, *Enhancement of the Spin Pumping Effect by Magnon Confluence Process in YIG/Pt Bilayers*, Phys. Status Solidi B, **256**, 1900121 (2019).

[47] D. A. Bozhko, P. Clausen, G. A. Melkov, V. S. L'vov, A. Pomyalov, V. I. Vasyuchka, A. V. Chumak, B. Hillebrands, A. A. Serga, *Bottleneck Accumulation of Hybrid Magnetoelastic Bosons*, Phys. Rev. Lett. **118**, 237201 (2017).

[48] M. D. Thomson, K. Rabia, F. Meng, M. Bykov, S. van Smaalen, and H. G. Roskos, *Phase-channel dynamics reveal the role of impurities and screening in a quasi-one-dimensional charge-density wave system*, Scientific Reports **7**, 2039 (2017).

[49] K. Warawa, N. Christophel, S. Sobolev, J. Demsar, H. G. Roskos, and M. D. Thomson, *Combined investigation of collective amplitude and phase modes in a quasi-one-dimensional charge-density-wave system over a wide spectral range*, arXiv:2303:08558 (2023).

[50] H. Schäfer, V. V. Kabanov, M. Beyer, K. Biljakovic, and J. Demsar, *Disentanglement of the Electronic and Lattice Parts of the Order Parameter in a 1D Charge Density Wave System Probed by Femtosecond Spectroscopy*, Phys. Rev. Lett. **105**, 066402 (2010).

[51] H. Schäfer, V. V. Kabanov, and J. Demsar, *Collective modes in quasi-one-dimensional charge-density wave systems probed by femtosecond time-resolved optical studies*, Phys. Rev. B **89**, 045106 (2014).

[52] R. Ott, T. V. Zache, and J. Berges, *Equal-time approach to real-time dynamics of quantum fields*, SciPost Phys. **14**, 011 (2023).

[53] V. Hahn and P. Kopietz, *Collisionless kinetic theory for parametrically pumped magnons*, Eur. Phys. J. B **93**, 132 (2020).

[54] V. Hahn and P. Kopietz, *Effect of magnon decays on parametrically pumped magnons*, Phys. Rev. B **103**, 094416 (2021).

[55] V. Hahn, P. Frey, A. A. Serga, V. I. Vasyuchka, B. Hillebrands, P. Kopietz und A. Rückriegel, *Accumulation of magnetoelastic bosons in yttrium iron garnet: Kinetic theory and wave-vector-resolved Brillouin light scattering*, Phys. Rev. B **105**, 144421 (2022).

[56] J. Fricke, *Transportgleichungen für quantenmechanische Vielteilchensysteme*, (Cuvillier-Verlag, Göttingen, 1996).

[57] P. C. Martin and J. Schwinger, *Theory of Many-Particle Systems. I*, Phys. Rev. **115**, 1342 (1959).

[58] J. Schwinger, *Brownian Motion of a Quantum Oscillator*, J. Math. Phys. **2**, 407 (1961).

[59] L. P. Kadanoff and G. Baym, *Quantum Statistical Mechanics* (Benjamin, New York, 1962).

[60] L. V. Keldysh, Zh. Eksp. Teor. Fiz. **47**, 1515 (1964) [*Diagram Technique for Nonequilibrium Processes*, Sov. Phys. JETP **20**, 1018 (1965)].

[61] P. Danielewicz, *Quantum Theory of Nonequilibrium Processes, I*, Ann. Phys. **152**, 239 (1984).

[62] J. Rammer, H. Smith, *Quantum field-theoretical methods in transport theory of metals*, Rev. Mod. Phys. **58**, 323 (1986).

[63] P. Lipavský, V. Špička and B. Velický, *Generalized Kadanoff-Baym ansatz for deriving quantum transport equations*, Phys. Rev. B **34**, 6933 (1986).

[64] K. Ando, S. Takahashi, J. Ieda, Y. Kajiwara, H. Nakayama, T. Yoshino, K. Harii, Y. Fujikawa, M. Matsuo, S. Maekawa, and E. Saitoh, *Inverse spin-Hall effect induced by spin pumping in metallic system*, J. Appl. Phys. **109**, 103913 (2011).

[65] C. W. Sandweg, Y. Kajiwara, A. V. Chumak, A. A. Serga, V. I. Vasyuchka, M. B. Jungfleisch, E. Saitoh, and B. Hillebrands, *Spin Pumping by Parametrically Excited Exchange Magnons*, Phys. Rev. Lett. **106**, 216601 (2011).

[66] N. Nagaosa, *Spin Currents in Semiconductors, Metals, and Insulators*, J. Phys. Soc. Jpn. **77**, 031010 (2008).

[67] T. Holstein and H. Primakoff, *Field Dependence of the Intrinsic Domain Magnetization of a Ferromagnet*, Phys. Rev. **58**, 1098 (1940).

[68] S. M. Rezende, F. M. de Aguiar, and A. Azevedo, *Magnon excitation by spin-polarized direct currents in magnetic nanostructures*, Phys. Rev. B **73**, 094402 (2006).

[69] A. Kreisel, F. Sauli, L. Bartosch, and P. Kopietz, *Microscopic spin-wave theory for yttrium-iron garnet films*, Eur. Phys. J. B **71**, 59 (2009).

[70] J. Hick, F. Sauli, A. Kreisel, and P. Kopietz, *Bose-Einstein condensation at finite momentum and magnon condensation in thin film ferromagnets*, Eur. Phys. J. B **78**, 429 (2010).

[71] R. N. Costa Filho, M.G. Cottam, and G.A. Farias, *Microscopic theory of dipole-exchange spin waves in ferromagnetic films: Linear and nonlinear processes*, Phys. Rev. B **62**, 6545 (2000).

[72] I. S. Tupitsyn, P. C. E. Stamp, and A. L. Burin, *Stability of Bose-Einstein Condensates of Hot Magnons in Yttrium Iron Garnet Films*, Phys. Rev. Lett. **100**, 257202 (2008).

[73] A.I. Akhiezer, V.G. Bar'yakhtar, S.V. Peletminskii, *Spin Waves* (North Holland, Amsterdam, 1968).

[74] D.C. Mattis, *The theory of magnetism made simple* (World Scientific, Singapore, 2006)

[75] F.J. Dyson, *General Theory of Spin-Wave Interactions*, Phys. Rev. **102**, 1217 (1956); *Thermodynamic Behavior of an Ideal Ferromagnet*, *ibid.* Phys. Rev. **102**, 1230 (1956).

[76] S. Maleev, *Scattering of Slow Neutrons in Ferromagnets*, Zh. Eksp. Teor. Fiz. **33**, 1010 (1957) [Sov. Phys. JETP **6**, 776 (1958)].

[77] J. Ziman, *Principles of the Theory of Solids* (Cambridge University Press, Cambridge, 1972).

[78] V. E. Demidov, O. Dzyapko, S. O. Demokritov, G. A. Melkov, and A. N. Slavin, *Thermalization of a Parametrically Driven Magnon Gas Leading to Bose-Einstein Condensation*, Phys. Rev. Lett. **99**, 037205 (2007).

[79] V. E. Demidov, O. Dzyapko, S. O. Demokritov, G. A. Melkov, and A. N. Slavin, *Observation of Spontaneous Coherence in Bose-Einstein Condensate of Magnons*, Phys. Rev. Lett. **100**, 047205 (2008).

[80] S. O. Demokritov, V. E. Demidov, O. Dzyapko, G. A. Melkov, and A. N. Slavin, *Quantum coherence due to Bose–Einstein condensation of parametrically driven magnons*, New J. Phys. **10**, 045029 (2008).

[81] P. Clausen, D. A. Bozhko, V. I. Vasyuchka, B. Hillebrands, G. A. Melkov, and A. A. Serga, *Stimulated thermalization of a parametrically driven magnon gas as a prerequisite for Bose-Einstein magnon condensation*, Phys. Rev. B **91**, 220402(R) (2015).

[82] A. G. Gurevich and G. A. Melkov, *Magnetization Oscillations and Waves* (CRC, Boca Raton, FL, 1996)

[83] R. Takahashi and N. Nagaosa, *Berry Curvature in Magnon-Phonon Hybrid Systems*, Phys. Rev. Lett. **117**, 217205 (2016).

[84] F. G. Eggers and W. Strauss, *A uhf Delay Line Using Single-Crystal Yttrium Iron Garnet*, J. Appl. Phys. **34**, 1180 (1963).

[85] P. Hansen, *Magnetostriction of Ruthenium-Substituted Yttrium Iron Garnet*, Phys. Rev. B **8**, 246 (1973).

[86] C. Kittel, *Interaction of Spin Waves and Ultrasonic Waves in Ferromagnetic Crystals*, Phys. Rev. **110**, 836 (1958).

[87] E. Zaremba, T. Nikuni, and A. Griffin, *Dynamics of Trapped Bose Gases at Finite Temperatures*, J. Low Temp. Phys. **116**, 277 (1999).

[88] S. Takada, K. Y. M. Wong, and T. Holstein, *Damping of charge-density-wave motion*, Phys. Rev. B **32**, 4639 (1985).

[89] H. Haug, A. Jauho, *Quantum kinetics in transport and optics of semiconductors* (Springer, Berlin, 2008).

8 Deutsche Zusammenfassung

8.1 Einleitung

In dieser Arbeit werden zwei verschiedene Systeme untersucht - Spinsysteme, die Spinwellen bzw. deren elementare Anregungen, Magnonen, aufweisen, und elektronische Systeme mit Elektron-Phononkopplung, in denen Ladungsdichtewellen beobachtet werden können. Die Untersuchungen von beiden Systemen sind motiviert durch experimentelle Beobachtungen. Das Ziel dieser Untersuchungen ist es, diese Beobachtungen theoretisch zu erklären. Dazu gehe ich von der mikroskopischen Dynamik des Systems aus, die mithilfe von kinetischen Gleichungen beschrieben wird.

8.2 Kinetische Gleichungen

8.2.1 Einleitung

Um die relevanten Systeme zu untersuchen, stelle ich kinetische Gleichungen auf, die die Zeitentwicklung der relevanten Verteilungsfunktionen beschreiben. Im Prinzip können die Bewegungsgleichungen für n-Punktverteilungsfunktionen aus den Heisenberg'schen Bewegungsgleichungen hergeleitet werden. Allerdings ist die Herleitung der kinetischen Gleichungen nicht die eigentliche Schwierigkeit. Im Allgemeinen erhält man nämlich eine unendliche Hierarchie von Bewegungsgleichungen für alle Ordnungen von n-Punktverteilungsfunktionen. Um diese unendliche Hierarchie von Bewegungsgleichungen lösen zu können, ist es notwendig, die Bewegungsgleichungen zu entkoppeln und die unendliche Hierarchie an einer bestimmten Ordnung zu trunkieren. In Ref. [44] ist gezeigt worden, dass es zu diesem Zweck vorteilhaft ist, die kinetischen Gleichungen über verbundene Korrelationsfunktionen darzustellen, denn in diesem Fall gibt es ein Schema, mit dem die Entkopplung der Bewegungsgleichungen systematisch in beliebiger Ordnung möglich ist [44]. Daher ist die Verwendung der Heisenberg'schen Bewegungsgleichungen unpraktisch.

Die Standardmethode, die in diesem Zusammenhang häufig in der Literatur verwendet wird, basiert auf dem Keldysh-Formalismus [57, 58, 59, 60, 61, 62]. Dieser verwendet Green'sche Funktionen und führt auf eine Dyson-Gleichung. Es werden zwei-zeitige Verteilungsfunktionen betrachtet. Für deren Handhabung wird ein bestimmter Integrationspfad in komplexer Zeit eingeführt, die sogenannte Keldysh-Kontur. Für meine Zwecke ist dieser Formalismus allerdings nicht ideal, denn er produziert Bewegungsgleichungen für zwei-zeitige Verteilungsfunktionen, wohingegen ich im Rahmen dieser Arbeit an ein-zeitigen Verteilungsfunktionen interessiert bin. Ein-zeitige Verteilungsfunktionen können in einem weiteren Schritt mithilfe des generalisierten Kadanoff-Baym-

Ansatzes [63] erhalten werden. Das vorgehen ist umständlich, weswegen ein einfacherer Formalismus gesucht ist, um direkt die Bewegungsgleichungen ein-zeitiger Verteilungsfunktionen zu erhalten. In Ref. [44] wurde eine solche Methode entwickelt, mit der eine perturbative Entwicklung in verbundenen, ein-zeitigen Korrelationen möglich ist. Dazu wurde von der Clusterentwicklung Gebrauch gemacht. Die Methode berücksichtigt Korrelationen als dynamische Größen und führt auf eine unendliche Hierarchie von Bewegungsgleichungen für verbundene, ein-zeitige Korrelationsfunktionen. Sie stellt aber auch ein Entkopplungsschema bereit, mit dem diese unendliche Hierarchie systematisch bei einer beliebigen Ordnung entkoppelt werden kann, sodass eine perturbative Entwicklung möglich ist [56]. Eine Erweiterung auf zwei-zeitige Größen ist prinzipiell möglich. Unter Verwendung der Methode der Green'schen Funktionen wird im Gegensatz dazu eine perturbative Entwicklung in Ein-Teilchenfunktionen durchgeführt. Eine weitere Methode, die kinetischen Gleichungen für ein-zeitige Verteilungsfunktionen herzuleiten, wurde in Refs. [45, 52] entwickelt. In Ref. [45] wurde eine exakte Differentialgleichung für die Zeitentwicklung des generierenden Funktionals der 1PI irreduziblen Korrelationen präsentiert. In Ref. [52] wurde darauf aufbauend eine diagrammatische Methode entwickelt. Der größte Unterschied zwischen dieser und der im Folgenden entwickelten Methode besteht darin, dass die Entwicklung in 1PI irreduziblen Korrelationen statt in verbundenen Korrelationsfunktionen durchgeführt wird. Verbundene Korrelationsfunktionen können anschließend aus den explizieten Ausdrücken für die 1PI irreduzieblen Korrelationen bestimmt werden. Dies stellt einen zusätzlichen Schritt in der Berechnung dar, was die Methode umständlicher macht. Andererseits ermöglicht dies nicht-perturbative Entwicklungen, wie z.B. die large-N Expansion [52].

8.2.2 Generierendes Funktional für verbundene Korrelationsfunktionen

In dieser Arbeit wird analog zu Ref. [52] unter Verwendung des generierenden Funktionals der verbundenen Korrelationsfunktionen eine Methode entwickelt, um kinetische Gleichungen über verbundene Korrelationsfunktionen herzuleiten. Im Vergleich zu der Methode aus Ref. [44] hat dieses Vorgehen den Vorteil, dass die Herleitung mathematisch einfacher ist.

Es wird ein allgemeiner Hamiltonian der Form

$$\mathcal{H} = \sum_{r,s} \Gamma^{r,s}_{q'_1,\ldots,q'_r;q_1,\ldots,q_s} \psi^\dagger_{q'_1} \ldots \psi^\dagger_{q'_r} \psi_{q_1} \ldots \psi_{q_s} \tag{8.1}$$

betrachtet, wobei $\psi^\dagger_k$ und ψ_k bosonische (oder fermionische) Erzeugungs- und Vernichtungsoperatoren sind. Hier sollen allerdings nur bosonische Operatoren betrachtet werden. Der Fall fermionischer Operatoren wird im Haupttext behandelt. Für diesen Hamiltonian kann ein erzeugendes Funktional für verbundene Korrelationsfunktionen $W[j;t]$ definiert werden, sodass

$$\langle \psi^\dagger_{q'_1} \ldots \psi^\dagger_{q'_r} \psi_{q_1} \ldots \psi_{q_s} \rangle^c_t = \left. \frac{\delta^n W[j;t]}{\delta j_{q'_1} \cdots \delta j_{q'_r} \delta j^*_{q_1} \cdots \delta j^*_{q_s}} \right|_{j_i = j^*_i = 0}, \tag{8.2}$$

wobei der Superskript c bedeutet, dass es sich um verbundene Korrelationsfunktionen handelt, und mit j_i die Quellenfelder bezeichnet werden. Die Korrelationsfunktionen werden also durch Ableiten des erzeugenden Funktionals und anschließender Bildung desjenigen Grenzwerts, in dem die Quellenfelder verschwinden, erzeugt.

In Ref. [45] wurde die Zeitentwicklung des erzeugenden Funktionals der n-Punktverteilungsfunktionen hergeleitet. Unter Verwendung dieses Ergebnisses ist es möglich, die Zeitentwicklung des erzeugenden Funktionals der verbundenen Korrelationsfunktionen zu bestimmen. Sie kann geschrieben werden als

$$\begin{aligned}\partial_t W\left[j;t\right] = &-i\sum_k j_k^* \sum_{r,s}\sum_{P\in P_{I_{r,s}}}\sum_{\substack{q_1',\ldots,q_{r-1}'\\ q_1,\ldots,q_s}} \Gamma^{r,s}_{q_1',\ldots,q_{r-1}',k;q_1,\ldots,q_s}\prod_{J\in P}\frac{\delta^{\#J}W\left[j;t\right]}{\delta j_{j_1}^{(*)}\ldots\delta j_{j_{\#J}}^{(*)}}\\ &+i\sum_k j_k \sum_{r,s}\sum_{P\in P_{I'_{r,s}}}\sum_{\substack{q_1',\ldots,q_r'\\ q_1,\ldots,q_{s-1}}} \Gamma^{r,s}_{q_1',\ldots,q_r';q_1,\ldots,q_{s-1},k}\prod_{J\in P}\frac{\delta^{\#J}W\left[j;t\right]}{\delta j_{j_1}^{(*)}\ldots\delta j_{j_{\#J}}^{(*)}},\end{aligned} \tag{8.3}$$

wobei

$$I_{r,s} = \left\{q_1',\ldots,q_{r-1}',q_1,\ldots,q_s\right\} \tag{8.4a}$$

und

$$\tilde{I}_{r,s} = \left\{q_1',\ldots,q_r',q_1,\ldots,q_{s-1}\right\}, \tag{8.4b}$$

und P_I die Menge aller Partitionen von I bezeichnet. Die Zeitentwicklung der Korrelationsfunktionen kann aus dieser Gleichung hergeleitet werden, indem Gl. (8.3) nach den entsprechenden Quellenfeldern abgeleitet wird und der Grenzwert betrachtet wird, in dem die Quellenfelder verschwinden.

8.2.3 Diagrammatische Methode

Um die Rechnung zu erleichtern, wird nun eine diagrammatische Methode entwickelt, mit der man die Zeitentwicklung der Korrelationsfunktionen erhält. Die Diagramme, die hier verwendet werden, unterscheiden sich von Feynman-Diagrammen. Sie stellen Beiträge zu den Bewegungsgleichungen der Korrelationsfunktionen dar. Daher enthalten sie auch keine Zeit- oder Energieintegration [44].

Es werden nun eine Reihe diagrammatischer Elemente eingeführt. Als erstes sollen externe Vertices eingeführt werden, die in Abb. 8.1 dargestellt sind. Sie repräsentieren einzelne Vernichtungs- oder Erzeugungsoperatoren. Das diagrammatische Element, dass den Wechselwirkungsvertex darstellt, ist in Abb. 8.2 dargestellt. Abb. 8.3 zeigt die Korrelationsblase, die Korrelationsfunktionen darstellt, deren Ordnung ungleich zwei ist. Korrelationsfunktionen der Ordnung zwei werden durch einzelne Linien dargestellt, wie in Abb. 8.4 gezeigt, und werden auch als Kontraktionen bezeichnet [44]. Der Grund hierfür liegt in der besonderen Rolle begründet, die Zwei-Punktkorrelationsfunktionen erfüllen. Dies hängt mit den Kommutatorrelationen zusammen, die die Korrelationsfunktionen erfüllen: Nur für Zwei-Punktkorrelationen sind diese nicht-trivial. Außerdem stellt eine der Kontraktionen mit dem Wechselwirkungsvertex denjenigen Term in der Zeitentwicklung des erzeugenden Funktionals (8.3) dar, der auf den Vorfaktor $j_{\boldsymbol{k}}$ bzw.

Figure 8.1: Externe Vertices, die die Erzeugungsoperatoren $\psi^\dagger_{\boldsymbol{k}'_r}$ (links) oder die Vernichtungsoperatoren $\psi_{\boldsymbol{k}_s}$ (rechts) darstellen.

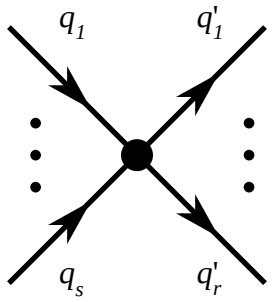

Figure 8.2: Der Wechselwirkungsvertex, der durch das Matrixelement $\Gamma^{r,s}_{q'_1,\ldots,q'_r,q_1,\ldots,q_s}$ beschrieben wird.

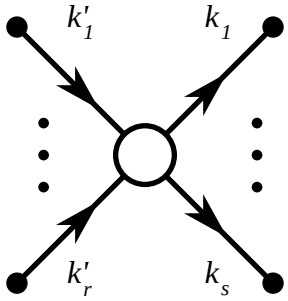

Figure 8.3: Die Korrelationsblase, die die Korrelationsfunktion $\langle \psi_{k_1} \ldots \psi_{k_s} \psi^\dagger_{k'_1} \ldots \psi^\dagger_{k'_r} \rangle^c$ repräsentiert.

Figure 8.4: Die Kontraktion, die die Zwei-Punktkorrelationsfunktion $\langle \psi_{k_s} \psi^\dagger_{k'_r} \rangle^c$ (auch Kontraktion genannt) darstellt.

$j^*_{\boldsymbol{k}}$ wirkt. Dieser Vorfaktor fällt daher weg. Andernfalls verschwindet der Beitrag im Grenzwert $j^* = j = 0$.

Die Zeitentwicklung der Korrelationsfunktionen kann nun in der Form [44]

$$\left[\frac{\mathrm{d}}{\mathrm{d}t} + i\left(\epsilon_{\boldsymbol{k}_1} + \cdots + \epsilon_{\boldsymbol{k}_s} - \epsilon_{\boldsymbol{k}'_1} - \cdots - \epsilon_{\boldsymbol{k}'_r}\right)\right] \langle \psi_{\boldsymbol{k}_1} \cdots \psi_{\boldsymbol{k}_s} \psi^\dagger_{\boldsymbol{k}'_1} \cdots \psi^\dagger_{\boldsymbol{k}'_r} \rangle^c_t$$
$$= -i \sum_{\text{diagrams}} \frac{1}{2^{n_e}} \sum_{\substack{\boldsymbol{q}'_1, \ldots, \boldsymbol{q}'_r \\ \boldsymbol{q}_1, \ldots, \boldsymbol{q}_s}} \Gamma^{r,s}_{\boldsymbol{q}_1,\ldots,\boldsymbol{q}_s;\boldsymbol{q}'_1,\ldots,\boldsymbol{q}'_r} X_{\text{Diagramm}} \tag{8.5}$$

geschrieben werden, wobei 2^{n_e} einen kombinatorischen Vorfaktor darstellt und der Ausdruck n_e im Haupttext erklärt wird. X_{Diagramm} bezeichnet den Stoßterm und wird aus der Zeitentwicklung des erzeugenden Funktionals (8.3) dadurch erzeugt, dass die Ableitungen nach den Quellenfeldern auf alle Terme auf der rechten Seite der Gleichung angewandt werden. Der Stoßterm kann nach bestimmten Regeln aus den Diagrammen bestimmt werden, welche ebenfalls im Haupttext erklärt werden. Er setzt sich zusammen aus dem Produkt

1. aller Korrelationen, die von Korrelationsblasen stammen,
2. aller Kontraktionen, die am Wechselwirkungsvertex starten und enden in normalgeordneter Form $\langle \psi^\dagger_{\boldsymbol{q}_i} \psi_{\boldsymbol{q}_j} \rangle^c$,
3. aller Kontraktionen, die an externen Vertices starten und enden in antinormalgeordneter Form $\langle \psi_{\boldsymbol{k}'_i} \psi^\dagger_{\boldsymbol{k}'_j} \rangle^c$ und
4. der übrigen Kontraktionen zwischen dem Wechselwirkungsvertex und den externen Vertices.

Der letzte Beitrag hat die Form

$$\langle \psi_{\boldsymbol{k}_1} \psi^\dagger_{\boldsymbol{q}_1} \rangle^c_t \cdots \langle \psi_{\boldsymbol{k}_s} \psi^\dagger_{\boldsymbol{q}_s} \rangle^c_t \left(-\langle \psi^\dagger_{\boldsymbol{k}'_1} \psi_{\boldsymbol{q}'_1} \rangle^c_t\right) \cdots \left(-\langle \psi^\dagger_{\boldsymbol{k}'_r} \psi_{\boldsymbol{q}'_r} \rangle^c_t\right)$$
$$- \left(-\langle \psi^\dagger_{\boldsymbol{q}_1} \psi_{\boldsymbol{k}_1} \rangle^c_t\right) \cdots \left(-\langle \psi^\dagger_{\boldsymbol{q}_s} \psi_{\boldsymbol{k}_s} \rangle^c_t\right) \langle \psi_{\boldsymbol{q}'_1} \psi^\dagger_{\boldsymbol{k}'_1} \rangle^c_t \cdots \langle \psi_{\boldsymbol{q}'_r} \psi^\dagger_{\boldsymbol{k}'_r} \rangle^c_t, \tag{8.6}$$

wobei s die Anzahl der vom Wechselwirkungsvertex ausgehenden Linien bezeichnet und r die Anzahl der eingehenden Linien.

8.3 Magnonen in YIG

8.3.1 Einleitung

Die erste Art von System, das untersucht werden soll, ist ein dünner Streifen eines Ferrimagneten. Besonders interessant ist der magnetische Isolator Yttrium-Eisen-Granat (YIG, $Y_3Fe_5O_{12}$), da dieser die kleinste bekannte Spinwellendämpfung aufweist [1]. Motiviert sind meine Untersuchungen von dem Experiment [46], in dem Magnonen

mithilfe eines oszillierenden magnetischen Feldes H_1 erzeugt werden. Für eine bestimmte Stärke des statischen magnetischen Feldes H_0 wird ein Peak oder ein Dip in der Magnonendichte im stationären Nicht-Gleichgewichtszustand als Funktion der externen Feldstärke beobachtet. Diese Feldstärke liegt in der Nähre der Konfluenzfeldstärke, bei der Konfluenzprozesse von zwei parametrisch gepumpten Magnonen mit gleichem Wellenvektor kinematisch möglich werden. Bei der Konfluenz von Magnonen werden zwei Magnonen vernichtet und ein Magnon, das die Gesamtenergie und den Gesamtimpuls beider vernichteter Magnonen trägt, wird erzeugt. Daher wird angenommen, dass Drei-Magnonprozesse relevant sind, um den beobachteten Effekt zu erklären. Prozesse, bei denen sich die Gesamtteilchenzahl ändert, sind dadurch möglich, dass es sich bei Magnonen um Quasiteilchen handelt.

8.3.2 Effektiver Hamiltonian

In diesem Kapitel wird ein Spinsystem untersucht. Die Methode, die im vorherigen Kapitel beschrieben wurde, ist jedoch nur anwendbar, falls die beteiligten Kommutatoren kanonische Vertauschungsrelationen erfüllen. Die Operatoren, die in dem effektiven Hamiltonian auftauchen, sind allerdings Spinoperatoren. Daher ist die Methode nicht direkt auf den Spin-Hamiltonian anwendbar. Um dieses Problem zu beheben, werden nun die Spinoperatoren mithilfe der Holstein-Primakoff-Transformation über bosonische Operatoren dargestellt, welche als Erzeugungs- und Vernichtungsoperatoren von Magnonen interpretiert werden können. Der sich aus der Transformation ergebende Hamiltonian kann in dem kleinen Parameter $1/S$ entwickelt werden,

$$\mathcal{H}_m(t) = \mathcal{H}_m^{(0)}(t) + \mathcal{H}_m^{(2)}(t) + \mathcal{H}_m^{(3)} + \mathcal{H}_m^{(4)} + \mathcal{O}(S^{-1/2}). \tag{8.7}$$

Hierbei enthält der Hamiltonian n-ter Ordnung $\mathcal{H}_m^{(n)}$ alle Terme der Ordnung n in den bosonischen Operatoren b_i und $b_i^\dagger$. In diesem Kapitel werden Terme höherer Ordnung als vierter Ordnung vernachlässigt. Der so approximierte Hamiltonian beschreibt kleine Fluktuationen um den klassischen Grundzustand [73, 74].

Um einen Hamiltonian zu erhalten, mit dem man leichter weiterarbeiten kann, wird eine Fourier-Transformation angewandt, sodass das System im Impulsraum betrachtet wird, und anschließend eine Bogoliubov-Transformation. Nach einer Transformation in das mit dem oszillierenden Feld mitrotierende Bezugssystem mit Kreisfrequenz ω_0 haben

die einzelnen Terme des Hamiltonian schließlich die Form [70]

$$\tilde{\mathcal{H}}_m^{(2)}(t) = \sum_{\boldsymbol{k}} \left[E_{\boldsymbol{k}} \tilde{a}_{\boldsymbol{k}}^\dagger \tilde{a}_{\boldsymbol{k}} + \frac{V_{\boldsymbol{k}}}{2} \tilde{a}_{\boldsymbol{k}}^\dagger \tilde{a}_{-\boldsymbol{k}}^\dagger + \frac{V_{\boldsymbol{k}}^*}{2} \tilde{a}_{-\boldsymbol{k}} \tilde{a}_{\boldsymbol{k}} \right], \tag{8.8}$$

$$\begin{aligned} \tilde{\mathcal{H}}_m^{(3)}(t) = \frac{1}{\sqrt{N}} \sum_{\boldsymbol{k}_1,\boldsymbol{k}_2,\boldsymbol{k}_3} \delta_{\boldsymbol{k}_1+\boldsymbol{k}_2+\boldsymbol{k}_3,0} \Bigg[& \frac{1}{2} \Gamma_{1;2,3}^{\bar{a}aa} e^{-i\omega_0 t/2} \tilde{a}_{-1}^\dagger \tilde{a}_2 \tilde{a}_3 + \frac{1}{2} \Gamma_{1,2;3}^{\bar{a}\bar{a}a} e^{i\omega_0 t/2} \tilde{a}_{-1}^\dagger \tilde{a}_{-2}^\dagger \tilde{a}_3 \\ & + \frac{1}{3!} \Gamma_{1,2,3}^{aaa} e^{-3i\omega_0 t/2} \tilde{a}_1 \tilde{a}_2 \tilde{a}_3 + \frac{1}{3!} \Gamma_{1,2,3}^{\bar{a}\bar{a}\bar{a}} e^{3i\omega_0 t/2} \tilde{a}_{-1}^\dagger \tilde{a}_{-2}^\dagger \tilde{a}_{-3}^\dagger \Bigg], \end{aligned} \tag{8.9}$$

$$\begin{aligned} \tilde{\mathcal{H}}_m^{(4)}(t) = \frac{1}{N} \sum_{\boldsymbol{k}_1,\boldsymbol{k}_2,\boldsymbol{k}_3,\boldsymbol{k}_4} \delta_{\boldsymbol{k}_1+\boldsymbol{k}_2+\boldsymbol{k}_3+\boldsymbol{k}_4,0} \Bigg[& \frac{1}{(2!)^2} \Gamma_{1,2;3,4}^{\bar{a}\bar{a}aa} \tilde{a}_{-1}^\dagger \tilde{a}_{-2}^\dagger \tilde{a}_3 \tilde{a}_4 \\ & + \frac{1}{3!} e^{-i\omega_0 t} \Gamma_{1;2,3,4}^{\bar{a}aaa} \tilde{a}_{-1}^\dagger \tilde{a}_2 \tilde{a}_3 \tilde{a}_4 + \frac{1}{3!} e^{i\omega_0 t} \Gamma_{1,2,3;4}^{\bar{a}\bar{a}\bar{a}a} \tilde{a}_{-1}^\dagger \tilde{a}_{-2}^\dagger \tilde{a}_{-3}^\dagger \tilde{a}_4 \\ & + \frac{1}{4!} e^{-2i\omega_0 t} \Gamma_{1,2,3,4}^{aaaa} \tilde{a}_1 \tilde{a}_2 \tilde{a}_3 \tilde{a}_4 + \frac{1}{4!} e^{2i\omega_0 t} \Gamma_{1,2,3,4}^{\bar{a}\bar{a}\bar{a}\bar{a}} \tilde{a}_{-1}^\dagger \tilde{a}_{-2}^\dagger \tilde{a}_{-3}^\dagger \tilde{a}_{-4}^\dagger \Bigg]. \end{aligned} \tag{8.10}$$

wobei die Koeffizienten $A_{\boldsymbol{k}}$ und $B_{\boldsymbol{k}}$ gegeben sind durch Gl. (3.18), die kubischen Vertices durch Gl. (3.15) gegeben sind, die quartischen Vertices durch Gl. (3.16) gegeben sind und $E_{\boldsymbol{k}} = \epsilon_{\boldsymbol{k}} - \omega_0/2$. Hier ist ω_0 die Kreisfrequenz des oszillierenden Feldes und $\epsilon_{\boldsymbol{k}}$ beschreibt die Dispersion der Magnonen und lautet

$$\begin{aligned} \epsilon_{\boldsymbol{k}} &= \sqrt{A_{\boldsymbol{k}}^2 - |B_{\boldsymbol{k}}|^2} \\ &\approx \sqrt{\left[h_0 + \rho \boldsymbol{k}^2 + \Delta \left(1 - f_{\boldsymbol{k}}\right) \sin^2 \theta_{\boldsymbol{k}}\right] \left[h_0 + \rho \boldsymbol{k}^2 + \Delta f_{\boldsymbol{k}}\right]}. \end{aligned} \tag{8.11}$$

$V_{\boldsymbol{k}}$ ist die Pumpenergie und lautet

$$V_{\boldsymbol{k}} = -\frac{h_1 B_{\boldsymbol{k}}}{2\varepsilon_{\boldsymbol{k}}}. \tag{8.12}$$

Die Dispersionsrelation und die Pumpenergie in Abhängigkeit des Wellenvektors sind in Abb. 3.2 dargestellt.

8.3.3 Kinetische Gleichungen

Zunächst soll das nicht-wechselwirkende System betrachtet werden. Es werden die folgenden diagonalen und anomalen verbundenen Magnonenverteilungsfunktionen eingeführt:

$$\tilde{n}_{\boldsymbol{k}}^c(t) \equiv \langle \tilde{a}_{\boldsymbol{k}}^\dagger(t) \tilde{a}_{\boldsymbol{k}}(t) \rangle^c = \langle a_{\boldsymbol{k}}^\dagger(t) a_{\boldsymbol{k}}(t) \rangle^c = n_{\boldsymbol{k}}^c(t), \tag{8.13a}$$

$$\tilde{p}_{\boldsymbol{k}}^c(t) \equiv \langle \tilde{a}_{-\boldsymbol{k}}(t) \tilde{a}_{\boldsymbol{k}}(t) \rangle^c = e^{i\omega_0 t} \langle a_{-\boldsymbol{k}}(t) a_{\boldsymbol{k}}(t) \rangle^c = e^{i\omega_0 t} p_{\boldsymbol{k}}^c(t), \tag{8.13b}$$

wobei $\langle \dots \rangle$ definiert ist als die Spur über einen Dichteoperator ρ_0, der für den Anfangszeitpunkt t_0 gegeben ist. Die Vakuumerwartungswerte der Magnonenoperatoren werden in diesem Kapitel vernachlässigt, da sie für die experimentellen Beobachtungen nicht relevant sind. Es wird nun ausschließlich der quadratische Hamiltonian $\tilde{\mathcal{H}}_m^{(2)}$

explizit betrachtet. Die Bewegungsgleichungen für die beiden Magnonenverteilungsfunktionen folgen dann aus den Heisenberg'schen Bewegungsgleichungen und lauten

$$\begin{aligned} \partial_t n^c_{\boldsymbol{k}}(t) + i\left[V_{\boldsymbol{k}}\left(\tilde{p}^c_{\boldsymbol{k}}(t)\right)^* - V^*_{\boldsymbol{k}}\tilde{p}^c_{\boldsymbol{k}}(t)\right] &= 0, & (8.14a)\\ \partial_t \tilde{p}^c_{\boldsymbol{k}}(t) + 2iE_{\boldsymbol{k}}\tilde{p}^c_{\boldsymbol{k}}(t) + iV_{\boldsymbol{k}}\left[2n^c_{\boldsymbol{k}}(t)+1\right] &= 0, & (8.14b)\end{aligned}$$

wobei $E_{\boldsymbol{k}} = E_{-\boldsymbol{k}}$ und $n_{\boldsymbol{k}} = n_{-\boldsymbol{k}}$ angenommen wurde. Diese Gleichungen haben eine exakte analytische Lösung [14]. Für $|E_{\boldsymbol{k}}| > |V_{\boldsymbol{k}}|$ zeigen die Lösungen ein oszillierendes Verhalten, wohingegen für $|V_{\boldsymbol{k}}| > |E_{\boldsymbol{k}}|$ die Lösungen exponentiell ansteigen und für $t \to \infty$ divergieren. Offenbar ist das nicht-wechselwirkende System nicht in der Lage, physikalisch sinnvolle Ergebnisse bei starkem Pumpen des Systems zu reproduzieren.

Es ist somit notwendig, Magnon-Magnonwechselwirkungen zu berücksichtigen, um ein sinnvolles Verhalten bei starker Kopplung zu beobachten. Die Wechselwirkungen führen dazu, dass die Magnonendichte saturiert. Dazu werden als nächstes Zwei-Teilchenwechselwirkungen mitberücksichtigt. Die einfachste geeignete Näherung ist die zeitabhängige selbstkonsistente Hartree-Fock Näherung. In der Literatur ist sie in diesem Kontext auch als "S-Theorie" bekannt [2, 5, 9, 11, 12]. Die Bewegungsgleichungen (8.14) werden ersetzt durch

$$\begin{aligned} \partial_t n^c_{\boldsymbol{k}}(t) + i\left[\tilde{V}_{\boldsymbol{k}}(t)\left(\tilde{p}^c_{\boldsymbol{k}}(t)\right)^* - \tilde{V}^*_{\boldsymbol{k}}(t)\tilde{p}^c_{\boldsymbol{k}}(t)\right] &= 0, & (8.15a)\\ \partial_t \tilde{p}^c_{\boldsymbol{k}}(t) + 2i\tilde{E}_{\boldsymbol{k}}(t)\tilde{p}^c_{\boldsymbol{k}}(t) + i\tilde{V}_{\boldsymbol{k}}(t)\left[2n^c_{\boldsymbol{k}}(t)+1\right] &= 0, & (8.15b)\end{aligned}$$

wobei $\tilde{E}_{\boldsymbol{k}}(t)$ und $\tilde{V}_{\boldsymbol{k}}(t)$ die renormierte Magnonendispersion und die renormierte Pumpenergie sind. Diese sind gegeben durch Gl. (3.40). Die Gleichungen (8.15) können auch mithilfe der diagrammatischen Methode hergeleitet werden, die in dieser Arbeit entwickelt wurde. Die relevanten Diagramme für die Zeitentwicklung der diagonalen Magnonenverteilungsfunktion sind in Abb. 3.3 dargestellt und die Diagramme für die anomale Verteilungsfunktion sind in Abb. 3.4 gezeigt. In den exakten Ausdrücken für die renormierte Magnonendispersion und die renormierte Pumpenergie tauchen schnell oszillierende Terme auf, die proportional zu $e^{\pm i\omega_0 t}$ oder $e^{\pm 2i\omega_0 t}$ sind. Diese Terme werden vernachlässigt, sodass [2, 5, 9, 11, 12]

$$\begin{aligned} \tilde{E}_{\boldsymbol{k}}(t) &= E_{\boldsymbol{k}} + \frac{1}{N}\sum_{\boldsymbol{q}} T_{\boldsymbol{k},\boldsymbol{q}} n^c_{\boldsymbol{q}}(t), & (8.16a)\\ \tilde{V}_{\boldsymbol{k}}(t) &= V_{\boldsymbol{k}} + \frac{1}{2N}\sum_{\boldsymbol{q}} S_{\boldsymbol{k},\boldsymbol{q}} \tilde{p}^c_{\boldsymbol{q}}(t), & (8.16b)\end{aligned}$$

mit

$$\begin{aligned} T_{\boldsymbol{k},\boldsymbol{q}} &= \Gamma^{\bar{a}\bar{a}aa}_{-\boldsymbol{k},-\boldsymbol{q};\boldsymbol{q},\boldsymbol{k}}, & (8.17a)\\ S_{\boldsymbol{k},\boldsymbol{q}} &= \Gamma^{\bar{a}\bar{a}aa}_{-\boldsymbol{k},\boldsymbol{k};-\boldsymbol{q},\boldsymbol{q}}. & (8.17b)\end{aligned}$$

8.3.4 Stoßintegrale

Nun werden Stoßintegrale auf der rechten Seite der Bewegungsgleichungen eingeführt, die die Drei-Magnonprozesse beschreiben, die bisher nicht berücksichtigt wurden. Die

Bewegungsgleichungen lauten nun also [54]

$$\partial_t n^c_{\boldsymbol{k}}(t) + i\left[\tilde{V}_{\boldsymbol{k}}(t)\,(\tilde{p}^c_{\boldsymbol{k}}(t))^* - \tilde{V}^*_{\boldsymbol{k}}(t)\tilde{p}^c_{\boldsymbol{k}}(t)\right] = I^n_{\boldsymbol{k}}(t), \tag{8.18a}$$

$$\partial_t \tilde{p}^c_{\boldsymbol{k}}(t) + 2i\tilde{E}_{\boldsymbol{k}}(t)\tilde{p}_{\boldsymbol{k}}(t) + i\tilde{V}_{\boldsymbol{k}}(t)\,[2n^c_{\boldsymbol{k}}(t)+1] = I^p_{\boldsymbol{k}}(t). \tag{8.18b}$$

Diese Stoßintegrale müssen mithilfe des kubischen Hamiltonians $\mathcal{H}^{(3)}_m$ hergeleitet werden. Dazu wird die zuvor beschriebene diagrammatische Methode verwendet. Die Diagramme, die zu der Bewegungsgleichung der diagonalen Magnonenkorrelationsfunktion $n^c_{\boldsymbol{k}}$ beitragen, sind in Abb. 3.9 gezeigt und die Diagramme, die zu der Bewegungsgleichung der anomalen Magnonenkorrelationsfunktion $\tilde{p}^c_{\boldsymbol{k}}$ beitragen, sind in Abb. 3.10 dargestellt. Die beiden unteren Diagramme von Abb. 3.9 entsprechen den komplex konjugierten oberen Diagrammen, sodass das Stoßintegral $I^n_{\boldsymbol{k}}$ reell ist. Alle Diagramme enthalten jeweils den Wechselwirkungsvertex und eine Dreipunktkorrelation. Die resultierenden Bewegungsgleichungen bilden somit kein geschlossenes Gleichungssystem. Es ist notwendig, die Bewegungsgleichungen für die Dreipunktkorrelationen herzuleiten. Diese Bewegungsgleichungen können formal integriert werden und anschließend in die Stoßintegrale $I^n_{\boldsymbol{k}}$ und $I^p_{\boldsymbol{k}}$ eingesetzt werden. Allerdings enthalten diese Ausdrücke höhere Korrelationsfunktionen. Es gibt eine unendliche Hierarchie von Bewegungsgleichungen. Um ein geschlossenes Gleichungssystem zu erhalten, muss diese unendliche Hierarchie bei einer endlichen Ordnung trunkiert werden. Daher werden in den Bewegungsgleichungen der Dreipunktkorrelationen die Terme, die Korrelationsfunktionen höherer Ordnung enthalten, vernachlässigt. Die Stoßintegrale können weiter vereinfacht werden, indem eine Markov-Näherung angewandt wird, bei der der Grenzwert $t_0 \to -\infty$ gebildet wird, wobei t_0 die Anfangszeit ist. Dies führt dazu, dass Dirac'sche Deltafunktionen auftreten, die Energieerhaltung sicherstellen. Diese Näherung kann dadurch gerechtfertigt werden, dass ich an dem stationären Nicht-Gleichgewichtszustand interessiert bin und nicht an der Dynamik für kleine Zeiten. Das Endergebnis für die Stoßintegrale ist in Gl. (3.63) und Gl. (3.64) zu finden. Auch hier werden schnell oszillierende Terme vernachlässigt.

8.3.5 Konfluenz von Magnonen

Aufgrund der Tatsache, dass der im Experiment beobachtete Effekt in der Nähe der Konfluenzfeldstärke auftritt, werden nun die Konfluenz- und Splittingprozesse von Magnonen untersucht. Die zuvor berechneten Stoßintegrale können in der Form

$$I^n_{\boldsymbol{k}} = I^n_{\boldsymbol{k},\mathrm{in}} - I^n_{\boldsymbol{k},\mathrm{out}}, \tag{8.19a}$$

$$I^p_{\boldsymbol{k}} = I^p_{\boldsymbol{k},\mathrm{in}} - I^p_{\boldsymbol{k},\mathrm{out}}, \tag{8.19b}$$

über einen In-Scattering-Term und einem Out-Scattering-Term dargestellt werden. Letzterer kann wiederum in der Form

$$I^n_{\boldsymbol{k},\mathrm{out}} = \gamma^n_{\boldsymbol{k}} n^c_{\boldsymbol{k}}, \tag{8.20a}$$

$$I^p_{\boldsymbol{k},\mathrm{out}} = \gamma^p_{\boldsymbol{k}} \tilde{p}^c_{\boldsymbol{k}}, \tag{8.20b}$$

dargestellt werden, wobei $\gamma_{\boldsymbol{k}}^n$ und $\gamma_{\boldsymbol{k}}^p$ Dämpfungskonstanten darstellen. Diese setzten sich wiederum aus einem Anteil zusammen, der von Konfluenzprozessen herrührt, und einem, der von Splittingprozessen herrührt. Sie lauten [54]

$$\gamma_{\boldsymbol{k}}^{n,\mathrm{con}} = \frac{\pi}{N} \sum_{\boldsymbol{q}} \delta\left(\epsilon_{\boldsymbol{k}} - \epsilon_{\boldsymbol{k}-\boldsymbol{q}} - \epsilon_{\boldsymbol{q}}\right) \left|\Gamma^{\bar{a}aa}_{\boldsymbol{k};\boldsymbol{k}-\boldsymbol{q},\boldsymbol{q}}\right|^2 \left(1 + n^c_{\boldsymbol{k}-\boldsymbol{q}} + n^c_{\boldsymbol{q}}\right) \tag{8.21a}$$

und

$$\gamma_{\boldsymbol{k}}^{n,\mathrm{split}} = \frac{2\pi}{N} \sum_{\boldsymbol{q}} \delta\left(\epsilon_{\boldsymbol{k}} + \epsilon_{\boldsymbol{q}-\boldsymbol{k}} - \epsilon_{\boldsymbol{q}}\right) \left|\Gamma^{\bar{a}aa}_{\boldsymbol{q};\boldsymbol{q}-\boldsymbol{k},\boldsymbol{k}}\right|^2 \left(n^c_{\boldsymbol{q}-\boldsymbol{k}} - n^c_{\boldsymbol{q}}\right). \tag{8.21b}$$

Im Folgenden wird angenommen, dass diese beiden Beiträge die dominanten Beiträge zu den Stoßintegralen sind. Die anderen Terme werden vernachlässigt.

Es soll nun ein stationärer Zustand gesucht werden, d.h. es ist eine Lösung für $n^c_{\boldsymbol{k}}$ und $\tilde{p}^c_{\boldsymbol{k}}$ gesucht, die $\partial_t n^c_{\boldsymbol{k}} = 0$ und $\partial_t \tilde{p}^c_{\boldsymbol{k}} = 0$ erfüllt. Unter der Annahme, dass die Dämpfungskonstanten $\gamma^n_{\boldsymbol{k}}$ und $\gamma^p_{\boldsymbol{k}}$ konstant sind, gibt es für den Fall $|V_{\boldsymbol{k}}| > \frac{1}{4}\gamma^n_{\boldsymbol{k}} \mathrm{Re}\left[\gamma^p_{\boldsymbol{k}}\right]$ einen stationären Nicht-Gleichgewichtszustand, der gegeben ist durch [54]

$$n^s_{\boldsymbol{k}} = \sqrt{\frac{\mathrm{Re}\left[\gamma^p_{\boldsymbol{k}}\right]}{\gamma^n_{\boldsymbol{k}}}} \left|\tilde{p}_{\boldsymbol{k}}\right|, \tag{8.22a}$$

$$\tilde{p}^s_{\boldsymbol{k}} = -\left(\sqrt{1 - \frac{\gamma^n_{\boldsymbol{k}} \mathrm{Re}\left[\gamma^p_{\boldsymbol{k}}\right]}{4\left|V_{\boldsymbol{k}}\right|^2}} + i\sqrt{\frac{\gamma^n_{\boldsymbol{k}} \mathrm{Re}\left[\gamma^p_{\boldsymbol{k}}\right]}{4\left|V_{\boldsymbol{k}}\right|^2}}\right) \left|\tilde{p}_{\boldsymbol{k}}\right|, \tag{8.22b}$$

$$\left|\tilde{p}^s_{\boldsymbol{k}}\right| = N \frac{\sqrt{\left|V_{\boldsymbol{k}}\right|^2 - \frac{1}{4}\gamma^n_{\boldsymbol{k}} \mathrm{Re}\left[\gamma^p_{\boldsymbol{k}}\right]} - \left|E_{\boldsymbol{k}} - \frac{1}{2}\mathrm{Im}\left[\gamma^p_{\boldsymbol{k}}\right]\right| \sqrt{\gamma^n_{\boldsymbol{k}} / \mathrm{Re}\left[\gamma^p_{\boldsymbol{k}}\right]}}{T_{\boldsymbol{k},\boldsymbol{k}} + \frac{1}{2} S_{\boldsymbol{k},\boldsymbol{k}}}. \tag{8.22c}$$

Für $\frac{1}{2}\gamma^n_{\boldsymbol{k}} = \frac{1}{2}\gamma^p_{\boldsymbol{k}} \equiv \gamma_{\boldsymbol{k}}$ reduziert sich dieses Ergebnis auf den aus der Literatur bekannten stationären Zustand in S-Theorie [2, 5, 9, 11, 12].

Allerdings sind nun die beiden Dämpfungskonstanten nicht konstant, sondern hängen nach Gl. (8.21a) und (8.21b) explizit von den diagonalen Magnonenkorrelationsfunktionen ab. Die Bewegungsgleichungen sind komplizierte Integro-Differentialgleichungen. Um diese zu vereinfachen, sollen nun nur zwei Gruppen von Magnonen explizit berücksichtigt werden. Die erste Gruppe von Magnonen sind die parametrischen Magnonen. Diese werden durch das oszillierende magnetische Feld generiert und haben die Energie $\epsilon_{\boldsymbol{k}} = \omega_0/2$. Sie liegen auf einer Schale im Impulsraum, die durch die Resonanzbedingung $\epsilon_{\boldsymbol{k}} = \omega_0/2$ definiert ist. Innerhalb der Näherungen von S-Theorie kann angenommen werden, dass nur diese Gruppe von Magnonen durch das parametrische Pumpen erzeugt werden. Hier ist ebenfalls eine weitere Gruppe von Magnonen explizit zu berücksichtigen: sekundäre Magnonen, die durch Konfluenzprozesse von zwei parametrischen Magnonen erzeugt werden. Sie haben dadurch die doppelte Energie $\epsilon_{\boldsymbol{k}} = \omega_0$. Auch diese Bedingung ist auf einer Schale im Impulsraum erfüllt [54].

Es wird angenommen, dass sich die anderen Magnonen im thermischen Gleichgewichtszustand befinden. Die entsprechenden Beiträge zu den Stoßintegralen müssen entsprechend berücksichtigt werden. Für die parametrischen und die sekundären Magnonen

vereinfachen sich die Stoßintegrale, da die Argumente der Dirac'schen Deltafunktionen nur verschwinden, wenn zwei der am Prozess beteiligten Magnonen parametrische Magnonen sind und eines der Magnonen ein sekundäres Magnon ist. Wenn mit $n_{\boldsymbol{k}}^{(0)}$ und $\tilde{p}_{\boldsymbol{k}}^{(0)}$ die Ein-Teilchenkorrelationsfunktionen für die parametrischen Magnonen bezeichnet werden und mit $n_{\boldsymbol{k}}^{(1)}$ und $\tilde{p}_{\boldsymbol{k}}^{(1)}$ diejenigen der sekundären Magnonen, sind die expliziten Ausdrücke für die Stoßintegrale in dieser Näherung gegeben durch die Gleichungen (3.82). Bei der Integration muss derjenige Wellenvektor $\boldsymbol{q}$ gefunden werden, der die beiden Bedingungen $\epsilon_{\boldsymbol{q}} = \omega_0$ und $\epsilon_{\boldsymbol{q}-\boldsymbol{k}} = \omega_0/2$ für die parametrischen Magnonen bzw. $\epsilon_{\boldsymbol{q}} = \omega_0/2$ und $\epsilon_{\boldsymbol{k}-\boldsymbol{q}} = \omega_0/2$ für die sekundären Magnonen gleichzeitig erfüllt. Dies ist nicht für alle Wellenvektoren $\boldsymbol{k}$ möglich. In diesem Fall gibt es keinen Beitrag zum Stoßintegral außer dem thermischen Anteil, der in jedem Fall berücksichtigt werden muss.

Die numerischen Berechnungen werden auf einem Gitter im Impulsraum durchgeführt. Die Magnonenkorrelationsfunktionen werden auf den Gitterpunkten definiert und es wird zwischen diesen Werten linear interpoliert. Es werden jeweils $N_\Theta = 40$ Gitterpunkte sowohl für parametrische als auch sekundäre Magnonen mit Winkeln Θ_i verwendet, die uniform aus dem Intervall $[0, \pi/2]$ gewählt werden. Die Längen der Wellenvektoren werden durch die numerische Lösung der Gleichungen $\epsilon_{\boldsymbol{k}_0} = \omega_0/2$ bzw. $\epsilon_{\boldsymbol{k}_1} = \omega_0$ bestimmt. Aufgrund der Symmetrie des Problems ist es ausreichend einen Quadranten des Impulsraums zu betrachten.

Die Anfangsbedingungen sind die thermische Verteilung der Magnonen außerhalb des Impulsgitters und Gl. (8.22) innerhalb des Impulsgitters mit dem Anfangswert $\gamma_{\boldsymbol{k}}^n = \gamma_{\boldsymbol{k}}^p = 2\gamma_0 = 1.05 \times 10^{-4}$ K für die Dämpfung. Die gesamte numerisch berechnete Magnonendichte, die durch Mittlung über die Gitterpunkte berechnet wurde, ist in Abb. 8.5 dargestellt. Bis etwa $H_0 \approx 100$ mT nimmt die Magnonendichte linear mit der Feldstärke zu. Bei $H_0 \approx 105$ mT können Peakstrukturen beobachtet werden. Im Einklang mit dem Experiment [46] sind für kleine Pumpstärken Dips zu sehen und für große Pumpstärken Peaks. Dieses Ergebnis kann nicht mithilfe von S-Theorie reproduziert werden. Dort wird eine näherungsweise lineare Abhängigkeit der Magnonendichte von der externen Feldstärke vorhergesagt.

Die Ursache für diesen Effekt sind die Konfluenz- und Splittingprozesse von Magnonen. Dies sieht man auch dadurch, dass ausschließlich diese Prozesse für die Berechnung der Stoßintegrale berücksichtigt wurden. In der Nähe der Konfluenzfeldstärke ist die Kopplung zwischen parametrischen und sekundären Magnonen wesentlich größer. Einerseits wird dadurch die Dämpfung erhöht, wodurch die Magnonendichte bei kleinen Pumpstärken kleiner ist. Falls die Pumpstärke allerdings groß genug ist, um diese Verluste auszugleichen, saturiert die Magnonendichte bei größeren Werten. Um zu diesem Ergebnis zu kommen, reicht es nicht aus, einen konstanten Dämpfungsterm einzuführen, so wie es häufig in der Literatur bezüglich S-Theorie anzufinden ist. Stattdessen muss die Abhängigkeit der Dämpfungskonstanten von der externen Feldstärke dadurch bestimmt werden, dass die Dämpfung aus der mikroskopischen Dynamik des Systems berechnet wird.

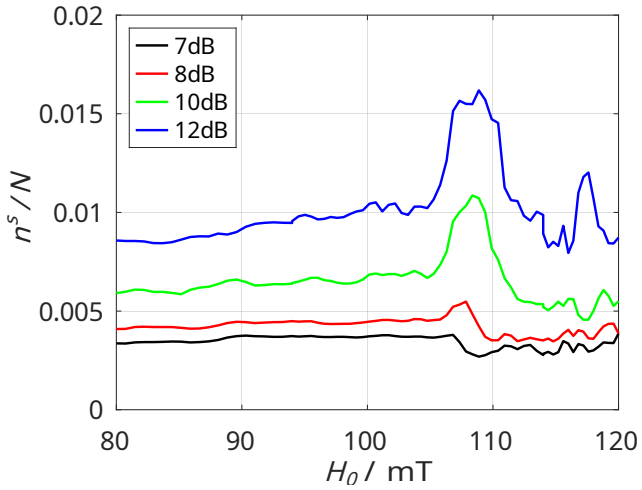

Figure 8.5: Die gesamte Magnonendichte im stationären Nicht-Gleichgewichtszustand ist über der externen magnetischen Feldstärke H_0 aufgetragen. Die Dicke des YIG-Films beträgt $d = 22.8$ µm und die Frequenz des oszillierenden magnetischen Feldes beträgt $\omega_0 = 13.857$ GHz. Die Stärke des oszillierenden Feldes wurde variiert, wobei 0 dB die Mindeststärke definiert, ab der parametrische Magnonen generiert werden.

8.4 Magnetoelastische Moden

8.4.1 Einleitung

Bisher wurden die Wechselwirkungen zwischen Magnonen und Phononen nicht explizit berücksichtigt. Auch in der Literatur wird dies häufig getan und die Phononen werden lediglich als Wärmebad berücksichtigt. Neue experimentelle und theoretische Methoden haben es jedoch besser möglich gemacht, Phänomene zu untersuchen, die von Mangon-Phononwechselwirkungen und der Hybridisierung von Magnonen und Phononen dominiert werden [21, 22, 23, 24, 25, 26, 27]. Daher ist dieses Thema in letzter Zeit interessanter geworden.

Ein weiteres interessantes Phänomen ist die Bildung einen Bose-Einsteinkondensats von Magnonen in YIG, das sowohl experimentell als auch theoretisch untersucht wurde [15, 17, 70]. Das Kondensat bildet sich im Minimum der Magnonendispersion, welches bei Wellenvektoren größer als null liegt. In einer Reihe kürzlich durchgeführter Experimente ist während des Kondensationsprozesses eine spontane Akkumulation von magnetoelastischen Bosonen beobachtet worden [28, 47]. Diese magnetoelastischen Moden haben etwa dieselbe Energie wie die kondensierten Magnonen im Minimum der Dispersion. Daher stellt sich die Frage, wie wichtig die Wechselwirkung zwischen den magnetoelastischen Moden und den kondensierten Magnonen ist. Obwohl das Phänomen bereits in Ref. [47] phänomenologisch untersucht worden ist, lässt diese phänomenologisch Untersuchung die Frage offen, ob die Akkumulation kohärent ist. Auch wenn diese nur in

einem sehr schmalen Bereich des Impulsraums beobachtet wird, ist dies kein eindeutiger Beleg für Kohärenz. Außerdem ist es erstrebenswert eine Theorie zu entwickeln, die von der mikroskopischen Dynamik des Systems ausgeht. Daher wird in diesem Kapitel dieselbe Methode wie im vorherigen Kapitel angewandt, um kinetische Gleichungen für die magnetoelastischen Moden aufzustellen.

8.4.2 Effektiver Magnon-Phonon-Hamiltonian

Neben dem magnonischen Teil des Hamiltonians, der bereits im vorherigen Kapitel eingeführt wurde, wird nun also explizit auch der phononische Teil des Hamiltonians betrachtet. Zunächst werden allerdings einige Vereinfachungen des Magnon-Hamiltonians vorgenommen. Da das System für große Zeiten nach abschalten des Pumpfeldes betrachtet wird, ist es nicht notwendig, ein oszillierendes Magnetfeld einzuführen. Die nebendiagonalen Terme tauchen daher im quadratischen Teil des Hamiltonians nicht auf. Die Drei-Magnonprozesse werden ebenfalls nicht berücksichtigt sowie diejenigen Magnon-Magnonwechselwirkungen, die die Zahl der Magnonen verändern. Dies ist dadurch begründet, dass nur kleine Wellenvektoren experimentell relevant sind. In diesem Bereich ist die Dispersionsrelation sehr flach. Um Energie- und Impulserhaltung für die Drei-Magnonprozesse und die Zwei-Teilchenprozesse, die die Anzahl der Magnonen ändern, zu erfüllen ist es daher notwendig, dass auch Magnonen mit sehr großen Energien und Impulsen involviert sind. Da diese Magnonen sich jedoch sehr nah am thermischen Gleichgewicht befinden, ist ihre Besetzung sehr klein. Diese Beiträge sind daher für die relevanten Effekte vernachlässigbar. Es gibt somit eine Näherungsweise $U(1)$ Symmetrie, was eine Voraussetzung für Bose-Einsteinkondensation ist [55].

Da in kollinearen Magneten die relativistischen Beiträge zu der Magnon-Phononkopplung bei kleinen Energien für gewöhnlich dominieren [82, 83], kann diese nicht einfach mithilfe eines effektiven Spin-Hamiltonians beschrieben werden. Denn die relativistischen Effekte beziehen die Ladungsfreiheitsgrade des Systems mit ein. Um den Wechselwirkungs-Hamiltonian aufzustellen, wird daher das Vorgehen gewählt, einen phänomenologischen Ausdruck für die magnetoelastische Energie zu quantisieren. Diese Methode basiert auf der Arbeit von Abrahams und Kittel [20] und ist in Ref. [21] im Detail beschrieben. Der gesamte Hamiltonian des Systems hat schließlich die Form [55]

$$\begin{aligned}\mathcal{H} &= \sum_{\boldsymbol{k}} \epsilon_{\boldsymbol{k}} b^\dagger_{\boldsymbol{k}} b_{\boldsymbol{k}} + \frac{1}{N} \sum_{\boldsymbol{k}_1,\ldots,\boldsymbol{k}_4} \delta_{\boldsymbol{k}_1+\cdots+\boldsymbol{k}_4,\boldsymbol{0}} \frac{1}{(2!)^2} \Gamma^{\bar{a}\bar{a}aa}_{1,2;3,4} b^\dagger_{-1} b^\dagger_{-2} b_3 b_4 \\ &\quad + \sum_{\boldsymbol{k},\lambda} \omega_{\boldsymbol{k},\lambda} \left(a^\dagger_{\boldsymbol{k},\lambda} a_{\boldsymbol{k},\lambda} + \frac{1}{2} \right) + \frac{1}{2} \sum_{\boldsymbol{k},\lambda} \gamma_{\boldsymbol{k},\lambda} \left(a_{-\boldsymbol{k},\lambda} + a^\dagger_{\boldsymbol{k},\lambda} \right) b_{\boldsymbol{k}} + \text{h.c.}, \quad (8.23)\end{aligned}$$

wobei $\omega_{\boldsymbol{k},\lambda}$ die Phononenergie ist und die Operatoren $a^\dagger_{\boldsymbol{k},\lambda}$ und $a_{\boldsymbol{k},\lambda}$ die Erzeugungs- und Vernichtungsoperatoren für Phonon der Mode λ sind. In der Summe über λ wird über eine longitudinale akustische Mode $\lambda = \parallel$ und zwei degenerierte transversale akustische Moden $\lambda = \perp 1, \perp 2$ summiert. Die Magnon-Phononkopplungskonstante $\gamma_{\boldsymbol{k},\lambda}$ ist im Haupttext angegeben ist. Durch die Magnon-Phononwechselwirkung kommt eine Hybridisierung von Magnonen und Phononen zu Stande. Der Hamiltonian kann mit einer

unitären Transformation diagonalisiert werden, sodass die beiden magnetoelastischen Bosonen durch einen quadratischen und einen quartischen Hamiltonian beschrieben werden. Die Dispersionsrelationen für die beiden magnetoelastischen Moden sind in Abb. 4.2 dargestellt. Die untere Mode ist in der Nähe des Hybridisierungsbereich mit dem Minimum der Magnonendispersion degeneriert.

Kinetische Gleichungen

Neben den Ein-Teilchenkorrelationsfunktionen für die beiden magnetoelastischen Moden

$$n^c_{\boldsymbol{k}\pm} \equiv \langle \psi^\dagger_{\boldsymbol{k}\pm} \psi_{\boldsymbol{k}\pm} \rangle^c \equiv \langle \psi^\dagger_{\boldsymbol{k}\pm} \psi_{\boldsymbol{k}\pm} \rangle - |\Psi_{\boldsymbol{k}\pm}|^2 \,, \tag{8.24}$$

ist es hier auch notwendig die Kondensatamplituden der magnetoelastischen Bosonen zu berücksichtigen, die definiert sind als der Vakuumerwartungswert der entsprechenden Vernichtungsoperatoren:

$$\Psi_{\boldsymbol{k}\pm} \equiv \langle \psi_{\boldsymbol{k}\pm} \rangle. \tag{8.25}$$

Die Korrelationsfunktionen erfüllen die Bewegungsgleichung

$$\partial_t n^c_{\boldsymbol{k}\pm} = I_{\boldsymbol{k}\pm}, \tag{8.26}$$

wobei $I_{\boldsymbol{k}\pm}$ ein Stoßintegral ist, das hier die Streuprozesse der magnetoelastischen Moden beschreibt. Die Kondensatamplituden erfüllen die übliche Gross-Pitaevskii-Gleichung, auf deren rechter Seite ebenfalls ein Stoßintegral eingeführt wird. Es ist außerdem notwendig, ein chemisches Potential μ_c einzuführen, das den Effekt des Pumpens auf das Magnonengas beschreibt. Die Bewegungsgleichung der Kondensatamplitude lautet also [55]

$$\begin{aligned} &\partial_t \Psi_{\boldsymbol{k}\pm} + i \left(E_{\boldsymbol{k}\pm} - \mu_c \right) \Psi_{\boldsymbol{k}\pm} + \frac{i}{2N} \sum_{\boldsymbol{q}_1, \boldsymbol{q}_2, \boldsymbol{q}_3} \delta_{\boldsymbol{q}_1 + \boldsymbol{q}_2 + \boldsymbol{q}_3, \boldsymbol{k}} \\ &\times \left[\Gamma^{\pm\pm\pm\pm}_{-\boldsymbol{k},1;2,3} \Psi^*_{-1\pm} \Psi_{2\pm} \Psi_{3\pm} + \Gamma^{\pm\pm\mp\mp}_{-\boldsymbol{k},1;2,3} \Psi^*_{-1\pm} \Psi_{2\mp} \Psi_{3\mp} \right] = \tilde{I}_{\boldsymbol{k}\pm}, \end{aligned} \tag{8.27}$$

Die Stoßintegrale werden analog zu dem Vorgehen im vorherigen Kapitel hergeleitet und sind in den Gleichungen (4.32) und (4.34) zu finden. Die approximierten kinetischen Gleichungen haben dieselbe Form wie die gewöhnlichen Boltzmann-Gleichungen, die aus der Literatur bekannt sind [87]. Der einzige Unterschied besteht darin, dass es zwei magnetoelastische Moden gibt.

8.4.3 Stationärer Nicht-Gleichgewichtszustand

Um die Thermalisierung des Systems beschreiben zu können, ist es notwendig, einen großen Bereich des Impulsraums zu berücksichtigen. Der Akkumulationsprozess findet andererseits in einem sehr kleinen Bereich in der Nähre des Hybridisierungsbereichs statt. Daher ist es schwierig, beide Prozesse gleichzeitig miteinzubeziehen. Stattdessen soll also nur der Akkumulationsprozess betrachtet werden. Zu diesem Zweck werden zwei Gitter

im Impulsraum eingeführt, je eines für die beiden magnetoelastischen Moden. Magnon-Magnonwechselwirkungen führen zu einer Thermalisierung des Magnonengases, sodass sich dieses in einem Quasigleichgewichtszustand befindet. Dieses wird mittels einer effektiven Temperatur T_m, welche sich eventuell von der Temperatur T der Phononen unterscheidet, und einem chemischen Potential μ_m beschrieben. Während des Pumpvorgangs formt sich ein Kondensat von Magnonen, wobei Magnonen durch Streuprozesse in das Minimum der Dispersionsrelation getrieben werden. Dabei nimmt das chemische Potential μ_m zu, bis es schließlich den Wert der Dispersion in ihrem Minimum erreicht [15, 16, 17, 78, 79, 80, 81]. Anschließend nimmt das chemische Potential nach Beendigung des Pumpvorgangs durch Magnon-Phononwechselwirkungen ab. Für die numerischen Berechnungen werden diese beiden Parameter selbstkonsistent bestimmt [55].

Ich nehme an, dass das Magnonengas außerhalb des Hybridisierungsbereichs thermalisiert ist. Innerhalb des Hybridisierungsbereichs kann die Magnonenverteilungsfunktion von der Bose-Verteilung abweichen. Auch hier wird die Verteilung im thermischen Quasigleichgewichtszustand als Anfangswert verwendet. Die Stoßintegrale verschwinden fast im gesamten Impulsraum. Lediglich in der Nähe des Hybridisierungsbereichs sind die Stoßintegrale von null verschieden. Außerdem muss der Bereich der oberen magnetoelastischen Mode berücksichtigt werden, für den die Energie mit der Energie im Hybridisierungsbereich übereinstimmt. Es werden also zwei Gitter im Impulsraum für beide magnetoelastischen Moden eingeführt. Es soll numerisch der stationäre Nicht-Gleichgewichtszustand des Systems auf eine selbstkonsistente Art und Weise bestimmt werden.

Die experimentellen Parameter sind $H = 145$ mT und $d = 6.7$ µm. Der Anfangswert für das chemische Potential wird als $\mu_m = 0.98\epsilon_{\boldsymbol{k}_{\min}}$ gewählt und die effektive Temperatur wird auf den Wert der Phononentemperatur gesetzt. Außerdem muss Berücksichtigt werden, dass das chemische Potential des Kondensats μ_c vom chemischen Potential des übrigen Magnonengases abweichen kann. Es wird auf den Wert $\mu_c = 0.995\epsilon_{\boldsymbol{k}_{\min}}$ festgesetzt. Die effektive Temperatur und das chemische Potential werden während den numerischen Berechnungen selbstkonsistent bestimmt. Es ergibt sich $T_m = 289.6$ K und $\mu_m = 0.978\epsilon_{\boldsymbol{k}_{\min}}$. Dass diese Werte nah an den Anfangswerten liegen, ist ein Anzeichen dafür, dass der Ansatz, den thermischen Quasigleichgewichtszustand zu verwenden, sinnvoll ist [55].

Die numerischen Ergebnisse für die Magnonendichte sind in Abb. 8.6 und 8.7 gezeigt. Man kann einerseits feststellen, dass es Abweichungen von dem thermischen Quasigleichgewichtszustand nur in zwei kleinen Bereichen des Impulsraums gibt, nämlich im Minimum der Magnonendispersion und im Hybridisierungsbereich für magnetoelastische Moden, die nahezu dieselbe Energie haben. Dieses Ergebnis stimmt zudem sehr gut mit dem Experiment überein [55]. Außerdem kann festgestellt werden, dass die Akkumulation der magnetoelastischen Moden vollkommen inkohärent ist, d.h. der Peak im Hybridisierungsbereich stammt ausschließlich von der verbundenen Korrelationsfunktion $n^c_{\boldsymbol{k}}$ und die Kondensatamplitude verschwindet überall außer im Minimum des Dispersion [55].

Weiterhin kann festgestellt werden, dass die Wechselwirkung der magnetoelastischen Moden mit dem Kondensat wesentlich für das beobachtete Phänomen ist. Dazu wird

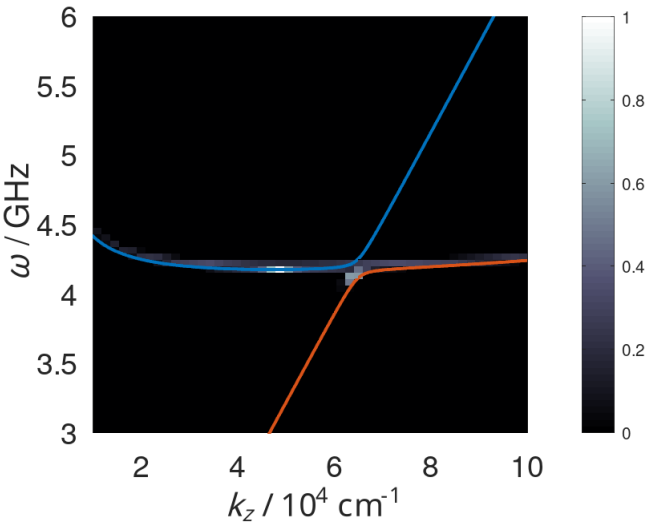

Figure 8.6: Die gesamte Magnonendichte normiert auf die Kondensatamplitude is in dem Phasenraum dargestellt, der durch den Wellenvektor in z-Richtung und die Anregungsenergie ω der Magnonen aufgespannt wird. Die blaue und rote Kurve stellt die Dispersion der oberen und unteren magnetoelastischen Moden senkrecht zum externen Magnetfeld dar.

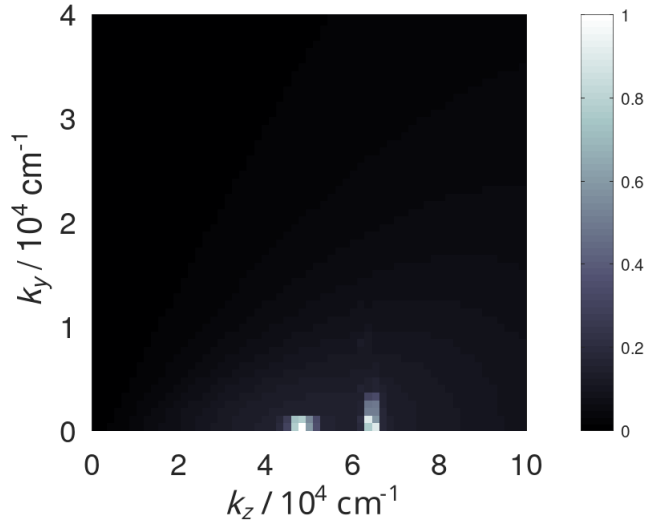

Figure 8.7: Die gesamt Magnonendichte ist im Impulsraum dargestellt. Diese ist dabei auf die Kondensatamplitude normiert. Der linke Peak ist auf das Kondensat zurückzuführen während der rechte Peak von dem Beitrag der inkohärenten magnetoelastischen Moden stammt. Die Magnonendichte ist wie in Abb. 8.6 normiert.

die numerische Simulation mit dem niedrigeren Wert $\mu_c = 0.75\epsilon_{\boldsymbol{k}_{\min}}$ für das chemische Potential durchgeführt, was den Fall beschreibt, dass das Magnonengas nicht stark genug gepumpt wurde, um ein Kondensat zu bilden. In diesem Fall ist der Peak der Magnonendichte im Hybridisierungsbereich wesentlich kleiner, aber noch vorhanden. Er hat dieselbe Größenordnung wie die thermische Verteilung der Magnonen im Minimum der Dispersion. Im Gegensatz dazu war die Größenordnung in der vorherigen Simulation diejenige der Kondensatamplitude. Auch dieses Ergebnis stimmt mit den Experimenten überein [47, 55].

8.5 Ladungsdichtewellen

8.5.1 Einleitung

In diesem Kapitel soll nun ein anderes System untersucht werden, nämlich ein elektronisches System, in dem Ladungsdichtewellen beobachtet werden können. Diese gehen aus einer Peierls-Instabilität hervor. Ladungsdichtewellen sind ein gutes Beispiel für spontane Symmetriebrechung in einem Festkörper. Diese kommt in diesem Fall dadurch zustande, dass die Energie des Ladungsdichtewellengrundzustands kleiner ist als die Energie des translationsinvarianten Grundzustands. Ich bin an dem Fall interessiert, dass der Wellenvektor der Ladungsdichtewellen inkommensurabel mit dem Gitter ist. In diesem Fall ist der Ordnungsparameter, der mit den Ladungsdichtewellen verbunden ist, komplexwertig. Weiterhin können die kollektiven Moden mittels einer Amplituden- und einer Phasenmode beschrieben werden. Fortschritte im Bereich der Terahertzspektroskopie haben detailliertere experimentelle Untersuchungen der Amplituden- und Phasenmoden ermöglicht [48, 50, 51]. Das Ziel in diesem Kapitel besteht darin, die Spektren der Amplituden- und Phasenmoden und die Temperaturabhängigkeit ihrer Dämpfung zu verstehen.

8.5.2 Hamiltonian

Der Ausgangspunkt für meine Untersuchungen ist der Fröhlich-Hamiltonian mit mehreren Phononmoden, der in der Literatur bereits zuvor verwendet wurde, um Ladungsdichtewellen zu untersuchen [30, 32]. Dabei beschränke ich mich auf den eindimensionalen Fall, da die relevanten Experimente an quasi-eindimensionalen Systemen durchgeführt wurden. Die Phononen müssen jedoch nach wie vor dreidimensional betrachtet werden. Der Hamiltonian lautet

$$\mathcal{H} = \sum_{\boldsymbol{k},\sigma} \epsilon_{\boldsymbol{k}} c^\dagger_{\boldsymbol{k},\sigma} c_{\boldsymbol{k},\sigma} + \sum_{\boldsymbol{q},\lambda} \omega_{\boldsymbol{q},\lambda} b^\dagger_{\boldsymbol{q},\lambda} b_{\boldsymbol{q},\lambda} + \frac{1}{\sqrt{\mathcal{V}}} \sum_{\boldsymbol{q},\boldsymbol{k},\lambda,\sigma} \gamma_{\boldsymbol{q},\lambda} c^\dagger_{\boldsymbol{k}+\boldsymbol{q},\sigma} c_{\boldsymbol{k},\sigma} X_{\boldsymbol{q},\lambda}, \tag{8.28}$$

wobei σ den Elektronenspin beschreibt, λ die Phononmode und $\boldsymbol{k}$ sowie $\boldsymbol{q}$ die Wellenvektoren der Elektronen und Phononen. Die Phononmoden können sowohl transversal als auch longitudinal sein. $X_{\boldsymbol{q},\lambda}$ ist das Verschiebungsfeld für Phononen, der definiert ist

als

$$X_{\boldsymbol{q},\lambda} = \frac{b_{\boldsymbol{q},\lambda} + (b_{-\boldsymbol{q},\lambda})^\dagger}{\sqrt{2\omega_{\boldsymbol{q},\lambda}}}. \tag{8.29}$$

Der Ordnungsparameter kann über die Erzeugungs- und Vernichtungsoperatoren der Phononen als

$$\Delta = \sum_\lambda \gamma_{\boldsymbol{Q},\lambda} \langle b_{\boldsymbol{Q},\lambda} + b^\dagger_{-\boldsymbol{Q},\lambda} \rangle \tag{8.30}$$

definiert werden, wobei $\boldsymbol{Q} = (0, 0, 2k_F)$ der Wellenvektor der Ladungsdichtewellen ist.

In der Mean-Field-Näherung wird der Verschiebungsoperator durch seinen Erwartungswert ersetzt. Es wird erwartet, dass in dem System Ladungsdichtewellen mit dem Wellenvektor $\boldsymbol{Q}$ auftreten, daher wird angenommen, dass der Erwartungswert nur für die Wellenvektoren $\pm\boldsymbol{Q}$ und $\boldsymbol{0}$ nicht-verschwindend ist. Der Verschiebungsoperator wird also ersetzt durch

$$X_{\boldsymbol{q},\lambda} \to X^{(0)}_{\boldsymbol{q},\lambda} = \sqrt{\mathcal{V}} \left[\delta_{\boldsymbol{q},\boldsymbol{0}} X^{(0)}_{\lambda,\boldsymbol{0}} + \delta_{\boldsymbol{q},\boldsymbol{Q}} X^{(0)}_{\boldsymbol{Q},\lambda} + \delta_{\boldsymbol{q},-\boldsymbol{Q}} X^{(0)}_{-\boldsymbol{Q},\lambda} \right], \tag{8.31}$$

wobei der Superskript null bedeutet, dass es sich um den Erwartungswert handelt. Innerhalb dieser Näherung ist es möglich, den elektronischen Teil des Hamiltonians mithilfe einer unitären Transformation zu diagonalisieren. Dies führt zu einem System mit zwei elektronischen Bändern, deren um die Fermifläche linearisierte Dispersion

$$E^\pm_{\boldsymbol{k}} \approx \pm E_{\boldsymbol{k}} = \pm\sqrt{v_F^2 k_z^2 + |\Delta|^2} \tag{8.32}$$

lautet. Die beiden elektronischen Fermionen werden durch die Erzeugungs- und Vernichtungsoperatoren $\left(d^\pm_{\boldsymbol{k}\sigma}\right)^\dagger$ und $d^\pm_{\boldsymbol{k}\sigma}$ beschrieben, die durch die im Haupttext beschriebene kanonische Transformation (5.15) eingeführt wurden. Dabei steht + für Leitungselektronen und − für Valenzelektronen.

In dieser Arbeit möchte ich allerdings über die Mean-Field-Näherung hinausgehen und den gesamten Fröhlich-Hamiltonian berücksichtigen. Später werde ich allerdings die kinetischen Gleichungen um das Mean-Field-Ergebnis herum linearisieren. Um einen Zusammenhang mit diesem herzustellen, wende ich die oben erwähnte unitäre Transformation auf den gesamten Fröhlich-Hamiltonian (8.28) an. Es ergeben sich dann dieselben beiden elektronischen Bänder, zusätzlich aber noch ein Elektron-Phononwechselwirkungsterm, in dem die Kopplung zu Phononen mit Wellenvektoren ungleich $\pm\boldsymbol{Q}$ auftaucht und der innerhalb der Mean-Field-Näherung vernachlässigt wird. Es wird sich später zeigen, dass dieser Wechselwirkungsterm zu einer Dämpfung des Ordnungsparameters im thermischen Mean-Field-Gleichgewichtszustand führt.

8.5.3 Kinetische Gleichungen

Es werden nun die elektronischen und phononischen Korrelationsfunktionen

$$f^{\pm}_{\boldsymbol{k},\sigma} \equiv \langle \left(d^{\pm}_{\boldsymbol{k},\sigma}\right)^{\dagger} d^{\pm}_{\boldsymbol{k},\sigma}\rangle^{c} = \langle \left(d^{\pm}_{\boldsymbol{k},\sigma}\right)^{\dagger} d^{\pm}_{\boldsymbol{k},\sigma}\rangle, \tag{8.33a}$$

$$\tilde{f}^{\pm}_{\boldsymbol{k},\sigma} \equiv \langle \left(d^{\pm}_{\boldsymbol{k},\sigma}\right)^{\dagger} d^{\mp}_{\boldsymbol{k},\sigma}\rangle^{c} = \langle \left(d^{\pm}_{\boldsymbol{k},\sigma}\right)^{\dagger} d^{\mp}_{\boldsymbol{k},\sigma}\rangle, \tag{8.33b}$$

$$n^{(1,2)}_{\boldsymbol{q},\lambda} \equiv \langle \left(b^{(1,2)}_{\boldsymbol{q},\lambda}\right)^{\dagger} b^{(1,2)}_{\boldsymbol{q},\lambda}\rangle^{c} = \langle \left(b^{(1,2)}_{\boldsymbol{q},\lambda}\right)^{\dagger} b^{(1,2)}_{\boldsymbol{q},\lambda}\rangle - \langle \left(b^{(1,2)}_{\boldsymbol{q},\lambda}\right)^{\dagger}\rangle\langle b^{(1,2)}_{\boldsymbol{q},\lambda}\rangle, \tag{8.33c}$$

eingeführt, für die kinetische Gleichungen aufgestellt werden müssen. $\left(b^{(1,2)}_{\boldsymbol{q},\lambda}\right)^{\dagger}$ und $b^{(1,2)}_{\boldsymbol{q},\lambda}$ sind die Erzeugungs- und Vernichtungsoperatoren von Amplituden- (1) und Phasenphononen (2). Es taucht eine gemischte Verteilungsfunktion $\tilde{f}^{\pm}_{\boldsymbol{k},\sigma}$ auf, die beide Arten von elektronischen Operatoren enthält. Es gibt zwei phononische Verteilungsfunktionen $n^{(1)}_{\boldsymbol{q},\lambda}$ und $n^{(2)}_{\boldsymbol{q},\lambda}$, wobei der Superskript 1 die Amplitudenmoden und 2 die Phasenmoden bezeichnet. Es ist außerdem notwendig, die Vakuumerwartungswerte der Vernichtungsoperatoren für die Amplituden- und Phasenmoden zu berücksichtigen, die definiert sind als

$$\psi^{(1)}_{\boldsymbol{q},\lambda} \equiv \langle b^{(1)}_{\boldsymbol{q},\lambda}\rangle, \tag{8.34a}$$

$$\psi^{(2)}_{\boldsymbol{q},\lambda} \equiv \langle b^{(2)}_{\boldsymbol{q},\lambda}\rangle. \tag{8.34b}$$

Die Bewegungsgleichungen des nicht-wechselwirkenden Systems ergeben sich, wie auch in den vorherigen Kapiteln, aus den Heisenberg'schen Bewegungsgleichungen für die quadratischen Hamiltonoperatoren. Auf der rechten Seite werden Stoßintegrale eingeführt, die die Elektron-Phononwechselwirkungen beschreiben. Die Bewegungsgleichungen lauten also

$$\frac{d}{dt} f^{\pm}_{\boldsymbol{k},\sigma} = I^{\pm}_{\boldsymbol{k},\sigma}, \tag{8.35a}$$

$$\frac{d}{dt} \tilde{f}^{\pm}_{\boldsymbol{k},\sigma} = \tilde{I}^{\pm}_{\boldsymbol{k},\sigma}, \tag{8.35b}$$

$$\frac{d}{dt} n^{(1,2)}_{\boldsymbol{q},\lambda} = I^{(1,2)}_{\boldsymbol{q},\lambda}, \tag{8.35c}$$

$$\frac{d}{dt}\psi^{(1,2)}_{\boldsymbol{q},\lambda} + i\omega_{\boldsymbol{q},\lambda}\psi^{(1,2)}_{\boldsymbol{q},\lambda} = J^{(1,2)}_{\boldsymbol{q},\lambda}. \tag{8.35d}$$

Das Vorgehen, um die Stoßintegrale herzuleiten, ist analog zu dem Vorgehen, das in den vorherigen zwei Kapiteln verwendet wurde. Details dazu finden sich im Haupttext. Für das Stoßintegral $\tilde{I}^{\pm}_{\boldsymbol{k},\sigma}$ der gemischten elektronischen Verteilungsfunktion ist allerdings zu beachten, dass das Stoßintegral komplexwertig ist. Im Gegensatz zu dem Stoßintegral $I^{\pm}_{\boldsymbol{k},\sigma}$ tauchen hier keine komplex konjugierten Beiträge auf, sodass der Imaginärteil übrig bleibt. Nun ist es so, dass der Hauptwert der Stoßintegrale, der im Zusammenhang mit der Markov-Näherung auftaucht, rein imaginär ist. In den vorherigen Kapiteln fiel der

Imaginärteil der Stoßintegrale weg, sodass der Hauptwert nicht berechnet werden musste. Für das Stoßintegral $\tilde{I}^{\pm}_{\boldsymbol{k},\sigma}$ ist der Hauptwert jedoch relevant. Dieser Beitrag beschreibt den Realteil der Selbstenergie und ist somit relevant für die Frequenzrenormierung des Ordnungsparameters. Daher muss der Hauptwert des Stoßintegrals $\tilde{I}^{\pm}_{\boldsymbol{k},\sigma}$ ebenfalls berechnet werden. Die Stoßintegrale für die phononischen Vakuumerwartungswerte sind in Gl. (5.33) zu finden und die Realteile der elektronischen Stoßintegrale sind in Gl.(5.35) zu finden. Die Hauptwerte des Stoßintegrals $\tilde{I}^{\pm}_{\boldsymbol{k},\sigma}$ finden sich in Gl. (5.39).

8.5.4 Linearisierte kinetische Gleichungen

Da die Ausdrücke für die Stoßintegrale kompliziert sind, sollen diese nun linearisiert werden. Außerdem ermöglicht dieses Vorgehen einen Vergleich der kinetischen Theorie zu anderen Methoden. Die Linearisierung erfolgt um den thermischen Mean-Field-Gleichgewichtszustand. Um diesen zu bestimmen, muss zunächst aus der Bewegungsgleichung der Vakuumerwartungswerte (8.35d) die Bewegungsgleichung für den Ordnungsparameter bestimmt werden. Es ist anschließend möglich, einen stationären Zustand dieser Gleichung zu finden. Im thermischen Gleichgewichtszustand reduziert sich die entsprechende Selbstkonsistenzgleichung auf die Mean-Field-Selbstkonsistenzgleichung, die aus der Literatur bekannt ist und lautet

$$1 = \frac{g_0}{\mathcal{V}} \sum_{\boldsymbol{k}} \frac{1}{2E_{\boldsymbol{k}}} \tanh\left(\frac{\beta E_{\boldsymbol{k}}}{2}\right), \tag{8.36}$$

wobei β die inverse Temperatur ist und g_0 eine Konstante ist. Diese Gleichung kann numerisch gelöst werden (siehe Abb. 5.6).

Die kinetischen Gleichungen werden nun um die Mean-Field-Lösung linearisiert, d.h. der Ordnungsparameter wird geschrieben als

$$\Delta(t) = \Delta_0 + \delta(t), \tag{8.37}$$

wobei Δ_0 der Mean-Field-Ordnungsparameter ist und $\delta(t)$ eine kleine Fluktuation bezeichnet. Die Verteilungsfunktionen $f^{\pm}_{\boldsymbol{k},\sigma}$, $\tilde{f}^{\pm}_{\boldsymbol{k},\sigma}$ und $n^{(1,2)}_{\boldsymbol{q},\lambda}$ werden auf die entsprechenden thermischen Verteilungen gesetzt. Für die Verteilungsfunktionen werden also Fluktuationen vernachlässigt. Die Bewegungsgleichung für die Ordnungsparameterfluktuation $\delta(t)$ kann in eine Form geschrieben werden, die dieselbe ist wie die Form der phänomenologischen Ginzburg-Landau-Gleichungen, wenn die Fluktuationen der Phononkoordinaten $\delta\xi_\lambda(t)$ eingeführt wird. Die Bewegungsgleichungen haben dann die Form

$$\frac{d^2}{dt^2}\delta(t) = -\sum_\lambda \omega_\lambda^2 \delta_\lambda(t) - \sum_\lambda |\gamma_\lambda|^2 \tilde{F}\delta(t) - C\tilde{\Gamma}\left[\frac{d}{dt}\delta(t) + \sum_\lambda \omega_\lambda \delta\xi_\lambda(t)\right], \tag{8.38a}$$

$$\frac{d^2}{dt^2}\delta\xi_\lambda(t) = -\omega_\lambda^2\delta\xi_\lambda(t) + \frac{\frac{|\gamma_\lambda|^2}{\omega_\lambda}}{\sum_\mu \frac{|\gamma_\mu|^2}{\omega_\mu^2}} \sum_\mu \omega_\mu \delta\xi_\mu(t) + |\gamma_\lambda|^2 \tilde{\Gamma}\delta(t) - C\tilde{F}\frac{\partial}{\partial t}\delta(t), \tag{8.38b}$$

wobei $\tilde{\Gamma}$ die dimensionslose Dämpfungskonstante ist, $\tilde{F}$ eine dimensionslose Konstante ist, die die Frequenzrenormierung durch die Selbstenergie beschreibt, und C eine Konstante ist. Abb. 5.8 zeigt die Temperaturabhängigkeit von $\tilde{\Gamma}$ und $\tilde{F}$. Der Ausdruck $\tilde{\Gamma}$ rührt von den elektronischen Stoßintegralen $\tilde{I}^{\pm}_{\boldsymbol{k}}$ her und ist auf die Wechselwirkung von Elektronen mit Nicht-$2k_F$-Phononen zurückzuführen, während der Ausdruck $\tilde{F}$ von den Hauptwerten der Stoßintegrale stammt.

Falls die Kopplung zwischen den Amplituden- und Phasenmoden vernachlässigt wird, ist die Frequenz der Amplitudenmoden gegeben durch

$$\tilde{\omega}_\lambda^2 = \omega_\lambda^2 + |\gamma_\lambda|^2 \, \tilde{F}, \tag{8.39}$$

während sich die Frequenz der Phasenmode dadurch ergibt, dass Gl. (8.38b) diagonalisiert wird. Die exakten Bewegungsgleichungen (8.38) können durch einen Exponentialansatz gelöst werden. Dies führt auf eine Selbstkonsistenzgleichung für die Frequenzen und Dämpfungskonstanten der Amplituden- und Phasenmoden, die numerisch gelöst werden kann. Die Ergebnisse der numerischen Berechnungen sind in Abb. 8.8 gezeigt, wobei die Phononfrequenzen ω_λ und die Elektron-Phononkopplungskonstanten γ_λ durch Fits an die experimentellen Daten aus Ref. [49] bestimmt wurden. Die Ergebnisse stimmen mit Ausnahme der untersten Phasenmode gut mit den experimentellen Daten überein.

Wie bereits erwähnt, stimmen die linearisierten Bewegungsgleichungen mit den phänomenologischen Bewegungsgleichungen überein, die sich innerhalb der Ginzburg-Landau-Theorie ergeben. Zu erwähnen ist, dass im Gegensatz zu der phänomenologischen Theorie die hier entwickelte kinetische Theorie von der mikroskopischen Dynamik des Systems ausgeht. Insbesondere ergibt sich die Frequenzrenormierung des Ordnungsparameters und die Dämpfungskonstante aus der mikroskopischen Dynamik des Systems, wohingegen bei der phänomenologischen Ginzburg-Landau-Theorie diese für gewöhnlich als weitere freie Parameter an experimentelle Daten gefittet werden.

Es lässt sich auch der Zusammenhang zu der Gauß'schen Näherung [37] feststellen. Innerhalb dieser taucht keine Dämpfung auf, sodass zwecks des Vergleichs der beiden Methoden die Dämpfungsterme in den linearisierten Bewegungsgleichungen vernachlässigt werden sollten. In diesem Fall erhält man zwei Selbstkonsistenzgleichungen für Amplituden- und Phasenmoden, da ohne die Dämpfungskonstante die beiden Gleichungen entkoppeln. Ein Exponentialansatz führt auf die beiden Selbstkonsistenzgleichungen

$$\left[\sum_\lambda \frac{|\gamma_\lambda|^2}{\omega_\lambda^2 - \nu_\lambda^2}\right]^{-1} + \tilde{F} = 0, \tag{8.40a}$$

$$\left[\sum_\lambda \frac{|\gamma_\lambda|^2}{\omega_\lambda^2 - \tilde{\nu}_\lambda^2}\right]^{-1} - \left[\sum_\lambda \frac{|\gamma_\lambda|^2}{\omega_\lambda^2}\right]^{-1} = 0. \tag{8.40b}$$

Die Form dieser Gleichungen ist konsistent mit der Gauß'schen Näherung, in welcher anstelle des Ausdrucks $\tilde{F}$ eine Polarisationsfunktion auftaucht, die Beiträge von Teilchen-Loch-Blasen enthält. Diese Funktion unterscheidet sich innerhalb der beiden Methoden

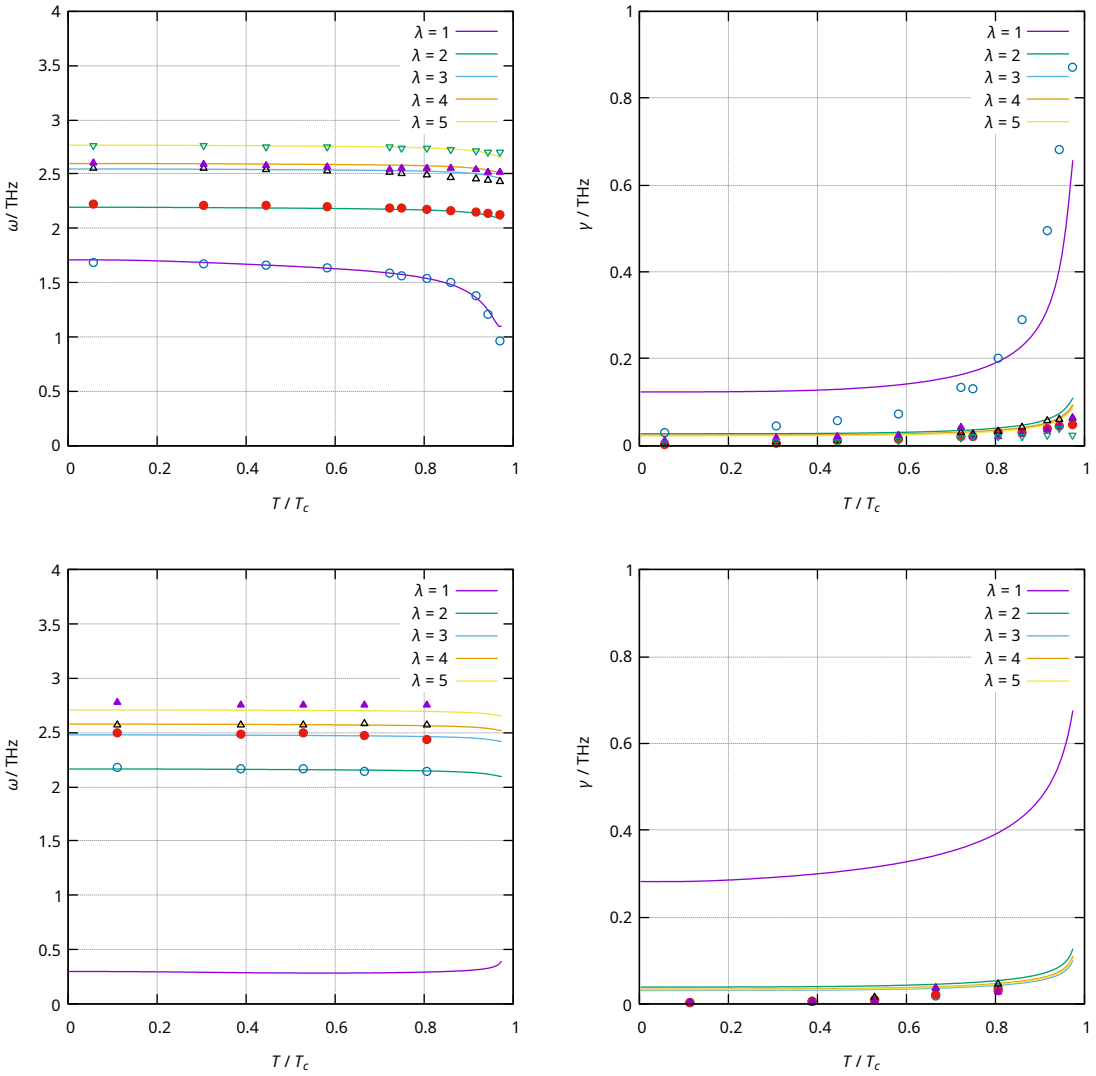

Figure 8.8: Numerische Auswertung der Frequenzen und Dämpfungsraten der Amplituden- und Phasenmoden, die aus der Lösung der Selbstkonsistenzgleichung (5.68) bestimmt wurden, während die Phononfrequenzen ω_λ und die Elektron-Phononkopplungskonstanten γ_λ durch Fits an die experimentelle Daten aus Ref. [49] bestimmt wurden. Die Punkte zeigen die experimentellen Daten. Für das Fitten wurde die niedrigste Phasenmode ignoriert.

quantitativ. Dies liegt daran, dass innerhalb der Methode der kinetischen Gleichungen zusätzlich zu Teilchen-Loch-Blasen ebenfalls Vertexkorrekturen aufsummiert werden, die innerhalb der Gauß'schen Näherung nicht auftauchen.

Schließlich wird ebenfalls die Coulomb-Wechselwirkung eingeführt und Abschirmung wird analog zu RPA mithilfe von kinetischen Gleichungen behandelt. Es stellt sich jedoch heraus, dass die aus der Coulomb-Wechselwirkung resultierenden Stoßintegrale im thermischen Gleichgewichtszustand verschwinden. Der Effekt der Coulomb-Wechselwirkung liegt in der Nähe des thermischen Gleichgewichtszustands hauptsächlich darin, dass die Dämpfung des Ordnungsparameters leicht erhöht wird. Somit ist die Coulomb-Wechselwirkung nicht relevant, um die experimentellen Beobachtungen zu erklären.

8.6 Zusammenfassung und Fazit

In dieser Arbeit wurden verschiedene Systeme im Nicht-Gleichgewicht untersucht. Dies erfolgte in allen Fällen mit derselben Methode. Es wurden kinetische Gleichungen mithilfe einer diagrammatischen Methode aufgestellt. Diese Methode wurde wiederum mithilfe von erzeugenden Funktionalen für verbundene Korrelationsfunktionen analog zu Ref. [52] hergeleitet; dieser Formalismus wurde schon in Ref. [44] eingeführt. Die Vorteile dieser Methode liegen zum einen darin, dass man direkt eine Hierarchie von Bewegungsgleichungen für ein-zeitige verbundene Korrelationsfunktionen erhält, und andererseits gibt es zudem ein Schema, mit dem die unendliche Hierarchie von Bewegungsgleichungen systematisch bei beliebiger Ordnung entkoppelt werden kann. Erst dadurch erhält man ein geschlossenes Differentialgleichungssystem, dass direkt numerisch gelöst werden kann.

Zunächst wurde die Dämpfung von parametrisch gepumpten Magnonen in YIG aus den mikroskopischen Stoßintegralen im stationären Nicht-Gleichgewichtszustand berechnet. Diese Stoßintegrale haben eine komplizierte Struktur, die zu einer nicht-monotonen Abhängigkeit von der Stärke des externen Magnetfeldes führt, welche scharfe Peakstrukturen in der Nähre der Konfluenzfeldstärke ausweist [54]. Diese Feldstärke ist dadurch definiert, dass dort Konfluenzprozesse von Magnonen mit gleichem Wellenvektor kinematisch möglich sind. Aufgrund der Nicht-Linearität der Magnonen führt dieser Peak in der Stärke der Dämpfung abhängig von der Pumpstärke entweder zu einem niedrigeren oder höheren Saturierungsniveau der Magnonendichte in Übereinstimmung mit den experimentellen Ergebnissen [46].

Indem explizit Magnon-Phononwechselwirkungen berücksichtigt werden, konnte ich die Akkumulation von magnetoelastischen Moden im stationären Quasigleichgewichtszustand in der Nähe des Magnon-Phononhybridisierungsbereichs beobachten [54]. Das Ergebnis stimmt gut mit den experimentellen Beobachtungen für YIG überein. In der Literatur werden Magnon-Phononwechselwirkungen häufig nicht explizit berücksichtigt und Phononen werden lediglich als zusätzliches Wärmebad für die Magnonen betrachtet. Diese Vorgehensweise wird üblicherweise damit begründet werden, dass die Magnon-Phononwechselwirkung sehr schwach ist. Für das hier untersuchte Phänomen ist allerdings die Magnon-Phononwechselwirkung verantwortlich, genauer die Hybridisierung

von Magnonen und Phononen. Die Dispersion der magnetoelastischen Moden hat einen Punkt, der die selbe Energie wie das Minimum der Magnonendispersion aufweist. Die Wechselwirkungen zwischen dem makroskopisch besetzten Magnonenkondensat und der energetisch degenerierten magnetoelastischen Mode führt zu dem beobachteten Akkumulationsphänomen, obwohl die Magon-Phononwechselwirkung relativ schwach ist.

Bezüglich Systemen, die Ladungsdichtewellen aufweisen, ist es mithilfe der kinetischen Theorie, die ich in dieser Arbeit entwickelt habe, möglich, die Zeitentwicklung des Ordnungsparameters auch weit entfernt vom thermischen Gleichgewicht zu untersuchen. Diese Möglichkeit wurde sicherlich noch nicht ausgereizt, was auch teilweise damit zusammenhängt, dass es nur wenige experimentelle Daten dazu gibt. In dieser Arbeit bin ich insbesondere auf die Situation im thermischen Gleichgewichtszustand eingegangen, um die theoretischen Ergebnisse mit experimentellen Daten zu vergleichen. Die Temperaturabhängigkeit der Frequenzen und der Dämpfungskonstanten der Amplituden- und Phasenmoden, die aus den linearisierten kinetischen Gleichungen bestimmt werden können, stimmt gut mit den experimentellen Beobachtungen überein [49]. Insbesondere gibt es eine starke Temperaturabhängigkeit der Dämpfung nahe der kritischen Temperatur. Außerdem wurde die hier entwickelte Methode mit anderen Methoden verglichen, nämlich mit den phänomenologischen Ginzburg-Landau-Gleichungen [48, 50, 51] und der Gauß'schen Näherung [37]. Es stellt sich heraus, dass die linearisierten kinetischen Gleichungen dieselbe Form wie die phänomenologischen Ginzburg-Landau-Gleichungen haben. Im Unterschied zu der phänomenologischen Methode wird hier allerdings die Dämpfung des Ordnungsparameters mithilfe von mikroskopischen Stoßintegralen bestimmt anstelle von Fits an experimentelle Daten. Der Vorteil der kinetischen Theorie bezüglich der Gauß'schen Näherung liegt einerseits darin, dass die Dämpfung relativ leicht bestimmt werden kann und dass andererseits die Zeitentwicklung des Ordnungsparameters und der elektronischen sowie phononischen Verteilungsfunktionen bestimmt werden kann - auch weit entfernt vom thermischen Gleichgewicht.

Schließlich wurde die Coulomb-Wechselwirkung in die Beschreibung des Systems aufgenommen. Dabei stellt sich allerdings heraus, dass sich das System in der Nähe des thermischen Gleichgewichtszustands qualitativ nicht anders verhält, wenn die Coulomb-Wechselwirkung explizit berücksichtigt wird. Der Haupteffekt liegt hier darin, dass die Dämpfung des Ordnungsparameters leicht zunimmt. Dieser Effekt ist allerdings zu klein, um für die hier berücksichtigten Experimente relevant zu sein. Die zusätzlichen Stoßintegrale, die von der Coulomb-Wechselwirkung stammen, verschwinden im thermischen Gleichgewichtszustand exakt. Daher liefern diese nur weit entfernt vom thermischen Gleichgewichtszustand potentiell einen signifikanten Beitrag. Dieser kann mit der hier hergeleiteten kinetischen Theorie untersucht werden und es ist zu vermuten, dass Effekte, die nur mithilfe der Coulomb-Wechselwirkung erklärbar sind, in diesem Bereich zu finden sind.

9 Publikationsliste

- M. O. Hansen, Y. Palan, V. Hahn, M. D. Thomson, K. Warawa, H. G. Roskos, J. Demsar, F. Pientka, O. Tsyplyatyev, and P. Kopietz, *Collective modes in the charge-density wave state of $K_{0.3}MoO_3$: The role of long-range Coulomb interactions revisited*, arXiv:2303.08580 (2023).

- V. Hahn, P. Frey, A. A. Serga, V. I. Vasyuchka, B. Hillebrands, P. Kopietz und A. Rückriegel, *Accumulation of magnetoelastic bosons in yttrium iron garnet: Kinetic theory and wave-vector-resolved Brillouin light scattering*, Phys. Rev. B **105**, 144421 (2022).

- V. Hahn and P. Kopietz, *Effect of magnon decays on parametrically pumped magnons*, Phys. Rev. B **103**, 094416 (2021).

- V. Hahn and P. Kopietz, *Collisionless kinetic theory for parametrically pumped magnons*, Eur. Phys. J. B **93**, 132 (2020).

GOETHE
UNIVERSITÄT
FRANKFURT AM MAIN